Mercury's Magnetospheric Cusps and Cross-Tail Current Sheet: Structure and Dynamics

by

Gang Kai Poh

A dissertation submitted in partial fulfillment
of the requirements for the degree of
Doctor of Philosophy
(Atmospheric, Oceanic and Space Sciences)
in The University of Michigan
2017

Doctoral Committee:
  Professor James A. Slavin, Co-Chair
  Professor Xianzhe Jia, Co-Chair
  Professor Mark J. Kushner
  Dr. Guan Le, NASA Goddard Space Flight Center
  Dr. Jim M. Raines

Gang Kai Poh

gangkai@umich.edu

ORCID ID: 0000-0002-5775-2006

DEDICATIONS

In Dedication To My Grandparents,

Who Always Inspire Me To Dream Big

And Reach For The Stars.

ACKNOWLEDGEMENTS

I would like to thank my committee members for taking the time to serve on my PhD committee. I would also like to give special thanks to Dr. Guan Le for flying out to Michigan for my defense.

It is my privilege to be under the tutelage of Jim Slavin in University of Michigan. Jim is an encouraging and nurturing mentor, who values my opinion as a space physicist and constantly pushes me to better myself, but never set goals that can't be reached. He also believes that every student should have the opportunity to show their work to the scientific community through conferences, meetings and visits. As a graduate student, I was fortunate to have the opportunity to attend conferences and interact with my peers/collaborators. Science is not the only thing that I learned from Jim over the course of my PhD. As a successful NASA executive himself, he occasionally shared with me how to maintain balance in life and career. Before I started graduate school, I was told by my peers that the relationship between a PhD advisor and student is equivalent to marriage. Looking back five years later, it is my honor to have studied under Jim Slavin.

I want to give thanks to my PhD co-advisor, Prof. Xianzhe Jia, who has been mentoring me on the data analysis of my thesis. Without any prior knowledge on numerical methods, I was having difficulties analyzing data using advanced analysis tools. Xianzhe patiently mentors and teaches me on how to analyze the data using various numerical methods. He also taught me how to appreciate numerical simulations when I was given the chance to work with the Michigan SWMF model for Mercury. I am grateful to have had the opportunity to be co-advised by Xianzhe.

I am also grateful to all my collaborators, who had worked with me to make this PhD thesis possible. In particular, I would like to thank Gina DiBraccio and Suzie Imber for being a good friend and mentor to me. In my first year of graduate school, I was still trying to get my feet wet in research and data analysis. They were very helpful in guiding me through the tedious process of coding up some of the analysis tools (e.g. MVA) and gave me helpful academic/career advice to help me with some of the important decision-making process. I want to also thank Jim Raines for assisting me with the FIPS data. Without it, this thesis and my PhD education wouldn't be complete.

There isn't a word in the lexicon that could fully express my gratitude to my parents for supporting my decision to pursue my academic interest in space physics in the United States. As my father always said to me, "You could achieve anything you want so long you put your mind into it"; that piece of advice has served me well till today. They firmly believed in me and my decision to pursue a degree in space physics seven years ago, and they couldn't be more proud to see me finish my doctoral degree.

I would also like to express my utmost appreciation to my wife, Christina. She has always been my one and only fan. She is the first to celebrate my accomplishment, no matter how small it is. Her creativity encourages me to see the brighter sides of things and her humor makes me laugh even when I am at my lowest. To my dog, Artemis, who wakes me up at 5 am every morning so that I could write my dissertation. Although I could have finished this dissertation two months earlier if she had learned how to "roll" sooner, she gives me joy with her silliness.

Lastly, I would like to extend my thanks to my two brothers and extended family for being there for me throughout my PhD. I would also like to thank my friends in "The Vault" (Doga Ozturk, Pat Tracy, Jamie Jasinki, Mojtaba Akhavantafti and Ryan Dewey) for being not just wonderful co-workers, but also good friends. Thank you for the group lunches, bar hopping, gossips and taking care of Artemis while I am away.

In short, it really does take a village to complete a PhD!

PS: English is my first language. And I am NOT Japanese, Vietnamese or Korean!

TABLE OF CONTENT

DEDICATION……………………………………………………………………….ii

ACKNOWLEDGEMENTS………………………………………………………....iii

LIST OF FIGURES………………………………………………………………..viii

LIST OF TABLES…………………………………………………………….....xviii

GLOSSARY OF TERMS..…………………………………………………….....xix

LIST OF SYMBOLS AND ACRONYMS……………….…………………………..xxi

ABSTRACT……………………………………………………………………...xxiii

CHAPTERS

I. INTRODUCTION………………………………………………………………1

1.1 Mercury's Magnetosphere…………………………………………………..1
1.2 Interplanetary Environment at Mercury….…………………………………7
1.3 Magnetic Reconnection……………………………………………………10
1.4 Flux Transfer Events……………………………………………………….13
1.5 Magnetotail X-lines and Substorms………………………………………..22
1.6 Magnetotail Dawn-Dusk Asymmetries…………………………………….26
1.7 Summary…………………………………………………………………...30
References……………………………………………………………………...32

II. MESSENGER MISSION AND INSTRUMENTATION…………………………….39

2.1 MESSENGER Mission……………………………………………………...39
2.2 Magnetometer……………………………………………………………..42
2.3 Fast Imaging Plasma Spectrometer…………………………………………44
References……………………………………………………………………….46

III. MHD CURRENT LAYERS, FILAMENTS AND FLUX ROPE ANALYSIS TECHNIQUES…………………………………………………………………47

3.1 Minimum Variance Analysis…………………………………………………...47
  3.1.1 Theory……………………………………………………………………47
  3.1.2 Application of Minimum Variance Analysis………………………………..51
  3.1.3 Limitation………………………………………………………………...54
3.2 deHoffmann-Teller Analysis……………………………………...…………55
  3.2.1 Theory……………………………………...…………………………….55
  3.2.2 Application of deHoffmann-Teller Analysis………………………………..56
  3.2.3 Limitation……………………………………...………………………57
3.3 Grad-Shafranov Reconstruction……………………………………...……...58
  3.3.1 Theory……………………………………..……................................58
  3.3.2 Application of Grad-Shafranov Reconstruction……………………………60
  3.3.3 Limitation……………………………………………………………...62
3.4 Conclusion……………………………………………………………………...64
References………………………………………………………………………65

IV. MESSENGER OBSERVATION OF CUSP PLASMA FILAMENT AT MERCURY………………………………………………………67

Abstract……………………………………………………………………………67
4.1 Introduction………………………………………………………………………68
4.2 MESSENGER Instrumentation and Cusp Filament Identification……………….70
4.3 Analysis Results for High-Altitude Filaments……………………………………77
  4.3.1 Population I……………………………………………………………………79
  4.3.1 Population II..…………………………………………………………………82
  4.3.1 Population III & IV……………………………………………………………84
  4.3.1 Flux Ropes…………………………………………………………………….87
  4.3.1 FIPS Plasma Measurements…...………………………………………………88
4.4 Analysis Results for Low-Altitude Filaments……………………………………90
4.5 Physical Properties and Spatial Distribution……………………………………...93
4.6 Discussion………………………………………………………………………101
References……………………………………………………………………...109

V. MERCURY’S CROSS-TAIL CURRENT SHEET: STRUCTURE, STRESS BALANCE AND X-LINE LOCATION……………………………………………115

Abstract…………………………………………………………………………...115
5.1 Introduction……………………………………………………………………...116
5.2 MESSENGER Instrumentation and Tail Current Sheet Crossing Identification……………………………………………………………..117
5.3 Analysis………………………………………………………………………….119
  5.3.1 Downtail Variation of CPS and Lobe Magnetic Field…………………….119
  5.3.2 Harris Current Sheet Modelling ……………………………………………..120

5.3.3 Downtail Variation of B_Z and Plasma Pressure in the Central Plasma Sheet…………………………………………………..123
5.3.4 Central Plasma Sheet Stress Balance…………………………………...124
5.4 Discussion……………………………………………………………………126
References…………………………………………………………………...129

VI. ON THE DAWN-DUSK ASYMMETRIES IN MERCURY’S CROSS-TAIL CURRENT SHEET……………………………………………………………….133

Abstract…………………………………………………………………….....133
6.1 Introduction………………………………………………………………...134
6.2 MESSENGER Instrumentation and Event Selection……………………………137
6.3 Analysis……………………………………………………………………….139
6.3.1 Cross-Tail Variation of B_Z……………………………………………………139
6.3.2 Plasma Beta β………………………………………………………...142
6.3.3 Current Sheet Thickness and Current Density…………………………….143
6.4 Discussion…………………………………………………………………….144
6.4.1 First Possible Observation of Mercury’s Substorm Current Wedge………145
6.4.2 Mercury’s Magnetotail Asymmetry……………………………………….149
References…………………………………………………………………...153

VII. CONCLUSION……………………………………………………………...160

VIII. FUTURE WORK…………………………………………………………....164

8.1 Case Studies of Mercury’s Flux Transfer Event and Filament Showers………..164
8.2 Mercury’s Substorm Current Wedge…………………………………………167
References…………………………………………………………………...168

LIST OF FIGURES

1.1 (a) Trajectory of Mariner 10 spacecraft and the projection of the magnetic field vectors in the ecliptic X–Z plane (top) and equatorial X–Y plane (bottom). (b) Magnitude of the magnetic field vectors measured during Mariner 10 third flyby encounter. Φ and ϑ represents the latitude with respect to the ecliptic and longitude with respect to the Sun-Mercury line respectively. Figure taken from *Ness et al.,* [1976]……………………………………………………………..2

1.2 Magnetic field measurements in the Mercury Solar Orbital (MSO) coordinate system observed by MESSENGER during a noon-midnight orbit on 20 November 2011. In the orthogonal MSO coordinate system, the origin is at Mercury's center, $+X$ is sunward, $+Y$ lies in the orbital plane and is positive towards dusk, and $+Z$, which is normal to the orbital plane, completes the right-handed system. Figure taken from *Johnson et al.,* [2012]………………………4

1.3 Illustration of Mercury's magnetosphere with each region of the magnetosphere labelled. The yellow lines connected to Mercury are planetary magnetic field lines. The yellow arrows labelled $\mathbf{J}_{\mathrm{MP}}$ on the magnetopause surface represent the Chapman-Ferraro magnetopause currents. The yellow arrows labelled $\mathbf{J}_{\mathrm{T}}$ in the plasma sheet represents the cross-tail current in Mercury's magnetotail. Figure taken from *Slavin* [2004]………………………………………………………..5

1.4 Wang-Sheeley-Arge (WSA) – ENLIL model results during MESSENGER's orbital mission period on 3rd March 2011. Left and right panel show the solar wind radial velocity (V_{r}) and product of the square of radial distance and number density (R^2N) in the equatorial plane, respectively. (b) Comparison of interplanetary magnetic field intensity observed by MESSENGER (black) and the ENLIL model (red) as a function of time. Figure taken from *Baker et al.,* [2013]………………………………………………………………………8

1.5 (a-b) WSA – ENLIL model results of solar wind radial velocity (V_{r}) and product of the square of radial distance and number density (R^2N) on 23rd November 2011. Format is similar to Figure 1.4a. (c-f) Magnetic field measurements of Mercury's magnetosphere observed by MESSENGER during a CME encounter on 23rd November 2011. The locations of closest approach (CA), cusp, magnetopause (MP) and bow shock (BS) crossings are also labelled. Figure taken from *Slavin et al.,* [2014]……………………………………………………………………..9

1.6 Two-dimensional schematic illustrating the microphysics of magnetic reconnection. Outer shaded region represents the Hall diffusion region and the inner darker shaded region represents the electron diffusion region. Figure taken from *MMS' Holy Grail: The Diffusion Region* (URL: http://mms.space.swri.edu/science-3.html)...11

1.7 Schematics illustrating the dayside magnetic reconnection and Dungey Cycle under southward (A-E) and northward (F) solar wind conditions. Figures taken from *Eastwood et al.*, [2015] and *Eriksson et al.*, [2005]……………………….12

1.8 (a) Flux transfer event (FTE) as viewed against the magnetopause surface. The red vectors represents the magnetosheath magnetic field draping over the FTE, the black vector represents the planetary magnetic field and the green lines marked the boundary of the FTE. (b) Side view of the FTE shown in Figure 1.8a. FTEs are flux ropes formed via multiple X-line reconnection at the dayside magnetopause, with one end connected to the solar wind and the other to the planet, and has a helical magnetic structure as shown by blue lines. Figure taken from *Slavin et al.*, [2014]……………………………………………………….14

1.9 (a-c) Schematics illustrating the formation of a pair of flux transfer events (i.e., flux ropes) from multiple X-line reconnection at the dayside magnetopause. (d) Side view of the FTEs forming on the magnetopause surface. Figures taken from *Lee and Fu*, [1985]…………………………………………………………..15

1.10 Spacecraft trajectories (red arrows) through a flux rope (a,c,d) and the travelling compression region (b), and their expected magnetic field signatures as observed by the spacecraft. The expected magnetic field observations are shown in the boundary normal coordinate system, where $\hat{\boldsymbol{N}}$ is normal to the magnetopause, $\hat{\boldsymbol{M}}$ is defined as the projection of $\hat{\boldsymbol{Z}}$ onto the surface tangential to the magnetopause surface and $\hat{\boldsymbol{L}}$ completes the right hand coordinate system. Green arrows represent the magnetosheath magnetic field and the yellow arrows represent the magnetospheric magnetic field…………………………………………………16

1.11 Histograms of the (a) Characteristic time, (b) angle between the model FTE velocity to model magnetopause surface, (c) speed and (d) the characteristic size of the FTEs observed by all four Cluster spacecraft. Figure taken from *Fear et al.*, [2007]…………………………………………………………………………..17

1.12 Magnetic field measurements in MSO coordinate sytem of two flux transfer events observed by MESSENGER during (a) first and (b) second flyby. Red line represents the best-fit curve of the data to the force-free flux rope model; the fitting interval is marked by two dashed lines. Figure taken from *Slavin et al.*, [2010a]…………………………………………………………………...20

1.13 (a) Magnetic field measurements in MSO coordinate observed by MESSENGER on 11 April 2011 during an encounter with a flux transfer event (FTE) shower while the spacecraft crosses Mercury's magnetopause. A total of 97 travelling compression regions (TCRs) and 66 flux-rope-type FTEs were identified; each FTEs and TCRs are marked with an arrow. (b) Schematics illustrating observation of the TCRs and FTEs passing over MESSENGER during a FTE shower as MESSENGER crosses Mercury's magnetopause. Figure taken from *Slavin et al.,* [2012]……………………………………………………………………..21

1.14 Schematics illustrating the formation of a substorm current wedge due to magnetic flux pile-up and braking of bursty bulk flows caused by near-Earth magnetotail reconnection. The resulting inertial current reduce the cross-tail current in the current sheet. The fast flow is diverted along the magnetic field lines into the ionosphere and azimuthally around the strong, dipolar near-Earth magnetic field, thus forming the substorm current wedge. Figure taken from *Shiokawa et al.,* [1997]…………………………………………………………23

1.15 Schematics illustrating the formation of earthward-travelling BBF-type flux ropes and tailward-travelling plasmoid-type flux ropes due to multiple X-line reconnection in the plasma sheet. The X-line with the highest reconnection rate and first reconnects open tail lobe magnetic field lines (Open FLR) is the Near Earth Neutral Line and flux ropes formed earthward (tailward) of this X-line is ejected earthward (tailward). Figure taken from Slavin et al., [2003]…………24

1.16 Spatial histogram of magnetotail flux ropes and travelling compression regions in the Y_{GSM} direction (i.e., dawn-dusk) as observed by (a) Cluster, (b) Geotail and (c) THEMIS spacecraft. Figures taken from *Slavin et al.,* [2005] and *Imber et al.,* [2011]……………………………………………………………………..28

1.17 (a) Observed Na^+ group number density (n_{obs}) in Mercury's magnetosphere projected onto the (top) meridional and (bottom) equatorial plane. Red trapezoid represents region with enhanced observed number density in Na^+. (b) Projection map of directional fluxes in MSM coordinate system for (top) H^+, (middle) He^{2+}, and (bottom) Na^+ ion groups averaged over the dusk side plasma sheet for solar wind velocity between 300 – 400 km/s. Figures taken from *Raines et al.,* [2013] and *Gershman et al.,* [2014]…………………………………………………29

2.1 Photographs and position of the instrument suites and processing unit onboard the MESSENGER spacecraft. Magnetic field and plasma measurements from the magnetometer (MAG) and Fast Imaging Plasma Spectrometer (FIPS) will be utilized in this dissertation. Figure taken from *Leary et al.,* [2007]……………40

2.2 (a) Schematic of a typical 12-hour “hot season” MESSENGER orbit, where the periapsis of the orbit is at the dayside magnetosphere. The Sun is to the left of Mercury. (b) The periapsis altitude and latitude of MESSENGER as a function of calendar date for the third and fourth MESSENGER orbital year. During the low-altitude campaign season, which lasted for ~ 2 months between August 2014 and October 2014, the periapsis altitude of MESSENGER decreases to within 50 km from Mercury’s surface at ~ 60°N latitude……………………………………..41

2.3 Schematics of the magnetometer onboard MESSENGER and its local coordinate system, which is chosen such that the boom is in the +Y (antisunward) direction during mission orbital phase. The payload adaptor is in the +Z-direction and +X-direction completes the orthogonal coordinate system. Figure taken from *Anderson et al.,* [2007]…………………………………………………………43

2.4 Schematics of the Fast Imaging Plasma Spectrometer (FIPS) onboard MESSENGER. It is a time-of-flight instrument, which measures the energy per charge of the incoming ion and identify the ion species from its mass-per-charge and time taken for the ion to travel the time-of-flight section. Figure taken from Andrew et al., [2007]……………………………………………………...45

3.1 Illustration of the variance ellipsoid. $\mathbf{x}_1$, $\mathbf{x}_2$, $\mathbf{x}_3$ represent the eigenvectors corresponding to the maximum, intermediate and minimum eigenvalues λ_1, λ_2, λ_3 (in order of decreasing magnitude), respectively. The half-length of each principal axis of the ellipsoid is given by the square root of the corresponding eigenvalue. Figure taken from *Sonnerup and Scheible,* [1998]……………………………49

3.2 Example of hodogram pairs for magnetopause crossing observed by AMPTE/IRM on October 19, 1984. Table shows the eigenvalues λ_i, eigenvectors $\mathbf{x}_i$ and average magnetic field values projected onto MVA coordinate system $\langle \mathbf{B} \rangle \cdot \mathbf{x}_i$. Figure taken from *Sonnerup and Scheible,* [1998]…………………………50

3.3 (a) Magnetic field measurements in boundary normal (i.e., MVA) coordinate observed by MESSENGER during magnetopause traversal on 21 November 2011. Solid black lines mark the interval of magnetopause crossing. The eigenvectors are: $\mathbf{x}_1$ = [-0.10, -0.20, 0.98], $\mathbf{x}_2$ = [0.45, 0.87, 0.22], $\mathbf{x}_3$ = [0.89, -0.46, 0.00]. The maximum to intermediate and intermediate to minimum eigenvalue ratio are 4.33 and 5.55, respectively. (b) Plot of magnetopause shear angle ϑ versus reconnection rate. Red histograms represents the average reconnection rate per 30 degrees shear angle bins. Figure taken from *DiBraccio et al.,* [2013]………52

3.4 (a) Magnetic field measurements in MVA coordinate of a flux rope encounter on 14 May 2012. B_1, B_2 and B_3 represents the minimum, intermediate and maximum variance direction, respectively. (b and c) Hodograms of magnetic field measurements shown in Figure 3.4a. Figure is taken from *DiBraccio et al.*, [2014]……………………………………………………………………..53

3.5 (a) Electric field and (b) Walen scatterplot for magnetopause crossing by AMPTE/IRM on 13 December 1985. $\mathbf{E}_C$ is the convection electric field and $\mathbf{E}_{HT}$ is the deHoffmann-Teller electric field. ($\mathbf{v} - \mathbf{v}_{HT}$) is the plasma velocity in the HT frame. In both scatterplot, the high correlation coefficient indicates that the HT frame is well-determined. Figure taken from *Chou and Hau*, [2012]…………57

3.6 GS reconstructions results for 30 October 1984 magnetopause crossing using AMPTE/IRM data. Top panel shows the reconstructed field map with the color plot representing B_Z (magnitude shown by color bar) and the bottom panel shows the same field map with color plot representing plasma pressure (magnitude shown by color bar). The contour lines for both maps represent the transverse magnetic field lines (i.e., B_X and B_Y). The yellow arrows along y = 0 for the top and bottom panel represents the initial transverse magnetic field and plasma velocity observed by the spacecraft, respectively. Figure taken from *Hu and Sonnerup,* [2003]……………………………………………………………….62

3.7 GS reconstruction results for flux ropes observed in the solar wind by WIND spacecraft on 2 May 1996 (left) and 13 March 1996 (right). The reconstruction map representations are similar to the reconstructed field map in Figure 3.6. Figure is taken from *Hu and Sonnerup,* [2001]…………………………………63

4.1 (a) An example MESSENGER orbit (black solid line) on 26 August 2011 projected onto the *X*-*Z* plane in aberrated Mercury solar magnetic (MSM') coordinates during a period without filamentary activities in the cusp. The aberration angle is -7.31°. The model bow shock (BS) and magnetopause (MP) from *Winslow et al.* [2013], scaled to fit observed boundary crossings (marked by the two dots at the dayside magnetosphere), are shown in dotted lines; the Sun is to the right. The thick portion of the orbit represents the cusp region, and the dot at the nightside magnetosphere represents the magnetotail current sheet (CS) crossing. The arrow denotes the spacecraft trajectory. (b) Full-resolution magnetic field measurements (top to bottom, *X*, *Y*, and *Z* components and field magnitude) acquired along the orbit shown in (a). The vertical dashed lines mark the boundary crossings shown in (a). CA denotes closest approach, and all times are in UTC……………………………………………………………………...71

4.2 (a) Magnetic field measurements during an example orbit on 20 May 2011 during which plasma filaments were observed in the cusp. Magnetic field components are in aberrated MSM' coordinates for an aberration angle of -6.31°. The format is similar to that of Figure 4.1b. (b) Close-up of magnetic field measurements in the cusp region for the time interval delimited by the dashed lines in (a) labeled cusp. Each cusp filament identified by the automated algorithm is denoted by a vertical dashed line……………………………………………………………..73

4.3 (a) Schematic illustration of the different time segments used in the quasi-automatic, scale-free identification algorithm. The red and yellow boxes represent a time segment T and "neighborhood" W, respectively; both are centered at time t. (b) Top: map of q values (color bar) for a 1-min interval at 09:51 UTC on 20 May 2011 for optimum values of $q_0 = 3.9$ and $s = 3$; the ordinate is duration dt, and the abscissa is time t within that interval. Middle: B for the same time interval. Vertical red dashed lines indicate the times of filaments identified by the automated method. Bottom: B for the same time interval with gray shaded areas representing $dt_{\max}$ values that correspond to $q_{\max}$ and yellow shaded areas spanning dt values that correspond to half maximum values of $q_{\max}$ at times $t_{\max}$……………………………………………………………………...74

4.4 Magnetic field variations during a Population I cusp plasma filament observed on 23 April 2013 at approximately 16:30:29 UTC. (a) Panels 1–3 (top to bottom) show the full-resolution magnetic field measurements in aberrated MSM' coordinates, panels 4–6 show the magnetic field measurements in MVA coordinates, and panel 7 shows the total magnetic field. (b) The top and middle panels show the MVA hodograms for the filament in Figure 4.4a. The bottom panel shows $\delta_{\min}$ versus δ_{int} for all Population I filaments identified in this study. The red lines represent the $\delta_{\text{i}} = 1$ condition……………………………………80

4.5 Magnetic field variations during a Population II cusp filament observed on 26 July 2013 at approximately 17:00:36 UTC. (a) Magnetic field measurements in aberrated MSM' and MVA coordinates; the format follows that of Figure 4.4a. (b) MVA hodograms for the same time interval as in (a) and a plot of $\delta_{\min}$ versus δ_{int} for all Population II events…………………………………………………83

4.6 Magnetic field variations during a Population III cusp plasma filament observed on 27 July 2013 at approximately 08:59:49 UTC (a) Magnetic field measurements in aberrated MSM' and MVA coordinates; the format follows that of Figure 4.4a. (b) MVA hodograms for the same interval as in (a) and a plot of $\delta_{\min}$ versus δ_{int} for all Population III events……………………………………………………84

4.7 Magnetic field variations during a Population IV cusp plasma filament observed on 23 April 2013 at approximately 16:30:54 UTC. (a) Magnetic field measurements in aberrated MSM' and MVA coordinates; the format follows that of Figure 4.4a. (b) MVA hodograms for the same interval as in (a) and a plot of $\delta_{\min}$ versus δ_{int} for all Population IV events……………………………………86

4.8 Magnetic field variations during a flux rope observed on 27 April 2013 at approximately 16:32:54 UTC. (a) Magnetic field measurements in aberrated MSM’ and MVA coordinates; the format follows that of Figure 4.4a. (b) MVA hodograms for the same interval as in (a)……………………………………….87

4.9 (a) Energy-resolved pitch angle distribution of 16 filaments. The filaments were selected to ensure coverage of the entire FIPS energy range and look angle. Each pixel represents a pitch angle bin size of 5°; phase space density (PSD) is represented by color. (b) Plot of PSD versus pitch angle for 11 filaments observed in the energy range 0.5–1 keV. Each filament event is represented by a different color……………………………………………………………………………89

4.10 (a) Magnetic field measurements in aberrated MSM’ coordinates during two successive orbits on 31 August 2014. (Top) A cusp crossing with no filaments detected. The aberration angle is -5.79°, and the vertical dashed line represents the magnetopause crossing. (Bottom) A cusp crossing 8 h later during which filaments were detected. Two vertical dashed lines delimit the cusp region. (b) Close up of magnetic field measurements within the cusp for the orbit in the bottom panel of (a). Each cusp filament identified by the automated algorithm is marked by a vertical dashed line……………………………………………….90

4.11 Magnetic field variations during a low-altitude Population III cusp plasma filament observed on 15 August 2014 at approximately 17:05:18 UTC. (a) Magnetic field measurements in aberrated MSM’ and MVA coordinates; the format follows that of Figure 4.4a. (b) MVA hodograms for the same interval as in (a) and a plot of δ_{min} versus δ_{int} for all low-altitude Population III events…..92

4.12 Histograms of the filament parameters (a,b) δB, (c,d) $\delta B/B$, (e,f) time duration, (g,h) size in proton gyroradii r_{L}, and (i,j) magnetic flux. Left and right columns show results for high- and low-altitude filaments, respectively………………...95

4.13 (a) Locations of cusp plasma filaments identified in this study, binned in 0.01-R_{M}- wide bins in the cylindrical coordinates ρ and X and color coded by perpendicular thermal pressure $P_{\mathrm{th},\perp}$. The black and red dashed lines show the extent in magnetic latitude (MLAT) of filament observations and the mean cusp boundaries of *Winslow et al.* [2012], respectively. (b) Plot of perpendicular thermal pressure versus altitude. Red squares represent mean values of $P_{\mathrm{th},\perp}$ averaged in 50-km-wide altitude bins, and the error bars show the standard errors for each “binned” value of $P_{\mathrm{th},\perp}$. The blue and red lines represent linear fits to the “un-binned” and “binned” data, respectively. The corresponding correlation coefficient (r) is -0.14 and -0.55, respectively. (c) Plot of perpendicular thermal pressure versus magnetic latitude at three different ranges of altitude, 0–250 (blue), 250–500 (red), and 500–750 (black) km. Each square represents mean

$P_{\mathrm{th},\perp}$ values averaged over 5°-wide latitude bins, and the error bars show the standard errors……………………………………………………………….97

4.14 (a-c) Binned plot of $P_{\mathrm{th},\perp}$ in the aberrated X'-Y' plane for different altitudes ranges: (a) 0–250 km altitude; (b) 250–500 km altitude; (c) 500–750 km altitude; (d) all altitudes. Colors denotes mean $P_{\mathrm{th},\perp}$ values in 0.01 R_{M} × 0.01 R_{M} bins. Dashed concentric circles depict magnetic latitude from 45° to 85°N at 10° intervals. Radial solid lines depict magnetic local time at 1 h intervals…………………..99

4.15 (a) Normalized rate of occurrence of filaments as a function of magnetic local time and (b) perpendicular thermal pressure $P_{\mathrm{th},\perp}$. (c) Histogram of MESSENGER dwell time as a function of magnetic local time. (d) Dwell-time-normalized rate of occurrence of filaments as a function of magnetic local time and (e) as a function of magnetic local time at different $P_{\mathrm{th},\perp}$ ranges. The $P_{\mathrm{th},\perp}$ ranges are 0–6 nPa (black), 6–12 nPa (red), 12–18 nPa (blue), 18–24 nPa (grey), and 24–30 nPa (green)……………………………………………………………………...101

4.16 (a) Distribution of total MESSENGER dwell time for the time period of this study. Each pixel spans 5° in MLAT, from 50° to 85°N, and 1 h in MLT, from 6 h to 18 h, with values represented by the color bar displayed. (b) Distribution of number of filaments in the same format. (c) Distribution of mean particle precipitation rate in the same format ($\log_{10}$ scale)…………………………………………..103

4.17 Magnetosheath plasma β_{MSH} versus IMF shear angle θ for the orbits of this study. The size of each symbol is proportional to the number of filaments identified on that orbit. β_{MSH} is computed under the assumption of pressure balance between the solar wind and the planetary magnetic field at the magnetopause, given that plasma pressure in the magnetosphere is approximately zero. θ is defined as the angle between the IMF and planetary field inside the dayside magnetosphere. The components and magnitude of the magnetic field in the solar wind and Mercury's magnetosphere are obtained by averaging 10s of magnetic field measurements immediately inbound and outbound of the magnetopause crossing. The dashed gray line shows the *Swisdak et al.* [2010] condition for diamagnetic suppression of magnetic reconnection at the dayside magnetopause $\Delta\beta > \frac{2L}{d_{\mathrm{i}}}\tan\left(\frac{\theta}{2}\right)$ with $L = d_{\mathrm{i}}$……………………………………………………………………106

5.1 (a) Full-resolution MESSENGER magnetic field measurements on February 3rd 2013. (b) Average positions of each CS crossing in the equatorial (left) and meridional (right) plane. Model bow shock (BS) and magnetopause (MP) from *Winslow et al.* [2013] are shown……………………………………………118

5.2 (a) B_{lobe} and (b) B_{CPS} as a function of X'_{MSM}. A power law relation was fitted to the data points (red line) with fitting coefficients shown in the table. The histogram for number of data points in each bin is also shown. (c) Normalized probability distributions of B_Z for four downtail regions and the colored arrows represent the mean of each respective distribution. (d) Σt as a function of X'_{MSM}. An exponential relation (red line) is fitted to the data points…………………121

5.3 (a) Meridional view of MESSENGER crossing of the cross-tail CS on 23 August 2011. Arrow denotes the spacecraft travelling direction. (b) B_X measurements as a function of Z'_{MSM}. A Harris CS model is fitted to the smoothed data. Histograms of (c) $2L$ and (d) J_{CS} calculated from Harris model fits. μ and M represents mean and median of the distribution, respectively…………………………………122

5.4 (a) Magnitude of measured B_Z and dipole magnetic field in the CPS and (b) δB_Z as a function of X'_{MSM}. (c) $P_{\text{th,FIPS}}$ as a function of X_{MSM}……………………..125

6.1 (a) Full-resolution magnetic field measurements of an example MESSENGER orbit on 28th August 2013 in aberrated Mercury solar magnetic (MSM') coordinates. The dotted lines and color bars separate each regions of Mercury's magnetotail, with blue, yellow and red color bars representing the northern/southern tail lobe, plasma sheet boundary layer and current sheet respectively. (b) The orbit of MESSENGER on 28th August 2013 in the equatorial (left) and meridional (right) plane. The model bow shock (BS) and magnetopause (MP) from *Winslow et al.,* [2013], scaled to fit observed average boundary crossings are shown in dotted lines; the Sun is to the left and the scaled T96 model magnetic field lines [*Tsyganenko,* 1995] using a linear scaling factor of 8 is shown in grey solid lines. Red line indicates the interval when MESSENGER traversed Mercury's current sheet……………………………………………………138

6.2 Plot of B_Z as a function of X'_{MSM} and Y'_{MSM}. B_Z is binned into four downtail distance from X'_{MSM} = -1.4 R_M to -2.6 R_M at bins of 0.3 R_M and dawn-dusk direction from Y'_{MSM} = -1.6 R_M to 1.6 R_M at bins of 0.4 R_M. The error bars are standard error of the mean B_Z in each bin and the error bars are magnified by 100 times for visual purposes. The strength of the dawn-dusk asymmetry in each downtail distance is determined by the slope of least-square fitted lines (black). Least-squares fitted red lines for closest (i.e. -1.4 $R_M > X'_{MSM} >$ -1.7 R_M) and furthest (i.e. -2.3 $R_M > X'_{MSM} >$ -2.6 R_M) represents magnetic flux pileup and enhanced reconnection region, respectively…………………………………..140

6.3 (a) Detrended B_Z as a function of Y'_{MSM} for downtail distance X'_{MSM} between -1.4 R_M to -1.7 R_M. The plot format is similar to Figure 6.2. The detrended B_Z values are calculated by subtracting B_Z values with the "baseline values", which is determined from the least-squares fitted line in panel 1 of Figure 6.2. The red line shows the persistent asymmetry of flux pile-up in the substorm current wedge after subtraction of baseline values. (b) Distribution of occurrence rate (in number per minute) of reconnection fronts observed by MESSENGER [*Sun et al.*, 2016]……………………………………………………………………….142

6.4 (a) Dawn-dusk distribution of current sheet plasma beta β_{CS} as shown by grey data points determined from the FIPS instrument. Red line represents the binned data points at bin size of $0.4R_M$ and the error bars represents the standard error of the mean for each bin. Note: the error bars are magnified 20 times for visual purposes. The blue line represents the binned current sheet plasma beta determined from the MAG instrument. (b) Current sheet full thickness $2L$ and (c) cross-tail current density J_Y of 234 current sheet crossings determined from the Harris current sheet model fitting. For both derived parameters, the data points (black) were binned into bins of 0.4 R_M between Y'_{MSM} = -1.6 R_M and 1.6 R_M as shown by the red data points. The error bars represent the standard error of the mean in each bin. Note: the error bars in (c) are multiplied by 1.5 for clarity…………………………...144

6.5 Schematic illustration of summary and explanation for all asymmetries in Mercury's current sheet observed in this study. Top and bottom panels represent the post-midnight (dawn) and pre-midnight (dusk) view, respectively……….147

8.1 (left) MESSENGER's orbit during magnetopause crossing on 28th April 2013. A scaled-T89 magnetic field model [Tsyganenko, 1996], with a model bow shock and magnetopause [Winslow et al., 2012], are also plotted. (right) Magnetic field measurements in the MSO coordinate system on 28th April 2013. Red shaded region represents the magnetopause crossing and blue shaded region represents cusp traversal…………………………………………………………………165

8.2 (top) Closed-up magnetic field measurements of magnetopause crossing on 28th April 2013. Red dashed lines represent identified FTEs/TCRs. Plot is shown in boundary normal coordinate. (bottom) Closed-up magnetic field measurements of cusp encounter on 28th April 2013. Red dashed lines represent identified cusp plasma filaments……………………………………………………………166

LIST OF TABLES

1.1 Typical solar wind conditions scaled from Earth's orbit at 1 AU to the orbits of other terrestrial planets. Solar wind values for perihelion and aphelion of Mercury's highly eccentric orbit were calculated. Basic parameters listed in the table are: radial distance of planet's orbit from the sun (R), solar wind velocity (V_{SW}), proton number density (n_p), interplanetary magnetic field (B), proton and electron temperature (T_p and T_e, respectively). The scaling of each parameter with R is also tabulated in their respectively columns. Table taken from *Slavin and Holzer*, [1981]…………………………………………………………………...7

1.2 Summary of asymmetries in magnetotail processes observed by various spacecraft missions. Table taken from *Walsh et al.*, [2014]…………………….28

GLOSSARY OF TERMS

TERM	DEFINITION
Aphelion	The point of spacecraft orbit that is furthest from the planet.
Auroral Oval	The region where the auroral occurs.
Bow Shock	The shock wave formed as a result of magnetospheres or unmagnetized planets encountering the supersonic solar wind.
Cluster Mission	A four-spacecraft European Space Agency mission to study Earth’s magnetosphere.
Coronal Mass Ejection	A cloud of highly energetic particles released from the Sun during strong solar flares and eruptions.
Cusp	The region of open magnetic field lines in the planetary polar cap where magnetosheath plasma precipitates; there are two cusp regions, each in the northern and southern hemisphere.
Cusp Plasma Filaments	Filamentary flux tubes observed in Mercury’s cusp.
Dipolarization	The process of a stretched magnetic field lines returning to a dipole field configuration.
Dungey Cycle	A convection pattern of open magnetic field lines in planetary magnetospheres.
Interplanetary Magnetic Field	The magnetic field of the Sun.
Ionosphere	The region of a planetary atmosphere that consist mainly of electrons and protons.
Jovian magnetospheres	Collective term referring to Jupiter’s, Saturn’s, Neptune’s and Uranus’ magnetosphere.
Magnetometer	The instrument to measure magnetic field.

Magnetopause	The boundary layer between the shocked solar wind and the planetary magnetosphere.
Magnetosheath	The region of shocked solar wind between the bow shock and the magnetopause.
Magnetosphere	The region of space surrounding the planet which is influenced by the planet's global magnetic field.
Magnetotail	The elongated nightside region of the magnetosphere.
PIC	Particle-in-Cell: Simulations that tracks each particles in continuous phase space.
Perihelion	The point of spacecraft orbit that is nearest to the planet.
Solar Wind	The continuous flow of charged particles (mainly proton and alpha particles) released from the Sun at supersonic speed.
Space Weathering	The process that affect the physical and chemical properties of the surface of planetary bodies through interaction with charged particles from outer space.
Substorm	A disturbance in the magnetosphere caused by sudden release and injection of energy from the magnetotail into the ionosphere.
Substorm Current Wedge	A current system in the near-Earth magnetotail tail region caused by braking of high speed plasma flow.

LIST OF SYMBOLS AND ACRONYMS

TERM	DEFINITION
nT	Nano-Tesla
nA	Nano-Amperes
keV	Kilo-electron volt
kHz	Kilo-Hertz
MWb	Mega-Weber
E/Q	Energy per charge
R_M	Radius of Mercury (1 R_M ~ 2440 km)
R_E	Radius of Earth (1 R_E ~ 6371 km)
IMF	Interplanetary Magnetic Field
MAG	Magnetometer
FIPS	Fast Imaging Plasma Spectrometer
GRS	Gamma-Ray Spectrometer
EPPS	Energetic Particle and Plasma Specrometer
EPS	Energetic Particle Spectrometer
MCP	Micro-channel plate
MESSENGER	MErcury, Surface, Space ENvironment, GEochemistry and Ranging
THEMIS	Time History of Events and Macroscale Interactions during Substorms
OCM	Orbital Correction Maneuvers
TOF	Time Of Flight

MHD	Magnetohydrodynamics
CME	Coronal Mass Ejection
FTE	Flux Transfer Event
TCR	Travelling Compression Region
BBF	Bursty Bulk Flow
MXR	Multiple X-line Reconnection
NENL	Near Earth Neutral Line
NMNL	Near Mercury Neutral Line
SCW	Substorm Current Wedge
CPS	Central Plasma Sheet
PSBL	Plasma Sheet Boundary Layer
CS	Current Sheet
MVA	Minimum Variance Analysis
MLT	Magnetic Local Time

ABSTRACT

Mercury has proven to be a unique natural laboratory for space plasma processes. Mercury's magnetosphere is formed by the interaction between its intrinsic planetary magnetic field and the supersonic solar wind. The structure of Mercury's magnetosphere is very similar to Earth's; yet the results from the MESSENGER mission to Mercury have shown that the spatial and temporal scales of magnetospheric processes are very different at Mercury. In this thesis, we analyze *in situ* observations from the MESSENGER spacecraft to characterize and understand the dynamic physical plasma processes occurring in Mercury's magnetosphere.

We identified and analyzed 345 plasma filaments in Mercury's northern magnetospheric cusp to determine their physical properties. Cusp plasma filaments are magnetic structures that are identified on the basis of their characteristic 2–3 seconds long decrease in magnetic field intensity. Our analysis indicates that these cusp filaments are cylindrical flux tubes filled with plasma, which causes a diamagnetic decrease in the magnetic field inside the flux tube. MESSENGER observations of flux transfer events (FTEs) and cusp filament suggests that cusp filaments properties are the low-altitude extension of FTEs formed at Mercury's dayside magnetopause.

We examined 319 central plasma sheet crossings observed by MESSENGER. Using a Harris model, we determined the physical properties of Mercury's cross-tail current sheet. Analysis of B_Z in the current sheet indicated that MESSENGER usually crossed the current sheet sunward of the Near Mercury Neutral Line. Magnetohydrodynamics-based analysis using the MESSENGER magnetic field and plasma measurements suggests that heavy planetary ions and/or ion temperature anisotropy may be important in maintaining radial stress balance within Mercury's central plasma sheet.

We report the observation of significant dawn-dusk variation in Mercury's cross-tail current sheet with thicker, lower plasma β dawn side current sheets than the dusk side.

Using the Harris current sheet model, we determined the peak current sheet current density and reported an asymmetry pattern for peak current density consistent with observed asymmetries in current sheet thickness. We propose that enhancement of heavy ions in the dusk side current sheet, due to centrifugal acceleration and gradient-curvature drift of ions from the cusp and current sheet, provides a partial explanation of the dawn-dusk current sheet asymmetries observed in this study. Furthermore, our results are consistent with earlier studies on reconnection-related structures and phenomenon, which suggest that the asymmetries observed in this study are associated with the asymmetric nature of magnetotail reconnection at Mercury. We also report the possible observation of an Earth-like substorm current wedge in the near-Mercury magnetotail. We calculate the total current in the Hermean substorm current wedge and found that the current close via the conductive planetary core. The current closure mechanism may be similar to the Region 1 currents observed in an earlier study.

From the above results, we conclude that the plasma processes occurring at Mercury are different from those at Earth due to difference in internal plasma composition, relative size of Mercury's magnetosphere and solar wind conditions at small heliospheric distances, despite many structural similarities in both magnetospheres. The results reported in this thesis have far-reaching implications for the physical processes in Mercury's magnetospheres and those of the other planets.

CHAPTER I

INTRODUCTION

1.1 Mercury's Magnetosphere

Mercury is the smallest planet in the solar system, with radius of ~ 2440 km, possessing a global magnetic field and a magnetosphere. Its close proximity to the Sun also means that Mercury's interaction with the local plasma environment is unique in the solar system. Mercury's magnetosphere is dwarfed by the other planetary magnetospheres and it is a combination of its size and proximity that makes Mercury's magnetosphere the most dynamic system in the solar system. Despite many structural similarities, the magnetospheres of Mercury and Earth are highly different with respect to the space plasma processes and dynamics that occur within each system. Therefore, understanding the physical processes that occurs within Mercury's magnetosphere will expand our current understanding of planetary magnetospheres and their interaction with the Sun. This introduction will provide a summary of our present understanding of Mercury's magnetosphere and the basic space plasma physics knowledge required to conduct the research in this thesis.

Mercury has been observed by many civilizations since antiquity. Little was known about the celestial mechanics of Mercury until significant advances in modern physics and astronomy. We now know that Mercury's rotation (~ 54 days) and orbital (~ 88 days) periods are locked in a 3:2 spin-orbit resonance, resulting in large temperature gradient between the dayside and nightside surfaces (~ 1000 K). Mercury also has a highly eccentric orbit around the Sun, with perihelion and aphelion at ~ 0.31 and 0.47 AU, respectively.

Assuming a simple inverse-square relation between solar wind parameters and radial distance from the Sun, Mercury's highly eccentric orbit can result in 40% change of solar wind density between perihelion and aphelion. Such difference in local plasma conditions is absent in other planetary magnetospheres and has huge implications in the dynamics of Mercury's magnetosphere.

It was initially thought that Mercury's rotation is too slow to support a dynamo in its core and sustain a global magnetic field. Furthermore, it was considered unlikely that its interior would have a molten region in which a dynamo might operate. That changed when NASA's Mariner 10 became the first spacecraft to visit Mercury in 1974. During the three close Mercury flybys performed by the Mariner 10 spacecraft, the magnetometer onboard detected an intrinsic global magnetic field that is very similar to Earth's in structure, but weaker by a factor of ~ 100 [*Ness et al.*, 1975; 1976]. This planetary magnetic field serves as a "magnetic shield", which deflects the solar wind around Mercury and creates a magnetosphere. Figure 1.1 shows (a) the orbit of Mariner 10 and (b) the magnetic field measurements during the third flyby.

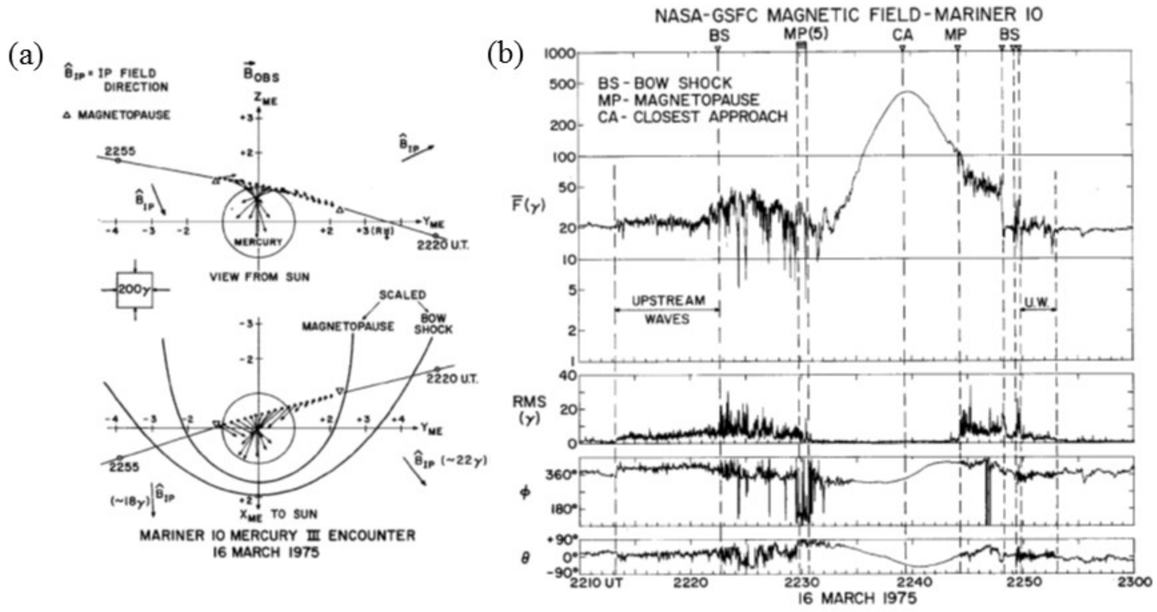

Figure 1.1 (a) Trajectory of Mariner 10 spacecraft and the projection of the magnetic field vectors in the ecliptic *X–Z* plane (top) and equatorial *X–Y* plane (bottom). (b) Magnitude of the magnetic field vectors measured during Mariner 10 third flyby encounter. Φ and ϑ represents the latitude with respect to the ecliptic and longitude with respect to the Sun-Mercury line respectively. Figure taken from *Ness et al.*, [1976].

The interval starts with Mariner 10 spacecraft in the solar wind as shown by the constant magnetic field at ~ 20 nT. [Note that 1 nanoTesla (nT) = 10^{-5} Gauss (G)]. Mariner 10 crosses the bow shock (BS) at ~ UT 22:23 when the magnetic field increases by 250% to ~ 50 nT. The spacecraft crosses the magnetopause (MP) at ~ UT 22:30 as identified by the sudden change in magnetic field direction. Magnetic field fluctuations also cease as Mariner 10 flew deeper into the planetary field before reaching the closest approach at ~ UT 22:40. The spacecraft encountered another magnetopause and bow shock crossing before exiting into the solar wind. By conducting a least square fit to the flyby measurements (Figure 1.1b), *Ness et al.,* [1976] concluded that Mercury's global magnetic field can be described with a centered dipole with 12° tilt and estimated the dipole moment to be ~ 350 nT-R_M^3. However, *Alexeev et al.,* [2008] argued that Mariner 10 flyby measurements of Mercury's magnetospheric magnetic field fit better to a paraboloid model with no dipole tilt, a northward dipole offset of ~ 0.18 R_M and a smaller dipole moment of ~ 195 nT-R_M^3.

The nature of Mercury's intrinsic global magnetic field was not verified until the MEcury, Surface, Space Environment, GEochemistry and Ranging (MESSENGER) spacecraft became the first spacecraft to orbit around Mercury in 2011. With the continuous magnetic field measurements from MESSENGER's magnetometer (MAG) during its orbital phase, *Anderson et al.*, [2011] confirmed that Mercury's dipole moment is almost aligned with its rotation axis (i.e., < 3° dipole tilt) with a value of ~ 195 nT-R_M^3 and is offset northward by ~ 484 km (or 0.2 R_M). Figure 1.2 shows an example of magnetic field measurements observed by MESSENGER during a noon-midnight orbit on 20 November 2011. The interval in Figure 1.2 started with MESSENGER crossing Mercury's nightside magnetopause and enters the magnetotail southern lobes. At ~ UT 09:30, MESSENGER encounters Mercury's cross-tail current sheet, followed by the northern lobes. Similar to the Mariner 10 observations, the magnetic field fluctuations ceased as MESSENGER observed the stronger planetary dipole field near the planet before reaching closest approach at ~ UT 10:10. The spacecraft subsequently observed the northern cusp as indicated by the diamagnetic decreases in magnetic field magnitude |**B**|, entered the dayside magnetosphere before crossing the dayside magnetopause and exits into the solar wind. The magnetic field measurements from MESSENGER are consistent with the data from

Mariner 10, indicating that Mercury possesses a well-developed global magnetosphere and it is structurally similar to Earth's. Unlike the terrestrial magnetosphere, Mercury occupies a significant volume of its entire magnetosphere. Mercury's magnetosphere is smaller in size than the Earth's, due to its smaller dipole moment and stronger solar wind conditions. In fact, the spatial dimensions of structural features in one magnetosphere may be scaled to the other in units of planetary radii using a linear scaling factor of 8 [*Ogilvie et al.*, 1977].

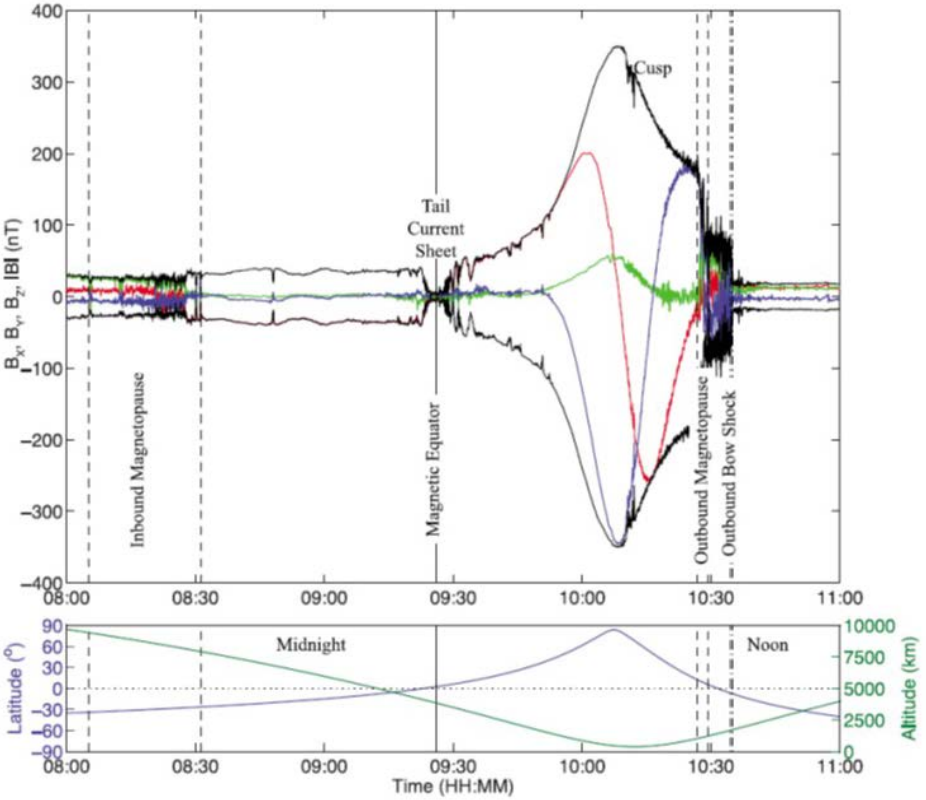

Figure 1.2 Magnetic field measurements in the Mercury Solar Orbital (MSO) coordinate system observed by MESSENGER during a noon-midnight orbit on 20 November 2011. In the orthogonal MSO coordinate system, the origin is at Mercury's center, +*X* is sunward, +*Y* lies in the orbital plane and is positive towards dusk, and +*Z*, which is normal to the orbital plane, completes the right-handed system. Red, green and blue lines represents magnetic field components B_X, B_Y and B_Z, respectively. Figure taken from *Johnson et al.*, [2012].

Similar to other planetary magnetospheres, Mercury's magnetosphere acts as an obstacle to the solar wind, which is a collisionless quasi-neutral plasma consisting primarily of proton and electrons flowing radially outward from the Sun at average (supersonic) speeds of ~ 400 km/s. The solar wind also carries with it an embedded interplanetary magnetic field (IMF). Without the shielding of the magnetosphere against the solar wind, charged particles can reach the planet's surface, or atmosphere, and undergo space weathering processes such as sputtering or atmospheric scavenging. Figure 1.3 shows an illustration of Mercury's magnetosphere. For the supersonic solar wind to adjust its density, pressure and velocity in the presence of Mercury's magnetosphere, it must first become subsonic. The transition between supersonic and subsonic flow is the bow shock. Across the shock discontinuity, the solar wind density and magnetic field increases while the velocity decreases across the shock. The bow shock is usually identified from the MAG data by its characteristic sudden increase in magnetic field magnitude. A statistical survey of MESSENGER magnetic field measurements shows that the bow shock has an average subsolar location of ~ 1.95 R_M (1 R_M = 2440 km) from the surface [*Winslow et al.,* 2013].

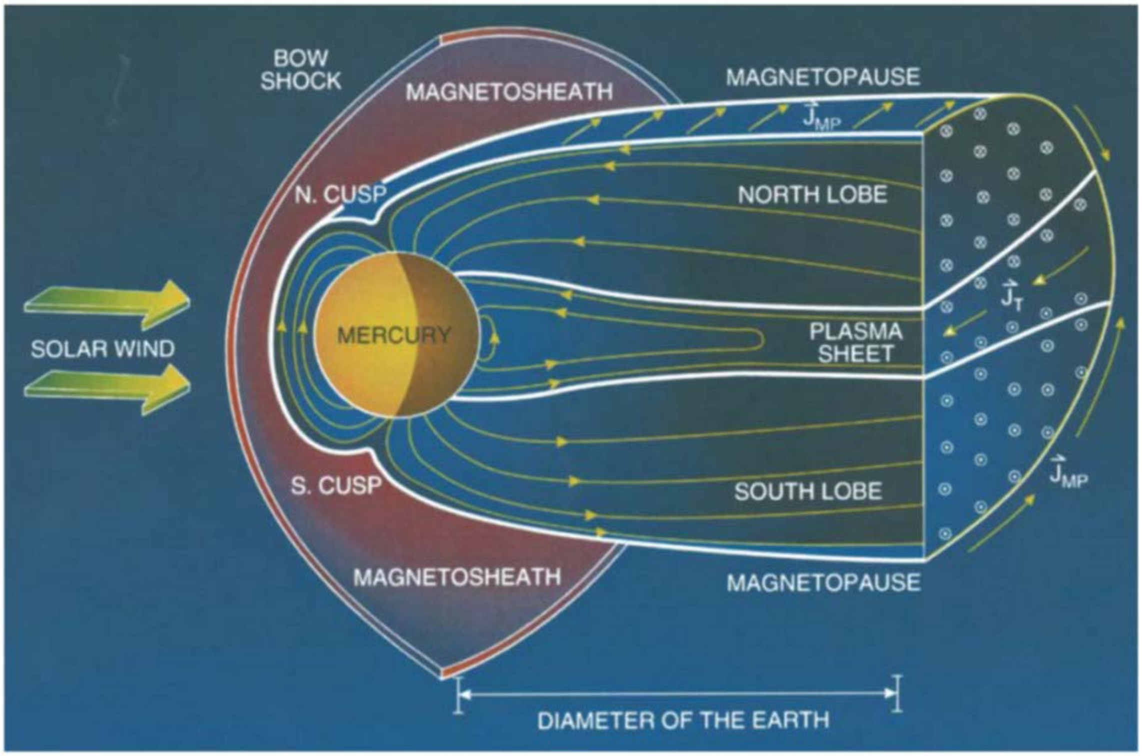

Figure 1.3 Illustration of Mercury's magnetosphere with each region of the magnetosphere labelled. The yellow lines connected to Mercury are planetary magnetic field lines. The yellow arrows labelled $\mathbf{J}_{MP}$ on the magnetopause surface represent the Chapman-Ferraro magnetopause currents. The yellow arrows labelled $\mathbf{J}_T$ in the plasma sheet represents the cross-tail current in Mercury's magnetotail. Figure taken from *Slavin* [2004].

The boundary surface that separates the shocked magnetosheath plasma and Mercury's magnetosphere is called the magnetopause. It is also the location where the total pressure (i.e., the sum of magnetic and plasma pressures) in the magnetosheath and magnetosphere are approximately balanced. By least square fitting a magnetopause model [*Shue et al.,* 1997] to magnetopause crossings observed by MESSENGER, *Winslow et al.,* [2013] calculated the average magnetopause standoff distance to be ~ 1.45 R_M. In the open magnetosphere model proposed by *Dungey* [1961], the IMF could be connected with Mercury's dayside planetary magnetic field via a process called magnetic reconnection, which will be discussed in Chapter 1.3. The resulting "open" magnetic field line has one end connected to the solar wind and the other to Mercury at the higher latitude region known as the cusp. In the absence of an ionosphere, magnetosheath plasma, with the sufficiently small pitch angles, now has direct access to Mercury's surface along those open field lines, into the cusp. The precipitating plasma can reduce the planetary field strength at the cusp (i.e., plasma diamagnetism). Hence, Mercury's cusp region can be easily identified from the magnetic field (plasma) data by its characteristic decrease (increase) in magnetic field magnitude (~ 1 keV particle flux).

Once reconnected, these newly-opened field lines convect antisunward over the polar caps into the nightside magnetosphere. As the solar wind convects past Mercury, it stretches the nightside magnetosphere into an elongated configuration known as the magnetotail. The anti-sunward transport of open field lines filled with magnetosheath-like plasma forms a thick boundary layer at high-latitude magnetotail called the plasma mantle. As depicted in Figure 1.3, the magnetotail also consist of two other regions, the magnetotail lobes and the plasma sheet. The north and south tail lobes are regions of open magnetic field lines with very low plasma density (i.e., low plasma beta β, which is the ratio between thermal and magnetic pressure). The north (south) tail lobes can also be identified in the MAG data by its stable and strong magnetic field in the sunward (antisunward) direction.

The plasma sheet is a region of closed magnetic field lines filled with hot, dense plasma (i.e., $\beta >> 1$ [*Raines et al.,* 2011]) and can be identified from the MAG data by its weak, fluctuating magnetic field. For an isotropic plasma in ideal steady state, the antisunward plasma thermal pressure gradient ($\nabla \mathbf{P}$) is in balance with the magnetic tension and magnetic pressure force ($\mathbf{J} \times \mathbf{B}$) of the stretched field lines. Anisotropy of plasma temperature and/or gradient of plasma flow kinetic energy are reasons for stress imbalance in the plasma sheet [*Rich et al.,* 1972]. The stress balance of Mercury's plasma sheet will be discussed further in Chapter V. Embedded within the plasma sheet is the cross-tail current sheet, which is formed as a result of oppositely-directing tail lobes fields. The simplest description of the current sheet is the Harris current sheet model [*Harris,* 1962], which is a one-dimensional (the north-south direction) model commonly used in many multi-spacecraft observational data analyses [e.g., *Nakamura et al.,* 2002] and PIC reconnection simulations [e.g., *Birn et al.,* 2001] to characterize the current sheet properties, such as the thickness and current density. More details on using the Harris current sheet model to describe Mercury's current sheet will be discussed in Chapter V. The Dungey cycle is complete when the two opposite lobe field lines convect towards the plasma sheet due to $E \times B$ drift, where E is the convection electric field and B is the lobe field magnitude, and reconnect. Note that, the magnetospheric regions described here represent the steady-state configuration of Mercury's magnetosphere. In reality, the solar wind conditions at Mercury are rarely steady and different regions of Mercury's magnetosphere can dynamically change in response to these solar wind variations.

1.2 Interplanetary Environment at Mercury

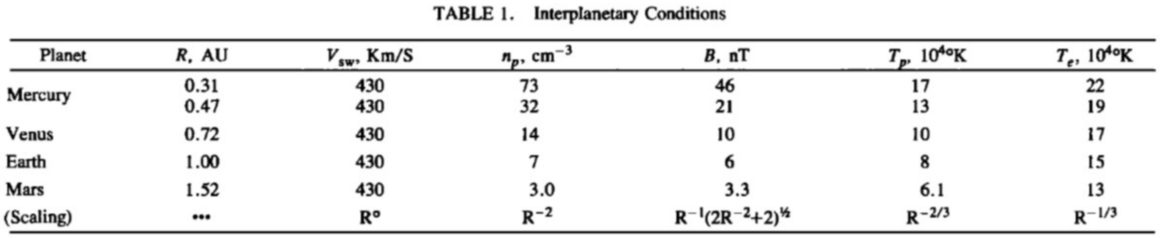

TABLE 1. Interplanetary Conditions

Planet	R, AU	V_{sw}, Km/S	n_p, cm^{-3}	B, nT	T_p, 10^4°K	T_e, 10^4°K
Mercury	0.31 0.47	430 430	73 32	46 21	17 13	22 19
Venus	0.72	430	14	10	10	17
Earth	1.00	430	7	6	8	15
Mars	1.52	430	3.0	3.3	6.1	13
(Scaling)	•••	R^{o}	R^{-2}	$R^{-1}(2R^{-2}+2)^{1/2}$	$R^{-2/3}$	$R^{-1/3}$

Table 1.1 Typical solar wind conditions scaled from Earth's orbit at 1 AU to the orbits of other terrestrial planets. Solar wind values for perihelion and aphelion of Mercury's highly eccentric orbit were calculated. Basic parameters listed in the table are: radial distance of planet's orbit from the sun (R), solar wind velocity (V_{SW}), proton number density (n_p), interplanetary magnetic field (B), proton and electron temperature (T_p and T_e, respectively). The scaling of each parameter with R is also tabulated in their respectively columns. Table taken from *Slavin and Holzer,* [1981].

Mercury's close proximity to the Sun and its eccentric orbit means that the local plasma environment at Mercury is ever-changing. The basic solar wind parameters that drive magnetospheric dynamics are the IMF, the solar wind plasma density, temperature and bulk flow velocity. For the ambient solar wind, all the quantities, except velocity, change with increasing radial distance from the Sun; the velocity of the solar wind is usually assumed to be constant. Table 1.1 shows a list of typical solar wind parameters calculated at different terrestrial planets and their radial dependences [*Slavin and Holzer,* 1981]. Solar wind values were also calculated for both perihelion and aphelion of Mercury's orbit. The solar wind proton density (n_p) and magnetic field intensity (B) at perihelion is ~ twice that at aphelion, demonstrating the range of the expected variations of Mercury's local plasma environment throughout its orbit around the Sun.

Having knowledge of the average solar wind condition at any given time is essential in conducting broader and more comprehensive studies with *in situ* measurements on solar wind interaction with planetary magnetospheres. At Earth, there are multiple solar wind upstream monitoring spacecraft [e.g. the Advanced Composition Explorer (ACE) to provide real-time solar wind conditions.

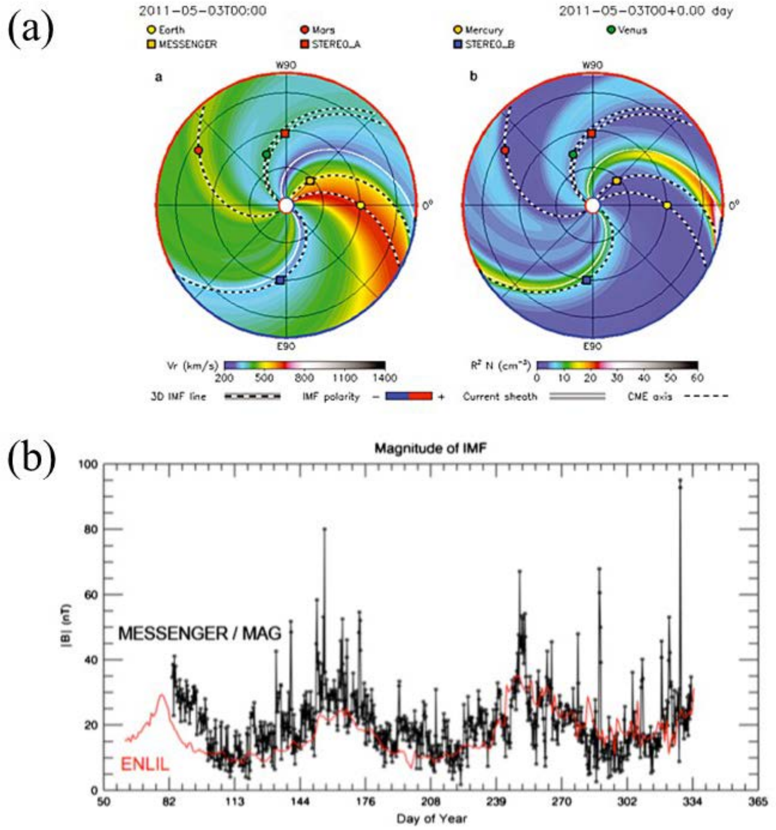

Figure 1.4 (a) Wang-Sheeley-Arge (WSA) – ENLIL model results during MESSENGER's orbital mission period on 3rd March 2011. Left and right panel show the solar wind radial velocity (V_r) and product of the square of radial distance and number density (R^2N) in the equatorial plane, respectively. (b) Comparison of interplanetary magnetic field intensity observed by MESSENGER (black) and the ENLIL model (red) as a function of time. Figure taken from *Baker et al.,* [2013].

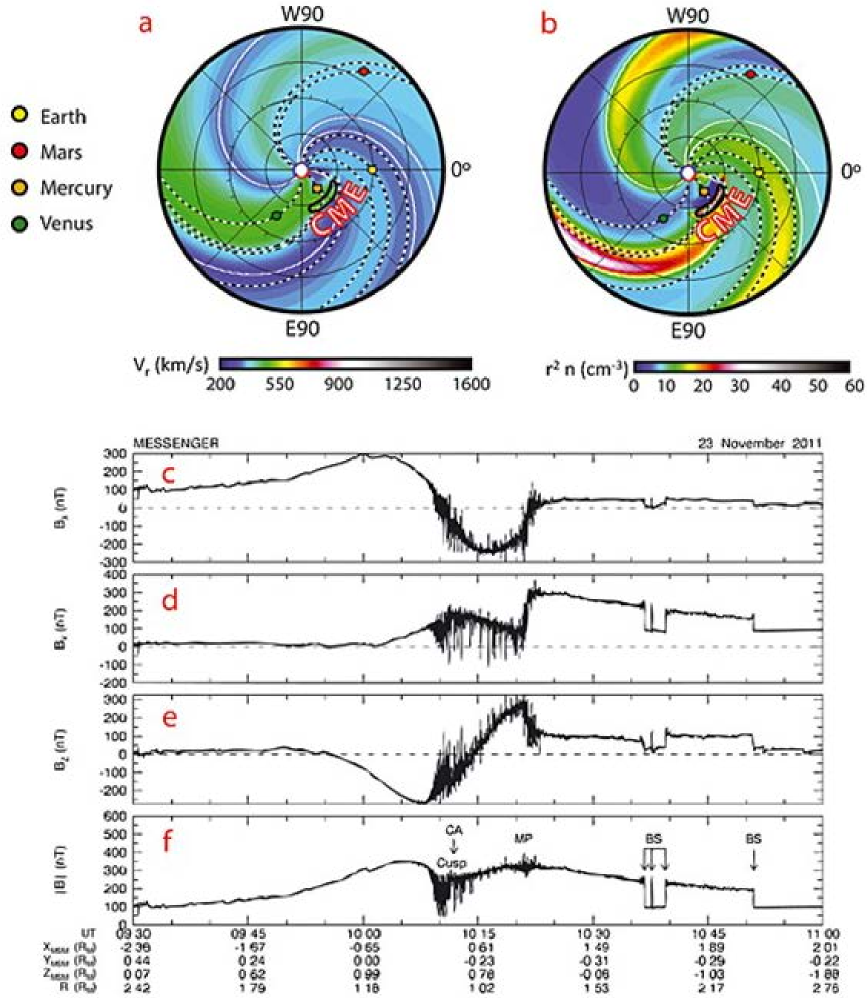

Figure 1.5 (a-b) WSA – ENLIL model results of solar wind radial velocity (V_r) and product of the square of radial distance and number density (R^2N) on 23rd November 2011. Format is similar to Figure 1.4a. (c-f) Magnetic field measurements of Mercury's magnetosphere observed by MESSENGER during a CME encounter on 23rd November 2011. The locations of closest approach (CA), cusp, magnetopause (MP) and bow shock (BS) crossings are also labelled. Figure taken from *Slavin et al.*, [2014].

At Mercury, MESSENGER can only provide single-point measurements and it is impossible to quantify the ambient solar wind conditions for each orbit when MESSENGER is inside the magnetosphere. *Baker et al.*, [2009] proposed the use of an empirical, physic-based global magnetohydrodynamic (MHD) model called the Wang-Sheeley-Arge (WSA) – ENLIL to provide specific ambient solar wind flow speed, plasma density, plasma temperature and magnetic field strength at Mercury. The ambient model results were validated with three MESSENGER flyby data [*Baker et al.*, 2011] and first year of MESSENGER orbital data [*Baker et al.*, 2013]. Figure 1.4a shows an example of the global map of inner heliospheric solar wind velocity and plasma density produced by the WSA-ENLIL model on 3 May 2011. The numerical model can also be run over extended period of time and Figure 1.4b shows comparison between MESSENGER data (black) and ambient model results (red) for solar wind magnetic field magnitude over the first 10 months of MESSENGER orbital mission. Even though the WSA-ENLIL model underestimated the magnetic field magnitude by a few nanotesla, it was able to capture the 88-day period orbital variation and show good general agreement with MESSENGER data. Figure 1.4b also shows large variances in the magnetic field measurements caused by the passage of transient interplanetary events [e.g. coronal mass ejections (CMEs)]. Transient events, such as CMEs, can be captured using the cone model extension to the WSA-ENLIL model, which was used extensively to study Mercury's magnetosphere under extreme solar wind conditions [e.g., *Slavin et al.*, 2014] as shown in Figure 1.5.

1.3 Magnetic Reconnection

Magnetic reconnection is a fundamental plasma process that occurs in laboratory, space and astrophysical plasma systems. It is the most efficient method to convert magnetic energy into plasma kinetic and thermal energy. In the case of magnetospheric physics, it is also responsible for the transfer of mass, energy and momentum across magnetospheric boundaries. To understand the physics of magnetic reconnection, we must first start with the generalized Ohm's law for collisionless plasma:

$$\mathbf{E} + \mathbf{v} \times \mathbf{B} = \eta \mathbf{J} + \frac{1}{ne} \mathbf{J} \times \mathbf{B} - \frac{1}{ne} \nabla \mathbf{P} + \frac{m_e}{ne^2} \frac{\partial \mathbf{J}}{\partial t} \tag{1.1}$$

where $\mathbf{E}$ is the total electric field, $\mathbf{J}$ is the current density, $\mathbf{v}$ is the velocity of plasma, $\mathbf{B}$ is the magnetic field, η is the resistivity of the plasma and $\mathbf{P}$ is the electron pressure tensor. Ideal MHD theory requires that $\mathbf{E} + \mathbf{v} \times \mathbf{B} = \mathbf{0}$. This means that the magnetic field lines move with the plasma (i.e., "frozen-in" to the plasma) and the electric field component parallel to $\mathbf{B}$, $E_{\parallel}$ is zero. Magnetic reconnection occurs when the ideal MHD "frozen-in" condition is violated and the right-hand terms in Equation 1.1 becomes significant at spatial scales on the order of ion and electron inertial lengths. Figure 1.6 illustrates the process of magnetic reconnection.

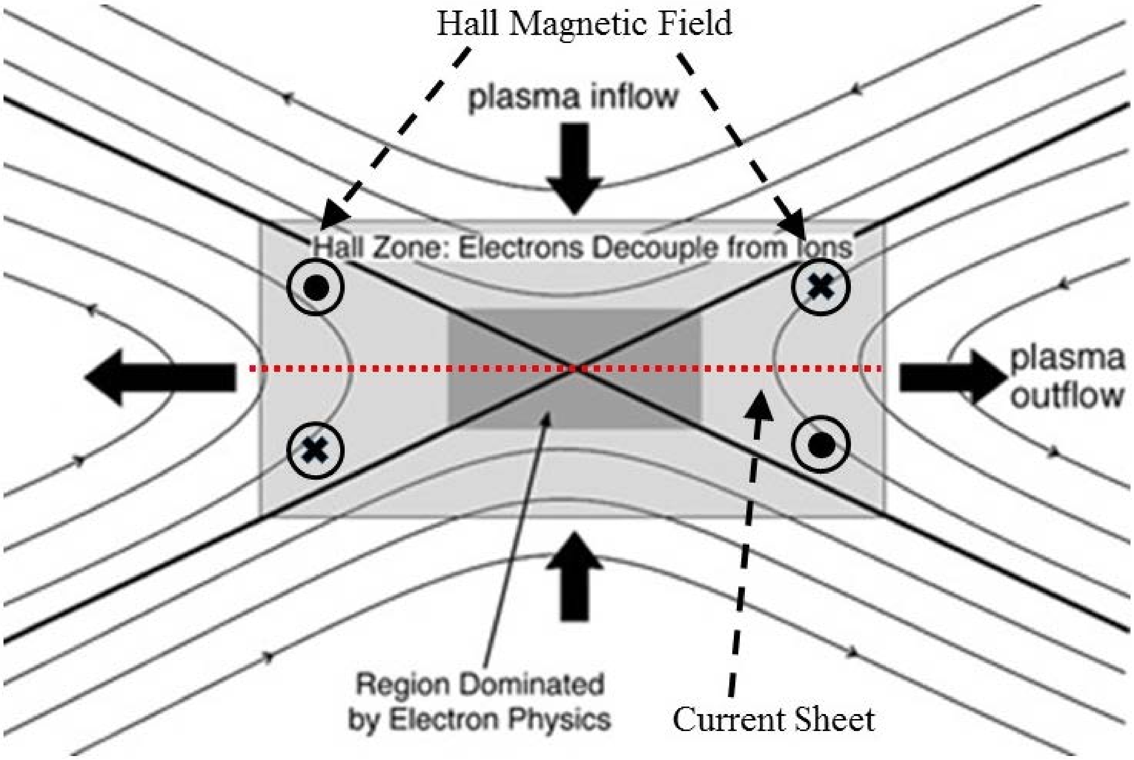

Figure 1.6 Two-dimensional schematic illustrating the microphysics of magnetic reconnection. Outer shaded region represents the Hall diffusion region and the inner darker shaded region represents the electron diffusion region. Figure taken from *MMS' Holy Grail: The Diffusion Region* (URL: http://mms.space.swri.edu/science-3.html).

As two oppositely-oriented magnetic field lines $\mathbf{E} \times \mathbf{B}$ drift towards each other, a current sheet is formed. When the current sheet thins to a spatial scale smaller than an ion inertial length, the ions become de-magnetized and exhibit non-ideal MHD behavior. This region is called the ion diffusion region, where the Hall term ($\frac{1}{ne}\, \mathbf{J} \times \mathbf{B}$) dominates the resistive term ($\eta\mathbf{J}$) in the generalized Ohm's Law. The electrons, which have smaller gyroradii, remain magnetized to the inflow magnetic field lines. The decoupling of protons and electrons also result in the characteristic quadrupolar Hall magnetic field in the ion diffusion region. The inflow magnetic field lines break and reconnect at the neutral point inside the electron diffusion region, where the electrons are de-magnetized. In the electron diffusion region, the electron pressure gradient and electron inertial terms ($\frac{1}{ne}\, \nabla\mathbf{P} + \frac{m_e}{ne^2}\frac{\partial\mathbf{J}}{\partial t}$) dominate other terms in the generalized Ohm's Law. The plasma is then accelerated away from the reconnection region at the local Alfvén speed when kinetic energy is transferred to the particles due to the **J** × **B** force from the newly-reconnected field lines as they relax into the lowest energy state.

Note that Figure 1.6 shows a simple, two-dimensional view of magnetic reconnection. In three-dimension, the magnetic field in the inflow regions reconnect at more than one neutral point, resulting in a reconnection line (i.e., an X-line). Furthermore, the magnetic field lines in the inflow region need not be exactly opposite to each other in order for reconnection to take place. Magnetic reconnection can potentially occur between any pair of magnetic field lines, where the shear angle between the two inflow magnetic field vectors is not 180°. This process is known as component reconnection and its importance on magnetic reconnection at Mercury will be discussed later.

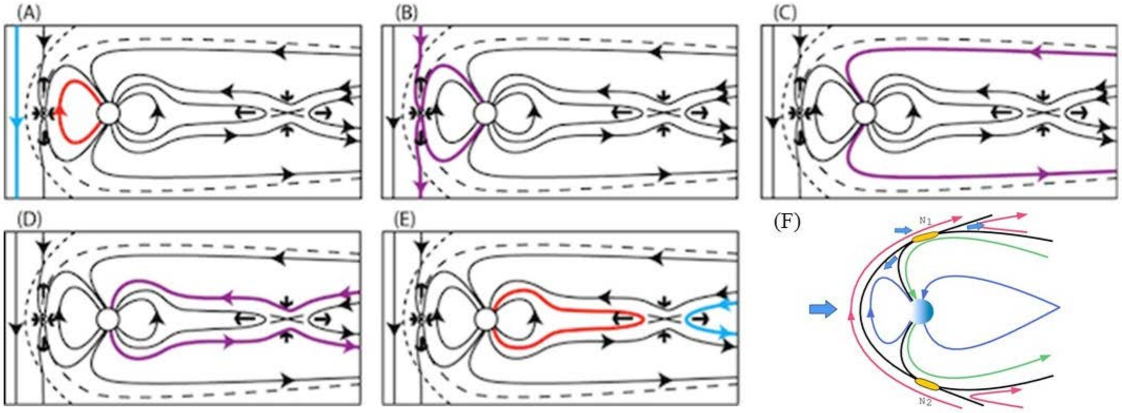

Figure 1.7 Schematics illustrating the dayside magnetic reconnection and Dungey Cycle under southward (A-E) and northward (F) solar wind conditions. Figures taken from *Eastwood et al.*, [2015] and *Dorelli J.C.*, UNH.

In magnetospheric physics, magnetic reconnection is known to occur at the dayside magnetopause and in the magnetotails of all planetary magnetospheres. As mentioned earlier in Section 1.1, it is believed that for all planetary magnetospheres in the solar system, the planetary magnetic field can connect to the IMF through magnetic reconnection. The process of opening and closing magnetic field at the magnetopause and in the magnetotail while conserving the total magnetic flux is called the Dungey cycle. Figure 1.7 shows a schematic of an open magnetosphere with a southward pointing magnetic dipole moment (e.g., Mercury and Earth) for southward IMF. As shown in Figure 1.7a, the southward IMF (blue) reconnects with the northward planetary field (red) at the subsolar point of the dayside magnetopause. The newly-reconnected magnetic field line (purple line in Figure 1.7b) convects over the polar cap and adds open flux to the magnetotail lobe (Figure 1.7c). The oppositely-directed tail lobe field lines $\mathbf{E} \times \mathbf{B}$ drift towards the central plasma sheet and reconnect again in the magnetotail, as depicted in Figure 1.7d. The newly-closed planetary field lines (red line in Figure 1.7e) will convect towards the planet and into the dayside magnetosphere, where the magnetic flux circulation process repeats again. Magnetic reconnection can also occur during northward IMF, as shown in Figure 1.7f. For northward IMF, it is thought that reconnection can occur at higher latitude but it doesn't open any magnetic flux of the magnetosphere. The Dungey cycle is highly dependent on the solar wind interaction with the magnetosphere. At Earth, the Dungey cycle time is ~1 – 3 hours while the Dungey cycle at Mercury is ~1 – 3 minutes, which is faster and more intense than Earth's due to more extreme solar wind forcing at Mercury.

1.4 Flux Transfer Events

One of the products of magnetic reconnection at the dayside magnetopause is the flux transfer events (FTEs), which are commonly observed at Earth and other planets, such as Mercury [*Slavin et al.,* 2012; *Imber et al.,* 2014], Jupiter [*Walker and Russell,* 1985] and Saturn [*Jasinski et al.,* 2016]. Since the first observation of FTEs at Earth by *Russell and Elphic* [1978], extensive research had been done to understand the structure, formation and evolution of this phenomenon. It is now well-established that FTEs are flux rope structures with the helical magnetic field wrapping around an axial core field, as shown in Figure 1.8. Since the FTEs are formed via dayside reconnection, it is also an open magnetic structure with one end connected to the planet and the other to the solar wind [*Lee and Fu,* 1985; *Hasegawa et al.,* 2006] and filled with plasma of magnetospheric and magnetosheath origin.

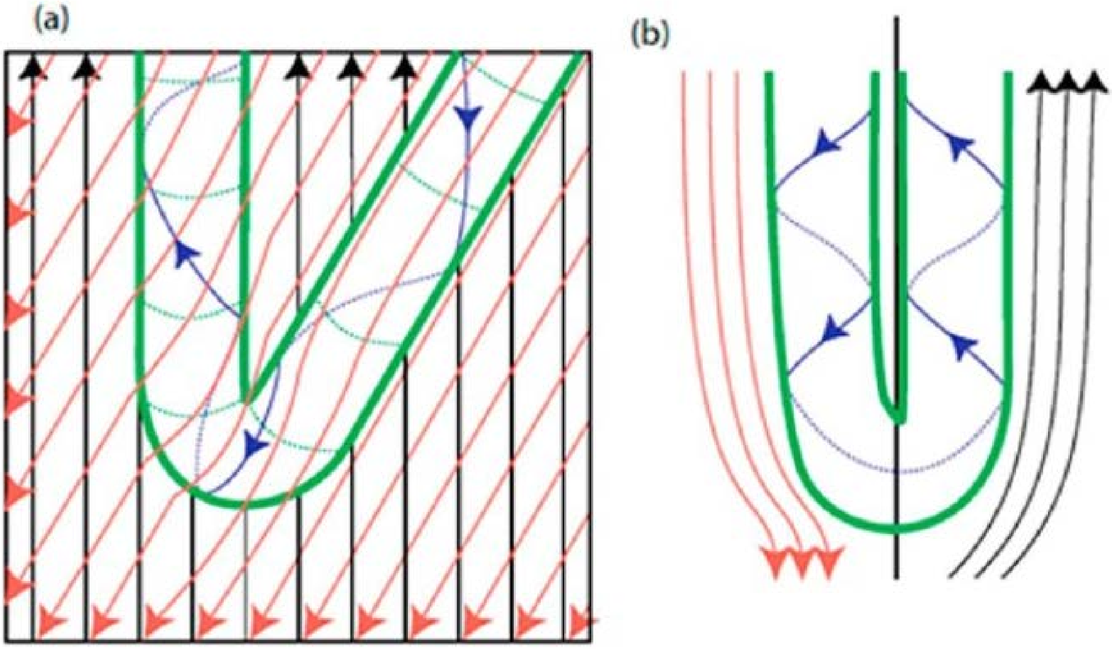

Figure 1.8 (a) Flux transfer event (FTE) as viewed against the magnetopause surface. The red vectors represents the magnetosheath magnetic field draping over the FTE, the black vector represents the planetary magnetic field and the green lines marked the boundary of the FTE. (b) Side view of the FTE shown in Figure 1.8a. FTEs are flux ropes formed via multiple X-line reconnection at the dayside magnetopause, with one end connected to the solar wind and the other to the planet, and has a helical magnetic structure as shown by blue lines. Figure taken from *Slavin et al.,* [2014].

Many models have been proposed for the formation of FTEs. The now widely accepted formation theory is the multiple X-line reconnection (MXR) model [*Lee and Fu,* 1985]. Figure 1.9 shows the schematics of the MXR model. In this model, two or more X-lines are formed simultaneously or sequentially on the magnetopause surface and a helical flux rope (i.e., FTE) is formed between each pair of X-lines (Figure 1.9a and 1.9b). After reconnection, the pair of FTEs will move in opposite direction due to the magnetosheath plasma flow and magnetic tension force associated with the kinking of magnetic field lines (Figure 1.9c and 1.9d). As these flux ropes are transported antisunward along the magnetopause surface, they compress the surrounding magnetic field lines and create another observable phenomenon called the travelling compression regions (TCRs). In the MXR model, the presence of a guide field (i.e., magnetic field component along the reconnection X-line) is necessary to form the core field, which is responsible for all the open magnetic flux in a FTE transferred to the magnetotail. Without a guide field, a magnetic loop, instead of a flux rope, is formed. It follows that the core field polarity of a FTE should be correlated to the guide field at the time magnetic reconnection occurs.

However, *Teh et al.,* [2014b] reported observations of FTEs with core field polarity opposite to the guide field. Similar observation was also reported by *Sibeck et al.,* [2008]. Teh et al., [2014a] proposed that during weak guide field reconnection, the quadrupolar Hall magnetic field formed in the ion diffusion region could provide the initial guide field needed to seed the formation of a core field. The question on the formation of the core field remains an open question.

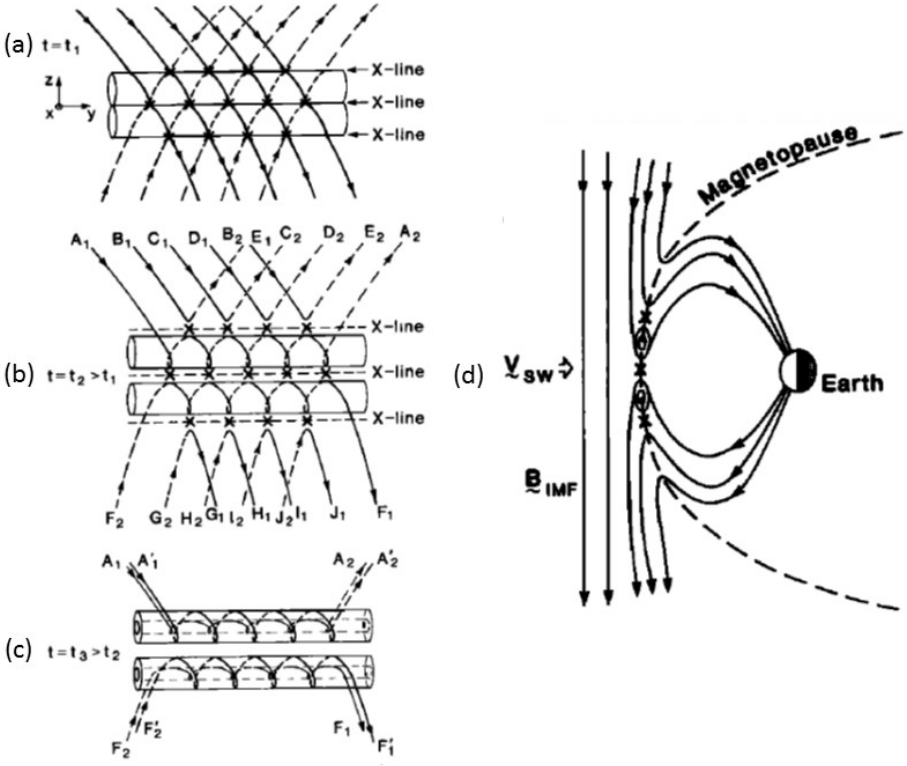

Figure 1.9 (a-c) Schematics illustrating the formation of a pair of flux transfer events (i.e., flux ropes) from multiple X-line reconnection at the dayside magnetopause. (d) Side view of the FTEs forming on the magnetopause surface. Figures taken from *Lee and Fu,* [1985].

The FTE evolves over time as it is transported from the dayside magnetopause, over the cusp and into the magnetotail. At the time of formation, the helical structure of the FTE, filled with plasma of magnetospheric and magnetosheath origin, exerts a radial pinching force due to magnetic tension. This increases the internal plasma pressure, resulting in the acceleration of ions and electrons along the flux rope. Since the FTE is magnetically connected to the planetary field at the cusp, these accelerated particles can precipitate into the planetary cusp. With the plasma beta inside the FTE decreasing, the structure collapses further until a pressure balance equilibrium (force-free) is reached between the outward magnetic pressure from the core field and the inward magnetic pressure (i.e., $\mathbf{J} \times \mathbf{B} = \mathbf{0}$ and $\mathbf{J}$ is parallel to $\mathbf{B}$). The field-aligned current along the FTE and its weak core field at the time of formation satisfy the right conditions for the newly-formed flux ropes to be kink unstable [*Treumann and Baumjohann,* 1977]. Laboratory plasma experiments have shown that plasma-filled flux ropes are kink unstable and could interact with either its environment or adjacent flux ropes [*Gekelman et al.*, 2014]. Kink instability could occur in FTEs, resulting in violent interaction between FTEs and highly complex magnetic structures [*Borg et al.,* 2012].

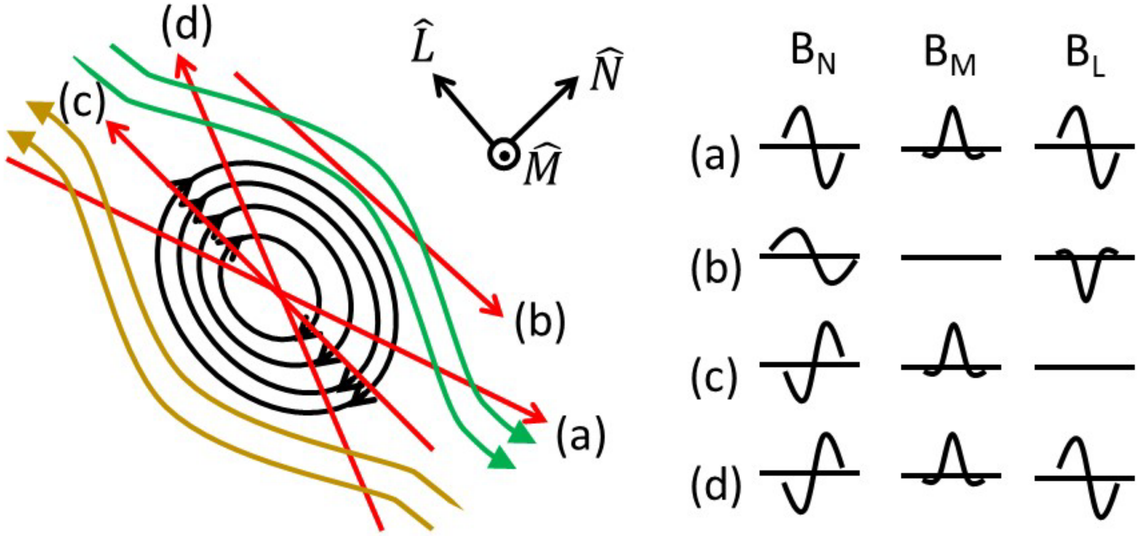

Figure 1.10 Spacecraft trajectories (red arrows) through a flux rope (a,c,d) and the travelling compression region (b), and their expected magnetic field signatures as observed by the spacecraft. The expected magnetic field observations are shown in the boundary normal coordinate system, where $\hat{\boldsymbol{N}}$ is normal to the magnetopause, $\hat{\boldsymbol{M}}$ is defined as the projection of $\hat{\boldsymbol{Z}}$ onto the surface tangential to the magnetopause surface and $\hat{\boldsymbol{L}}$ completes the right hand coordinate system. Green arrows represent the magnetosheath magnetic field and the yellow arrows represent the magnetospheric magnetic field.

FTEs are usually identified from its distinct bipolar magnetic field signature in one or two of the magnetic field components with an enhancement in the third component due to its core field. However, the observation of the bipolar signature in either of the magnetic field components is highly dependent on both the orientation of the FTE and the spacecraft trajectory across the flux rope. Hence, it is necessary to first transform the magnetic field measurements into a local magnetopause boundary LMN coordinate system [*Russell and Elphic,* 1978]. In this coordinate system, $\hat{\boldsymbol{N}}$ is normal to the magnetopause and can be calculated using a magnetopause model [*Shue et al.*, 1997] or minimum variance analysis (MVA) [*Sonnerup and Cahill*, 1967]. $\hat{\boldsymbol{M}}$ is defined as the projection of $\hat{\boldsymbol{Z}}$ onto the surface tangential to the magnetopause surface and $\hat{\boldsymbol{L}}$ completes the right hand coordinate system [*Berchem and Russell*, 1982]. The bipolar signature should then be observed in the normal component of the magnetic field. Figure 1.10 shows the illustration of an FTE in boundary normal coordinate system and the magnetic field observations for different spacecraft trajectories. In the ideal situation where the spacecraft traverse directly through the center of the flux rope [i.e., case (c)], the bipolar and peak core magnetic field signature is observed in the $\hat{\boldsymbol{N}}$ and $\hat{\boldsymbol{M}}$ direction, respectively. There is no signature in the $\hat{\boldsymbol{L}}$ direction. However, the spacecraft usually encounters the FTE at an angle [e.g. case (a) and (d)] and the bipolar signature can be observed in both $\hat{\boldsymbol{N}}$ and $\hat{\boldsymbol{L}}$ direction with peak core field in the $\hat{\boldsymbol{M}}$ direction. The expected magnetic field signature is also shown in case (b).

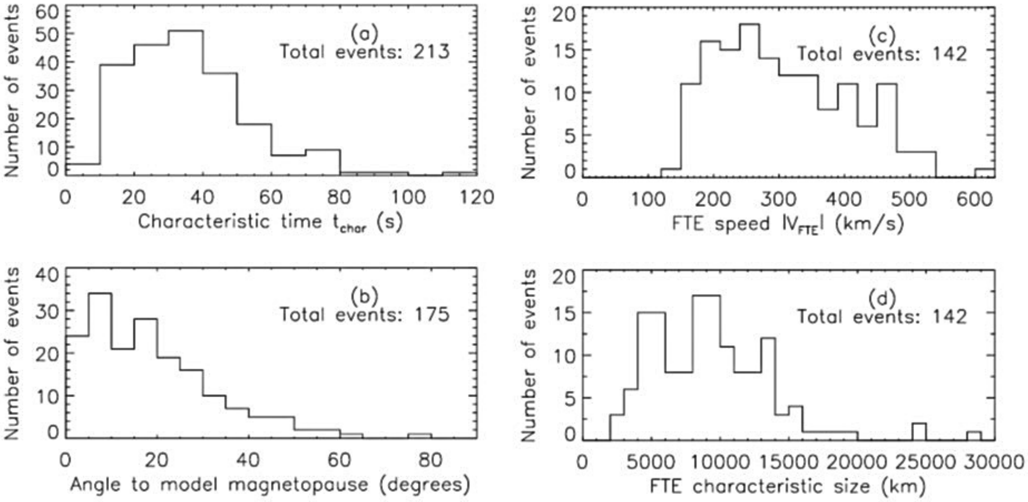

Figure 1.11 Histograms of the (a) Characteristic time, (b) angle between the model FTE velocity to model magnetopause surface, (c) speed and (d) the characteristic size of the FTEs observed by all four Cluster spacecraft. Figure taken from *Fear et al.*, [2007].

In the recent years, multi-spacecraft missions, such as the Cluster and Magnetospheric Multi-Scale (MMS) missions, have enabled new understanding of the FTEs formed at Earth's magnetopause with multi-point measurements. Extensive statistical studies have been done to characterize properties of the terrestrial FTEs [e.g., *Wang et al.*, 2005; *Fear et al.*, 2005; 2007]. FTEs at Earth are generally 30 seconds long in duration and travel at average speeds of ~ 300 km/s across the magnetopause surface, as shown in Figure 1.11.

This translates to an average FTE size of ~ 1.4 R_E (1 R_E = 6371 km). *Owen et al.,* [2001] used Cluster plasma and magnetic field measurements to show that FTEs have substructures within spatial scale of Cluster's 4-spacecraft separation (i.e., ~5000 km), which cannot be achieved previously with single spacecraft measurements. *Hasegawa et al.,* [2010] also applied the Grad-Shafranov reconstruction technique [*Sonnerup and Guo,* 1996] to Cluster's magnetic field and plasma measurements to reconstruct a 2.5-dimensional map of the internal plasma structure of the FTE. More recently, *Eastwood et al.,* [2016] reported the first observation of ion-scale FTEs at the dayside magnetopause using MMS measurements.

The unique solar wind environment at Mercury makes it a perfect natural laboratory to study the formation and evolution of flux transfer events. *Russell and Walker* [1985] reported the first observation of FTE at Mercury using Mariner 10 flyby data. The observed FTEs lasted for ~ 1 second and hence, had a diameter of ~ 400 km for an assumed travelling speed of ~ 400 km/s. *Slavin et al.,* [2010a] conducted a comprehensive survey of MESSENGER's data during its first two Mercury flybys and reported observations of 3 – 7 seconds long FTEs. Figure 1.12 shows the magnetic field measurements of two largest FTEs identified during the (a) first and (b) second flyby. To better estimate the actual diameter of the observed FTEs, *Slavin et al.,* [2010a] fitted MESSENGER's observation to a force-free flux rope model [*Lepping et al.,* 1990] using a least-squares method as shown by the red line in Figure 1.12. This model assumes that the flux rope is cylindrically symmetric and its current density **J** is linearly proportional to the magnetic field **B** by a constant α (i.e., **J** = α**B**). The analytical magnetic field model for the cylindrically symmetric, force-free flux rope is then given by the following Bessel functions [*Lundquist,* 1950]:

$$B_z(r) = B_0 J_0(\alpha^2)$$

$$B_\theta(r) = B_0 H J_1(\alpha^2)$$

$$B_r = 0 \tag{1.2}$$

where B_0 is the peak axial magnetic field intensity and H is the handedness of flux rope with values equal ± 1. Using this least-square fitting technique, *Slavin et al.,* [2010a]

(1.2)

estimated the diameter of the flux ropes to be ~ 0.078 – 0.52 R_M (1 R_M = 2440 km) and axial magnetic flux to be ~ 0.001 – 0.2 MWb. Note that the magnetic field measurements of the FTE shown in Figure 1.12b fits poorly to a force-free flux rope model and exhibits high frequency magnetic field fluctuation within the structure. This strongly suggests that the stresses acting on the flux rope are not balanced and shows substructures within the FTE itself. Subsequently, *Imber et al.,* [2014] conducted a statistical study of FTEs using MESSENGER's orbital data and identified a total of 58 large-amplitude FTEs (i.e., core field of FTE is larger than magnetopause field intensity) over 90 MESSENGER orbits. Using the same force-free flux rope fitting, they calculated an average magnetic flux content of ~ 0.06 MWb and estimated that FTEs carried ~ 30% of the total magnetic flux transferred to the nightside as compared to Earth's 2%. This clearly shows the importance of FTEs in Mercury's magnetospheric dynamics.

Low-β solar wind conditions ($\beta << 1$) lead to faster magnetic reconnection rate at the dayside magnetopause. As a result, magnetic reconnection is constantly occurring at Mercury's dayside magnetopause for all shear angles [*DiBraccio et al.,* 2013]. The high reconnection rate also creates a FTE phenomenon unique to Mercury, where FTEs were formed in rapid successions. *Slavin et al.,* [2012] reported the first observations of these intervals of quasiperiodic FTEs in MESSENGER magnetic field data and termed them FTE shower. Figure 1.13 shows the magnetic field measurements of a FTE shower example on 11 April 2011. During this 25 minute interval, a total of 163 FTEs were identified and consecutive FTEs are separated by ~ 8 – 10 seconds. Out of these 163 FTEs, the first 97 events are identified as TCRs caused by the passage of a FTE and the last 66 events are observed directly as flux ropes. In this study, *Slavin et al.,* [2012] used a non-force-free, instead of a force-free, flux rope model [*Hidalgo et al.,* 2002a; 2002b], which does not assume a cylindrical shape for the flux rope. They calculated a mean semi-major axis for the flux ropes to be ~ 373 km, with mean eccentricity of ~ 0.86 (0 is a circle and 1 is a parabola). Their results indicate that these flux ropes are much smaller than those FTEs observed in earlier studies [e.g., *Slavin et al.,* 2010a]. They are also extremely "flattened", which is not surprising since external stresses from the magnetosheath are constantly exerted on these flux ropes as they are transported along the magnetopause surface.

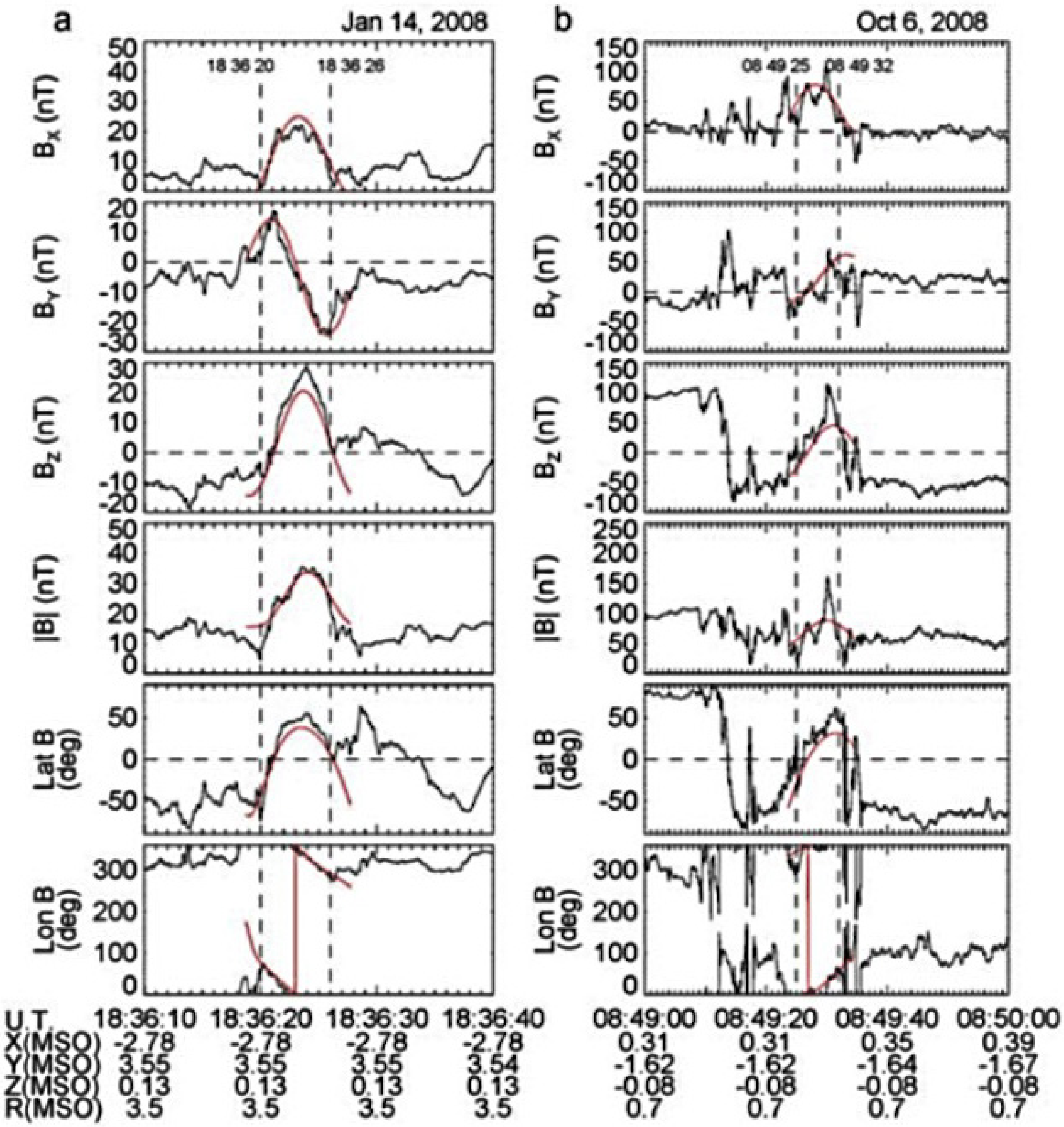

Figure 1.12 Magnetic field measurements in MSO coordinate sytem of two flux transfer events observed by MESSENGER during (a) first and (b) second flyby. Red line represents the best-fit curve of the data to the force-free flux rope model; the fitting interval is marked by two dashed lines. Figure taken from *Slavin et al.*, [2010a].

From the above discussions, it is clear that the intense solar wind conditions at Mercury have a significant impact on the physical properties of FTEs formed at the dayside magnetopause and the roles the FTEs played in Mercury's magnetospheric dynamics. FTEs also have huge impact on cusp dynamics at Mercury. Since FTEs are flux ropes with one end magnetically connected to Mercury's planetary field at the cusp, magnetosheath plasma inside the FTEs at the time of formation can move along the field line and precipitate into the cusp. Since the magnetic field lines converge at the cusp, they act like a magnetic bottle similar to laboratory plasma confinement system and precipitating particles experience a mirror force. Hence, particles in the loss cone can interact directly

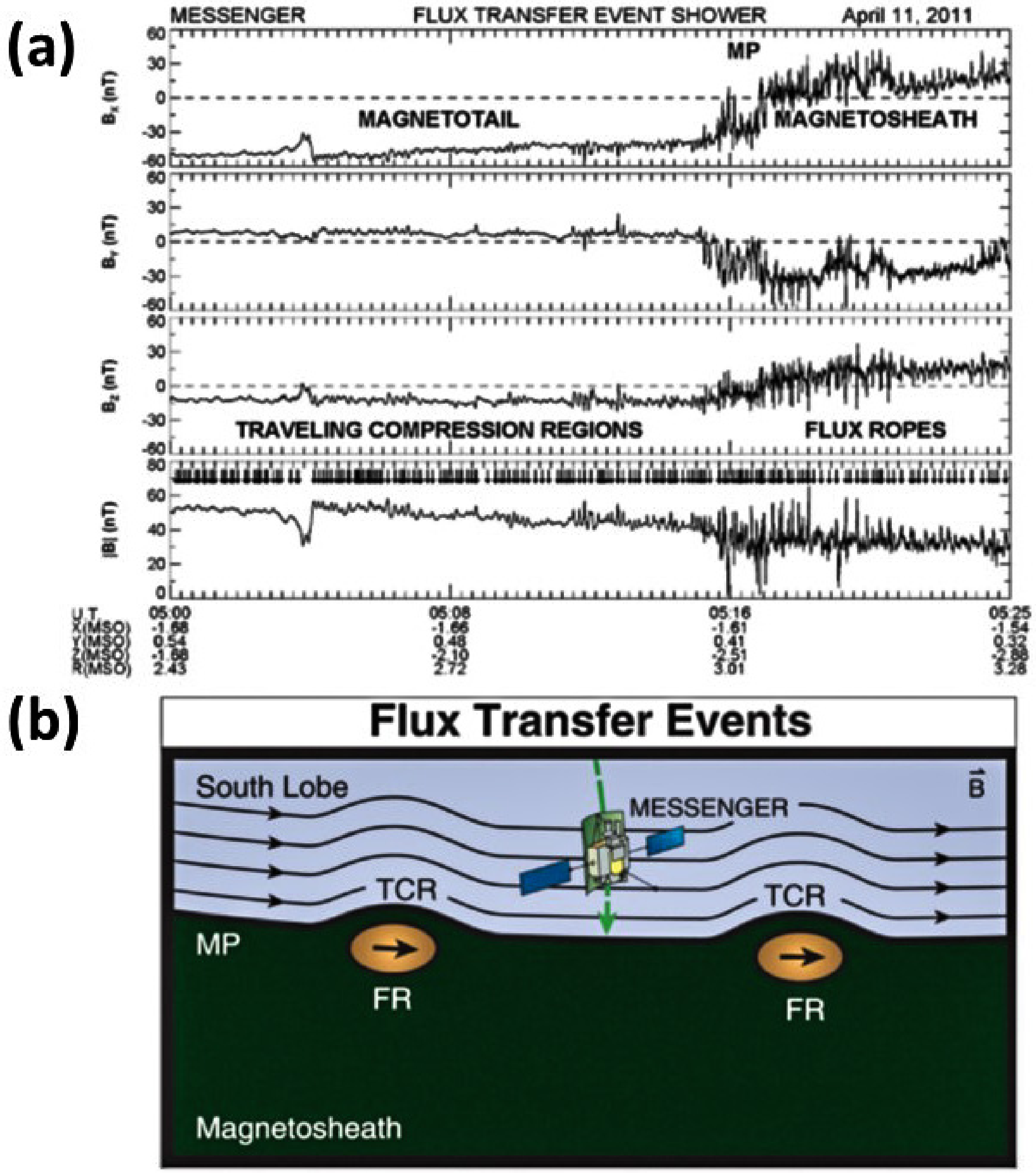

Figure 1.13 (a) Magnetic field measurements in MSO coordinate observed by MESSENGER on 11 April 2011 during an encounter with a flux transfer event (FTE) shower while the spacecraft crosses Mercury's magnetopause. A total of 97 travelling compression regions (TCRs) and 66 flux-rope-type FTEs were identified; each FTEs and TCRs are marked with an arrow. (b) Schematics illustrating observation of the TCRs and FTEs passing over MESSENGER during a FTE shower as MESSENGER crosses Mercury's magnetopause. Figure taken from *Slavin et al.*, [2012].

with Mercury's surface due to the lack of an atmosphere. The effect of precipitating magnetosheath particles associated with FTEs manifested as filamentary flux tubes observed at Mercury's cusp known as cusp plasma filaments [*Slavin et al.,* 2014; *Poh et al.,* 2016]. To date, observations of cusp plasma filaments are unique to Mercury because of its intense solar wind environment and they were shown to be related to extreme solar wind dynamic pressure events [*Slavin et al.,* 2014]. Detailed analysis of the cusp plasma filaments and its relation to FTEs will be discussed further in Chapter IV.

FTEs at Mercury are also known to carry about one-third of the total magnetic flux transported into the magnetotail [*Imber et al.,* 2014]. At Earth, FTEs are known to carry only ~ 2% of the total magnetic flux transported into the magnetotail, which is determined to be severely underestimated due to the lack of knowledge of the actual number of FTEs formed at the magnetopause at any given time [*R. Fear*, private communication]. This is also true in the case of Mercury and initial analysis of MESSENGER data had already shown the wide spectrum of FTEs types being formed at the magnetopause. Hence, FTEs at Mercury contributes majority of the magnetic flux needed for reconnection-related phenomenon, such as substorms, in the magnetotail.

1.5 Magnetotail X-Lines and Substorms

A major consequence of magnetic reconnection in the magnetotail is the occurrence of substorms, which was first phenomenologically described by *Akasofu*, [1964] in terms of auroral activity in the Earth's ionosphere. The motivation to understand the substorm process at Earth stems from our need to understand how it can affect the plasma environment in the near-Earth region, which is extremely important as human progress into the space age. Over the last five decades, many substorm models have emerged. *In-situ* measurements from numerous missions put the Near-Earth Neutral Line (NENL) model as the leading substorm model. Magnetic reconnection as the source of energy for the occurrence of substorm by converting magnetic energy stored in the tail lobe into kinetic energy of the particles in the plasma sheet forms the basis of the NENL model. Figure 1.14 shows the schematics for the current NENL model.

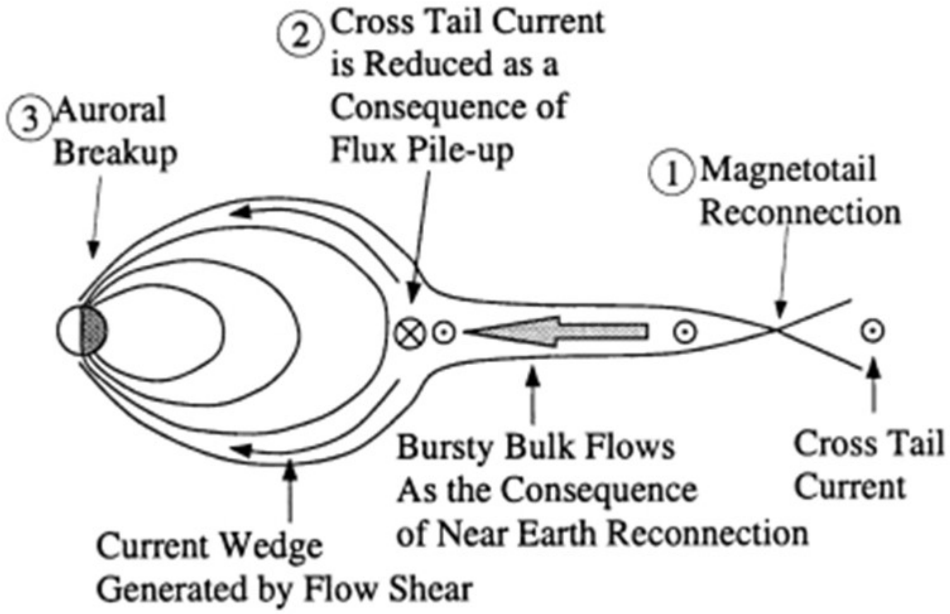

Figure 1.14 Schematics illustrating the formation of a substorm current wedge due to magnetic flux pile-up and braking of bursty bulk flows caused by near-Earth magnetotail reconnection. The resulting inertial current reduces the cross-tail current in the current sheet. The fast flow is diverted along the magnetic field lines into the ionosphere and azimuthally around the strong, dipolar near-Earth magnetic field, thus forming the substorm current wedge. Figure taken from *Shiokawa et al.,* [1997].

The substorms process starts when the tail lobe is loaded with magnetic flux (and magnetic energy) due to the imbalance in dayside and nightside magnetic reconnection rate. This is also known as the substorm growth phase, which typically lasts for ~ 1 hour [*Russell and McPherron,* 1973]. Initial magnetic reconnection in the plasma sheet is slow and the Alfvénic outflow speed is low (~100 km/s) due to the high plasma beta (β ~ 3 [*Baumjohann et al.,* 1989b]) environment in the plasma sheet. When the low-β tail lobe field lines start to reconnect, there is a sudden increase in reconnection rate and release of magnetic energy into the magnetotail. The X-line location at which magnetotail reconnection occurs is called the Near-Earth Neutral Line (Point 1).

As reconnection proceeds, the X-line retreats antisunward at ~10% of the local Alfvén speed. Magnetic field lines planetward of the NENL are closed field with each end of the field line magnetically connected to each pole of the planet. Once reconnected, these “stretched” closed field lines will then travel away from the X-line at high speeds due to magnetic tension. Hence, they are often associated with discrete high-speed plasma flow enhancements called bursty bulk flow (BBF), due to intermittent, bursty nature of reconnection, [*Angelopoulos et al.*, 1992] and dipolarization of ambient magnetic field (i.e., piling of magnetic flux due to difference in flow speed). The leading edge of the dipolarized magnetic flux tubes is called dipolarization fronts.

As these closed, dipolarized flux tubes travel close to Earth, they encounter the stronger, dipolar planetary magnetic field of the inner magnetosphere. The antisunward-directing force from the outward plasma pressure gradient and magnetic pressure due to magnetic flux pile-up increase and oppose the sunward-directing magnetic tension force and slow down the plasma flow. When force balance is achieved, the flow brakes (Point 2) and magnetic field increases due to flux pile-up, which generate a dawnward inertial current and reduce the local duskward cross-tail current [*Shiokawa et al.*, 1997]. The plasma flow is diverted into the ionosphere, resulting in establishment of the substorm current wedge (SCW) [*Birn et al.*, 1999]. Auroral activities observed at Earth (Point 3) are the direct consequence of the development of the SCW.

The substorm process also occurs in other planetary magnetospheres and its effects have been observed everywhere. For example, the main aurora oval in the Jovian magnetospheres is thought to be caused by an internally-driven substorm-like process [e.g. *Kronberg et al.*, 2005]. The loading and unloading of Mercury's tail, which is indicative of substorm occurrence, was observed during MESSENGER's third flyby [*Slavin et al.*, 2010] and orbital phase [*Imber et al.*, manuscript in prep]. More recently, direct observation of Mercury's substorm process was also made [*Sun et al.*, 2015]. Although the process is similar to Earth's, the timescale at Mercury is much shorter. Intense dayside reconnection at Mercury aggravates the imbalance between dayside and nightside reconnection rate.

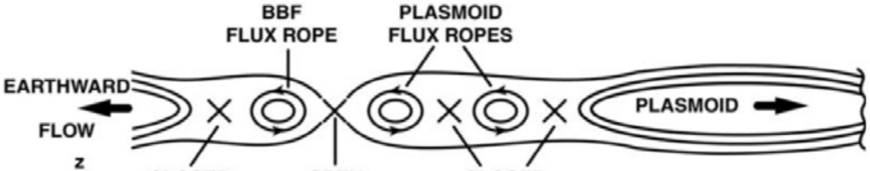

Figure 1.15 Schematics illustrating the formation of earthward-travelling BBF-type flux ropes and tailward-travelling plasmoid-type flux ropes due to multiple X-line reconnection in the plasma sheet. The X-line with the highest reconnection rate and first reconnects open tail lobe magnetic field lines (Open FLR) is the Near Earth Neutral Line and flux ropes formed earthward (tailward) of this X-line is ejected earthward (tailward). Figure taken from *Slavin et al.*, [2003].

The substorm growth (or loading) phase at Mercury is ~ 1 – 3 mins [*Slavin et al.,* 2010b; *Sun et al.,* 2015]. Magnetic reconnection occurs at the Near-Mercury Neutral Line (NMNL), sending high speed plasma flows and dipolarized flux tubes (or dipolarization events) towards Mercury. Using MESSENGER's magnetic field measurements, *Sundberg et al.,* [2012] conducted a statistical survey of dipolarization events at Mercury and concluded that the average duration of a dipolarization event is ~ 10 s. Unfortunately, MESSENGER's ion plasma instrument, Fast Imaging Plasma Spectrometer (FIPS), was unable to observe the high speed BBFs due to MESSENGER's sunshade obscuring significant portions of its field-of-view. However, the Gamma-Ray Spectrometer (GRS) was able to detect sharp increase in energetic electron counts associated with dipolarization fronts [*Dewey et al.,* manuscript in prep]. It is still an open question if a substorm current wedge can be formed at Mercury. If it does exist, how does the current close? This question was first examined by *Slavin et al.,* [1997] and, to date, the formation of a planetary substorm current wedge, other than Earth, has not been observed. The first possible observation of a substorm current wedge at Mercury and potential current closure mechanism will be discussed in Chapter VI.

The statistical location of the neutral line is important for understanding the plasma sheet condition at the time of substorm initiation. There are multiple methods of determining the statistical location of the neutral line using either magnetic field or plasma measurements. As the X-line retreats across the spacecraft, it observes a sunward (antisunward) plasma flow and northward (southward) magnetic field when it is planetward (tailward) of the neutral line. *Nagai et al.,* [1998a] conducted the statistical study using Geotail data on the spatial distribution of earthward and tailward high speed plasma flow and concluded that the NENL is located between 20 – 30 R_E downtail.

Another method was to study spatial distribution of reconnection products, such as magnetotail flux ropes. Similar to the dayside magnetopause, magnetic reconnection can occur at multiple X-lines and create flux ropes as shown in Figure 1.15. The reconnection X-line that first reconnects open tail lobe field lines becomes the dominant X-line (i.e., NENL), which has the fastest outflow speed. As a result, flux ropes sunward (antisunward) of the NENL will be "pushed" earthward (tailward). Since these flux ropes can also create

TCRs as they move in the plasma sheet, similar analysis of TCRs can be done too. *Imber et al.,* [2011] analyzed a total of 135 flux ropes in Earth's magnetotail using Time History of Events and Macroscale Interaction during Substorms (THEMIS) spacecraft data and estimated an average NENL of ~30 R_E downtail. The location calculated in this study agrees with earlier study by *Nagai et al.,* [1998a], even though it is at the upper limit of the range. Note that the study by *Imber et al.,* [2011] was conducted during solar minimum and X-lines are known to form further downtail when solar wind activity is weaker.

At Mercury, limited availability of MESSENGER plasma data means that only magnetic field measurements can be used to determine the location of the NMNL. Using the linear factor of 8 scaling [*Ogilvie et al.,* 1977], we would expect the NMNL to be located at ~2.5 – 3.8 R_M downtail. *DiBraccio et al.* [2015] analyzed 49 magnetotail flux ropes and determined the location of the NMNL to be between ~2 – 3 R_M based on the spatial distribution of sunward and anti-sunward flux ropes. We could also estimate the NMNL location using B_Z and more details about the statistical analysis on the spatial distribution of B_Z will be discussed in Chapter V.

1.6 Magnetotail Dawn-Dusk Asymmetries

Large scale statistical studies have shown that asymmetries are present and common in planetary magnetotails. The increasing ability to conduct these statistical studies due to availability of *in situ* magnetic field and plasma measurements has improved greatly our understanding of the observed asymmetries and their influences on magnetotail dynamics. With the large number of spacecraft in the geospace, Earth's magnetotail asymmetries are the most extensively studied and often used as a basis of comparison to other planetary magnetotails. Many observations have shown that physical properties and dynamic processes occurring in the terrestrial magnetotail are predominantly asymmetric in the dawn-dusk direction [*Walsh et al.,* 2014]. The most obvious magnetotail asymmetry is observed in the current sheet, where the dusk side current sheet is thinner than the dawn side [*Fairfield et al.,* 1981]. From Ampere's Law, it follows that there is an opposite asymmetry in the magnetotail current density [e.g., *Runov et al.,* 2005]. It was observed by the Cluster spacecraft that the dusk-side and dawn-side magnetotail current density ranges from 6 – 25 nA/m^2 and 4 – 10 nA/m^2, respectively [*Artemyev et al.,* 2011]. The dusk side current density is ~ 2 times higher than the dawn side. If accurate determination of the current sheet thickness and current density is not possible due to instrumental limitation, the magnitude of north-south component of the magnetic field (i.e., B_Z) could also be used as an indicator for the magnetic field geometry of the current sheet. A strong B_Z indicates a thicker and less stretched current sheet while a weaker B_Z indicates a thinner and more stretched current sheet. Dawn-dusk asymmetry in B_Z at Earth was observed to be similar to that of the current sheet thickness [*Baumjohann et al.,* 1990; *Wang et al.,* 2006; *Vasko et al.,* 2015].

Since magnetic reconnection occurs when the current sheet is thin, one would naturally expect the occurrence of reconnection and its products to possess asymmetry properties similar to that of current sheet thickness. In fact, studies have shown that a peak in the occurrence of substorm onset location in the pre-midnight (i.e., dusk side) sector of the current sheet [e.g., *Frey and Mende,* 2007]. Occurrence of dispersionless energetic particle (ion and electron) injections related to substorms was also found to have pronounced asymmetry towards dusk side [*Nagai et al.,* 1982; *Birn et al.,* 1997a]. By surveying a 16-year-long Geotail data set, *Nagai et al.,* [2013] found that the occurrence rate of reconnection-related high speed plasma flow is also higher in the pre-midnight than the post-midnight (i.e., dawn side) sector of the current sheet. As mentioned in the previous section, magnetotail reconnection results in the formation of flux ropes, which also creates the TCRs as it travels earthward or tailward in the plasma sheet, and dipolarization fronts. As shown in Figure 1.16, statistical studies on the dawn-dusk spatial distribution of flux ropes and TCRs using Cluster, Geotail [*Slavin et al.,* 2005] and THEMIS [*Imber et al.,* 2011] concluded that the probability of flux ropes/TCRs occurrence shows a strong duskward preference. Statistical analysis of the occurrence of dipolarization fronts conducted by *Liu et al.,* [2013] also shows similar asymmetry pattern. The dawn-dusk asymmetry of reconnection-related signatures persisted in the distant tail region (i.e., 100 – 180 R_E downtail). Negative B_Z (indicative of spacecraft being tailward of the X-line), fast tailward plasma flow [*Slavin et al.,* 1985] and plasmoids observations at lunar orbit [*Li et al.,* 2014] were also predominantly observed in the pre-midnight sector of the distant tail current sheet. The asymmetries mentioned here are summarized in Table 1.2. The reader is referred to *Walsh et al.,* [2014] for a complete review of all magnetospheric asymmetries (dayside and nightside) in Earth's magnetosphere.

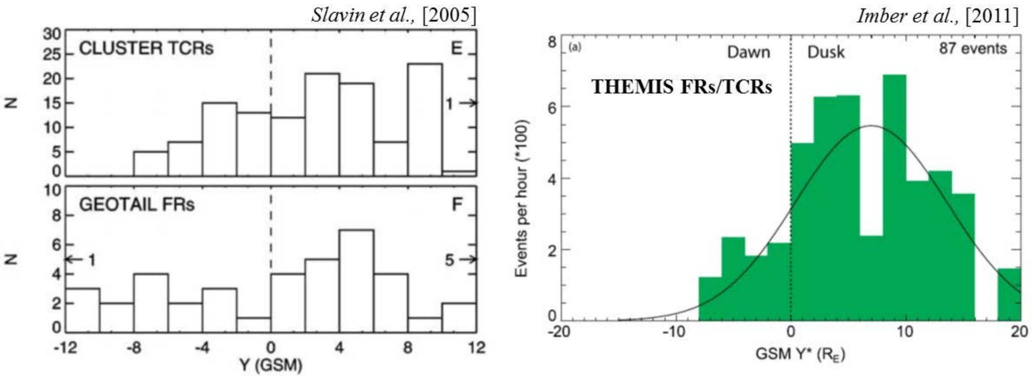

Figure 1.16 Spatial histogram of magnetotail flux ropes and travelling compression regions in the Y_{GSM} direction (i.e., dawn-dusk) as observed by (a) Cluster, (b) Geotail and (c) THEMIS spacecraft. Figures taken from *Slavin et al.,* [2005] and *Imber et al.,* [2011].

Continuous magnetic field and plasma measurements from MESSENGER allow us to conduct similar large scale statistical studies to investigate any persistent asymmetry features in Mercury's magnetotail. Using the plasma measurements from FIPS, *Raines et al.,* [2013] showed that there is a duskward enhancement in the observed heavy ion (O^+ and Na^+) density in Mercury's magnetotail as shown in Figure 1.17a. *Gershman et al.,* [2014] calculated maps of fluxes for different ion groups (H^+, He^{2+} and Na^+) in all visible directions (Figure 1.17b) and reported similar observation of Na^+ flux enhancement in the

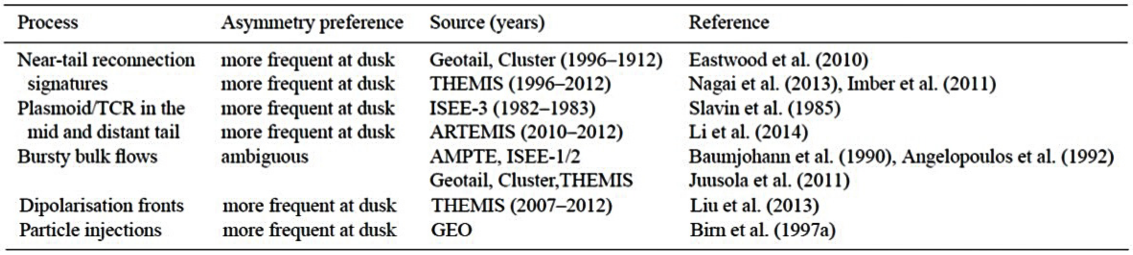

Process	Asymmetry preference	Source (years)	Reference
Near-tail reconnection signatures	more frequent at dusk	Geotail, Cluster (1996–1912)	Eastwood et al. (2010)
	more frequent at dusk	THEMIS (1996–2012)	Nagai et al. (2013), Imber et al. (2011)
Plasmoid/TCR in the mid and distant tail	more frequent at dusk	ISEE-3 (1982–1983)	Slavin et al. (1985)
	more frequent at dusk	ARTEMIS (2010–2012)	Li et al. (2014)
Bursty bulk flows	ambiguous	AMPTE, ISEE-1/2	Baumjohann et al. (1990), Angelopoulos et al. (1992)
		Geotail, Cluster,THEMIS	Juusola et al. (2011)
Dipolarisation fronts	more frequent at dusk	THEMIS (2007–2012)	Liu et al. (2013)
Particle injections	more frequent at dusk	GEO	Birn et al. (1997a)

Table 1.2 Summary of asymmetries in magnetotail processes observed by various spacecraft missions. Table taken from *Walsh et al.,* [2014].

pre-midnight plasma sheet. The Na^+ ion flux shows ~5 times enhancement in the dusk side magnetotail while H^+ and He^{2+} shows minor overall flux variations (~ 15% and 25%, respectively). Using the magnetic field measurements, *DiBraccio et al.,* [2014] conducted a statistical study on the spatial distribution of magnetotail flux ropes and observed no systematic asymmetry. *Sun et al.,* [2016] conducted a similar study, but used a different dataset and reported observations of a dawnward preference in the occurrence of plasmoids and reconnection fronts. More recently, *Lindsay et al.,* [2016] reported a similar dawnward preference in the occurrence of X-ray fluorescence events induced by precipitating energetic electrons due to magnetotail reconnection. This is consistent with *Dewey et al.,* [manuscript in prep], who observed more energetic electron events associated with dipolarization front dawn side of Mercury's magnetotail. Analysis of the asymmetry feature in magnetic field topology of Mercury's current sheet will be discussed further in Chapter VI.

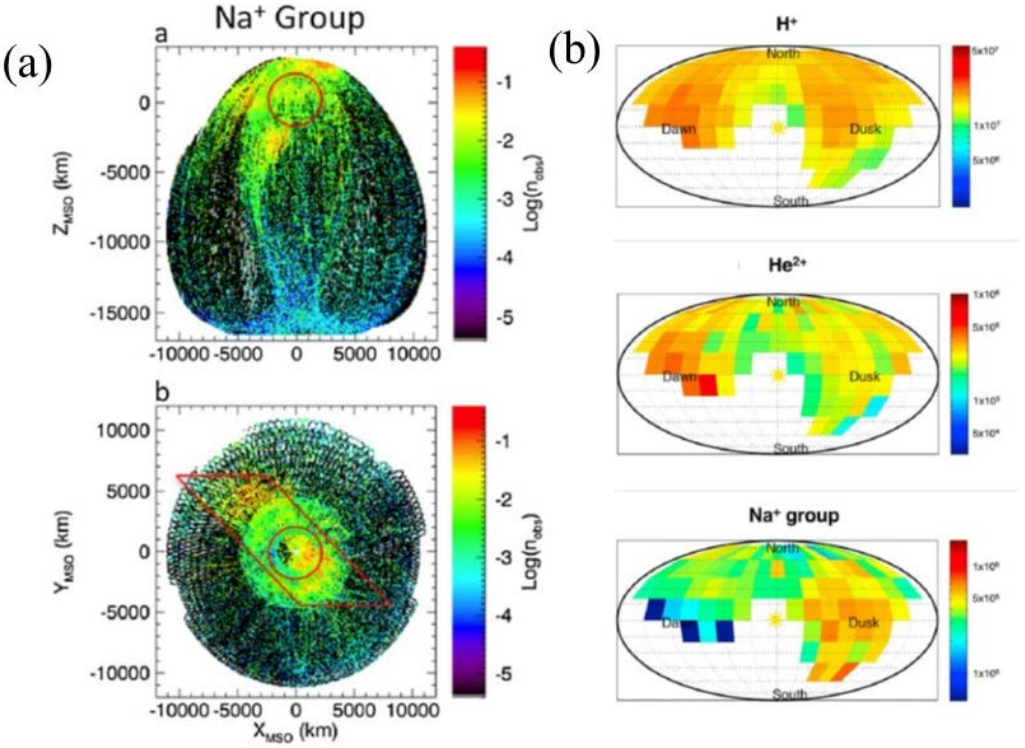

Figure 1.17 (a) Observed Na^+ group number density (n_{obs}) in Mercury's magnetosphere projected onto the (top) meridional and (bottom) equatorial plane. Red trapezoid represents region with enhanced observed number density in Na^+. (b) Projection map of directional fluxes in MSM coordinate system for (top) H^+, (middle) He^{2+}, and (bottom) Na^+ ion groups averaged over the dusk side plasma sheet for solar wind velocity between 300 – 400 km/s. Figures taken from *Raines et al.*, [2013] and *Gershman et al.*, [2014].

1.7 Summary

In this chapter, we have discussed the physics of the plasma processes occurring in Mercury's dayside magnetosphere and magnetotail. Being the smallest and closest planet to the Sun, Mercury's magnetosphere experience the most intense solar wind condition. It is Mercury's unique position among other planet that makes its magnetosphere a natural laboratory for studying many space plasma processes. The magnetic field and plasma data from the MESSENGER mission provided the perfect opportunity to conduct the research to understand and characterize the structure and dynamics of Mercury's magnetosphere. Below are the three guiding science questions that this thesis addresses in order to reach that new level of understanding of Mercury's magnetosphere:

Q1. What are cusp plasma filaments? What impact do they have on Mercury's cusp region?

In this chapter, we discussed the occurrence of magnetic reconnection at Mercury's magnetopause, which creates "open" magnetic field lines with one end connected to the planet and the other connected to the solar wind. Plasma with magnetosheath-like energies accelerate via magnetic reconnection along the field line and precipitate into the planetary cusp region. At Mercury, these precipitating plasma forms filamentary flux tubes called cusp plasma filaments. The occurrence of cusp filaments are unique to Mercury and have never been observed at other planetary cusp. Naturally, the questions of whether the plasma inside these cusp filaments precipitates to Mercury's surface in the cusp region and how will they interact with the surface also arise. Therefore, characterizing and determining the formation mechanism of these cusp filaments are important in our understanding of the solar wind-surface interaction at Mercury.

Q2. What is the structure of Mercury's cross-tail current sheet? Do the stresses measured by MESSENGER balance? What is the location of the statistical X-line in Mercury's current sheet?

Embedded inside of Mercury's plasma sheet is the cross-tail current sheet. It is also the region where magnetotail reconnection occurs. Hence, understanding the structure and stress balance of Mercury's cross-tail current sheet is important to understanding the nature and location of tail reconnection. MESSENGER provides the opportunity to study Mercury's cross-tail current sheet because of its unique near polar orbit around Mercury, which traverses the current sheet in the north-south direction.

Q3. Are asymmetries present in Mercury's cross-tail current sheet?

Magnetotail asymmetries were observed in Earth's and other planetary magnetospheres (e.g., Jupiter and Saturn). It is an active area of research because it is crucial in understanding plasma dynamics in planetary magnetotail. Naturally, one would ask if there are any asymmetries observed in Mercury's magnetotail. Here, we will quantify and characterize magnetotail asymmetries in Mercury's magnetotail and provide a possible explanation for the observed magnetotail asymmetries

References

Alexeev, I. I., E. S. Belenkaya, S. Yu. Bobrovnikov, J. A. Slavin, and M. Sarantos (2008), Paraboloid model of Mercury's magnetosphere, *J. Geophys. Res., 113*, A12210, doi:10.1029/2008JA013368.

Akasofu, S. I. (1964). The development of the auroral substorm. *Planetary and Space Science*, *12*(4), 273-282.

Anderson, B. J., C. L. Johnson, H. Korth, M. E. Purucker, R. M. Winslow, J. A. Slavin, S. C. Solomon, R. L. McNutt Jr., J. M. Raines, and T. H. Zurbuchen (2011), The global magnetic field of Mercury from MESSENGER orbital observations, *Science, 333*, 1859–1862, doi:10.1126/science.1211001.

Angelopoulos, V., W. Baumjohann, C. F. Kennel, F. V. Coroniti, M. G. Kivelson, R. Pellat, R. J. Walker, H. Lühr, and G. Paschmann (1992), Bursty bulk flows in the inner central plasma sheet, *J. Geophys. Res.*, *97*(*A4*), 4027–4039, doi:10.1029/91JA02701.

Artemyev, A. V., A. A. Petrukovich, R. Nakamura, and L. M. Zelenyi (2011), Cluster statistics of thin current sheets in the Earth magnetotail: Specifics of the dawn flank, proton temperature profiles and electrostatic effects, *J. Geophys. Res.*, *116*, A09233, doi:10.1029/2011JA016801.

Baker, D. N., et al. (2009), Space environment of Mercury at the time of the first MESSENGER flyby: Solar wind and interplanetary magnetic field modeling of upstream conditions, *J. Geophys. Res.*, *114*, A10101, doi:10.1029/2009JA014287.

Baker D.N., Odstrcil D., Anderson B.J., Arge C.N., Benna M., Gloeckler G., Korth H., Mayer L.R., Raines J.M., Schriver D., Slavin J.A., Solomon S.C., Trávníček P.M., Zurbuchen T.H. (2011), The space environment of Mercury at the times of the second and third MESSENGER flybys, Planetary and Space Science, 59(15), 2066-2074, doi:10.1016/j.pss.2011.01.018.

Baker, D. N., et al. (2013), Solar wind forcing at Mercury: WSA-ENLIL model results, *J. Geophys. Res. Space Physics*, *118*, 45–57, doi:10.1029/2012JA018064.

Baumjohann, W., G. Paschmann, and C. A. Cattell (1989b), Average plasma properties in the central plasma sheet, *J. Geophys. Res.*, *94*(*A6*), 6597–6606, doi:10.1029/JA094iA06p06597.

Baumjohann, W., G. Paschmann, and H. Lühr (1990), Characteristics of high-speed ion flows in the plasma sheet, *J. Geophys. Res.*, *95*(*A4*), 3801–3809, doi:10.1029/JA095iA04p03801.

Berchem, J. and Russell, C.T. (1982). Magnetic field rotation through the magnetopause: ISEE 1 and 2 observations, *Journal of Geophysical Research, 87*, doi: 10.1029/JA087iA10p08139.

Birn, J., M. F. Thomsen, J. E. Borovsky, G. D. Reeves, D. J. McComas, R. D. Belian, and M. Hesse (1997a), Substorm ion injections: Geosynchronous observations and test particle orbits in three-dimensional dynamic MHD fields, *J. Geophys. Res.*, *102*(*A2*), 2325–2341, doi:10.1029/96JA03032.

Birn, J., M. Hesse, G. Haerendel, W. Baumjohann, and K. Shiokawa (1999), Flow braking and the substorm current wedge, *J. Geophys. Res.*, *104*(*A9*), 19895–19903, doi:10.1029/1999JA900173.

Birn, J., and M. Hesse (2001), Geospace Environment Modeling (GEM) magnetic reconnection challenge: Resistive tearing, anisotropic pressure and Hall effects, *J. Geophys. Res.*, *106*(*A3*), 3737–3750, doi:10.1029/1999JA001001.

Borg A.L. et al., (2012), Observations of magnetic flux ropes during magnetic reconnection in the Earth's magnetotail, *Ann. Geophys.*, *30*, 109–117, doi:10.5194/angeo-30-109-2012.

DiBraccio, G. A., J. A. Slavin, S. A. Boardsen, B. J. Anderson, H. Korth, T. H. Zurbuchen, J. M. Raines, D. N. Baker, R. L. McNutt Jr., and S. C. Solomon (2013), MESSENGER observations of magnetopause structure and dynamics at Mercury, *J. Geophys. Res. Space Physics*, *118*, 997–1008, doi:10.1002/jgra.50123.

DiBraccio, G. A. et al., (2014), MESSENGER observations of flux ropes in Mercury’s magnetotail, *Planetary and Space Science, Volume 115*, Pages 77-89, ISSN 0032-0633, http://dx.doi.org/10.1016/j.pss.2014.12.016.

Dungey, J. W. (1961). Interplanetary magnetic field and the auroral zones. *Physical Review Letters*, *6*(2), 47.

Eastwood, J.P. et al., (2015), What Controls the Structure and Dynamics of Earth’s Magnetosphere, *Space Sci Rev*, *188(251)*, doi:10.1007/s11214-014-0050-x

Eastwood, J. P., et al. (2016), Ion-scale secondary flux-ropes generated by magnetopause reconnection as resolved by MMS, *Geophys. Res. Lett.*, *43*, 4716–4724, doi:10.1002/2016GL068747.

Elphic, R. C., and C. T. Russell (1983), Magnetic flux ropes in the Venus ionosphere: Observations and models, *J. Geophys. Res.*, *88*, 58–72, doi:10.1029/JA088iA01p00058.

Fairfield, D. H., R. P. Lepping, E. W. Hones Jr., S. J. Bame, and J. R. Asbridge (1981), Simultaneous measurements of magnetotail dynamics by IMP spacecraft, *J. Geophys. Res.*, *86*(*A3*), 1396–1414, doi:10.1029/JA086iA03p01396.

Fear, R. C., A. N. Fazakerley, C. J. Owen, and E. A. Lucek (2005), A survey of flux transfer events observed by Cluster during strongly northward IMF, *Geophys. Res. Lett.*, *32*, L18105, doi:10.1029/2005GL023811.

Fear R.C. et al., (2007), Motion of flux transfer events: a test of the Cooling model, *Ann. Geophys., 25*, 1669-1690, doi:10.5194/angeo-25-1669-2007.

Frey, H. U. and Mende, S. B., (2007) Substorm onsets as observed by IMAGE-FUV, *Proceedings of the Eighth International Conference on Substorms (ICS-8)*, edited by: Syrjäsuo, M. T. and Donovan, E., 71–75, University of Calgary, Alberta, Canada.

Gekelman W., B. Van Compernolle, T. DeHaas, and S. Vincena, (2014) Chaos in magnetic flux ropes, *Plasma Phys. Controlled Fusion*, *56*, 064002.

Gershman, D. J., J. A. Slavin, J. M. Raines, T. H. Zurbuchen, B. J. Anderson, H. Korth, D. N. Baker, and S. C. Solomon (2014), Ion kinetic properties in Mercury's pre-midnight plasma sheet, *Geophys. Res. Lett.*, *41*, 5740–5747, doi:10.1002/2014GL060468.

Harris, E. G. (1962), On a plasma sheath separating regions of oppositely directed magnetic field, *Nuovo Cimento, 23*, 115–121.

Hasegawa, H., Sonnerup, B. U. Ö., Owen, C. J., Klecker, B., Paschmann, G., Balogh, A., and Rème, H., (2006) The structure of flux transfer events recovered from Cluster data, *Ann. Geophys., 24*, 603-618, doi:10.5194/angeo-24-603-2006.

Hasegawa, H., et al. (2010), Evidence for a flux transfer event generated by multiple X-line reconnection at the magnetopause, *Geophys. Res. Lett.*, *37*, L16101, doi:10.1029/2010GL044219.

Hidalgo, M. A., and C Cid, (2002a), A non-force-free approach to the topology of magnetic clouds in the solar wind, *J. Geophys. Res.*, *107*(*01*), doi:10.1029/2001JA900100.

Hidalgo, M. A., T. Nieves-Chinchilla, and C. Cid, (2002b), Elliptical cross-section model for the magnetic topology of magnetic clouds, *Geophys. Res. Lett.*, *29*(*13*), doi:10.1029/2001GL013875.

Imber, S. M., J. A. Slavin, H. U. Auster, and V. Angelopoulos (2011), A THEMIS survey of flux ropes and traveling compression regions: Location of the near-Earth reconnection site during solar minimum, *J. Geophys. Res.*, *116*, A02201, doi:10.1029/2010JA016026

Imber, S. M., J. A. Slavin, S. A. Boardsen, B. J. Anderson, H. Korth, R. L. McNutt Jr., and S. C. Solomon (2014), MESSENGER observations of large dayside flux transfer events: Do they drive Mercury's substorm cycle?, *J. Geophys. Res. Space Physics*, *119*, 5613–5623, doi:10.1002/2014JA019884.

Jasinski, J. M., J. A. Slavin, C. S. Arridge, G. Poh, X. Jia, N. Sergis, A. J. Coates, G. H. Jones, and J. H. Waite Jr. (2016), Flux transfer event observation at Saturn's dayside magnetopause by the Cassini spacecraft, Geophys. Res. Lett., 43, 6713–6723, doi:10.1002/2016GL069260.

Johnson, C. L., et al. (2012), MESSENGER observations of Mercury's magnetic field structure, *J. Geophys. Res.*, *117*, E00L14, doi:10.1029/2012JE004217.

Kronberg, E. A., J. Woch, N. Krupp, A. Lagg, K. K. Khurana, and K.-H. Glassmeier (2005), Mass release at Jupiter: Substorm-like processes in the Jovian magnetotail, *J. Geophys. Res.*, *110*, A03211, doi:10.1029/2004JA010777.

Lee, L. C., and Z. F. Fu (1985), A theory of magnetic flux transfer at the Earth's magnetopause, *Geophys. Res. Lett.*, *12*, 105–108.

Lepping, R. P., J. A. Jones, and L. F. Burlaga (1990), Magnetic field structure of interplanetary magnetic clouds at 1 AU, *J. Geophys. Res.*, *95*(*A8*), 11957–11965, doi:10.1029/JA095iA08p11957.

Li, S.-S., V. Angelopoulos, A. Runov, and S. A. Kiehas (2014), Azimuthal extent and properties of midtail plasmoids from two-point ARTEMIS observations at the Earth-Moon Lagrange points, *J. Geophys. Res. Space Physics*, *119*, 1781–1796, doi:10.1002/2013JA019292.

Lindsay S.T., M.K. James, E.J. Bunce, S.M. Imber, H. Korth, A. Martindale, T.K. Yeoman, MESSENGER X-ray observations of magnetosphere–surface interaction on the nightside of Mercury (2016), *Planetary and Space Science, Volume 125*, Pages 72-79, ISSN 0032-0633, http://dx.doi.org/10.1016/j.pss.2016.03.005.

Liu, J., V. Angelopoulos, A. Runov, and X.-Z. Zhou (2013), On the current sheets surrounding dipolarizing flux bundles in the magnetotail: The case for wedgelets, *J. Geophys. Res. Space Physics*, *118*, 2000–2020, doi: 10.1002/jgra.50092.

Lundquist, S., Magnetohydrostatic fields, *Ark. Fys.*, **2**, 361, 1950.

Nagai, T., (1982) Observed magnetic substorm signatures at synchronous altitude, *J. Geophys. Res.*, *87*, 4405–4417.

Nagai, T., M. Fujimoto, Y. Saito, S. Machida, T. Terasawa, R. Nakamura, T. Yamamoto, T. Mukai, A. Nishida, and S. Kokubun (1998a), Structure and dynamics of magnetic reconnection for substorm onsets with Geotail observations, *J. Geophys. Res.*, *103*(*A3*), 4419–4440, doi:10.1029/97JA02190.

Nagai, T., I. Shinohara, S. Zenitani, R. Nakamura, T. K. M. Nakamura, M. Fujimoto, Y. Saito, and T. Mukai (2013), Three-dimensional structure of magnetic reconnection in the magnetotail from Geotail observations, *J. Geophys. Res. Space Physics*, *118*, 1667–1678, doi:10.1002/jgra.50247.

Nakamura, R., et al., (2002) Motion of the dipolarization front during a flow burst event observed by Cluster, *Geophys. Res. Lett.*, *29*(*20*), 1942, doi:10.1029/2002GL015763.

N.F. Ness, K.W. Behannon, R.P. Lepping, and Y.C. Whang (1975), The magnetic field of Mercury, 1, *J. Geophys. Res.*, *80(19)*, 2708–2716, doi:10.1029/JA080i019p02708.

N.F. Ness, K.W. Behannon, R.P. Lepping, Y.C. Whang (1976), Observations of Mercury's magnetic field, *Icarus, 28(4)*, 479–488, doi:10.1016/0019-1035(76)90121-4.

Ogilvie, K. W., J. D. Scudder, V. M. Vasyliunas, R. E. Hartle, and G. L. Siscoe (1977), Observations at the planet Mercury by the plasma electron experiment: Mariner 10, *J. Geophys. Res.*, *82*, 1807–1824, doi:10.1029/JA082i013p01807.

Owen, C. J., et al. (2001), Cluster PEACE observations of electrons during magnetospheric flux transfer events, *Ann. Geophys.*, *19*, 1303.

Poh, G., et al. (2016), MESSENGER observations of cusp plasma filaments at Mercury, *J. Geophys. Res. Space Physics*, *121*, 8260–8285, doi:10.1002/2016JA022552.

Raines, J. M., et al. (2013), Distribution and compositional variations of plasma ions in Mercury's space environment: The first three Mercury years of MESSENGER observations, *J. Geophys. Res. Space Physics*, *118*, 1604–1619, doi:10.1029/2012JA018073.

Rich, F. J., V. M. Vasyliunas, and R. A. Wolf (1972), On the balance of stresses in the plasma sheet, *J. Geophys. Res.*, *77(25)*, 4670–4676, doi:10.1029/JA077i025p04670.

Runov A., V.A. Sergeev, R. Nakamura, W. Baumjohann, T.L. Zhang, Y. Asano, M. Volwerk, Z. Vörös, A. Balogh, H. Rème, (2005), Reconstruction of the magnetotail current sheet structure using multi-point Cluster measurements, Planetary and Space Science, Volume 53, Issues 1–3, 237-243, ISSN 0032-0633, http://dx.doi.org/10.1016/j.pss.2004.09.049.

Russell, C. T., and R. L. McPherron (1973), Semiannual variation of geomagnetic activity, *J. Geophys. Res.*, *78*(*1*), 92–108, doi:10.1029/JA078i001p00092.

Russell, C. T., and R. J. Walker (1985), Flux transfer events at Mercury, *J. Geophys. Res.*, *90*(*A11*), 11067–11074, doi:10.1029/JA090iA11p11067.

Shiokawa, K., Baumjohann, W., & Haerendel, G. (1997). Braking of high-speed flows in the near-Earth tail. *Geophysical research letters*, *24*(10), 1179-1182, doi:10.1029/97GL01062.

Shue, J.-H., et al. (1998), Magnetopause location under extreme solar wind conditions, *J. Geophys. Res.*, *103*(*A8*), 17691–17700, doi:10.1029/98JA01103.

Sibeck, D. G., M. Kuznetsova, V. Angelopoulos, K.-H. Glassmeier, and J. P. McFadden (2008), Crater FTEs: Simulation results and THEMIS observations, *Geophys. Res. Lett.*, *35*, L17S06, doi:10.1029/2008GL033568.

Slavin, J. A., and R. E. Holzer (1981), Solar wind flow about the terrestrial planets 1. Modeling bow shock position and shape, *J. Geophys. Res.*, *86*(A13), 11401–11418, doi:10.1029/JA086iA13p11401.

Slavin, J. A., E. J. Smith, D. G. Sibeck, D. N. Baker, R. D. Zwickl, and S.-I. Akasofu (1985), An ISEE 3 study of average and substorm conditions in the distant magnetotail, *J. Geophys. Res.*, *90*(*A11*), 10875–10895, doi:10.1029/JA090iA11p10875.

Slavin J.A., J.C.J. Owen, J.E.P. Connerney, S.P. Christon, Mariner 10 observations of field-aligned currents at Mercury, (1997), *Planetary and Space Science, Volume 45, Issue 1,* Pages 133-141, ISSN 0032-0633, doi:/10.1016/S0032-0633(96)00104-3.

Slavin, J. A., R. P. Lepping, J. Gjerloev, D. H. Fairfield, M. Hesse, C. J. Owen, M. B. Moldwin, T. Nagai, A. Ieda, and T. Mukai, (2003), Geotail observations of magnetic flux ropes in the plasma sheet, *J. Geophys. Res.*, *108*(*A1*), 1015, doi:10.1029/2002JA009557.

Slavin, J. A., E. I. Tanskanen, M. Hesse, C. J. Owen, M. W. Dunlop, S. Imber, E. A. Lucek, A. Balogh, and K.-H. Glassmeier (2005), Cluster observations of traveling compression regions in the near-tail, *J. Geophys. Res.*, *110,* A06207, doi:10.1029/2004JA010878.

Slavin J.A. (2004), Mercury's magnetosphere, *Advances in Space Research, 33(11)*, 1859–1874, doi:10.1016/j.asr.2003.02.019.

Slavin, J. A., et al. (2010a), MESSENGER observations of large flux transfer events at Mercury, *Geophys. Res. Lett.*, *37,* L02105, doi:10.1029/2009GL041485.

Slavin, J. A., et al. (2012), MESSENGER observations of a flux-transfer-event shower at Mercury, J. Geophys. Res., 117, A00M06, doi:10.1029/2012JA017926.

Slavin, J. A., et al. (2014), MESSENGER observations of Mercury's dayside magnetosphere under extreme solar wind conditions, *J. Geophys. Res. Space Physics*, *119,* 8087–8116, doi:10.1002/2014JA020319.

Sonnerup, B. U., and L. J. Cahill Jr. (1967), Magnetopause structure and attitude from Explorer 12 observations, *J. Geophys. Res.*, *72*(*1*), 171–183, doi:10.1029/JZ072i001p00171.

Sonnerup, B. U. Ö., and M. Guo, Magnetopause transects, *Geophys. Res. Lett.*, *23*, 3679–3682, 1996.

Sun, W.-J., J. A. Slavin, S. Fu, J. M. Raines, Q.-G. Zong, S. M. Imber, Q. Shi, Z. Yao, G. Poh, D. J. Gershman, Z. Pu, T. Sundberg, B. J. Anderson, H. Korth, and D. N. Baker (2015), MESSENGER observations of magnetospheric substorm activity in Mercury's near magnetotail, *Geophys. Res. Lett.*, *42*, 3692–3699, doi: 10.1002/2015GL064052.

Sun, W. J., S. Y. Fu, J. A. Slavin, J. M. Raines, Q. G. Zong, G. K. Poh, and T. H. Zurbuchen (2016), Spatial distribution of Mercury's flux ropes and reconnection fronts:

MESSENGER observations, *J. Geophys. Res. Space Physics*, *121*, 7590–7607, doi:10.1002/2016JA022787.

Sundberg, T., et al. (2012), MESSENGER observations of dipolarization events in Mercury's magnetotail, *J. Geophys. Res.*, *117*, A00M03, doi:10.1029/2012JA017756.

Teh, W.-L., R. Nakamura, H. Karimabadi, W. Baumjohann, and T. L. Zhang (2014a), Correlation of core field polarity of magnetotail flux ropes with the IMF B_y: Reconnection guide field dependency, *J. Geophys. Res. Space Physics*, *119*, 2933–2944, doi:10.1002/2013JA019454.

Teh, W.-L., M. Abdullah, and A. M. Hasbi (2014b), Evidence for the core field polarity of magnetic flux ropes against the reconnection guide field, *J. Geophys. Res. Space Physics*, *119*, 8979–8983, doi:10.1002/2014JA020509.

Treumann, R. A. and W. Baumjohann, *Advanced Space Plasma Physics, 381* pp., Imperial College, London, 1997.

Vasko, I. Y., A. A. Petrukovich, A. V. Artemyev, R. Nakamura, and L. M. Zelenyi (2015), Earth's distant magnetotail current sheet near and beyond lunar orbit, *J. Geophys. Res. Space Physics*, *120*, 8663–8680, doi:10.1002/2015JA021633.

Wang, Y., et al. (2005), Initial results of high-latitude magnetopause and low-latitude flank flux transfer events from 3 years of Cluster observations, *J. Geophys. Res.*, *110*, A11221, doi:10.1029/2005JA011150.

Wang, Y. L., R. C. Elphic, B. Lavraud, M. G. G. T. Taylor, J. Birn, C. T. Russell, J. Raeder, H. Kawano, *and* X. X. Zhang *(*2006*)*, Dependence of flux transfer events on solar wind conditions from 3 years of Cluster observations, *J. Geophys. Res., 111, A04224, doi:*10.1029/2005JA011342.

Walker, R. J., and C. T. Russell (1985), Flux transfer events at the Jovian magnetopause, *J. Geophys. Res.*, *90*(*A8*), 7397–7404, doi:10.1029/JA090iA08p07397.

Walsh A.P., et al., (2014), Dawn-dusk asymmetries in the coupled solar-wind-magnetosphere-ionosphere system: a review, *Annales Geophysicae, 32(7),*705-737, doi:10.5194/angeo-32-705-2014.

Winslow, R. M., B. J. Anderson, C. L. Johnson, J. A. Slavin, H. Korth, M. E. Purucker, D. N. Baker, and S. C. Solomon (2013), Mercury's magnetopause and bow shock from MESSENGER Magnetometer observations, *J. Geophys. Res. Space Physics*, *118*, 2213–2227, doi:10.1002/jgra.50237.

CHAPTER II

MESSENGER MISSION AND INSTRUMENTATION

2.1 MESSENGER Mission

Mariner 10 became the first spacecraft to visit Mercury when it performed three planetary flybys in 1974 and 1975. While important discoveries were made during these three short flybys, many questions were also raised about the local plasma environment and magnetospheric dynamics occurring at Mercury. The ability to answer these questions is limited by the brevity of the encounters, the nature of the trajectories and the lack of *in situ* plasma ion measurements during Mariner 10 flybys. The MEcury, Surface, Space Environment, GEochemistry and Ranging (MESSENGER) mission was selected for flight in July 1999 as part of the National Aeronautics and Space Administration (NASA) Discovery Program to answer six fundamental Mercury science questions [*Solomon et al.*, 2007]:

1. *What planetary formational processes led to Mercury's high ratio of metal to silicate?*
2. *What is the geological history of Mercury?*
3. *What are the nature and origin of Mercury's magnetic field?*
4. *What are the structure and state of Mercury's core?*
5. *What are the radar-reflective materials at Mercury's poles?*

6. *What are the important volatile species and their sources and sinks near Mercury?*

As shown in Figure 2.1, the MESSENGER spacecraft is designed to carry seven instruments plus radio science. Out of the seven instruments, the Magnetometer (MAG) and the Energetic Particle and Plasma Spectrometer (EPPS), in particular the Fast Imaging Plasma Spectrometer (FIPS), is crucial in helping us understand the nature of Mercury's magnetic field (science question 3). Further details on the working principles of the MAG and FIPS will be discussed in Section 2.2 and 2.3. Another important aspect of the MESSENGER spacecraft was the use of a ceramic cloth sunshade to shield the payload from the intense solar thermal radiation throughout its entire mission duration. The spacecraft is three-axis stabilized such that the sunshade is constantly pointing towards the Sun to keep the instruments' temperature below 65 °C.

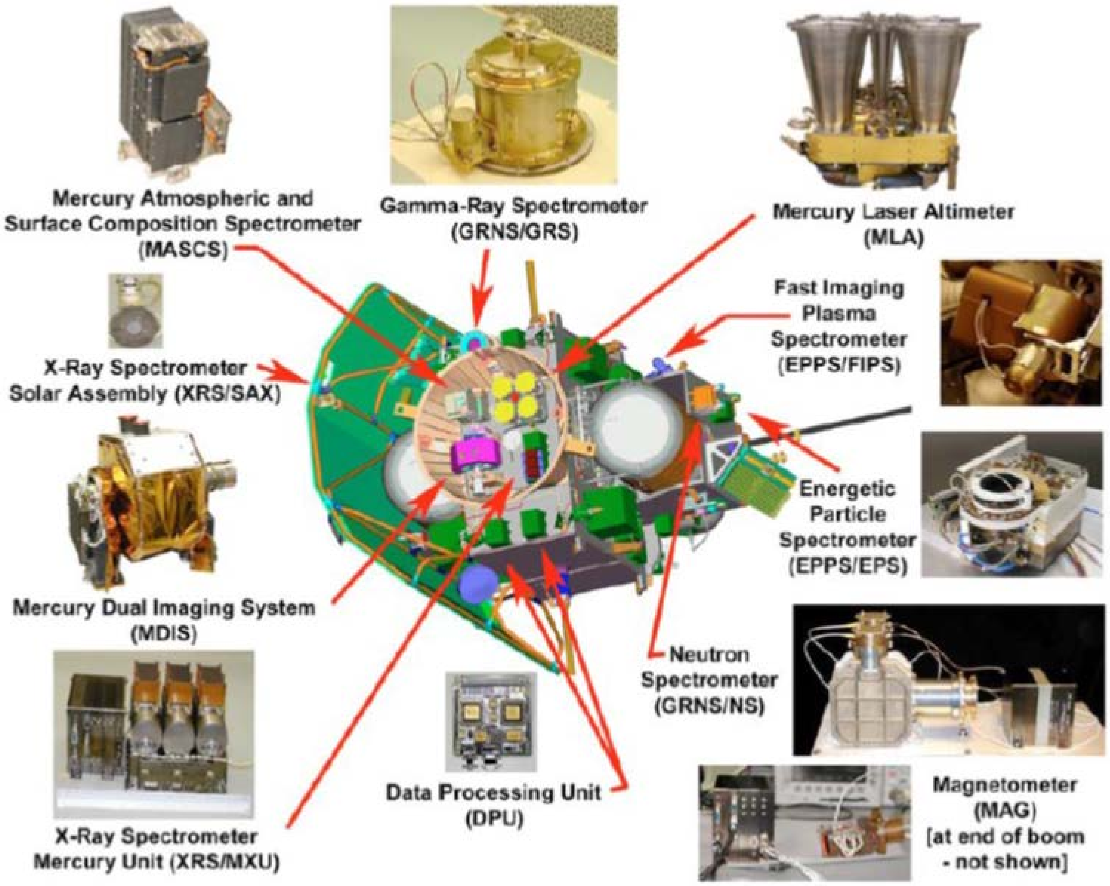

Figure 2.1 Photographs and position of the instrument suites and processing unit onboard the MESSENGER spacecraft. Magnetic field and plasma measurements from the magnetometer (MAG) and Fast Imaging Plasma Spectrometer (FIPS) will be utilized in this dissertation. Figure taken from *Leary et al.*, [2007].

Launched with a Delta II rocket from Cape Canaveral Air Force Station in Florida on 3 August 2004, MESSENGER began its 6.6-years-long journey to Mercury. MESSENGER performed a total of six planetary flybys (1 Earth, 2 Venus and 3 Mercury) during its cruise phase to reduce its cruising speed as it falls into the Sun's gravity well. Figure 2.2 shows the timeline and trajectory during the cruising phase of the mission. MESSENGER successfully went into orbit around Mercury on 18 March 2011 and became the first spacecraft to orbit the innermost planet in the solar system. During the 1-Earth-year-long primary mission phase, MESSENGER was put in a 12-hour near polar (~80°

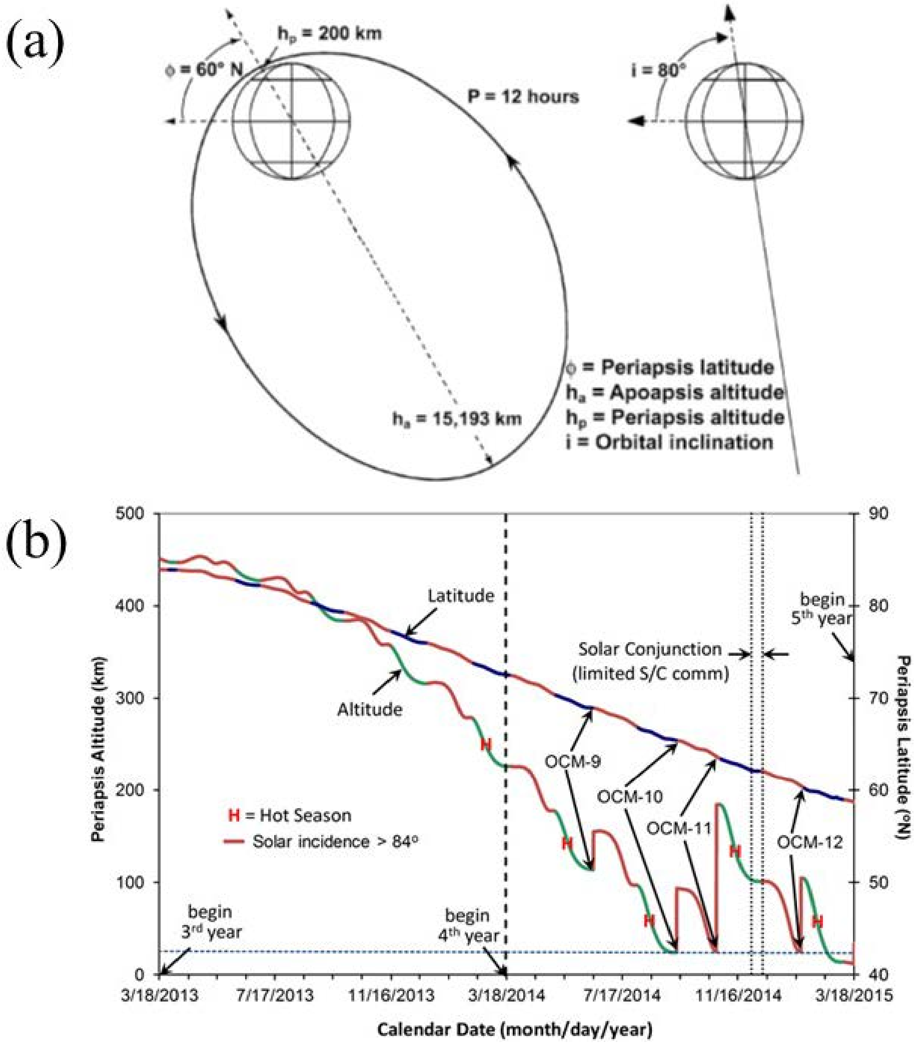

Figure 2.2 (a) Schematic of a typical 12-hour "hot season" MESSENGER orbit, where the periapsis of the orbit is at the dayside magnetosphere. The Sun is to the left of Mercury. (b) The periapsis altitude and latitude of MESSENGER as a function of calendar date for the third and fourth MESSENGER orbital year. During the low-altitude campaign season, which lasted for ~ 2 months between August 2014 and October 2014, the periapsis altitude of MESSENGER decreases to within 50 km from Mercury's surface at ~ 60°N latitude.

inclination to the equator) elliptical orbit. As depicted in Figure 2.3a, the periapsis of the orbit is 60°N in latitude and 200 km in altitude; the apoapsis altitude is ~15,000 km [*Solomon et al.,* 2007]; the Sun is to the left. The spacecraft orbit completed a full precession every 88 days in a counter-clockwise manner. The orbit shown in Figure 2.3a is called a "hot season" orbit since the periapsis is in the dayside. Not shown here, as the orbit makes half a precession, the periapsis is in the nightside and this orbit is called the "warm season" orbit. For magnetopause studies, "hot season" orbits are preferred since the spacecraft crosses the magnetopause boundary closer to the subsolar region, where reconnection is more likely to occur. After the primary mission phase, MESSENGER went into its first extended mission phase (XM1). The spacecraft reduced its orbit period to 8 hours through a series of orbital correction maneuvers (OCMs), with the apoapsis altitude decreasing to ~10,000 km while maintaining the periapsis altitude. In the second extended mission phase (XM2), the periapsis altitude was reduced as shown in Figure 2.3b and MESSENGER began the "low-altitude campaign" at the beginning of XM3 (August through October 2014), where the periapsis of MESSENGER decreased to within ~50 km from Mercury's surface. The importance of the low-altitude mission campaign in studying low-altitude cusp plasma filaments will be discussed further in Chapter IV. After 4 years and 4105 orbits around Mercury, the MESSENGER mission ended on 30 April 2015 with the spacecraft crashing onto Mercury's surface.

2.2 Magnetometer

The primary objective of the magnetometer (MAG) on board MESSENGER is to investigate the structure of Mercury's intrinsic magnetic field and the magnetic field measurements made by the magnetometer are heavily utilized in this thesis. The MAG instrument is a low-noise, tri-axial fluxgate magnetometer with sensors mounted at the end of a 3.6-m-long deployable boom. It is a collaborative effort by the NASA Goddard Space Flight Center and John Hopkins University Applied Physics Laboratory. Figure 2.4 shows the location and orientation of the magnetometer relative to the spacecraft. The local coordinate system is chosen such that the boom is in the +Y (antisunward) direction during mission orbital phase. The payload adaptor is in the +Z-direction and +X-direction completes the orthogonal coordinate system. The basic working principle of fluxgate magnetometers on MESSENGER involves running a 15 kHz alternating current through the triaxial ring coils, which wraps around a core. The input alternating current will induce an alternating cycle of magnetic saturation within the core, which will, in turn, induce an output alternating current in a secondary ring coil. If there is no background magnetic field, the input and output current will cancel out. In the presence of a background magnetic field, the induced output current is out of step with the input current. The output current from each detector is applied to a high-gain integrator and the output voltage from the integrator is directly proportional to the component of the magnetic field along each orthogonal axis. The analog signal from the three axes detectors are then low-pass filtered and sampled simultaneously by three 20-bit analog-to-digital converters every 50 ms. The instrument microprocessor processed the digital signals and output 11 data frequencies from 0.01 s^{-1} to 20 s^{-1}. The MAG instrument has two dynamic ranges, the “low” and “high” range, for each of the three orthogonal axes. The commonly-used “low” range measurement has a full scale of ±1530 nT per axis and telemetered resolution of ~ 0.047 nT. The reader is referred to *Anderson et al.,* [2007] for more information on MESSENGER’s magnetometer instrument.

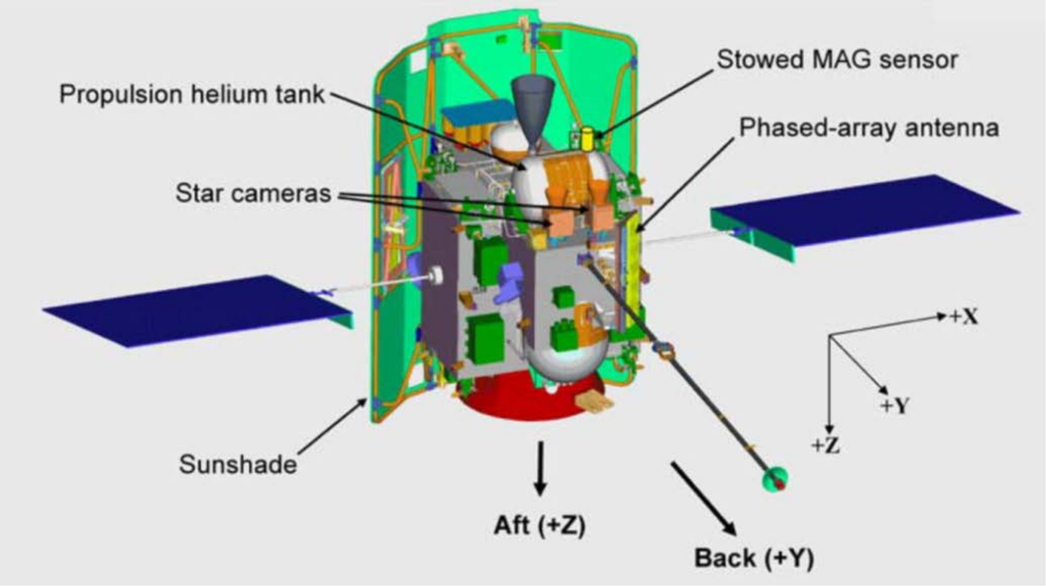

Figure 2.3 Schematics of the magnetometer onboard MESSENGER and its local coordinate system, which is chosen such that the boom is in the +Y (antisunward) direction during mission orbital phase. The payload adaptor is in the +Z-direction and +X-direction completes the orthogonal coordinate system. Figure taken from *Anderson et al.,* [2007].

2.3 Fast Imaging Plasma Spectrometer

The Fast Imaging Plasma Spectrometer (FIPS) is one of the two sensors in the Energetic Particle and Plasma Spectrometer (EPPS) package on the MESSENGER spacecraft; the other sensor is the Energetic Particle Spectrometer (EPS) [*Andrews et al.*, 2007]. FIPS measures the energy, angular and compositional distribution of the low-energy component of the ion distributions (< 50 eV/charge to 20 keV/charge); EPS measures the high-energy component of the electron (> 20 keV) and ion (> 5 keV/nucleon) distribution. In the interest of magnetospheric ion dynamics, we primarily utilized plasma measurements from the FIPS since we are interested in the energy range observed by FIPS.

Built by the University of Michigan, FIPS was designed specifically to address three of the six fundamental science questions on the nature and origin of Mercury's magnetic field, radar-reflective materials at the poles, and the source and sink of volatile species near Mercury. The design requirements of FIPS include a wide field of view (FOV), large dynamic range for energy-per-charge (E/Q) and good mass resolution. To resolve the mass and energy-per-charge of the incoming ions, the FIPS instrument comprised of an Electrostatic Analyzer (ESA) and a Time-of-Flight (TOF) subsystem as depicted in Figure 2.5. FIPS has a ~1.4π sr instantaneous field of view and the ions enter the ESA through a small annular aperture. The ESA serves as an energy-per-charge filter by stepping through series of voltage to deflect the incoming ions; only ions of a very specific energy-per-charge and curved trajectory will pass through the collimators and into the TOF subsystem. The "hourglass-shaped" region between the two collimators serves to suppress ultra-violet (UV) radiation. To allow the lowest energy ions to pass through the carbon foil in the TOF section and reduce energy straggling, the ions are post-accelerated with a potential drop (V_{PAV}) of -15 keV before entering the TOF section. As the ion passes through the carbon foil, a secondary electron is produced, deflected into the start micro-channel plate (MCP) by a mirror harp and initiates a start signal. The ion, on the other hand, remains undeflected, travels a distance d of ~ 7cm into the stop MCP and initiates a stop signal. The TOF is then calculated from the time difference between the start and stop signal.

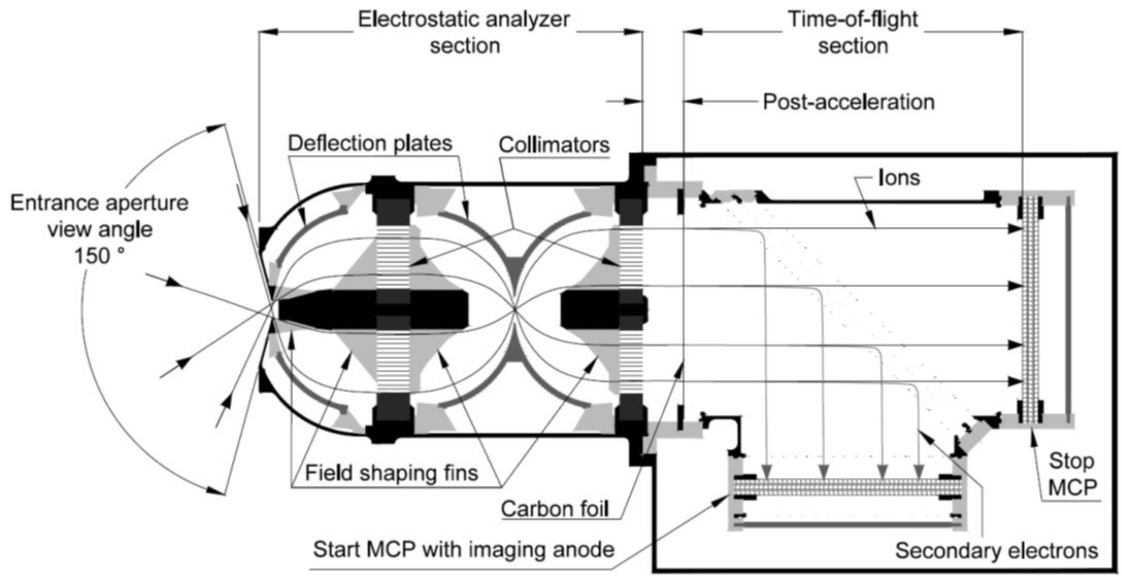

Figure 2.4 Schematics of the Fast Imaging Plasma Spectrometer (FIPS) onboard MESSENGER. It is a time-of-flight instrument, which measures the energy per charge of the incoming ion and identifies the ion species from its mass-per-charge and time taken for the ion to travel the time-of-flight section. Figure taken from Andrew et al., [2007].

To identify the ion species from its mass-per-charge (m/q), a TOF forward model is used [*Raines et al.*, 2013]. As the ion passes through the carbon foil, a fraction of its energy is lost (i.e., E_{loss}). The value of E_{loss}, which is dependent on the incident energy and the mass of a particular ion (m), is measured in laboratory calibrations. Hence, the total energy of the ion in the TOF section (E_{tot}) is given by the equation:

$$E_{\text{tot}} = q\left[\left(\frac{E}{q}\right)_{\text{ESA}} - V_{\text{PAV}}\right] - E_{\text{loss}} \tag{2.1}$$

The velocity of the ion (v) is then given by the equation:

$$\text{v} = 439\sqrt{\left(\frac{E_{\text{tot}}}{m}\right)} \tag{2.2}$$

For a particular ion, the TOF can then be calculated using the equation:

$$\text{TOF} = 10^4\,\frac{d}{\text{v}} - \tau_e - \tau_{MCP} \tag{2.3}$$

where τ_e and τ_{MCP} is the time correction for the flight time of electrons from the carbon foil to the start MCP and detection times within the MCP, respectively. A model E/Q versus

TOF plot is calculated for each ion species and compared to the observed raw FIPS data to identify the ion species. For more details on the working principles of the FIPS instrument and analysis of the FIPS data, the reader is referred to *Andrews et al.,* [2007] and *Raines et al.,* [2013].

References

Anderson, B.J., Acuña, M.H., Lohr, D.A. et al. (2007), The Magnetometer instrument on MESSENGER, *Space Sci Rev, 131, 417*, doi:10.1007/s11214-007-9246-7.

Andrews, G.B., Zurbuchen, T.H., Mauk, B.H. et al. (2007), The Energetic Particle and Plasma Spectrometer Instrument on the MESSENGER Spacecraft, *Space Sci Rev,131,523*, doi:10.1007/s11214-007-9272-5.

Leary, J. C. et al., (2007), The MESSENGER spacecraft. In *The MESSENGER Mission to Mercury* (pp. 187-217), Springer New York.

Raines, J. M., et al. (2013), Distribution and compositional variations of plasma ions in Mercury's space environment: The first three Mercury years of MESSENGER observations, *J. Geophys. Res. Space Physics*, *118*, 1604–1619, doi:10.1029/2012JA018073.

Solomon, S.C., McNutt, R.L., Gold, R.E. et al. (2007), MESSENGER mission overview, *Space Sci Rev,131,3*,doi:10.1007/s11214-007-9247-6.

CHAPTER III

MHD CURRENT LAYER, FILAMENT AND FLUX ROPE ANALYSIS TECHNIQUES

3.1 Minimum Variance Analysis

The minimum variance analysis (MVA) technique was first employed by *Sonnerup and Cahill,* [1967] to determine the normal to the magnetopause current layer using magnetic field observations from Explorer 12. Since then, the MVA technique became the most commonly used technique to analyze the properties of any current layer, wave front or MHD discontinuity in space plasmas. It was also applied to flux rope analysis where the MVA technique is used to determine the direction of flux rope axis and motion with great success. In this section, we will discuss the theory, application and limitations of the MVA technique as outlined by Sonnerup and Scheible, [1998].

3.1.1 Theory

Given a set of magnetic field vector measurements $\mathbf{B}^{(m)}$ (m = 1, 2, 3, …, M) made during the traversal of a current layer, the aim of the MVA technique is to determine the direction where the magnetic field varies the least (i.e., minimum variance). The minimum variance direction corresponds to the normal to the current layer $\hat{\boldsymbol{n}}$. Therefore, $\hat{\boldsymbol{n}}$ can be calculated by the minimization of the quantity σ^2 given by the equation:

$$\sigma^2 = \frac{1}{M}\sum_{m=1}^{M}\left|\left(\boldsymbol{B}^{(m)} - \langle\boldsymbol{B}\rangle\right)\cdot\hat{\boldsymbol{n}}\right|^2 \tag{3.1}$$

where $\langle\boldsymbol{B}\rangle$ is defined as:

$$\langle\boldsymbol{B}\rangle = \frac{1}{M}\sum_{m=1}^{M}\boldsymbol{B}^{(m)} \tag{3.2}$$

The minimization of σ^2 is subjected to the normalization constraint of $|\hat{\boldsymbol{n}}|^2 = 1$. Using a Lagrange multiplier λ, the normalization constraint can be written as a set of three homogeneous linear equations:

$$\frac{\partial}{\partial n_i}\left(\sigma^2 - \lambda(|\hat{\boldsymbol{n}}|^2 - 1)\right) = 0 \tag{3.3}$$

where *i* represents components of the Cartesian coordinate system *X*, *Y*, *Z* in which the magnetic field measurements $\mathbf{B}^{(m)}$ were made. Equation 3.3 can be re-written in matrix form as:

$$\sum_{\nu=1}^{3} M_{\mu\nu}^{B} n_\nu = \lambda n_\mu \tag{3.4}$$

where μ, ν denote Cartesian components *X*, *Y*, *Z* and *M* is the magnetic covariance matrix. Each term in the matrix *M* can be calculated from the following equation:

$$M_{\mu\nu}^{B} = \langle B_\mu B_\nu\rangle - \langle B_\mu\rangle\langle B_\nu\rangle \tag{3.5}$$

Equation 3.4 can be solved as an eigenvalue problem, which leads to three real eigenvalues λ_1, λ_2, λ_3 (in order of decreasing magnitude) and their corresponding orthogonal eigenvectors $\mathbf{x}_1$, $\mathbf{x}_2$, $\mathbf{x}_3$. The eigenvectors $\mathbf{x}_1$, $\mathbf{x}_2$, $\mathbf{x}_3$ represent the maximum, intermediate and minimum magnetic variance direction, respectively. The eigenvector $\mathbf{x}_3$ is used as an estimator for the vector normal to the current sheet while its corresponding eigenvalue λ_3 represents the variance of the magnetic field in the normal direction. In the "magnetic variance space", the square root of each eigenvalue (i.e., $\sqrt{\lambda_i}$) represents the half-length of its corresponding principal-axis of the variance ellipsoid, as shown in Figure 3.1. Therefore, the degeneracy of the covariance matrix M and the variance ellipsoid is determined by the relative values of the three eigenvalues, which is also commonly used to assess the quality of the MVA results.

When the eigenvalues of the variance matrix are distinct (i.e., $\lambda_1 >> \lambda_2 >> \lambda_3$), it means that the variance ellipsoid is non-degenerate and all three eigenvectors are well-defined. There are three possible types of degeneracy: (1) $\lambda_1 \approx \lambda_2$, (2) $\lambda_2 \approx \lambda_3$, (3) $\lambda_1 \approx \lambda_2 \approx \lambda_3$. For the first type of degeneracy ($\lambda_1 \approx \lambda_2$), only the eigenvector $\mathbf{x}_3$ is well-determined while $\mathbf{x}_1$ and $\mathbf{x}_2$ are not. Hence, any vectors that lie on the plane normal to $\mathbf{x}_3$ can be used as $\mathbf{x}_1$ and $\mathbf{x}_2$ for basis vectors of the minimum variance coordinate system. The same is true for the second type of degeneracy ($\lambda_2 \approx \lambda_3$). Note that the normal direction of the current sheet determined from MVA result, which shows the first type of degeneracy may still be used since $\mathbf{x}_3$ is well-determined. This does not hold for the second type of degeneracy as both λ_2 and λ_3 are degenerate. The third type of degeneracy ($\lambda_1 \approx \lambda_2 \approx \lambda_3$) produce no meaningful results since all three eigenvectors are ill-determined and no information on the normal or tangential direction of the current sheet could be obtained from MVA.

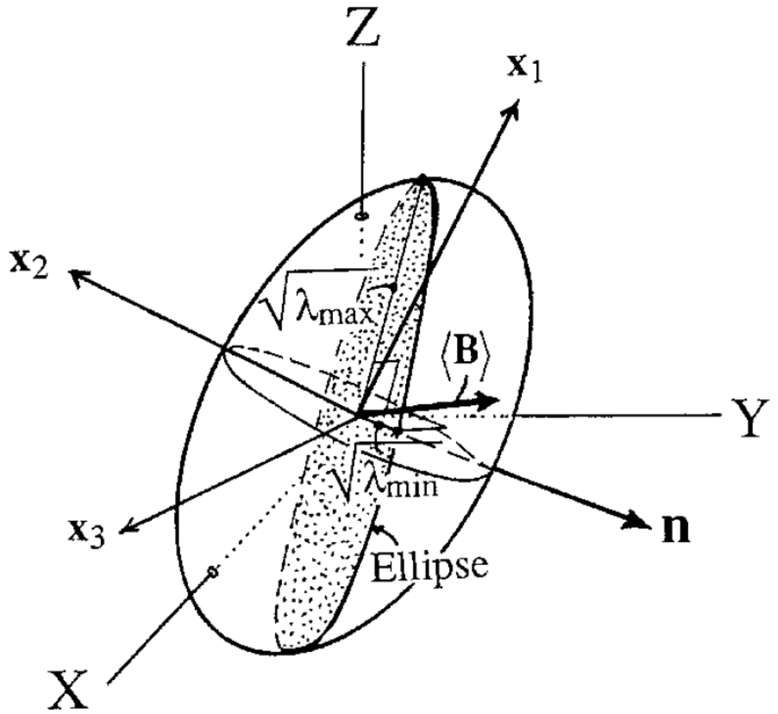

Figure 3.1 Illustration of the variance ellipsoid. $\mathbf{x}_1$, $\mathbf{x}_2$, $\mathbf{x}_3$ represent the eigenvectors corresponding to the maximum, intermediate and minimum eigenvalues λ_1, λ_2, λ_3 (in order of decreasing magnitude), respectively. The half-length of each principal axis of the ellipsoid is given by the square root of the corresponding eigenvalue. Figure taken from *Sonnerup and Scheible,* [1998].

To determine if any pair of eigenvalues are nearly the same (i.e., degenerate), one could compute the ratio between each pair of eigenvalues $\frac{\lambda_i}{\lambda_j}$, where $i \neq j = 1, 2, 3$. The user will decide the cutoff value of eigenvalue ratios to determine if any pair of eigenvalues is distinct or degenerate and this criteria could varies between different studies. For example, *Sonnerup and Cahill*, [1967] only accepts magnetopause crossings at Earth with ratio of intermediate to minimum eigenvalue exceeding 1.5 while *DiBraccio et al.*, [2013] applied the MVA technique to Mercury's magnetopause and set a criteria for the intermediate to minimum eigenvalue ratio to be no less than 5.

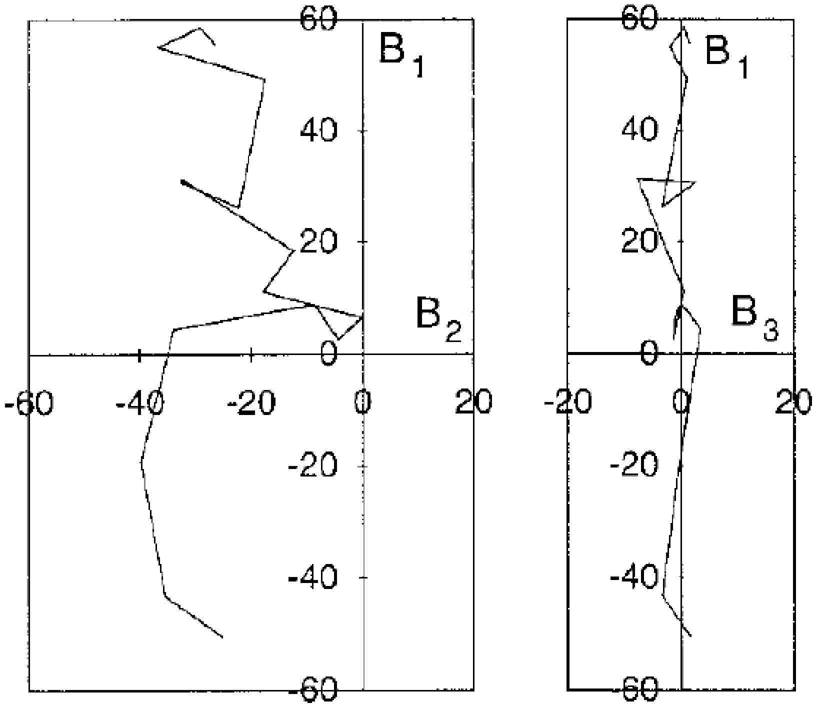

i	λ_i (nT)^2	$\mathbf{x}_i$			$\langle\mathbf{B}\rangle\cdot\mathbf{x}_i$ (nT)
1	1012.86	(−0.4061,	−0.6845,	0.6055)	15.36
2	138.01	(−0.2886,	−0.5326,	−0.7957)	−23.40
3	7.08	(0.8671,	−0.4978,	0.0187)	−0.58

Figure 3.2 Example of hodogram pairs for magnetopause crossing observed by AMPTE/IRM on October 19, 1984. Table shows the eigenvalues λ_i, eigenvectors $\mathbf{x}_i$ and average magnetic field values projected onto MVA coordinate system $\langle\mathbf{B}\rangle \cdot \mathbf{x}_i$. Figure taken from *Sonnerup and Scheible*, [1998].

To analyze the results obtain from the MVA technique, it is a common practice to plot the MVA results in a pair of magnetic hodograms, which are curves constructed by drawing the vectors in MVA coordinates, following the time in which they are measured, and connecting the arrow heads of the vectors with a straight line. The tangential (B_1 versus B_2) and side view (B_2 versus B_3) projections of each magnetic field vector measurement in the MVA-space are usually displayed. Using these hodograms, we can deduce the structure of the current layer. For example, Figure 3.2 shows the hodograms to determine the structure of the magnetopause during a traversal observed by AMPTE/IRM on 19th October 1984. The intermediate to minimum and maximum to intermediate eigenvalue ratios are ~ 19.7 and 7.3, respectively. Hence, the eigenvectors are well-determined and the direction normal to the magnetopause is $\hat{\boldsymbol{n}}$ = [0.8671, -0.4978, 0.0187]. The average value of B_3 (i.e., $\langle \mathbf{B} \rangle \cdot \mathbf{x}_3$) is calculated to be ~ -0.58, which is very small as compared to the average values of B_1 and B_2. This means that there is little or no magnetic field component in the normal direction. Hence, this magnetopause current layer is a tangential discontinuity, where the total pressure across the current layer is conserved and there is no plasma flow across the current layer. This also indicates that magnetic reconnection did not occur at the dayside magnetopause. Magnetic reconnection produces a rotational discontinuity when $< B_3 > \neq 0$ (i.e., there is a constant magnetic field component across the current layer).

3.1.2 Application of MVA Techniques

Mercury's Magnetopause

The minimum variance analysis technique was first performed by *Sonnerup and Cahill,* [1967] on magnetopause traversals at Earth to determine the normals of the magnetopause. The simplicity and use of only the magnetic field measurements in the MVA technique means that it is the ideal analysis tool for planetary magnetosphere studies since the plasma measurements are often lacking or limited in scope on planetary missions. For example, *DiBraccio et al.,* [2013] performed MVA on a total of 89 crossing of Mercury's magnetopause by MESSENGER. Only 43 magnetopause crossings, which met the criteria of eigenvalue ratios less than 5 and the error in B_N less than 8 nT, were selected for further analysis and modelling. Figure 3.3a shows an example of magnetic field observations transformed from MSM to MVA coordinates during MESSENGER's crossing of Mercury's magnetopause on 21 November 2011. The MVA results show that there is a normal component of ~ 6.7 nT with uncertainty of ~ 3.2 nT [See *Sonnerup and Schieble,* 1998]. Hence, the magnetopause current layer is a rotational discontinuity. Using the values of B_N computed from the MVA results for each magnetopause crossings, *DiBraccio et al.,* [2013] calculated its corresponding dimensionless reconnection rate and plotted it as a function of magnetic shear angle ϑ as shown in Figure 3.3b. From their analysis, *DiBraccio et al.,* [2013] concluded that there is little correlation between reconnection rate and magnetic shear angle at Mercury and reconnection can occur for a large range of shear angles. This study by *DiBraccio et al.,* [2013] exemplifies the importance of the MVA technique for the current sheet analysis at Mercury and other planets.

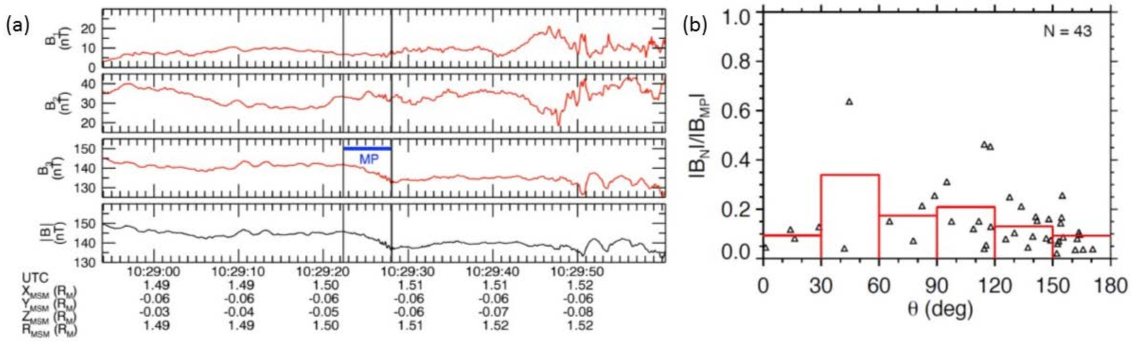

Figure 3.3 (a) Magnetic field measurements in boundary normal (i.e., MVA) coordinate observed by MESSENGER during magnetopause traversal on 21 November 2011. Solid black lines mark the interval of magnetopause crossing. The eigenvectors are: $\mathbf{x}_1$ = [-0.10, -0.20, 0.98], $\mathbf{x}_2$ = [0.45, 0.87, 0.22], $\mathbf{x}_3$ = [0.89, -0.46, 0.00]. The maximum to intermediate and intermediate to minimum eigenvalue ratio are 4.33 and 5.55, respectively. (b) Plot of magnetopause shear angle ϑ versus reconnection rate. Red histograms represents the average reconnection rate per 30 degrees shear angle bins. Figure taken from *DiBraccio et al.,* [2013]

Flux Ropes and Cusp Plasma Filaments

As discussed earlier, flux ropes are usually observed at the dayside magnetopause as flux transfer events (FTEs) or in the nightside magnetotail current sheet. It is important to first transform the magnetic field measurements into a coordinate system that is local to the magnetic structure. In this new coordinate system local to the flux rope, we can identify a flux rope from the bipolar magnetic field and the core field in the maximum and intermediate variance direction directions, respectively [e.g., *Xiao et al.,* 2004]. Figure 3.4

shows an example of the magnetic field measurements and hodograms for a flux rope identified in Mercury’s cross-tail current sheet. Figure 3.4a shows a clear bipolar reversal in B_3 (maximum variance direction) and a corresponding peak in B_2 (intermediate variance direction). The magnetic field is constant in the B_1 (minimum variance) direction. Both magnetic field signatures are also shown in the B_3 versus B_2 hodogram by the “semi-circle” curve.

Once a flux rope is identified through MVA, the eigenvectors are used as estimators for the direction of flux rope axis and motion [e.g., *Xiao et al.*, 2004]. Similar to the use of MVA on magnetopause crossings, the quality of the eigenvectors are also determined from the eigenvalue ratios. Here, the eigenvectors were considered well-determined if the eigenvalues ratios are greater than 4 [*DiBraccio et al.*, 2014]. As depicted in Figure 1.10, the minimum eigenvector $\mathbf{x}_3$ is parallel to the flux rope motion while the intermediate eigenvector $\mathbf{x}_2$ is parallel to the axis of the flux rope if it is quasi-force free.

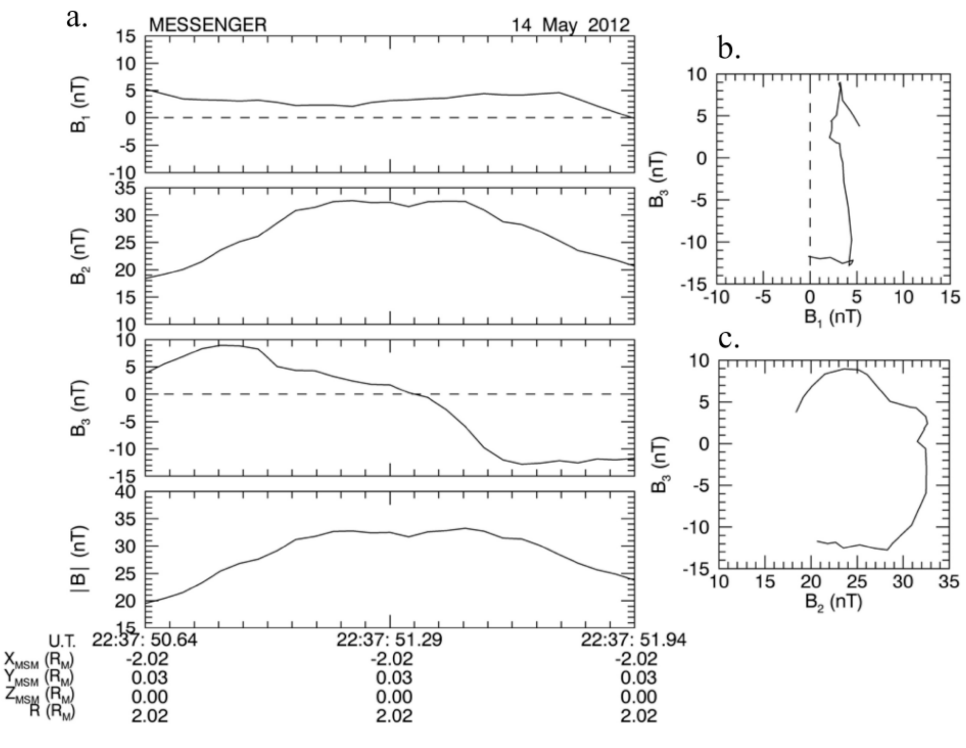

Figure 3.4 (a) Magnetic field measurements in MVA coordinate of a flux rope encounter on 14 May 2012. B_1, B_2 and B_3 represents the minimum, intermediate and maximum variance direction, respectively. (b and c) Hodograms of magnetic field measurements shown in Figure 3.4a. Figure is taken from *DiBraccio et al.*, [2014].

Flux rope events with eigenvalue ratios less than 4 are usually discarded as the eigenvectors are considered degenerate and ill-determined. However, the “eigenvalue ratio rule” is not always applicable in the use of MVA on the magnetic field measurements of certain magnetic structures. One such example is the cusp plasma filaments. As mentioned earlier in Chapter 1.4 and later in Chapter IV, cusp plasma filaments are filamentary flux tubes observed in Mercury’s cusp. They are formed as a result of plasma diamagnetism effect by precipitating plasma on the magnetic field inside the flux tubes. Hence, the magnetic field variation will be the highest in the direction parallel to the flux tube; this corresponds to the direction of maximum variance. In an ideal filamentary flux tube where the plasma inside the flux tube is evenly distributed in the plane normal to the axis of the flux tube, magnetic field variations due to plasma diamagnetism will be equal in all directions in this plane. Unlike the flux ropes, the MVA results would show no “twist” (i.e., no bipolar magnetic field in the maximum variance direction) in the magnetic field topology of a cusp filament (See Figure 4.4 in Chapter IV). Therefore, any vectors lying on the plane normal to the flux tube axis can be used as the intermediate and minimum eigenvectors (i.e., $\lambda_{min} \approx \lambda_{int}$, where min and int represents minimum and intermediate, respectively). In such cases, the “eigenvalue ratio rule” is not applicable. In fact, the different types of degeneracy between the eigenvalues can be used to infer the structural differences between different populations of cusp filaments. This will be discussed further in Chapter IV.

3.1.3 Limitations

Despite its extensive use to analyze MHD current layers, flux ropes and cusp filaments, the MVA technique is not without its limitations. It assumes that the magnetic field measurements do not change with time as the spacecraft traverses the structure. This is usually not the case for Mercury where temporal and spatial variations in magnetic field can occur within the current layer or flux ropes on timescales shorter than the time to traverse the structure. High frequency fluctuations in the magnetic field due to waves or turbulences can make it difficult to determine accurately the beginning and ending of the event. For this reason, the time interval upon which to perform the MVA technique can be uncertain, thereby increasing the errors in the MVA results. In many cases, smoothing of the magnetic field data is necessary to ensure reasonable results.

The reliability and accuracy of performing MVA on flux ropes to infer its orientation and structure has been examined by *Xiao et al.,* [2004]. In this study, MVA was performed on four different flux rope models. It was found that the intermediate eigenvector from the MVA results best fit a force-free flux rope axial direction, but MVA estimates of the central axis orientation for a non-force-free flux rope can be very uncertain. They also determined that the directions of the eigenvectors are dependent on the spacecraft trajectory relative to the flux rope axis and structure in these situations. Hence, it is important for the user to understand these limitations before making any inference about properties of the flux rope using MVA.

3.2 deHoffmann-Teller Analysis

In ideal MHD, the frozen-in condition requires the presence of a convection electric field **E** in the observer frame of reference. This electric field is the result of plasma flow perpendicular to the magnetic field and is given by the equation $\mathbf{E} = -\mathbf{v} \times \mathbf{B}$. Hence, there exists a frame of reference in the plasma where **E** vanishes. This frame transformation method, also called a deHoffmann-Teller (HT) analysis, was first introduced by *deHoffmann and Teller,* [1950] to analyze conditions across MHD discontinuities. The use of HT analysis can also be extended to flux rope analysis and other structures. Here, we present the non-iterative, least-square HT method first developed by *Sonnerup et al,* [1987; 1990] to determine the HT frame velocity $\mathbf{v}_{\mathrm{HT}}$ used in the analysis. This technique is also discussed in detail by *Khrabrov and Sonnerup,* [1998].

3.2.1 Theory

The main idea behind the HT technique developed by *Sonnerup et al,* [1987; 1990] is to determine the frame velocity by minimization of the residual electric field. For a set of plasma bulk velocity $\mathbf{v}^{(m)}$ and magnetic field $\mathbf{B}^{(m)}$ (m = 1, 2, 3, …, M) data, we can define the mean square of the electric field $D(\mathbf{v})$ to be:

$$D(\mathbf{v}) = \frac{1}{M}\sum_{m=1}^{M}\left|\mathbf{E}'^{(m)}\right|^2 = \frac{1}{M}\sum_{m=1}^{M}\left|\left(\mathbf{v}^{(m)} - \mathbf{v}_{\mathrm{HT}}\right) \times \mathbf{B}^{(m)}\right|^2 \tag{3.6}$$

Hence, the minimization of the electric field can then be expressed as:

$$\nabla_V D(\mathbf{v}) = 0 \tag{3.7}$$

And the solution to the above equation is:

$$K_0 \mathbf{v}_{HT} = \langle K^{(m)} \mathbf{v}^{(m)} \rangle \tag{3.8}$$

where $K_0 \equiv \langle K^{(m)} \rangle$. $K^{(m)}$ is defined as the projection matrix onto the plane perpendicular to $B^{(m)}$ multiplied by $B^{(m)2}$ and is given by the equation:

$$K_{\nu\mu}^{(m)} = B^{(m)2}\left(\delta_{\nu\mu} - \frac{B_\mu^{(m)} B_\nu^{(m)}}{B^{(m)2}}\right) \tag{3.9}$$

where $\delta_{\nu\mu}$ is the kronecker delta function. Assuming that the matrix K_0 is non-singular, equation 3.8 can be rearranged as:

$$\mathbf{v}_{HT} = K_0^{-1} \langle K^{(m)} \mathbf{v}^{(m)} \rangle \tag{3.10}$$

Hence, to compute the HT velocity, we must first construct the matrix $K^{(m)}$ and multiply it by the plasma bulk velocity $\mathbf{v}^{(m)}$. The resulting vector is then averaged over all M data points and multiply by K_0^{-1} to obtain $\mathbf{v}_{HT}$. After the HT velocity is computed, we could transform the plasma velocity into the HT frame $\boldsymbol{V}^{(m)}$ by subtracting $\mathbf{v}_{HT}$ from $\mathbf{v}^{(m)}$. A Walen test is conducted by comparing the components of the $\boldsymbol{V}^{(m)}$ with the locally measured Alfvén velocity $\mathrm{v_A} = \frac{\mathrm{B}^{(m)}}{\sqrt{\mu_0 \rho^{(m)}}}$. This test is useful in determining whether the current layer is a tangential or rotational discontinuity. If the plasma flow in the HT frame is close to the local Alfvén velocity, the current layer is a rotational discontinuity and it may be undergoing magnetic reconnection.

It is also important for the user to quantitatively examine the quality of the computed HT frame. One such method [See *Khrabrov and Sonnerup*, 1998] is a comparison between the convection ($\mathbf{E}_C = -\mathbf{v} \times \mathbf{B}$) and HT ($\mathbf{E}_{HT} = -\mathbf{v}_{HT} \times \mathbf{B}$) electric fields. A high degree of correlation between these two electric fields values mean that the HT frame is well determined, while a low correlation means that the HT frame is poorly determined.

3.2.2 Applications of deHoffmann-Teller Analysis

Using the HT analysis method discussed in the previous section, the electric field and Walen Plot is constructed for the AMPTE/IRM magnetopause crossing on 13 December 1985 as shown in Figure 3.5. The electric field scatterplot shows good correlation and the slope of the best fit line to the data points is unity. Hence, the HT frame is well determined. The Walen scatterplot shows that the data points lie close to the "negative" diagonal (i.e., $\boldsymbol{V} = v_A$) and the best fit line has a slope of -0.91 (i.e., $\boldsymbol{V} \approx v_A$). The data points are also highly correlated with a correlation coefficient of -0.98. Hence, the Walen Test is successful for this magnetopause crossing. Since the plasma velocity in the HT frame is ~ 90% of the local Alfvén speed, the HT result indicates likely occurrence of magnetopause reconnection, which further suggests that the current layer is a rotational discontinuity.

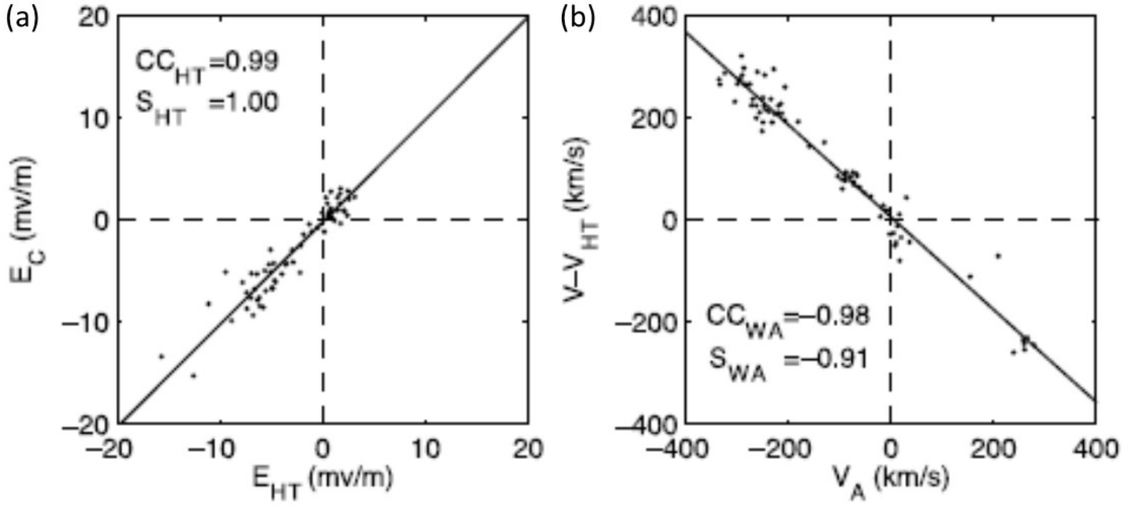

Figure 3.5 (a) Electric field and (b) Walen scatterplot for magnetopause crossing by AMPTE/IRM on 13 December 1985. $\mathbf{E}_C$ is the convection electric field and $\mathbf{E}_{HT}$ is the deHoffmann-Teller electric field. ($\mathbf{v} - \mathbf{v}_{HT}$) is the plasma velocity in the HT frame. In both scatterplot, the high correlation coefficient indicates that the HT frame is well-determined. Figure taken from *Chou and Hau,* [2012]

The above magnetopause crossing example shows a successful HT frame analysis. However, if the data points in the Walen Plot lie near $\boldsymbol{V} = 0$, the plasma velocity in the HT frame is negligible as compared to the local Alfvén velocity. This would constitute a failed Walen Test, which turns out to be ideal for another advanced analysis method called the

Grad-Shafranov Reconstruction. As shown in the next section, a failed Walen test satisfy the assumption in the Grad-Shafranov equation that the convective inertia term in the momentum equation is negligible and can be ignored.

3.2.2 Limitations

From the above discussion, we have shown that the deHoffmann-Teller analysis method is an important tool for analysis of MHD discontinuities. Similar to the MVA techniques, there are limitations to the HT technique. In this section, we derived the constant HT velocity from the data set. However, the theory does not rule out the possibility of an accelerating HT frame. As a result, the HT velocity becomes time-dependent and this requires an acceleration correction term in the computation of the HT velocity.

This technique also requires the knowledge of all three components of the plasma velocity **v** and density ρ in time cadence smaller than the time for the spacecraft to traverse the current layer or flux rope. However, high time-resolution plasma measurements are not available to MESSENGER as the presence of a heat shield prevents the observation of plasma velocity primarily in the Sun-Mercury direction (i.e., *X*-direction). Therefore, the use of HT analysis to MHD current layers and flux ropes observed at Mercury is reserved for future Mercury missions (e,g., Bepi-Colombo).

3.3 **Grad-Shafranov Reconstruction**

The governing equation for this reconstruction technique is the classical Grad-Shafranov (GS) equation. It was formulated by H. Grad, H. Rubin and Vitalii Dmitrievich Shafranov [*Grad and Rubin,* 1958; *Shafranov,* 1966]. The GS equation is an elliptic partial differentiation equation derived by reducing the ideal MHD equations to two-dimensions. This technique was first applied to the reconstruction of tokamak equilibria. It was first used in space application by *Sonnerup and Guo*, [1996]. The main difference between use of this reconstruction technique in tokamaks and space is the boundary conditions used.

3.3.1 Theory

Before deriving the Grad-Shafranov equation, the following assumptions are made:

I. The magnetic structure is 2-dimensional with the Cartesian Z axis as the invariant axis for all quantities i.e. $\frac{\partial}{\partial z} = 0$

II. The structure must be time stationary i.e. $\frac{\partial}{\partial t} = 0$

III. Ignore all convective inertial effects on the system (i.e. eliminating the $\mathbf{u} \cdot \nabla\mathbf{u}$ term in the momentum equation)

The magnetic field can be expressed as:

$$\mathbf{B} = \nabla \times \mathbf{A} \tag{3.11}$$

where **A** is the magnetic vector potential. With the assumption that $\frac{\partial}{\partial z} = 0$, the magnetic field vector **B** can be rewritten as:

$$\mathbf{B} = \left(\frac{\partial \mathrm{A}}{\partial x}, \ \frac{\partial \mathrm{A}}{\partial y}, \ B_{\mathrm{z}}(\mathrm{x,y})\right) = (\boldsymbol{\nabla}\mathrm{A} \times \hat{\mathbf{z}}) + B_{\mathrm{z}}\,\hat{\mathbf{z}} \tag{3.12}$$

From equation 3.12, the gradient of A is perpendicular to **B** everywhere. This means that **A** is constant along any magnetic field line. For a two-dimensional, coherent magnetohydrostatic structure, the momentum equation simplifies to a simple pressure balance equation:

$$\boldsymbol{\nabla}_{\mathbf{t}}\mathrm{P} = \mathbf{J} \times \mathbf{B} \tag{3.13}$$

Where $\boldsymbol{\nabla}_{\mathbf{t}}$ is the gradient operator in the transverse direction (i.e. cartesian *X* and *Y*), P is the transverse pressure, which is the sum of the thermal pressure P_{th} and magnetic pressure P_{mag}, and **J** is the current density. From equation 3.13, the transverse plasma pressure P is a field-line invariant (i.e. only depends on the magnetic vector potential A) as $\boldsymbol{\nabla}_{\mathbf{t}}\mathrm{P}$ is perpendicular to **B** and constant along any field line. Substituting equation 3.12 into 3.13,

$$\boldsymbol{\nabla}_{\mathbf{t}}\mathrm{P} = j_{\mathrm{z}}(\boldsymbol{\nabla}\mathrm{A} \times \hat{\mathbf{z}}) + B_{\mathrm{z}}\,(\mathbf{J}_{\perp} \times \hat{\mathbf{z}}) \tag{3.14}$$

Where $\mathbf{J}_{\perp}$ is the current density in the plane perpendicular to $\hat{\mathbf{z}}$. Substituting equation 3.12 into Ampere's Law and rearranging the terms, one could also express $\mathbf{J}_{\perp}$ and j_{z} as

$$\mathbf{J}_{\perp} = \frac{1}{\mu_0} \boldsymbol{\nabla}\mathrm{B} \times \hat{\mathbf{z}}\,,\; j_z = \frac{1}{\mu_0} \boldsymbol{\nabla}^2 \mathrm{A} \tag{3.15}$$

Substituting equation 3.15 into 3.14 and after some algebra, equation 3.14 becomes:

$$\boldsymbol{\nabla}_{\mathbf{t}}\mathrm{P} = -\left[\left(\frac{1}{\mu_0}\right)\boldsymbol{\nabla}^2\mathrm{A}\right]\boldsymbol{\nabla}\mathrm{A} - \left(\frac{1}{\mu_0}\right)B_z\boldsymbol{\nabla}B_z \tag{3.16}$$

Since P and B_Z are field line invariants, they are only dependent on the magnetic potential A. Hence, the gradients of both quantities can be written as,

$$\boldsymbol{\nabla}\mathrm{P} = \frac{\mathrm{dp}}{\mathrm{dA}}\,\boldsymbol{\nabla}\mathrm{A}\,, \boldsymbol{\nabla}B_z = \frac{\mathrm{d}B_z}{\mathrm{dA}}\,\boldsymbol{\nabla}\mathrm{A} \tag{3.17}$$

Substituting equation 3.17 into 3.16, the Grad-Shafranov equation is given by:

$$\boldsymbol{\nabla}^2\mathrm{A} = -\mu_0 \frac{\mathrm{d}}{\mathrm{dA}}\left(\mathrm{P} + \frac{B_z^2}{2\mu_0}\right) \tag{3.18}$$

The GS equation is a field equation that provides an analytical method to solve the ideal MHD equations. The numerical scheme to perform the GS reconstruction consist of multiple steps. First, MVA is performed on the magnetic structure to determine the invariant axis for the reconstruction map. The deHoffmann-Teller frame of the magnetic structure and the functional form of $\left(\mathrm{P} + \frac{B_z^2}{2\mu_0}\right)$ is then determined and the equation is solved numerically as a Cauchy problem to obtain the reconstructed field map of the magnetic structure.

3.3.2 Applications of Grad-Shafranov Reconstruction

The Grad-Shafranov reconstruction technique is a powerful analysis method with many applications, if use appropriately. One of the benefits of the GS reconstruction is that the technique solves the ideal MHD equations analytically without imposing any physical boundaries (i.e., shape and size etc) or plasma properties constraint on the magnetic structure. Hence, the reconstruction technique has many applications in magnetopause current layer and flux rope analysis.

Magnetopause Current Layer

The Grad-Shafranov reconstruction technique was first used in magnetopause analysis [*Sonnerup and Guo*, 1996]. Figure 3.6 shows an example of a reconstruction field map for a magnetopause crossing observed by AMPTE/IRM on 30 October 1984 [*Hu and Sonnerup*, 2003]. The AMPTE/IRM spacecraft was travelling through the magnetosheath region and crosses the magnetopause into the magnetosphere. The contours in the reconstructed map represent transverse magnetic field lines (i.e., B_X and B_Y). From the separations of the contours lines, it is seen in the reconstructed map that the transverse magnetic field in the magnetosheath region is weaker than that in the magnetosphere. The magnetosheath and magnetosphere regions are separated by the magnetopause current layer, which contains interconnected field lines, reconnection X-lines and a small magnetic island structure. The reconstruction result is consistent with our understanding of magnetic reconnection occurring at the dayside magnetopause to form flux ropes (i.e., flux transfer events).

Flux Ropes

Another application of GS reconstruction is the reconstruction of flux ropes. The reconstruction technique has been applied to flux ropes in the solar wind [*Hu and Sonnerup*, 2001; 2002; *Hu et al.*, 2003] and flux transfer events [*Sonnerup et al.,* 2004]. An example of flux rope reconstruction is shown in Figure 3.7. The reconstructed maps represent flux ropes in the solar wind observed by the WIND spacecraft on 2 May 1996 (left) and 13 March 1996 (right). It is evident from the reconstruction maps that the flux rope in both events are asymmetrical and non-cylindrical. Note that a circular cross-section is a common assumption, at least if the flux rope appears force-free. However, the 13 March flux rope reconstructed map shows irregularities in its internal magnetic structure. It is likely to be non-force-free and in the process of moving towards its minimum energy (i.e., force-free) equilibrium state.

The color shading in Figure 3.7 represents the magnitude of the out-of-plane component of the magnetic field, which corresponds to the axial magnetic field in the flux rope. Both flux ropes shows a peak core field of ~ 8–10 nT. The reconstructed map also shows the chirality (also known as the magnetic helicity) of the flux ropes, which is the sense of twist of the flux rope. The chirality can be either left or right handed. For the 2 May flux rope, the WIND spacecraft measured "upward" transverse magnetic field during its ingress and "downward" transverse magnetic field during egress. Hence, the flux rope is left-handed. Similarly, the WIND spacecraft measured "downward" transverse magnetic field during its ingress and "upward" transverse magnetic field during egress for the 13 March flux rope. Hence it is right-handed. From the reconstructed map, we can also determine the diameter of the flux ropes to be ~ 10^5–10^6 km with impact parameter (shortest distance between spacecraft to the center of the flux rope) of ~ 10^4–10^5 km.

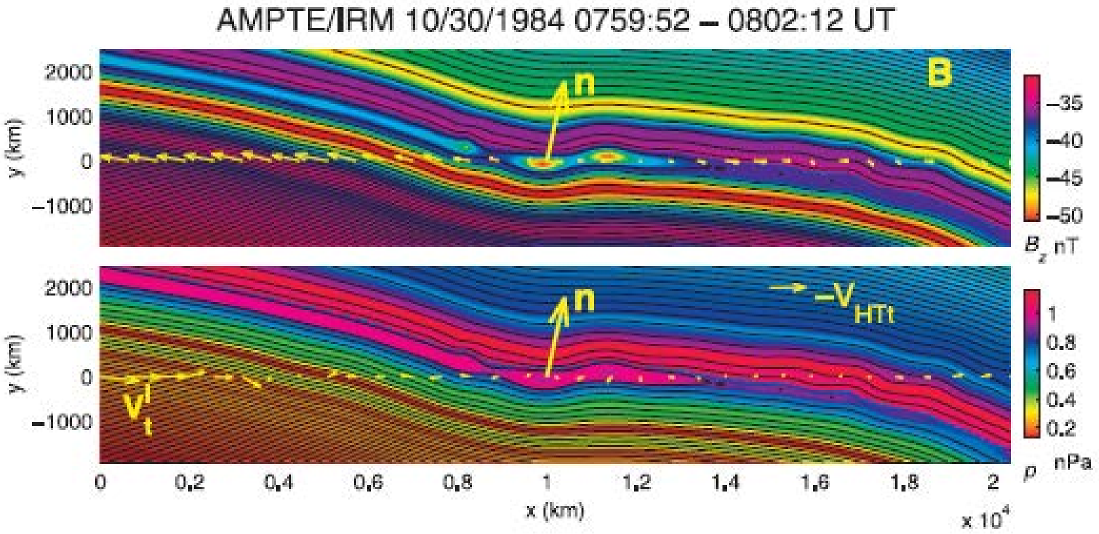

Figure 3.6 GS reconstructions results for 30 October 1984 magnetopause crossing using AMPTE/IRM data. Top panel shows the reconstructed field map with the color plot representing B_Z (magnitude shown by color bar) and the bottom panel shows the same field map with color plot representing plasma pressure (magnitude shown by color bar). The contour lines for both maps represent the transverse magnetic field lines (i.e., B_X and B_Y). The yellow arrows along y = 0 for the top and bottom panel represents the initial transverse magnetic field and plasma velocity observed by the spacecraft, respectively. Figure taken from *Hu and Sonnerup,* [2003].

3.3.3 Limitations

The GS reconstruction technique is a useful analysis tool to infer the magnetic and plasma properties of magnetic structures through field map reconstruction using the ideal MHD equations. One of the benefits of GS reconstruction of flux ropes is that it does not assume symmetry in the physical structure of the flux ropes. The most common method for the determination of flux ropes properties involves fitting the Lundquist solution, which assumes cylindrical symmetry and a specific force-free topology to the measured magnetic field during an arbitrary traversal. Hence, GS reconstruction is a more robust method of determining flux ropes properties because it does not make assumptions regarding the physical shape of flux rope or magnetic field. However, as with any other numerical methods, GS reconstruction has its limitations.

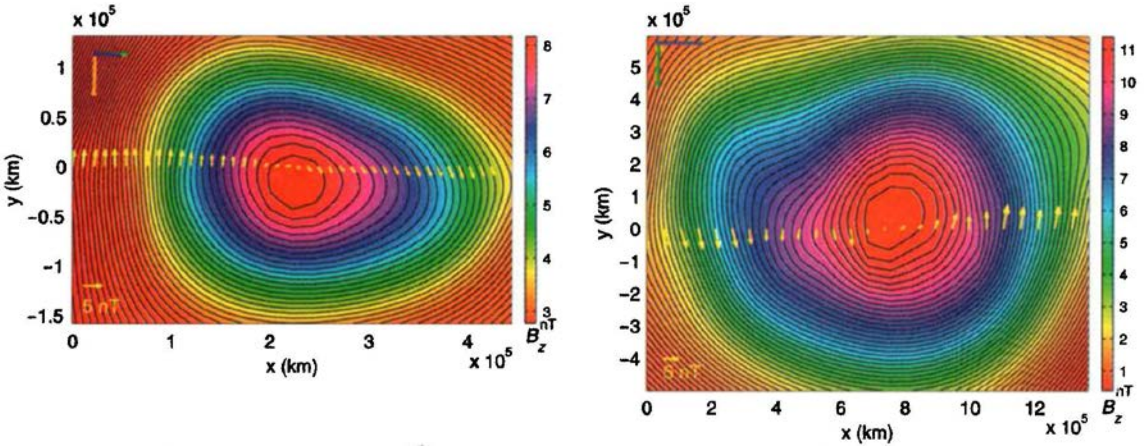

Figure 3.7 GS reconstruction results for flux ropes observed in the solar wind by WIND spacecraft on 2 May 1996 (left) and 13 March 1996 (right). The reconstruction map representations are similar to the reconstructed field map in Figure 3.6. Figure is taken from *Hu and Sonnerup,* [2001].

One of the limitations is that the GS reconstruction technique cannot be applied to regions with rapid temporal variations, which will violates its quasi-static assumption. Examples of such regions include boundary layers, where Kelvin-Helmholtz vortices are often observed, and reconnection sites. Another limitation is numerical instability and the maximum integration domain. Solving the Poisson-like GS equation as a Cauchy problem is highly unstable due to the nature of its exponential solutions; this placed a constraint on the maximum reconstruction domain. Although the problem of numerical instability can be solved using suppression algorithms [*Hau and Sonnerup,* 1999; *Hu and Sonnerup,* 2003], each reconstruction is unique and requires different *ad hoc* methodologies.

However, the major limitation of the GS reconstruction is the limited temporal resolution of most spacecraft data sets and the interpolation/extrapolation method used in the reconstruction process. Although GS reconstruction can provides information of the magnetic structure, it is not used extensively in terrestrial and/or planetary studies due to the unavailability of high resolution plasma data. If the time taken to traverse the reconstructed structure is less than or similar to the time cadence of the plasma instrument, GS reconstruction cannot be performed on that structure. At Mercury, for example, flux ropes have typical time durations of ~ 2–3 seconds while it takes the FIPS instrument on MESSENGER to complete a full 10 seconds energy scan. Therefore, the use of GS reconstruction is not applicable for Mercury's studies given the available data set. For spacecraft with "high enough" resolution (AMPTE, WIND and Cluster), data interpolation is required due to the differences in resolution between plasma and magnetic field data. Hence, the question of the accuracy of the interpolation arises because it can suppress variations between data points that are essential to the accurate determination of the real spatial gradients.

3.4 Conclusions

In this chapter, we explored three analysis techniques used to analyze MHD current layers, flux ropes and cusp plasma filament. The limitations of each technique were also discussed. Minimum variance analysis is the most commonly-used techniques for the analysis of current sheets and flux ropes. We also discussed degeneracy in the MVA eigenvectors and the use of this condition to identify filamentary flux tubes. This technique has applications for study of cusp plasma filaments observed in Mercury's cusp, which will be discussed further in Chapter IV. The use of deHoffmann-Teller and Grad-Shafranov reconstruction technique is generally limited to Earth studies due to unavailability of high-resolution comprehensive plasma measurements on planetary missions. Therefore, these analysis techniques cannot be used for Mercury's magnetosphere, which is the subject of this thesis. However, as technology advances and more compact, yet capable plasma instruments are developed, there is a high possibility that the HT analysis and GS reconstruction be used for future planetary studies.

References:

Chou, Y.-C., and L.-N. Hau (2012), A statistical study of magnetopause structures: Tangential versus rotational discontinuities, *J. Geophys. Res.*, *117*, A08232, doi:10.1029/2011JA017155.

Hasegawa, H., Sonnerup, B. U. Ö., Dunlop, M. W., Balogh, A., Haaland, S. E., Klecker, B., Paschmann, G., Lavraud, B., Dandouras, I., and Rème, H. (2004) Reconstruction of two-dimensional magnetopause structures from Cluster observations: verification of method, *Ann. Geophys.*, *22*, 1251-1266, doi:10.5194/angeo-22-1251-2004.

Hasegawa, H., Sonnerup, B. U. Ö., Owen, C. J., Klecker, B., Paschmann, G., Balogh, A., and Rème, H. (2006) The structure of flux transfer events recovered from Cluster data, *Ann. Geophys., 24*, 603-618, doi:10.5194/angeo-24-603-2006.

Hasegawa, H., R. Nakamura, M. Fujimoto, V. A. Sergeev, E. A. Lucek, H. Rème, and Y. Khotyaintsev (2007), Reconstruction of a bipolar magnetic signature in an earthward jet in the tail: Flux rope or 3D guide-field reconnection? *J. Geophys. Res.*, *112*, A11206, doi:10.1029/2007JA012492.

Hasegawa, H., B. U. Ö. Sonnerup, and T. K. M. Nakamura (2010), Recovery of time evolution of Grad-Shafranov equilibria from single-spacecraft data: Benchmarking and application to a flux transfer event, *J. Geophys. Res.*, *115*, A11219, doi:10.1029/2010JA015679.

Hau, L.-N., and B. U. Sonnerup (1999), Two-dimensional coherent structures in the magnetopause: Recovery of static equilibria from single-spacecraft data, *J. Geophys. Res.*, *104*(*A4*), 6899–6917, doi:10.1029/1999JA900002.

Hu, Q., and B. U. Ö. Sonnerup (2001), Reconstruction of magnetic flux ropes in the solar wind, *Geophys. Res. Lett.*, *28*, 467–470, doi:10.1029/2000GL012232.

Hu, Q., and B. U. Ö. Sonnerup, (2002) Reconstruction of magnetic clouds in the solar wind: Orientations and configurations, *J. Geophys. Res.*, *107*(*A7*), doi:10.1029/2001JA000293.

Hu, Q., and B. U. Ö. Sonnerup (2003), Reconstruction of two-dimensional structures in the magnetopause: Method improvements, *J. Geophys. Res.*, *108*(*A1*), 1011, doi:10.1029/2002JA009323.

Hu, Q., C. W. Smith, N. F. Ness, and R. M. Skoug (2003), Double flux-rope magnetic cloud in the solar wind at 1AU, *Geophys. Res. Lett.*, *30*(*7*), 1385, doi:10.1029/2002GL016653.

Khrabrov, A. W., and B. U. Ö. Sonnerup (1998), DeHoffmann-Teller analysis, Analysis Methods for Multi-Spacecraft Data, ISSI Sci. Rep. SR-001, edited by G. Paschmann, and P. W. Daly, p. 221, Springer, New York.

Sonnerup, B. U. Ö., and M. Scheible (1998), Minimum and maximum variance analysis, *in* Analysis Methods for Multi-spacecraft Data, edited by G. Paschmann and P. W. Daly, chap. 8, pp. 185–220, Int. Space Sci. Inst., Bern, Switzerland.

Sonnerup, B. U. Ö., H. Hasegawa, and G. Paschmann (2004), Anatomy of a flux transfer event seen by Cluster, *Geophys. Res. Lett., 31*, L11803, doi:10.1029/2004GL020134.

Sonnerup, B. U. Ö., and H. Hasegawa (2005), Orientation and motion of two-dimensional structures in a space plasma, *J. Geophys. Res., 110*, A06208, doi:10.1029/2004JA010853.

Sonnerup, B. U. Ö., H. Hasegawa, W.-L. Teh, and L.-N. Hau (2006), Grad-Shafranov reconstruction: An overview, *J. Geophys. Res., 111*, A09204, doi:10.1029/2006JA011717.

Sonnerup, B. U. Ö., W.-L. Teh, and H. Hasegawa (2008), Grad-Shafranov and MHD reconstructions, in Multi-spacecraft Analysis Methods Revisited, Rep. ISSI SR-008, edited by G. Paschmann and P. W. Daly, pp. 81–90, Eur. Space Agency, Paris.

Xiao, C. J., Z. Y. Pu, Z. W. Ma, S. Y. Fu, Z. Y. Huang, and Q. G. Zong (2004), Inferring of flux rope orientation with the minimum variance analysis technique, *J. Geophys. Res., 109*, A11218, doi:10.1029/2004JA010594.

Chapter IV

MESSENGER OBSERVATION OF CUSP PLASMA FILAMENTS AT MERCURY

This chapter is taken from Gangkai Poh, James A. Slavin, Xianzhe Jia, Gina A. DiBraccio, Jim M. Raines, Suzanne M. Imber, Daniel J. Gershman, Wei-Jie Sun, Brian J. Anderson, Haje Korth, Thomas H. Zurbuchen, Ralph L. McNutt, Jr., and Sean C. Solomon (2016), MESSENGER observations of cusp plasma filaments at Mercury, *J. Geophys. Res. Space Physics, 121*, 8260–8285, doi:10.1002/2016JA022552.

Abstract

The MESSENGER spacecraft while in orbit about Mercury observed highly localized, ~3-s-long reductions in the dayside magnetospheric magnetic field, with amplitudes up to 90% of the ambient intensity. These magnetic field depressions are termed cusp filaments because they were observed from just poleward of the magnetospheric cusp to mid-latitudes, i.e., ~55° to 85° N. We analyzed 345 high- and low-altitude cusp filaments identified from MESSENGER magnetic field data to determine their physical properties. Minimum variance analysis indicates that most filaments resemble cylindrical flux tubes within which the magnetic field intensity decreases toward its central axis. If the filaments move over the spacecraft at an estimated magnetospheric convection speed of ~35 km/s, then they have a typical diameter of ~105 km or ~7 gyro-radii for 1 keV H^+ ions in a 300

nT magnetic field. During these events, MESSENGER's Fast Imaging Plasma Spectrometer observed H^+ ions with magnetosheath-like energies. MESSENGER observations during the spacecraft's final low-altitude campaign revealed that these cusp filaments likely extend down to Mercury's surface. We calculated an occurrence-rate-normalized integrated particle precipitation rate onto the surface from all filaments of $(2.70\pm0.09) \times 10^{25}$ s^{-1}. This precipitation rate is comparable to published estimates of the total precipitation rate in the larger-scale cusp. Overall, the MESSENGER observations analyzed here suggest that cusp filaments are the magnetospheric extensions of the flux transfer events that form at the magnetopause as a result of localized magnetic reconnection.

4.1 Introduction

Since the discovery by Mariner 10 that Mercury possesses an intrinsic dipolar magnetic field [*Ness et al.,* 1974], much interest has been focused on the interaction between the solar wind and Mercury's small magnetosphere. The MErcury Surface, Space ENvironment, GEochemistry, and Ranging (MESSENGER) spacecraft was the first to orbit Mercury. It provided magnetic field [*Anderson et al.,* 2007] and plasma ion [*Andrews et al.,* 2007] measurements to characterize magnetospheric structure and dynamics at Mercury [*Anderson et al.,* 2008; *Slavin et al.,* 2009; *Raines et al.,* 2014]. With these data, a number of discoveries have been made about Mercury's magnetosphere and its interaction with the solar wind. We now know that Mercury's dipole moment is offset in the northward direction by 484 ± 11 km [*Alexeev et al.,* 2010; *Anderson et al.,* 2011; *Johnson et al.,* 2012; *Winslow et al.,* 2014]. The planet's magnetosphere is small, with a standoff distance from Mercury's center that averages 1.45 R_M [*Winslow et al.,* 2013], where R_M is Mercury's radius (2440 km), and decreases to less than 1.1 R_M during coronal mass ejections (CMEs) [*Slavin et al.,* 2014]. Because of Mercury's close proximity to the Sun, the solar wind not only has higher dynamic pressure, but also has lower plasma β – the ratio of plasma thermal pressure to magnetic pressure – and Alfvénic Mach number than typically seen at Earth. These conditions produce a thick plasma depletion layer in the magnetosheath, adjacent to the dayside magnetopause [*Gershman et al.,* 2013] as well as high rates of magnetopause reconnection [*Slavin and Holzer,* 1979; *Slavin et al.,* 2009;

DiBraccio et al., 2013]. The solar wind interaction with Mercury also produces frequent, large flux transfer events (FTEs) observed from the subsolar region to the high-latitude magnetopause downstream of the cusp [*Slavin et al.,* 2009, 2010, 2012; *Imber et al.,* 2014]. Fully developed Kelvin-Helmholtz waves are observed along the low-latitude magnetopause, but only along the dusk flank [*Boardsen et al.,* 2010; *Sundberg et al.,* 2012; *Liljeblad et al.,* 2014; *Gershman et al.*, 2015].

The magnetospheric cusps separate the closed dayside magnetic flux at lower latitudes from the open flux tubes in the polar caps that map to the north and south lobes of the magnetotail. The cusp is characterized by newly opened magnetic flux that is created by magnetic reconnection at the dayside magnetopause and moves poleward to join the high latitude magnetotail. Along the flux tubes that transit the cusp, plasma flows from reconnection sites at the magnetopause toward the surface. A portion of this plasma mirrors at low altitude and moves back up the flux tube to form the plasma mantle, just inside the magnetopause tailward of the cusp [*Hill and Reiff,* 1977; *Newell and Meng,* 1987; *DiBraccio et al.,* 2015]. Planetary magnetospheric cusps are important because they are one of the sites for solar wind mass and energy transfer into the magnetosphere. Recent studies of Mercury's cusps [*Winslow et al.,* 2014; *Raines et al.,* 2014] suggest that such regions also play an important role in magnetosphere-surface interaction as sites for the upward escape of sputtered Na^+.

Slavin et al. [2014] first reported observations of discrete diamagnetic field decreases, lasting only a few seconds in duration, on top of the average cusp diamagnetic depression during the CME event observed by MESSENGER on 23 November 2011. The structures corresponding to these short-term field changes were termed "cusp plasma filaments" to reflect their occurrence within and in the region surrounding Mercury's cusp. *Slavin et al.,* [2014] hypothesized that the filaments were diamagnetic in origin and caused by the injection of magnetosheath plasma into discrete flux tubes by reconnection at the magnetopause. The maximum field decrease in these filaments was observed to be ~200 nT, equivalent to ~16 nPa of plasma pressure [*Slavin et al.,* 2014]. To date, such large-amplitude filamentary structures within a cusp region have not been observed at planets other than Mercury.

This paper aims to answer the following questions. What is the magnetic structure of cusp filaments? What are the spatial and temporal ranges of their physical properties? How frequently are they observed? What are the characteristics of the plasma responsible for the diamagnetic reduction in their core field? How are cusp filaments related to the FTEs observed at the magnetopause? Do these filaments extend to low altitudes, and do they reach the surface? What is the flux of ions precipitating to the surface from the filaments and what is their aggregate contribution to the solar wind flux to the surface? What aspects of the solar wind lead to cusp filament formation?

The paper is organized as follows. In the next section we summarize a survey of 3 years of MESSENGER magnetic field observations for the presence of cusp filaments conducted with a scale-free quantitative identification method. In section 3 we present the minimum variance analysis (MVA) applied to each filament event to infer mean orientation and magnetic structure. In section 4 we summarize an examination of the first 3 months of magnetic field data from MESSENGER's end-of-mission low-altitude campaign, i.e., August through October 2014, a period during which the spacecraft periapsis was within 50 km of Mercury's surface. In section 5 we summarize the outcome of statistical analyses performed to determine the physical properties and geographic distribution of the filaments inferred from combined high- and low-altitude data. In section 6 we provide an estimate of the flux of ions that precipitate onto Mercury's surface and an assessment of upstream solar wind conditions as a guide to the factors that influence filament formation. We conclude that the filaments are most likely the low-altitude extensions of FTEs occurring at the dayside magnetopause, and the plasma within each filament adds to the total plasma flux precipitating onto Mercury's surface.

4.2 MESSENGER Instrumentation and Cusp Filament Identification

In this study, we use the full-resolution measurements from MESSENGER's Magnetometer (MAG) (20 samples/s) and Fast Imaging Plasma Spectrometer (FIPS) (1 energy scan every 10 s), both data sets of which are available for all cusp crossings and the entire orbital mission. We surveyed the orbits during which the spacecraft traversed the average cusp location [*Winslow et al.,* 2012]. We selected orbits during which MESSENGER traversed the dayside magnetopause within 8.5–15.5 h of magnetic local time (MLT) to ensure that the magnetic signatures observed in the cusp are not related to other flank magnetopause dynamic phenomena such as Kelvin-Helmholtz waves.

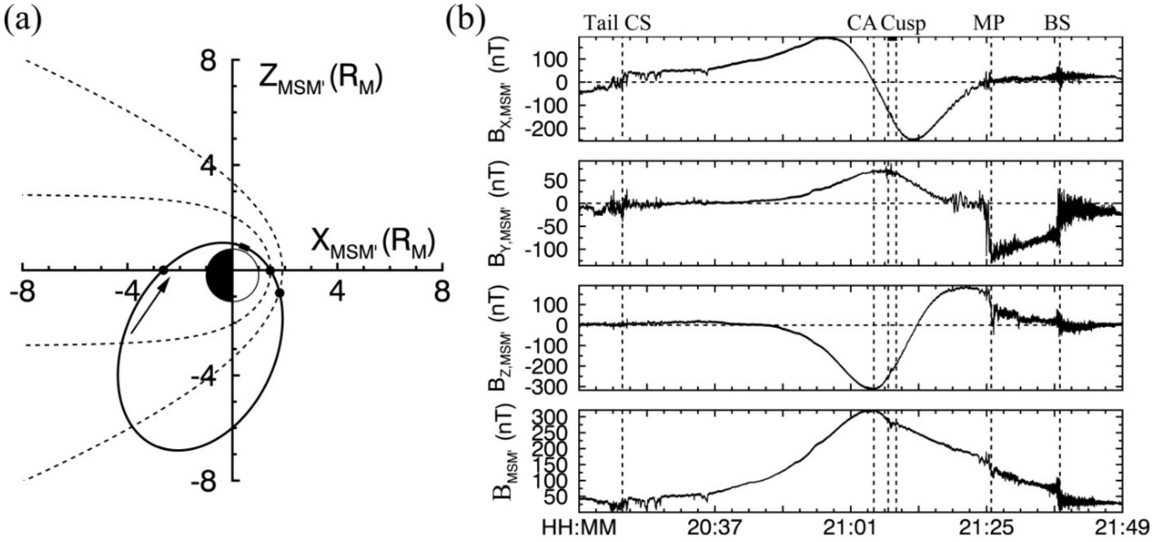

Figure 4.1 (a) An example MESSENGER orbit (black solid line) on 26 August 2011 projected onto the *X-Z* plane in aberrated Mercury solar magnetic (MSM') coordinates during a period without filamentary activities in the cusp. The aberration angle is -7.31°. The model bow shock (BS) and magnetopause (MP) from *Winslow et al.* [2013], scaled to fit observed boundary crossings (marked by the two dots at the dayside magnetosphere), are shown in dotted lines; the Sun is to the right. The thick portion of the orbit represents the cusp region, and the dot at the nightside magnetosphere represents the magnetotail current sheet (CS) crossing. The arrow denotes the direction of spacecraft trajectory. (b) Full-resolution magnetic field measurements (top to bottom, *X*, *Y*, and *Z* components and field magnitude) acquired along the orbit shown in (a). The vertical dashed lines mark the boundary crossings shown in (a). CA denotes closest approach, and all times are in UTC.

An example of magnetic field data acquired along a MESSENGER orbit during an interval when no cusp plasma filaments were seen (on 26 August 2011) is shown in Figure 4.1. Figure 4.1a shows the example orbit in an aberrated adjustment to the Mercury solar magnetospheric (MSM) coordinate system. In the MSM system, centered on Mercury's internal dipole, the *X*-axis and *Z*-axis are sunward and along the northern spin axis, respectively, and the *Y*-axis completes the right-handed system and is in a direction opposite to that of Mercury's orbital motion. Because of the orbital motion of Mercury with respect to the solar wind, we have accounted for the aberration effect by rotating the MSM coordinate system in the *X-Y* plane by an aberration angle into the aberrated MSM coordinate system (MSM'). Because of the highly eccentric shape of Mercury's orbit, the aberration angle was calculated on a daily basis under the assumption that the solar wind velocity is radial to the Sun at 400 km/s.

The full-resolution magnetic field measurements along the orbit depicted in Figure 4.1a are shown in Figure 4.1b. The magnetic field was relatively quiet during this orbital pass. The interval began with MESSENGER crossing Mercury's magnetotail current sheet (CS) as shown from the reversal in polarity of the X component of the magnetic field vector $\mathbf{B}$ at 20:22 UTC. As MESSENGER moved closer to the planet, the magnetic field strength increased until the spacecraft reached closest approach (CA) where B was at its maximum. The magnetic field showed little fluctuation near this time, indicating that the spacecraft was deep within Mercury's magnetosphere. The spacecraft encountered the northern magnetospheric cusp about 3 min later as evidenced by the broad depression in the magnetic field magnitude. MESSENGER exited the dayside magnetosphere at ~ 21:25:00 UTC and remained in the magnetosheath until it crossed the bow shock into the solar wind at ~ 21:37:00 UTC.

An example of magnetic field data acquired along a MESSENGER orbit during an interval when plasma filaments were seen in the cusp (on 20 May 2011) is shown in Figure 4.2. Figure 4.2a displays full-resolution magnetic field measurements acquired from the spacecraft crossing of the magnetotail current sheet through the cusp region and outward thereafter. In addition to observing a magnetic field depression in the cusp similar to that shown in Figure 4.1b, MESSENGER also recorded short-duration cusp filaments as it flew into the cusp and moved to lower magnetic latitudes. The spacecraft crossed the magnetopause at 10:07:00 UTC and encountered the bow shock at 10:23:00 UTC. MESSENGER also observed large-amplitude fluctuations in B associated with FTEs near the dayside magnetopause in the magnetosheath region [*Slavin et al.,* 2012; *Imber et al.,* 2014]. Figure 4.2b shows a close-up of the magnetic field measurements in the cusp region. The background magnetic field displays 4-min-long fluctuations around a mean field of ~300 nT, behavior consistent with our understanding of plasma diamagnetism in Mercury's magnetospheric cusp [*Winslow et al.,* 2012; *Raines et al.,* 2014]. However, MESSENGER also clearly measured highly localized magnetic field decreases that we identify here as cusp filaments.

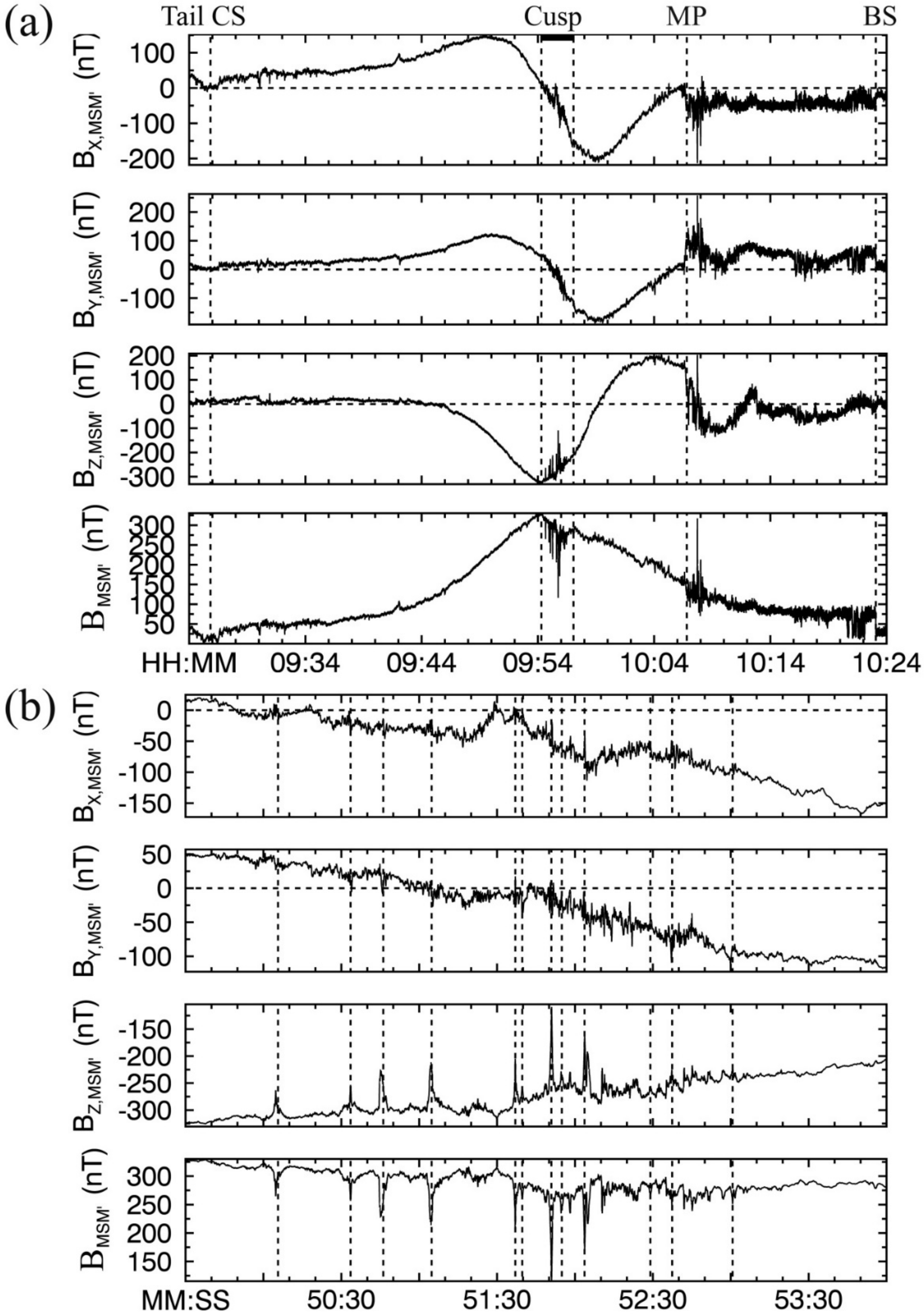

Figure 4.2 (a) Magnetic field measurements during an example orbit on 20 May 2011 during which plasma filaments were observed in the cusp. Magnetic field components are in aberrated MSM' coordinates for an aberration angle of -6.31°. The format is similar to that of Figure 4.1b. (b) Close-up of magnetic field measurements in the cusp region for the time interval delimited by the dashed lines in (a) labeled cusp. Each cusp filament identified by the automated algorithm is denoted by a vertical dashed line.

We visually identified a total of 63 cusp crossings from March 2011 to May 2015 that contained cusp filaments. For each cusp crossing, we identified the cusp filament events with a scale-free algorithm adapted from the scale-free approach developed by *Stevens and Kasper* [2007] (hereafter referred as SK07) to identify magnetic holes in the solar wind. The SK07 method is highly applicable to the study here because it uses the decrease of the magnetic field magnitude B in the identification process, and such a decrease is also the main magnetic signature of cusp filaments. However, it must be made clear that, although the cusp filaments and solar wind magnetic holes possess similar magnetic signatures, their formation process is not believed to be similar.

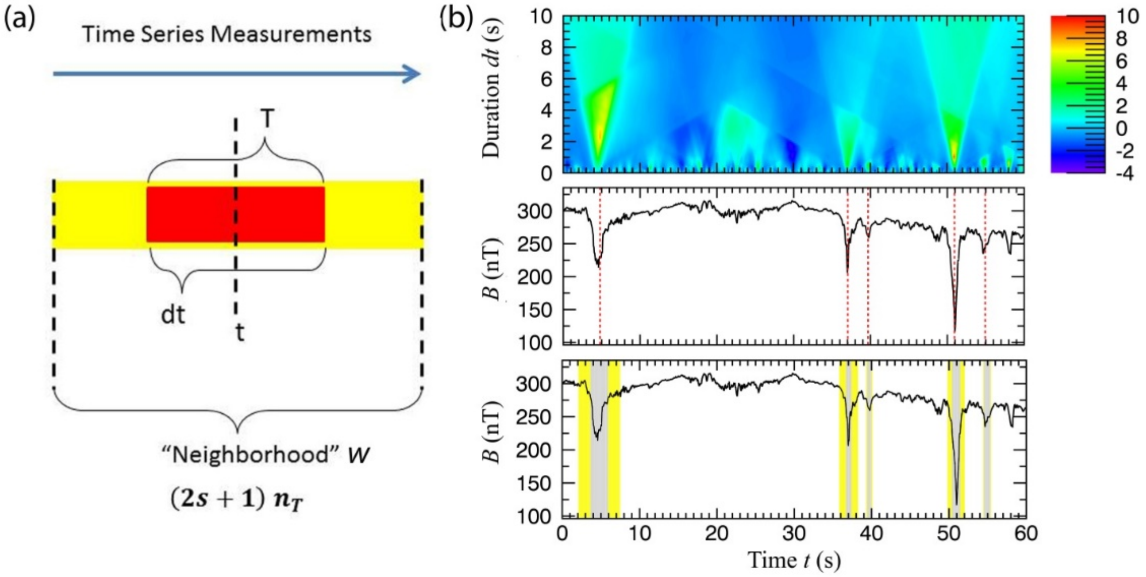

Figure 4.3 (a) Schematic illustration of the different time segments used in the quasi-automatic, scale-free identification algorithm. The red and yellow boxes represent a time segment T and "neighborhood" W, respectively; both are centered at time t. (b) Top: map of q values (color bar) for a 1-min interval at 09:51 UTC on 20 May 2011 for optimum values of $q_0 = 3.9$ and $s = 3$; the ordinate is duration dt, and the abscissa is time t within that interval. Middle: B for the same time interval. Vertical red dashed lines indicate the times of filaments identified by the automated method. Bottom: B for the same time interval with gray shaded areas representing $dt_{\max}$ values that correspond to $q_{\max}$ and yellow shaded areas spanning dt values that correspond to half maximum values of $q_{\max}$ at times $t_{\max}$.

For each filament, we first determined an amplitude δB and a time duration dt. δB is the decrease in B within the filament and is given by the relation $\delta B = B_0 - B_1$ where B_0 is the magnitude of the ambient magnetic field just outside the filament and B_1 is the minimum field magnitude inside the filament. Previous studies of magnetic holes in the solar wind used arbitrary event selection criteria to determine δB and dt [e.g., *Turner et al.*, 1977; *Winterhalter et al.*, 1994], a procedure that inevitably introduces scaling biases. The study of cusp filaments here faces the same challenge, i.e., accurately determining both parameters without introducing significant bias. For the cusp filaments, the low signal-to-noise ratio in the background magnetic field resulting from intense magnetospheric activity in the cusp introduces additional challenges. Hence, a scale-free identification method is needed to minimize scaling biases.

The process for identifying cusp filaments is illustrated schematically in Figure 4.3a. To begin the identification process, we divided each cusp-crossing interval into 1-min subintervals. For each 1-min subinterval, there is a time series of B observations at a cadence τ (0.05 s for MESSENGER). Consider a segment T centered on time t within that subinterval that contains n_{T} measurements and has a total duration dt, where $dt = n_{\mathrm{T}}\,\tau$. Consider a longer neighborhood segment W also centered on time t and defined so that it contains $n_{\mathrm{W}} = (2s+1)n_{\mathrm{T}}$ measurements, where s is the isolation factor, an integer representing how isolated each filament must be relative to the adjacent filament to be considered independent. In the SK07 method, a constant value of s is used for the study. In our filament study, the isolation factor is one of two free parameters in the identification process and is allowed to vary for each 1-min subinterval. The choice of s for each subinterval is discussed further below. We define the significance q of segment T relative to its neighborhood segment W as:

$$q(dt, t) = \frac{\langle B\rangle_{\mathrm{W-T}} - \langle B\rangle_{\mathrm{T}}}{\sigma_{\mathrm{W-T}}} \tag{4.1}$$

where $\langle B\rangle_{\mathrm{T}}$ is the mean value of B within time segment T, $\langle B\rangle_{\mathrm{W-T}}$ is the mean value of B within the time segment w outside of the interval T (segment $W - T$), and $\sigma_{\mathrm{W-T}}$ is the standard deviation of B in that same segment ($W - T$). By varying the size of the time segment T, q is maximized when t and dt coincide with the center and duration of the filament, respectively. If segment T contains no filament, q fluctuates between 1 and -1.

From equation 4.1, we constructed maps of q as a function of dt and t as shown in Figure 4.3b for an example cusp crossing at 09:51 UTC on 20 May 2011, with q ranging from -4 to 10 as represented in the color bar. There are six pronounced maxima in q on the map, each corresponding to a sharp decrease in B, i.e. a plasma filament. We also defined a cutoff value q_0 such that any maximum in q less than q_0 is considered to be a "false detection" of a filament resulting from background noise or turbulence. Hence, q_0 is another free parameter. The use of the two free parameters, s and q_0, optimizes the number of filament events that the algorithm selects while minimizing the number of false positive detections. For each 1-min subinterval, we determined the best values of the free parameters by running the algorithm through that subinterval for different combinations of s and q_0. The combination of s and q_0 with the most (least) number of true (false) positive was chosen for that subinterval. For the case in Figure 4.3b, a value of $s = 3$ and $q_0 = 3.9$ was determined. For such a value of q_0, the random fluctuations between $t = 15$ s and $t = 28$ s are not detected by the algorithm as filaments. A search algorithm (see the appendix of SK07 for further details) was then applied to identify each maximum in q and its corresponding values of time t_{max} and duration dt_{max} as shown in Figure 4.3b for the example.

The procedure described to this point closely follows the SK07 method. However, because of high-frequency magnetic field fluctuations in Mercury's cusp, the value of dt corresponding to each maximum tends to underestimate the time duration of each filament (see the gray-shaded areas in the bottom panel of Figure 4.3b). Low-pass filtering of the data could avoid high-frequency magnetic field fluctuations that mask the filament signatures in the selection algorithm. However, we did not elect such an approach as the error associated with low-pass filtering increases with decreasing dt and increasing δB. Hence, instead of using dt_{max}, we used a value for dt equal to the interval over which q equaled or exceeded half the maximum value of q at time t_{max}. This estimate for duration $dt_{\mathrm{half\text{-}max}}$ is illustrated by the yellow-shaded regions in Figure 4.3b (the yellow-shaded regions should be understood as also including the gray-shaded regions).

Our scale-free algorithm proved to be effective in identifying filaments for the entire dataset from Mercury. This method is not flawless, however, as it could identify "false positives" or fail to identify candidate filaments (e.g., the candidate filament event at $t = 58$ s in Figure 4.3b) as a result of the choice of free parameters or background fluctuations in segment $(w - T)$. The first possibility can be remedied by introducing a threshold value of $\delta B/B$. For high-altitude portions of MESSENGER's orbit, a threshold value of $\delta B/B = 0.05$ was set to filter any false positives identified by the algorithm. As shown in Figure

4.2b, typical random magnetic field fluctuations are ~10–15 nT, or ~3–5% of the background magnetic field (~300 nT), so a threshold $\delta B/B$ value of 0.05 is appropriate. We also conducted a sensitivity test of our results on the threshold $\delta B/B$ value, which will be further discussed in Section 5. Although there is no easy fix to the second possibility, there is no loss in generality if some events are missed, given the large number of filaments identified. Since the statistical error is inversely proportional to $\sqrt{N}$, where N is the total number of events (i.e., 319), and the percentage error in our results is no more than 10%. Nevertheless, our scale-free algorithm provides consistency in the selected time interval of each filament, whereas a non-quantifiable random bias would be introduced to our statistical analysis if the selection were done visually.

For most of MESSENGER's orbital mission, the spacecraft traversed Mercury's cusp at altitudes between ~300 and ~700 km, and for these cusp crossings we apply the term high-altitude observations. In late July 2014, MESSENGER's periapsis altitude fell below 100 km for the first time, and between August and October that year the spacecraft completed multiple traverses of Mercury's cusp at altitudes less than 100 km. For these cusp crossings we apply the term low-altitude observations. We describe the high-altitude and low-altitude observations of filaments separately in the sections that follow.

4.3 Analysis Results for High-altitude Filaments

From 62 high-altitude observations, a total of 301 filaments were identified using the algorithm described in the previous section. To understand their magnetic structure, MVA was performed on each filament event over the interval $dt_{\text{half-max}}$. MVA transforms magnetic field measurements from MSM' coordinates into a new orthogonal coordinate system based on the directions of minimum (min), intermediate (int), and maximum (max) variance in the magnetic field measurements [*Sonnerup and Cahill,* 1967]. The method has been used extensively at Mercury to analyze the orientation of current sheets and other structures [*Slavin et al.,* 2012; *DiBraccio et al.,* 2013; *Imber et al.,* 2014]. The three variance directions were computed by solving the covariance matrix as an eigenvalue problem. The results are three eigenvalues (λ_{i}) and their corresponding eigenvectors ($\boldsymbol{x}_{\text{i}}$), where the subscript *i* variously represents min, int, or max. The eigenvector with the largest eigenvalue corresponds to the direction with maximum magnetic variance, and so forth. To quantify the errors associated with the eigenvectors, we used the error estimation procedure developed by *Sonnerup and Scheible* [1998] whereby the angular rotation uncertainty of eigenvector $\boldsymbol{x}_\mathrm{i}$ to or away from $\boldsymbol{x}_\mathrm{j}$ and the statistical uncertainty in the component of average magnetic field along each eigenvector are given by the following:

$$\left|\Delta\varphi_{\mathrm{ij}}\right| = \sqrt{\frac{\lambda_3}{(M-1)}\frac{\left(\lambda_\mathrm{i}+\lambda_\mathrm{j}-\lambda_3\right)}{\left(\lambda_\mathrm{i}-\lambda_\mathrm{j}\right)^2}}, \quad i \neq j \tag{4.2a}$$

$$|\Delta\langle \boldsymbol{B}\cdot\boldsymbol{x}_\mathrm{i}\rangle| = \sqrt{\frac{\lambda_\mathrm{i}}{(M-1)} + \sum_{i\neq j}\left(\Delta\varphi_{\mathrm{ij}}\langle \boldsymbol{B}\rangle\cdot\boldsymbol{x}_\mathrm{j}\right)^2} \tag{4.2b}$$

Ratios of eigenvalues are often used as indicators of the quality of the determination of MVA principal axes. Degeneracy occurs if any two eigenvalues are approximately equal, i.e., when any two orthogonal vectors lying on the plane that contains the two eigenvectors are nearly equally valid as the basis for the MVA coordinate system [*Sonnerup and Scheible*, 1998]. For this reason, earlier studies that used this technique for magnetopause and flux rope analysis required a minimum eigenvalue ratio of 1.5–5 [*Sonnerup and Cahill*, 1967; *DiBraccio et al.*, 2013]. Even though degeneracy can lead to large uncertainties in the eigenvectors, it can also be utilized to infer the magnetic structure of the filaments. In this study, we grouped filament events according to their ratios of intermediate to minimum (int/min) and maximum to intermediate (max/int) eigenvalues, and we chose a minimum eigenvalue ratio of 4 for any two eigenvectors to be considered well determined. On the basis of this definition, we identified four different populations of filaments:

1. Population I: $\frac{\lambda_{\mathrm{int}}}{\lambda_{\mathrm{min}}} < 4$ and $\frac{\lambda_{\mathrm{max}}}{\lambda_{\mathrm{int}}} > 4$
2. Population II: $\frac{\lambda_{\mathrm{int}}}{\lambda_{\mathrm{min}}} > 4$ and $\frac{\lambda_{\mathrm{max}}}{\lambda_{\mathrm{int}}} < 4$
3. Population III: $\frac{\lambda_{\mathrm{int}}}{\lambda_{\mathrm{min}}} \sim \frac{\lambda_{\mathrm{max}}}{\lambda_{\mathrm{int}}} > 4$
4. Population IV: $\frac{\lambda_{\mathrm{int}}}{\lambda_{\mathrm{min}}} \sim \frac{\lambda_{\mathrm{max}}}{\lambda_{\mathrm{int}}} < 4$

4.3.1 Population I

For Population I filaments, the minimum and intermediate eigenvectors are considered to be degenerate (i.e., $\frac{\lambda_{\text{int}}}{\lambda_{\text{min}}} < 4$) on the basis of our chosen threshold, whereas the maximum eigenvector is well determined (i.e., $\frac{\lambda_{\text{max}}}{\lambda_{\text{int}}} > 4$). A total of 130 filament events (~ 43% of the filaments identified) can be classified in this group. Figure 4.4 shows an example of a typical Population I filament identified on 23 April 2013. The top three panels of the figure show the magnetic field components for this example in MSM' coordinates. B_X and B_Y show comparatively small variations and are mostly less than 0 nT, whereas B_Z shows a large peak at ~ 16:30:29 UTC. The bottom 4 panels in the figure show the magnetic field in the MVA coordinate system and the total scalar field. The maximum, intermediate, and minimum eigenvectors in MSM' are (0.059, 0.116, 0.992), (-0.998, -0.015, 0.061), and (-0.022, 0.993, -0.115), and the max/int and int/min eigenvalue ratios are 9.70 and 2.11, respectively. The mean values for B_{min} and B_{int} are -1.69 ± 1.59 nT and 8.64 ± 3.50 nT, respectively. B_{min} and B_{int} show only small variations, but there is a clear unipolar variation in B_{max}. Figure 4.4b shows the corresponding max/min and max/int hodograms.

From the magnetic signatures in the MVA coordinate system, we can infer that this filament population is quasi-cylindrically shaped because the magnetic field varies primarily in the maximum direction. Such magnetic structure could be explained with magnetohydrodynamic (MHD) theory and an ideal cylindrical plasma-filled flux tube with the background magnetic field and its invariant axis in the axial direction. From the inverse Gaussian shape of the decrease in the magnetic field magnitude in the filaments, we may infer a Gaussian spatial distribution for the plasma pressure across the flux tube. MESSENGER should have measured regions of weaker field strength toward the center of flux tube because of diamagnetic effects as it traversed the flux tube. In this basic picture of a plasma filament, the direction of maximum variance will be parallel to the axis of the flux tube. Hence, we would expect the maximum eigenvector to have a strong Z-component and be approximately field-aligned. Given plasma homogeneity in the azimuthal and axial (i.e., Z) directions, diamagnetic effects will reduce the field only in the axial direction. Hence, there will be no variance of the field in the minimum and intermediate directions.

This degeneracy produces a prolate variance ellipsoid [*Sonnerup and Scheible,* 1998], independent of the impact parameter, defined as the perpendicular distance between the path of the spacecraft and the center of the flux tube, and the inclination angle at which the spacecraft traverses the flux tube. In this ideal model of a plasma filament, the mean magnetic field along the intermediate and minimum eigenvectors is expected to be ~ 0 nT.

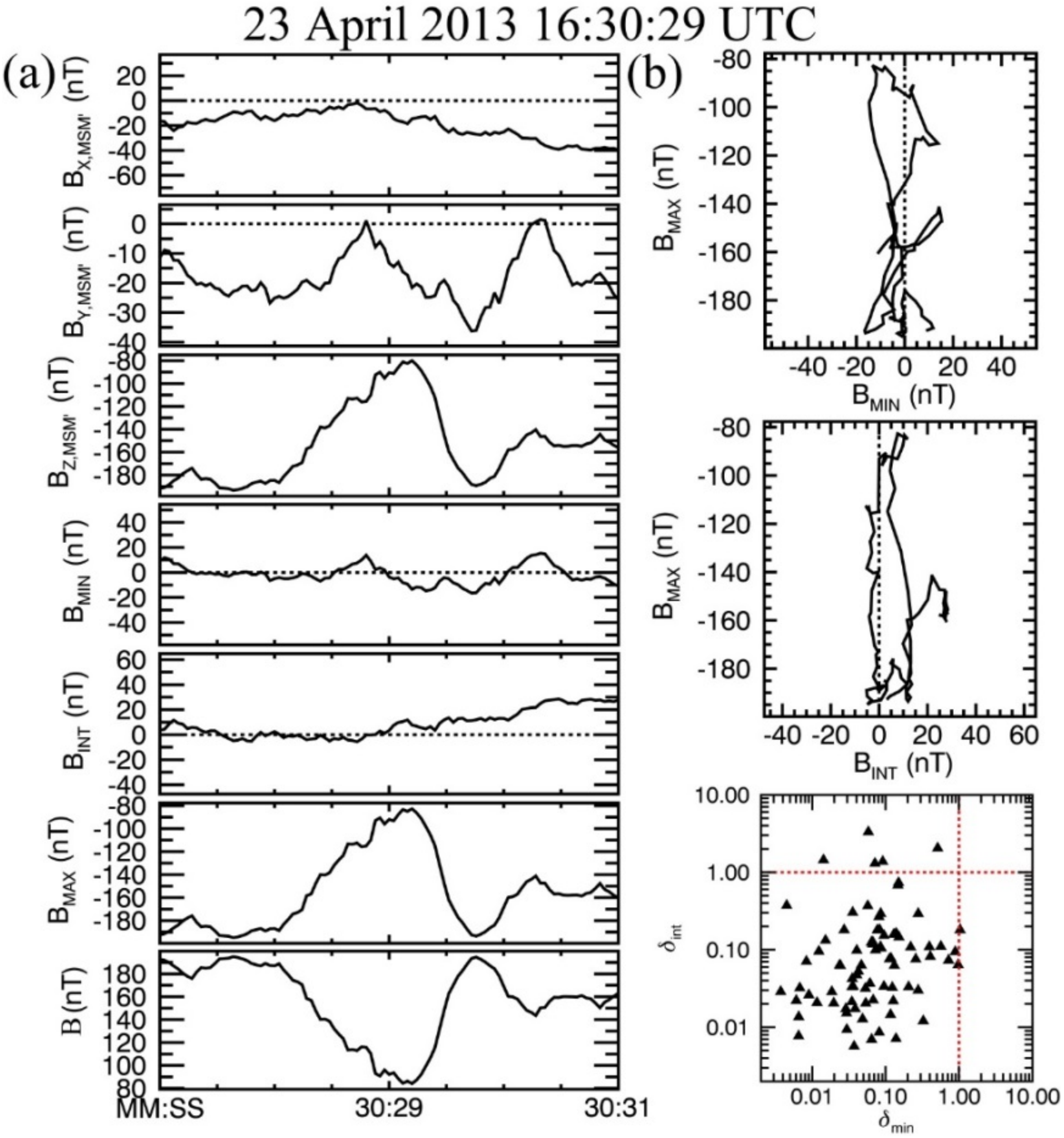

Figure 4.4 Magnetic field variations during a Population I cusp plasma filament observed on 23 April 2013 at approximately 16:30:29 UTC. (a) Panels 1–3 (top to bottom) show the full-resolution magnetic field measurements in aberrated MSM' coordinates, panels 4–6 show the magnetic field measurements in MVA coordinates, and panel 7 shows the total magnetic field. (b) The top and middle panels show the MVA hodograms for the filament in Figure 4.4a. The bottom panel shows δ_{min} versus δ_{int} for all Population I filaments identified in this study. The red lines represent the $\delta_i = 1$ condition.

The example shown in Figure 4.4 has slight average offsets of 0.1 nT and 5.14 nT from 0 nT in the minimum and intermediate directions, respectively. To determine if these offsets are within the errors in the mean of the magnetic field in the direction of the eigenvector, we defined the fraction δ_{i} as

$$\delta_{\mathrm{i}} = \frac{|\Delta\langle \boldsymbol{B}\cdot\boldsymbol{x}_{\mathrm{i}}\rangle|}{|\langle \boldsymbol{B}\cdot\boldsymbol{x}_{\mathrm{i}}\rangle|}\ , i = min, int, \mathrm{max} \tag{4.3}$$

where $|\langle \boldsymbol{B}\cdot\boldsymbol{x}_{\mathrm{i}}\rangle|$ is the average magnetic field along the eigenvector $\boldsymbol{x}_{\mathrm{i}}$ and $|\Delta\langle \boldsymbol{B}\cdot\boldsymbol{x}_{\mathrm{i}}\rangle|$ is given by equation 4.2b. If $\delta_{\mathrm{i}} > 1$, the offset is within the error uncertainty of the average magnetic field whereas $\delta_{\mathrm{i}} < 1$ signifies that the offset is outside the range of the error uncertainty and is likely a real magnetic signature.

A plot of δ_{int} versus δ_{min} for all Population I filament events is shown in the bottom panel of Figure 4.4b, and the red dashed lines in the figure represents $\delta_{\mathrm{i}} = 1$. The majority of the events have both δ_{int} and $\delta_{\mathrm{min}} << 1$, and for only a fraction of events is either δ_{int} or $\delta_{\mathrm{min}} > 1$. Thus for most filaments in this population the offset in the minimum and intermediate direction away from $<B_{\mathrm{min}}> = <B_{\mathrm{int}}> = 0$ is likely to be “real.” Such a deviation from the ideal cylindrical plasma filament model could be the result of a plasma density gradient in the axial direction arising from variability in magnetic reconnection and energy dispersion of the plasma flowing into the cusp region from the magnetopause, as observed at Earth [*Lockwood and Smith*, 1989]. Mercury’s cusp is known to be a region of high variability, both spatially and in the distribution of energies [*Raines et al.*, 2014]. Particles with higher energies than the bulk plasma will flow into the cusp first, followed by the lower-energy particles. Depending on the energy distribution of the accelerated particles from the dayside magnetopause, this difference in timing could result in inhomogeneity in the plasma density along the axis of the filament or sub-structures within the filament. Such an inhomogeneity might create an offset in either or both the minimum and intermediate directions, leading to these filaments departing from a quasi-cylindrical magnetic structure. The 10 s time resolution of FIPS, relative to the 1–2 s duration of these filaments, makes further investigation of this hypothesis difficult.

4.3.2 Population II

For filaments in Population II, the minimum and intermediate eigenvectors are well determined but the maximum eigenvectors are less well defined. A total of 80 filaments (~ 27% of the filament events) were classified as Population II. Figure 4.5 shows a typical example of a filament (on 26 July 2013) that satisfies these eigenvalue ratio conditions. The maximum, intermediate, and minimum eigenvectors for this event are (0.396, -0.105, 0.912), (0.331, -0.910, -0.249) and (-0.856, -0.400, 0.326), and the min/int and max/int eigenvalue ratios are 43.90 and 2.27 respectively. The mean values for B_{min} and B_{int} are 75.66 ± 0.34 nT and 4.91 ± 1.83 nT, respectively.

In a manner similar to the Population I filaments, B_{min} in Figure 4.5 shows little variation, but there is a clear unipolar variation in B_{max} at ~ 17:00:35 UTC. However, there is also a weak bipolar rotation in B_{int}, and the center of this rotation corresponds to the peak in B_{max}. The bipolar rotation in B_{Int} indicates weak magnetic helicity in the flux tube, which we term as “residual twist.” This MVA result is different from that expected for a flux rope, for which B_{max} would show a bipolar signature with a corresponding peak in the intermediate direction because of the presence of a core field [*Elphic and Russell,* 1983; *Xiao et al.,* 2004]. Since the bipolar rotation is in the intermediate direction, this pattern suggests that Population II filaments are weakly helical structures without a core field.

A plot of δ_{int} versus δ_{min} for all Population II filament events is shown in the bottom panel of Figure 4.5b. This plot shows that for this population, too, the majority of the events have a significant offset in the mean magnetic field in the intermediate and minimum directions. However, because of the two-dimensional nature of the structure, this offset could be caused by the spacecraft trajectory across the filament, from which we could determine the impact parameter from the center of the filament by solving the MHD pressure balance equation $J \times B = \nabla P$ if the plasma pressure were known.

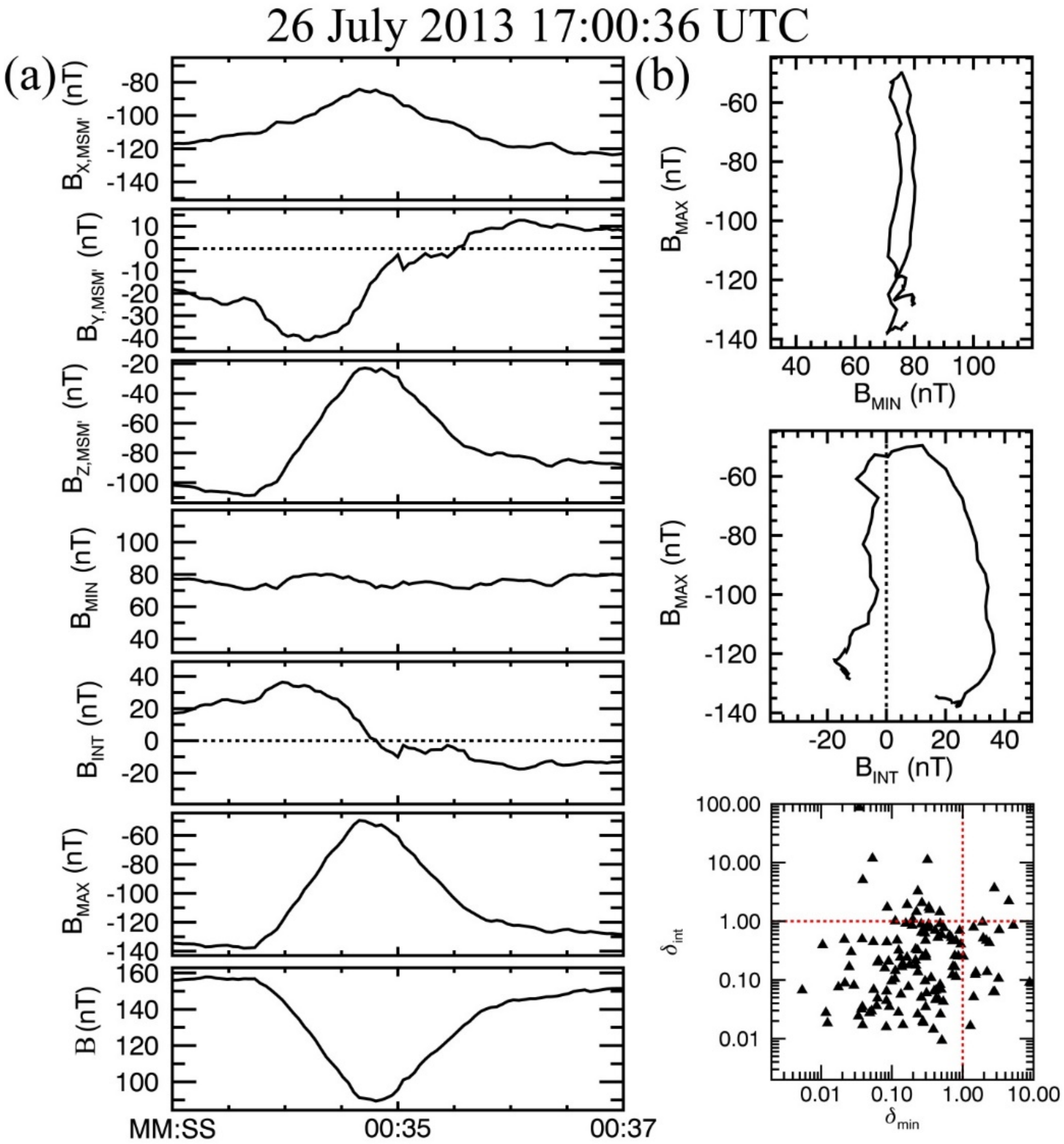

Figure 4.5 Magnetic field variations during a Population II cusp filament observed on 26 July 2013 at approximately 17:00:36 UTC. (a) Magnetic field measurements in aberrated MSM' and MVA coordinates; the format follows that of Figure 4.4a. (b) MVA hodograms for the same time interval as in (a) and a plot of δ_{min} versus δ_{int} for all Population II events.

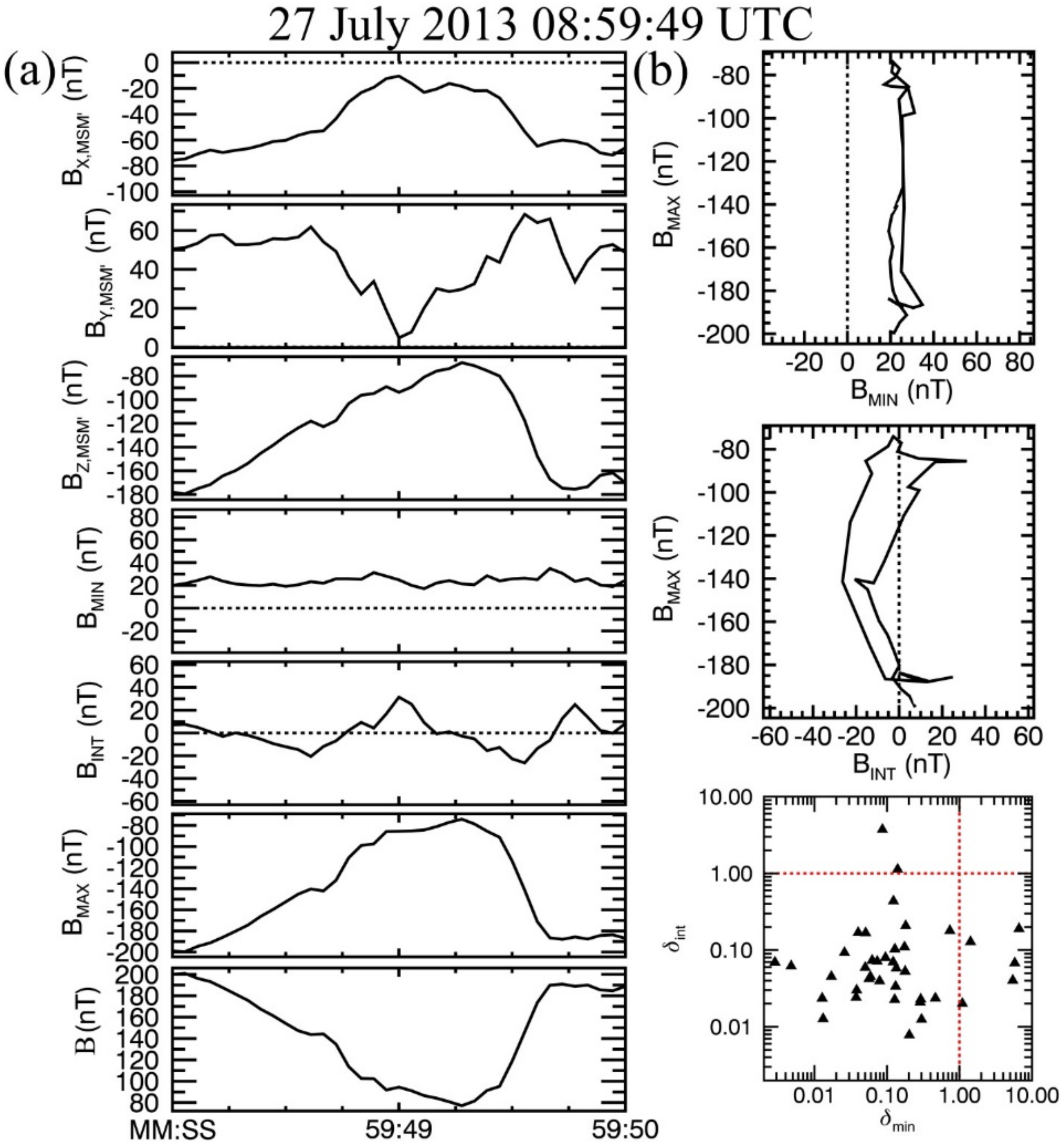

Figure 4.6 Magnetic field variations during a Population III cusp plasma filament observed on 27 July 2013 at approximately 08:59:49 UTC (a) Magnetic field measurements in aberrated MSM' and MVA coordinates; the format follows that of Figure 4.4a. (b) MVA hodograms for the same interval as in (a) and a plot of δ_{min} versus δ_{int} for all Population III events.

4.3.3 Populations III and IV

For Population III and IV filaments, the two eigenvalue ratios are both greater or less than 4, respectively. This means that for the former group the eigenvector basis is well determined, whereas for the latter group it is not. Population III filaments make up 13% of the events identified in this study, and Population IV filaments make up 17%; therefore, each of these groups is less likely to be observed than Populations I or II. Figures 6 and 7 show, respectively, typical examples of Population III (on 27 July 2013) and Population IV (on 23 April 2013) filaments. For the Population III example, the maximum, intermediate, and minimum eigenvectors are (0.500, -0.179, 0.847), (0.407, -0.814, -0.413), and (0.764, 0.552, -0.334), the corresponding min/int and max/int eigenvalue ratios are 12.20 and 11.60, and B_{min} and B_{int} are ~ 23.75 ± 2.05 nT and -0.26 ± 0.970 nT, respectively. For the Population IV example, the maximum, intermediate, and minimum eigenvectors are (-0.374, 0.603, 0.705), (0.418, 0.788, -0.453), and (0.828, -0.125, 0.546), the corresponding min/int and max/int eigenvalue ratios are 2.72 and 2.79, and B_{min} and B_{int} are ~ -108.40 ± 3.58 nT and 24.38 ± 2.22 nT, respectively.

In the examples for these two populations, B_{max} shows unipolar rotation with respect to the minimum direction. However, although B_{int} for the Population III filament in Figure 4.6a shows little variance in the intermediate direction, B_{int} for the Population IV filament in Figure 4.6b shows a weak rotation with respect to the maximum direction. Analysis of the max-int hodograms for Population III (not shown here) indicates that the MVA results for Population III are similar to those for Population I. This result begs the question of why the MVA magnetic field results are reproducible for these two populations of filaments but the qualities of their eigenvector bases are different. Furthermore, the δ_{i} plot in Figure 4.6b shows that the Population III filaments have similar constant offset from near-zero values of $\langle B_{\mathrm{min}} \rangle$ and $\langle B_{\mathrm{int}} \rangle$.

A survey of Population IV filaments shows that there could either be a rotation or no variation in the intermediate direction with respect to the maximum direction. Such an outcome is expected since all the eigenvectors are ill-defined and have high uncertainties. The δ_{i} plot in Figure 4.7b is also consistent with the results for Population I and II filaments in that a majority of the events have a significant offset in either the mean intermediate or minimum field. However, this offset might also be an artifact of the high level of uncertainties in the MVA results for these near-degenerate cases of filament events. Care is thus warranted in any inferences on the magnetic structure of these events from the MVA results.

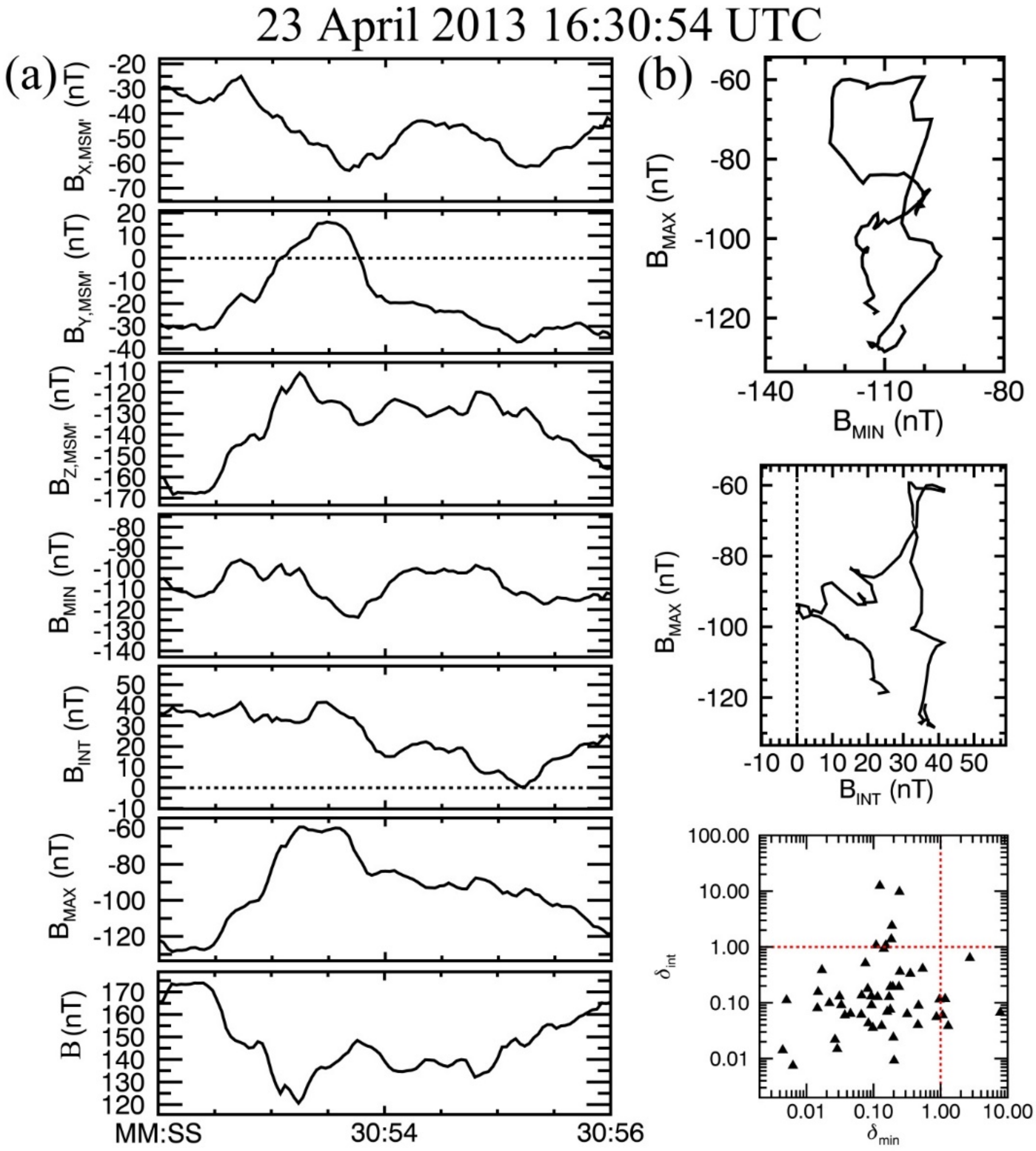

Figure 4.7 Magnetic field variations during a Population IV cusp plasma filament observed on 23 April 2013 at approximately 16:30:54 UTC. (a) Magnetic field measurements in aberrated MSM' and MVA coordinates; the format follows that of Figure 4.4a. (b) MVA hodograms for the same interval as in (a) and a plot of δ_{min} versus δ_{int} for all Population IV events.

4.3.4 Flux Ropes

In addition to the 301 filaments, the search algorithm identified 32 flux ropes in the cusp regions. Flux ropes are helical flux tubes with a strong core field formed as a result of multiple X-line reconnection. When MVA is performed on these events, we expect to see the characteristic rotation of the magnetic field in the int-max hodogram with a reverse in polarity of B_{max} (i.e. bipolar rotation in B_{max}) [*Xiao et al.,* 2004].

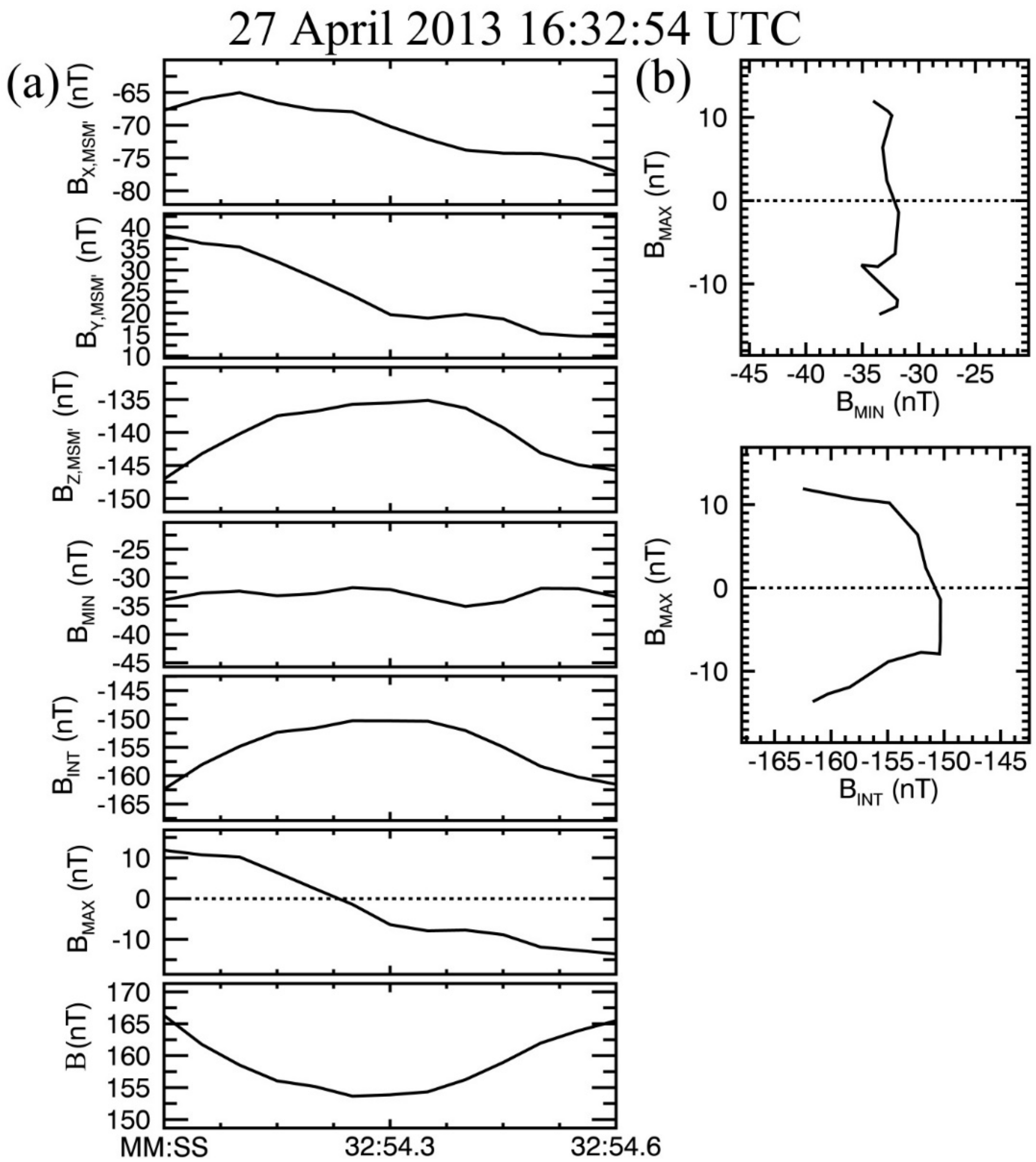

Figure 4.8 Magnetic field variations during a flux rope observed on 27 April 2013 at approximately 16:32:54 UTC. (a) Magnetic field measurements in aberrated MSM' and MVA coordinates; the format follows that of Figure 4.4a. (b) MVA hodograms for the same interval as in (a).

Figure 4.8 shows the MVA results of a flux rope example identified on 27 April 2013. The max-int hodogram (middle panel) shows a distinct bipolar rotation in the maximum variance direction and a peak in the intermediate variance direction. These MVA signatures are indicative of a flux rope with a core field in the direction of intermediate variance. We calculated the maximum, intermediate, and minimum eigenvectors to be (0.397, 0.917, -0.026), (0.262, -0.087, 0.961), and (0.879, -0.389, -0.275), and the max/int and int/min eigenvalue ratios to be ~ 4.5 and 18.9, respectively, which indicates that the eigenvectors are well determined. Since the calculated intermediate eigenvector is predominantly in the *Z*-direction, the axis of the flux rope is field-aligned and occurrences of these flux ropes are likely related to the filaments. This finding has important implications for the formation mechanism for cusp filaments, a topic that will be discussed further below.

3.3.5 FIPS Plasma Measurements

Because the duration of each filament, ~ 1–2 s, is less than the ~ 10 s energy scan time for FIPS measurements, we are unable to measure the plasma properties for individual filaments. However, we performed a superposed epoch analysis, which utilizes the portion of the energy spectrum and pitch angle distribution sampled for each filament and adds them together to build the energy-resolved pitch angle distribution of a typical filament. A total of 16 high-altitude filaments were selected for their phasing relative to the start time of a FIPS energy scan, with a ~ 1 s uncertainty in that start time. Figure 4.9a shows the field-of-view-normalized aggregate energy-resolved pitch angle distribution for the 16 selected filaments, with color representing phase space density (PSD). Note that each pitch angle bin in Figure 4.9a is sampled by at least one of the 16 filament events selected for this analysis; the white color bins in the energy-resolved pitch angle distribution are energy and pitch angles sampled for which FIPS saw no counts in any of 16 filaments. There is an enhancement in the PSD in the energy range ~ 0.4–1 keV and the pitch angle range ~ 0–90°. Additional analysis indicates that most of the filaments have similar-looking pitch angle distributions, as shown in Figure 4.9b of PSD versus pitch angle for 11 filament events observed in the energy range 0.5–1 keV. Figure 4.9b shows evidence of systematic pitch angle isotropy for energy between 0.5 and 1 keV. This result is in agreement with the proton-reflectometry work of *Winslow et al.* [2014], who observed a near-isotropic proton count between 0° and 90° pitch angle at high latitudes in the cusp. This outcome is consistent with our understanding of filaments filled with plasma of magnetosheath-like energies and pitch-angle-independent flow. This result also supports our idea of filaments as diamagnetic effects of precipitating magnetosheath particles in the cusp region with a non-zero perpendicular fluid velocity.

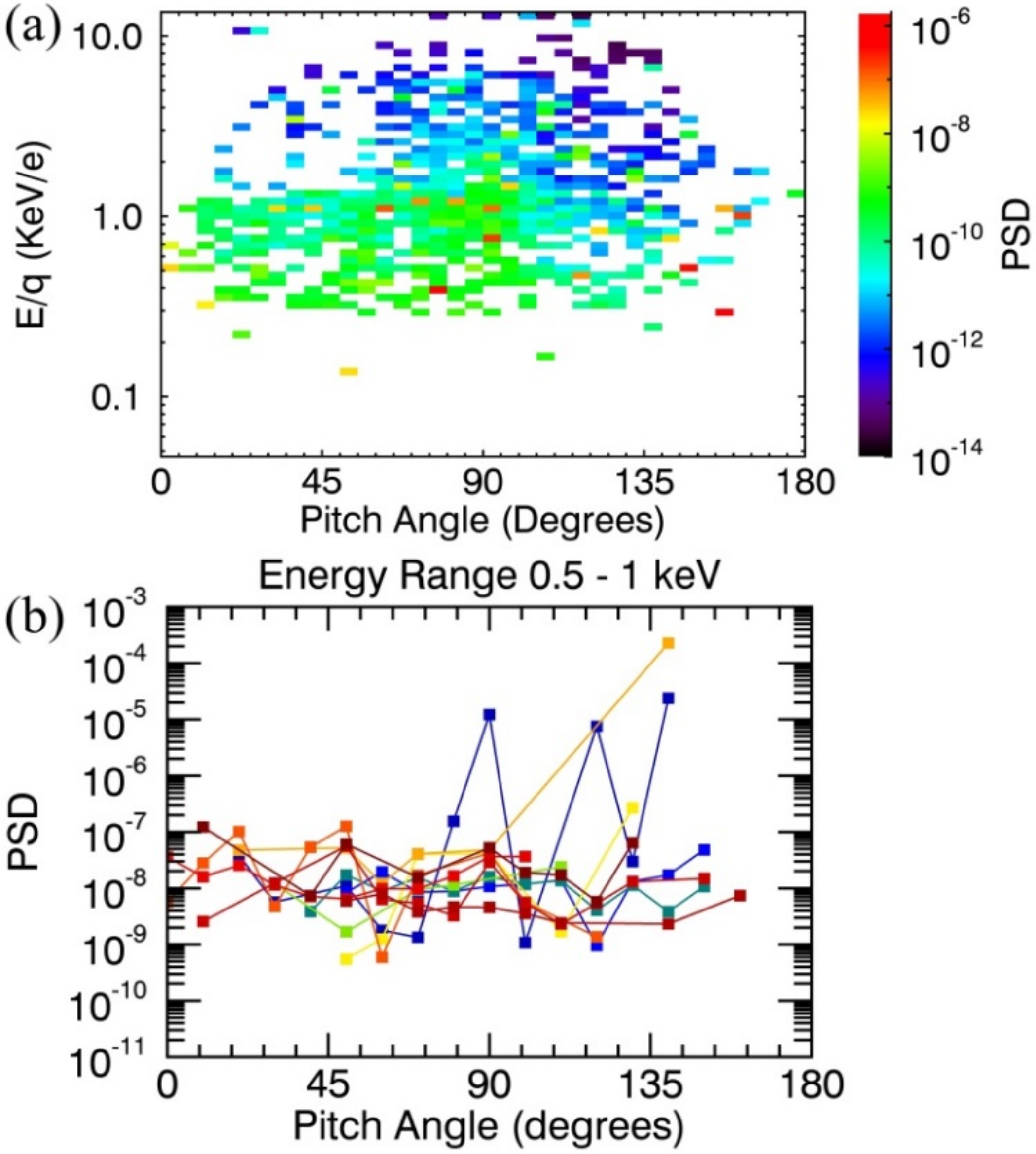

Figure 4.9 (a) Energy-resolved pitch angle distribution of 16 filaments. The filaments were selected to ensure coverage of the entire FIPS energy range and look angle. Each pixel represents a pitch angle bin size of 5°; phase space density (PSD) is represented by color. (b) Plot of PSD versus pitch angle for 11 filaments observed in the energy range 0.5–1 keV. Each filament event is represented by a different color.

4.4 Analysis Results for Low-altitude Filaments

From August to October 2014, MESSENGER completed the first phase of a low-altitude campaign during which the spacecraft's periapsis was less than 100 km above Mercury's surface. The magnetic field measurements during this interval provide us with the opportunity to determine if cusp filaments are found near the surface. During these 3 months, MESSENGER was in its "warm season" orbital configuration during which the trajectory was near the noon-midnight meridian but periapsis occurred on Mercury's nightside. We identified 18 low-altitude cusp observations with filament activity.

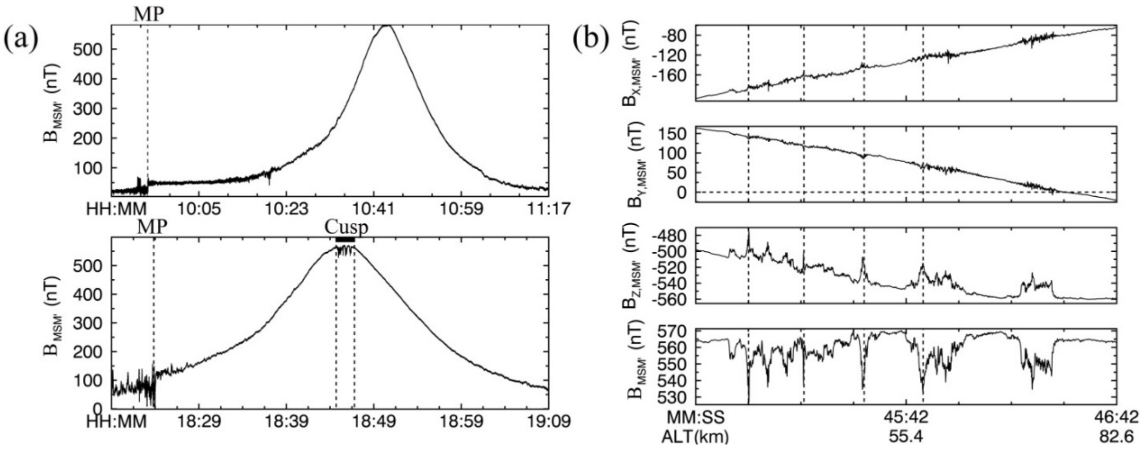

Figure 4.10 (a) Magnetic field measurements in aberrated MSM' coordinates during two successive orbits on 31 August 2014. (Top) A cusp crossing with no filaments detected. The aberration angle is -5.79°, and the vertical dashed line represents the magnetopause crossing. (Bottom) A cusp crossing 8 h later during which filaments were detected. Two vertical dashed lines delimit the cusp region. (b) Close up of magnetic field measurements within the cusp for the orbit in the bottom panel of (a). Each cusp filament identified by the automated algorithm is marked by a vertical dashed line.

As an example, Figure 4.10 shows two consecutive cusp crossings on 31 August 2014 in MSM' coordinates. The first orbit showed no filament activity in the cusp region, but filaments were observed in the cusp during the second orbit (Figure 4.10a). For both orbits, the magnetic field strength increased as the spacecraft flew deeper into the magnetosphere. Because of the low-altitude periapsis, the peak in *B* was ~ 575 nT compared with the typical value of ~ 300 nT seen during orbits with high-altitude periapses. Under "quiet" conditions when no filaments were observed in the cusp (top panel of Figure 4.10a), the field strength at lower altitudes was so strong that low-energy ions would have magnetically mirrored at higher altitudes, so the diamagnetic effect of gyrating ions was not observed. In contrast, during "active" conditions (bottom panel of Figure 4.10a), MESSENGER observed filaments near closest approach. Figure 4.10b shows a close-up of magnetic field measurements around closest approach. For each filament identified by the algorithm, every decrease in B corresponds to a decrease in the magnitude of B_Z with little variation in B_X or B_Y. Observations of structures with similar magnetic signature as the high-altitude filaments support our idea that we are indeed observing cusp filaments at altitudes as low as 50 km, and most likely the filaments deliver plasma directly to the surface.

As with the analysis of high-altitude cusp crossings, for each low-altitude cusp crossing, we employed the scale-free algorithm to identify cusp filaments. A total of 45 filaments were identified among the 18 low-altitude cusp crossings by the algorithm after applying a threshold value of $\delta B/B = 0.01$ to filter out false positives. We elected to use a lower threshold value for $\delta B/B$ for low-altitude crossings because the spacecraft was deeper into the cusp region where the diamagnetic effects of ions in the filaments are weaker as a result of the stronger background field and more particles are magnetically mirrored in the deep cusp region. A lower threshold value for low-altitude filaments accounts for this spatial variability. MVA was performed on all filament events, and each event was classified into the populations described in section 3. 27% of the low-altitude filaments were classified as Population I, 40% as Population II, and 33% as Population III filaments. No Population IV filaments, for which the eigenvalues ratios are less than 4, were observed at low altitudes. This last result is not unexpected since the planetary field strength is stronger and filaments with poorly defined magnetic variance directions are less likely to occur at low altitudes.

An example of a Population III filament identified on 15 August 2014 during the low-altitude campaign is shown in Figure 4.11. For this event, the maximum, intermediate, and minimum eigenvectors are (0.299,0.289,0.910), (-0.156,-0.974,0.161), and (-0.873,-0.303,0.383), and the corresponding eigenvalues are 36.41, 1.76, and 0.13, respectively. As with the high-altitude filaments, B_{min} and B_{int} show little or no variation relative to the variation in B_{max}, and the maximum eigenvalue is predominantly in the Z-direction with the peak in B_{max} corresponding to the maximum dip in B (Figure 4.11a). The bottom panel of Figure 4.11b shows an error analysis plot for all low-altitude Population III filaments similar to those for the high-altitude filaments. All except one of the low-altitude Population III filaments have significant offsets from 0 in $\langle B_{\mathrm{min}} \rangle$ and $\langle B_{\mathrm{int}} \rangle$. This result is

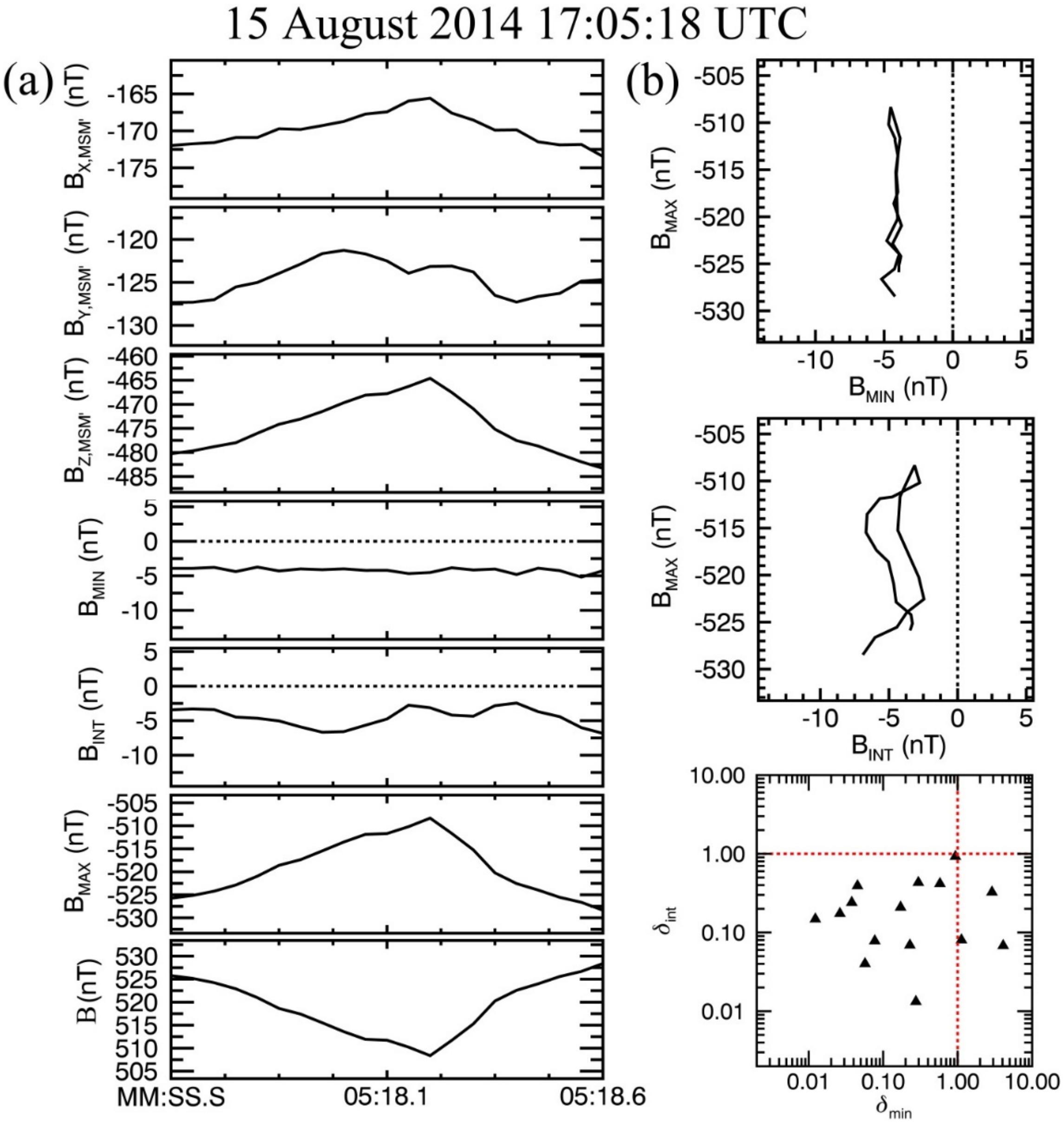

Figure 4.11 Magnetic field variations during a low-altitude Population III cusp plasma filament observed on 15 August 2014 at approximately 17:05:18 UTC. (a) Magnetic field measurements in aberrated MSM’ and MVA coordinates; the format follows that of Figure 4.4a. (b) MVA hodograms for the same interval as in (a) and a plot of δ_{min} versus δ_{int} for all low-altitude Population III events.

again consistent with that for the high-altitude filaments and suggests inhomogeneity in the plasma density distributions at the sites of the low-altitude filaments. The low-altitude filaments in other population groups show MVA results that are similar to those for their high-altitude counterparts, reinforcing the idea that we were observing the same phenomenology at low altitudes. For these energetic ions to be observed deep in the cusp regions, they must have sufficient energy parallel to the local magnetic field to overcome the mirroring effect of the converging field lines deep in the cusp. Observations of filaments at such low altitudes suggest that the energetic ions inside each low-altitude filament have a high probability of precipitating onto Mercury's surface.

We also identified six flux ropes in the low-altitude cusp passes. Not shown here, the hodograms of the low-altitude flux ropes show MVA signatures consistent with the high-altitude flux ropes, with the intermediate eigenvector, corresponding to the central axis of the flux rope, having a large *Z*-component. The high percentage occurrence of Population II filaments and flux ropes at low altitudes suggests that most of these filaments still possess "residual twist" with or without a core field. This finding challenges our understanding of near-surface magnetic field topology in the cusp region, where the magnetic field vector is expected to be predominantly normal to the surface, particularly at Mercury where the conducting core occupies most of the planet's volume [*Smith et al.,* 2012] and the normal component of the magnetic field has to be continuous across the boundary between the core and the mantle.

4.5 Physical Properties and Spatial Distribution

For the high- and low-altitude filaments identified, histograms of the parameters δB, $\delta B/B$, and *dt*, defined by the scale-free algorithm, are displayed in Figure 4.12a–f. The high-altitude filaments have a mean δB of ~ 56 nT and a mean *dt* of 3 s, whereas the low-altitude filaments have a mean δB of ~ 20 nT and a mean *dt* of 2 s. Plasma diamagnetism locally reduces the field intensity inside a filament by an average of ~ 22% (Figure 4.12c) and 4% (Figure 4.12d) for high- and low-altitude observations, respectively. We emphasize that a 4% decrease in field intensity at 50 km above the planet's surface, where background field fluctuations should be minimal, shows the intensity of the magnetospheric dynamics at Mercury's northern cusp.

As discussed above, we cannot accurately determine the plasma properties of these several-second-long cusp filaments with FIPS, because of the 10 s cycle time for the instrument. Without plasma measurements, we cannot determine the plasma velocity and hence the size of each filament. However, we can estimate the size of each filament with a simple convection speed model. Under the assumption of conservation of magnetic flux at the polar caps, we can derive an equation for the magnetospheric convection speed at which each filament is drifting across the cusp:

$$v_{\text{filament}} = \frac{\varphi}{L_0\left(\frac{r}{r_0}\right)^{\frac{3}{2}}B} \tag{4.4}$$

where r_0 is a reference distance from the center of the dipole magnetic field, L_0 is the diameter of the polar cap at $r = r_0$, φ is the cross polar cap electric potential, and B is the background magnetic field magnitude. The quantities r_0, L_0, and φ are calculated to be ~ 1.3 R_M, 2 R_M [*Jia et al.*, 2015] and 30 kV [*Slavin et al.*, 2009]. This model yields a mean filament velocity of ~ 36 km/s with distribution from ~ 25 to 55 km/s. The estimated velocity is consistent with the convection velocity observed in MHD simulations [*Jia et al.*, 2015]. The observed spatial size of the filaments can be determined by multiplying the velocity for each filament by its corresponding time duration under the assumption that the spacecraft velocity is much smaller than the filament velocity. This assumption is a good one, as the spacecraft velocity across the cusp at apoapsis is typically less than 1–2 km/s (~ 0.03% of the mean filament velocity). The statistical results for low- and high-altitude filaments are shown in Figure 4.12e and 3.12f normalized to the gyro-radius of a 1 keV proton r_L calculated from the local background magnetic field. The mean gyro-radii for high and low-altitude filaments are ~ 12 km and 6 km, respectively. Figure 4.12e and 3.12f show that the high-altitude filaments have a mean size of ~ 8.5 $r_L$with a maximum of ~35 r_L, whereas the low-altitude filaments have a somewhat smaller mean size of ~7.1 $r_L$with a maximum of ~30 r_L. This outcome is consistent with the canonical view that magnetic field lines converge closer to the surface in the cusp region. We also note that this approximation provides only a lower limit on the size of the filaments since we are unable to characterize the impact parameter. Even though this model is a simple one, it nonetheless provides a useful estimate for filament size.

We also calculated the magnetic flux Φ within each filament. Without knowledge of the impact parameter and cross-sectional shape of the filament, we assumed a circular cross-section and that MESSENGER traversed the center of the filament. We then multiplied the mean magnetic field inside each filament by the area of a circle of diameter

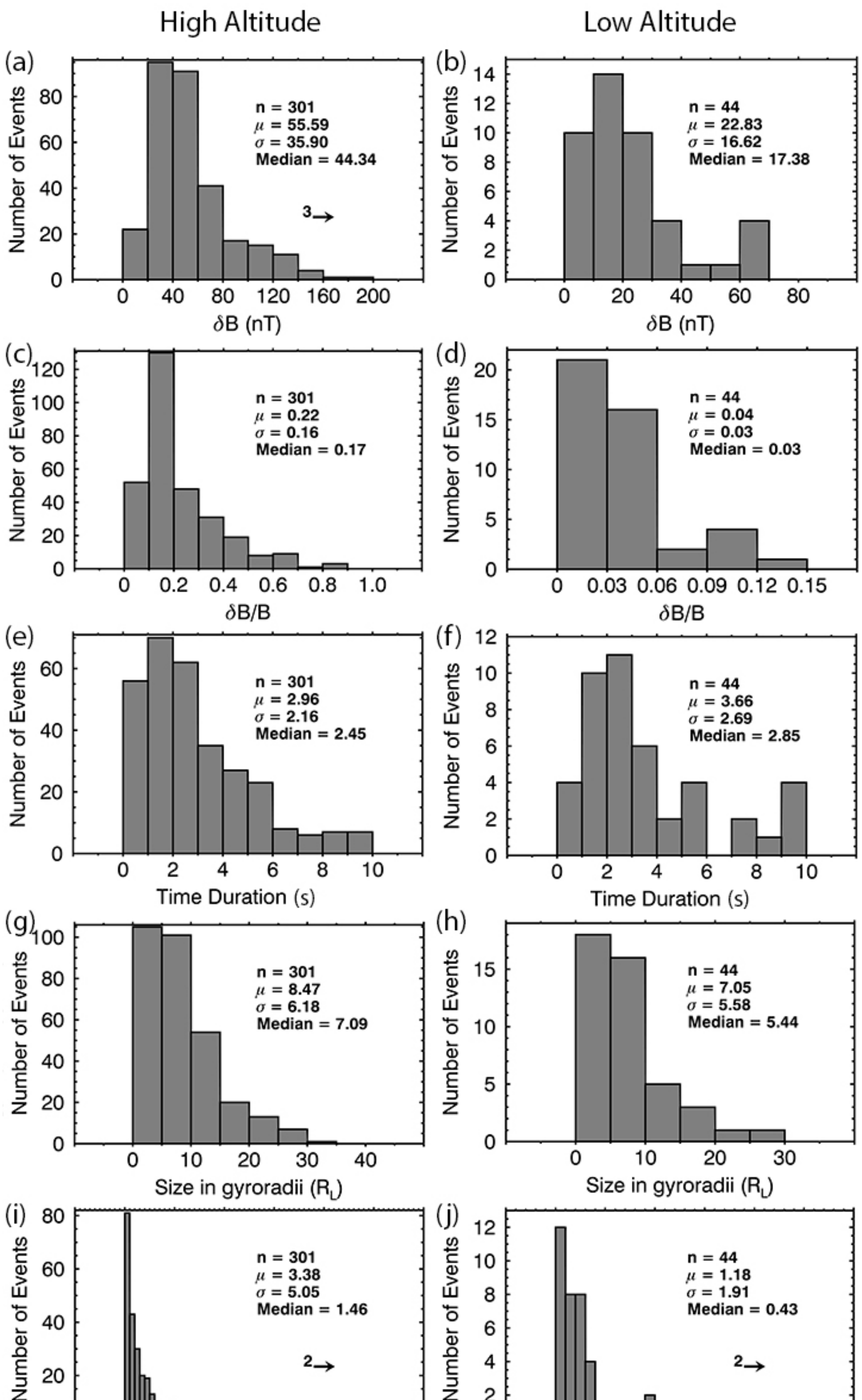

Figure 4.12 Histograms of the filament parameters (a,b) *δB*, (c,d) *δB/B*, (e,f) time duration, (g,h) size in proton gyroradii r_L, and (i,j) magnetic flux. Left and right columns show results for high- and low-altitude filaments, respectively.

equal to the size of the filament to estimate the total magnetic flux. Figure 4.12g and 4.12h show histograms of the magnetic flux for the high- and low-altitude filaments, respectively. The high-altitude filaments have a mean flux of ~3.4 kWb, and the low-altitude filaments have a mean flux of ~1.2 kWb. Both histograms also show that the number of filaments identified decays approximately exponentially with respect to magnetic flux. The assumptions that go into our calculation of the magnetic flux impart a large uncertainty to the flux values. Similar to our calculation of the filament size, this method provides only a lower limit on the magnetic flux inside the filaments.

To test the sensitivity of our statistical results in Figure 4.12 with respect to the threshold $\delta B/B$ value, we increased the threshold $\delta B/B$ value for the high-altitude filaments to 0.1 and calculated the new mean values for the time duration, filament size, and magnetic flux to be ~ 3.03 s, 8.67 R_L and 3.57 kWb, respectively. Comparing with the means of the distributions in Figure 4.12, the new mean values for the time duration, filament size, and magnetic flux are larger by ~ 0.07 s, 0.2 R_L and 0.19 kWb, respectively. Since the fractional error in the means for the distributions in Figure 4.12 is ~0.1–0.4, the increase in the mean is, to first order, insensitive to the changes in the threshold $\delta B/B$ value. This result provides further justification for our choice of the threshold $\delta B/B$ values.

Given pressure balance between the total pressure inside a filament and the ambient magnetic pressure, the thermal pressure perpendicular to magnetic field lines inside the filament $P_{th,\perp}$ is given by the equation:

$$P_{\mathrm{th},\perp} = \frac{1}{2\mu_0}\left(2B_0\delta B - \delta B^2\right) \tag{4.5}$$

where B_0 is the ambient magnetic field intensity. For each filament, we calculated $P_{th,\perp}$ from the highest magnetic field intensity before or after the diamagnetic decrease in B as a proxy for B_0 and δB from Figures 4.12a and 4.12b. $P_{th,\perp}$ is a good indicator of the strength of a filament (i.e., the amount of plasma within each filament) since it is linearly proportional to the density and perpendicular temperature of the plasma in the filament. Sampling at different altitudes gives us a “three-dimensional” view of the longitudinal and latitudinal variation of the cusp filaments.

The distribution of perpendicular thermal pressure $P_{th,\perp}$ with filament location is illustrated in Figure 4.13a. The locations of filaments identified in this study shown in Figure 4.13a are in the aberrated cylindrical coordinates X' and $\rho = [Y'^2 + Z'^2]^{0.5}$. The color plot shows the mean $P_{th,\perp}$ for each position binned every 0.01 $R_M \times 0.01$ R_M with values represented by the color bar displayed. The black dashed lines represent the magnetic latitudinal extent of all filaments identified in this study, a range that agrees well with the latitudinal boundaries of the northern cusp calculated by *Winslow et al.* [2012]. The latitudinal extent of the filaments also decreases with decreasing altitude. This "funneling shape" in the occurrence of cusp filaments is consistent with the downward convergence of magnetic field lines in the cusp.

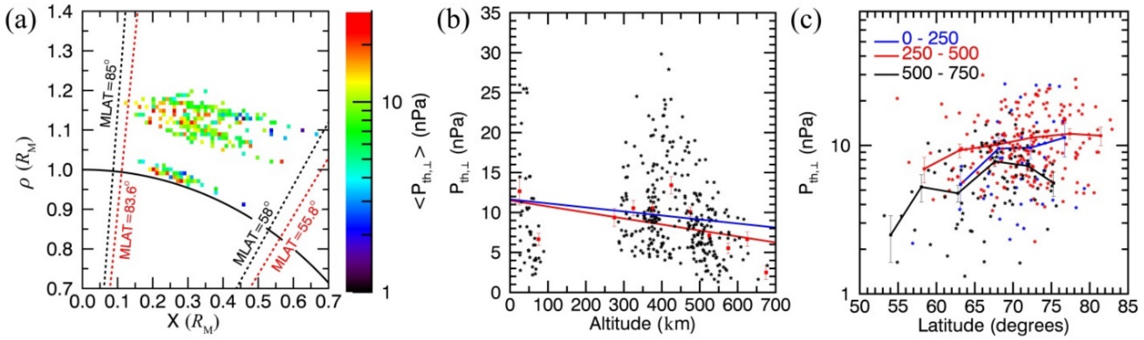

Figure 4.13 (a) Locations of cusp plasma filaments identified in this study, binned in 0.01-R_M- wide bins in the cylindrical coordinates ρ and X and color coded by perpendicular thermal pressure $P_{th,\perp}$. The black and red dashed lines show the extent in magnetic latitude (MLAT) of filament observations and the mean cusp boundaries of *Winslow et al.* [2012], respectively. (b) Plot of perpendicular thermal pressure versus altitude. Red squares represent mean values of $P_{th,\perp}$ averaged in 50-km-wide altitude bins, and the error bars show the standard errors for each "binned" value of $P_{th,\perp}$. The blue and red lines represent linear fits to the "un-binned" and "binned" data, respectively. The corresponding correlation coefficient (r) is -0.14 and -0.55, respectively. (c) Plot of perpendicular thermal pressure versus magnetic latitude at three different ranges of altitude, 0–250 (blue), 250–500 (red), and 500–750 (black) km. Each square represents mean $P_{th,\perp}$ values averaged over 5°-wide latitude bins, and the error bars show the standard errors.

To explore the variation of $P_{th,\perp}$ with altitude, we averaged the data points over bins of 50 km width (Figure 4.13b). There is a data gap between 150 km to 250 km altitude because MESSENGER did not sample the cusp at those altitudes on the orbits selected for this study. We then fit a least squares linear relation to the binned data points and calculated the linear correlation coefficient to be ~ -0.55. The poor linear correlation suggests that $P_{th,\perp}$ does not vary linearly with altitude, although the fact that altitudes within the cusp are not equally sampled by our selected orbits may have contributed. To investigate further this nonlinear dependence of $P_{\mathrm{th},\perp}$ with altitude, we calculated the invariant latitude of each $P_{\mathrm{th},\perp}$ measurement using a simple dipole field, which is a good approximation for altitudes less than 700 km. We then binned the data points into 5°-wide bins of invariant latitude bins between 55° and 80°. Not shown here, the results show that the correlation between $P_{\mathrm{th},\perp}$ and altitude remains poor. This result suggests that the nonlinear dependence of $P_{\mathrm{th},\perp}$ with invariant altitude is not statistical. If the straight line is nonetheless extrapolated to the surface, the average perpendicular thermal pressure of the surface filaments would be ~ 11.5 nPa.

To explore the variation of $P_{\mathrm{th},\perp}$ with magnetic latitude, we divided the points into three altitude ranges; 0–250, 250–500, and 500–750 km (Figure 4.13c). We then binned the points in 5°-wide latitudinal bins and determined the mean $P_{\mathrm{th},\perp}$ value and its standard error for each bin. Figure 4.13c shows that the perpendicular thermal pressure increases nonlinearly with latitude at all altitudes. Since $P_{\mathrm{th},\perp}$ is proportional to the plasma density within filaments, the plasma density also increases with latitude, which suggests temporal growth in diamagnetism within the filaments if we take latitudinal variations as proxies for temporal evolution and assume that temperature is constant with latitude. This result is consistent with the energy dispersion of ions injected into the cusp. The more energetic ions with higher velocities parallel to the background magnetic field will be injected into the polar region first. These "faster" ions, with lower perpendicular energy and higher parallel energy, have a weaker diamagnetic effect on the background field than their "slower" counterparts. Ions with smaller velocities are injected at a later time, which also corresponds to higher latitude as the flux tube convects poleward.

The variation of $P_{\mathrm{th},\perp}$ in the aberrated X-Y plane, and effectively in MLT, is shown in Figure 4.14, separately at altitude ranges of 0–250, 250–500, and 500–750 km and for all altitudes. The dashed concentric circles represent magnetic latitude (MLAT) at 10° intervals from 55° to 85°, and the solid radial lines represent MLT at steps of 1 h local time (LT) from 06:00 to 18:00. The color plot also shows the mean $P_{\mathrm{th},\perp}$ for each position binned at $0.01\ R_M \times 0.01\ R_M$ with values represented by the color bar displayed. Just as Figure 4.13 showed that the latitudinal extent of observed filaments increases with altitude, with the third-dimension view shown in Figure 4.14, we also see distinct local-time dependence for the strength of the filaments. This dependence is not an aberration effect, since we have already corrected the filament positions with the aberration angle for each orbit. Figure 4.14a clearly shows that events with larger amplitude are mostly observed at the dawn side of the magnetosphere at altitudes below 250 km. We note, however, that there are few observations on the dusk side of the magnetosphere at these low altitudes. At higher altitudes (i.e., 250–500 km), the dependence of amplitude on amplitude is still evident and remains a distinctive feature in Figure 4.14b, exhibited by the larger number of red points on the dawn side. At 500–750 km, the dependence of amplitude on local time is weaker. This pattern is partly the result of a lack of observations near the dawn side of the magnetopause at 500–750 km altitude. However, this result suggests that there might be a general relation between local time and $P_{\mathrm{th},\perp}$.

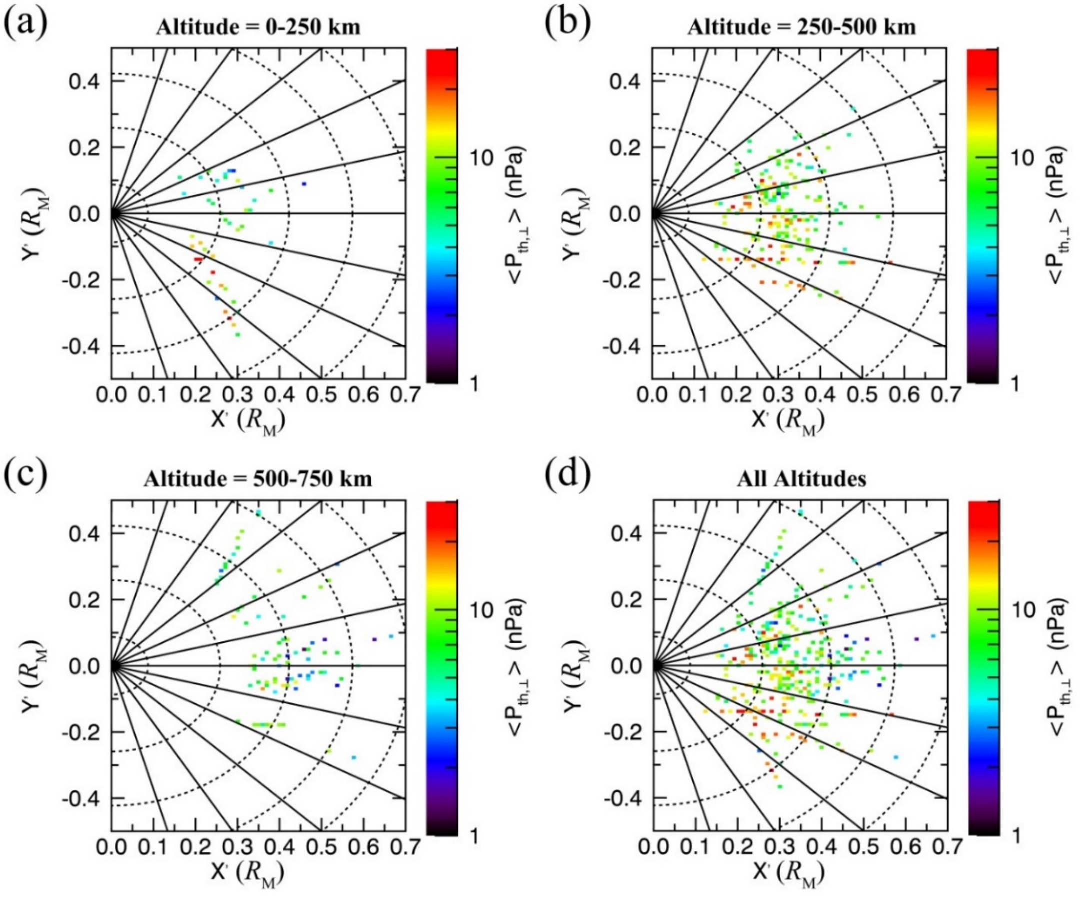

Figure 4.14 (a-c) Binned plot of $P_{\mathrm{th},\perp}$ in the aberrated X'-Y' plane for different altitudes ranges: (a) 0–250 km altitude; (b) 250–500 km altitude; (c) 500–750 km altitude; (d) all altitudes. Colors denotes mean $P_{\mathrm{th},\perp}$ values in 0.01 $R_M \times 0.01\ R_M$ bins. Dashed concentric circles depict magnetic latitude from 45° to 85°N at 10° intervals. Radial solid lines depict magnetic local time at 1 h intervals.

To further explore this idea, we plotted the normalized distribution of filament occurrences by MLT and $P_{\mathrm{th},\perp}$ in Figure 4.15. The distributions indicate that filaments have a high probability to occur near local noon and at $P_{\mathrm{th},\perp}$ values of ~ 6–9 nPa with significant occurrence rates at higher values of $P_{\mathrm{th},\perp}$. To remove orbital selection bias, we also took into consideration the total spacecraft dwell time for each 0.5 h bin in MLT. Figure 4.15c, which shows the distribution of total dwell time, indicates that MESSENGER did spend much of the time around local noon for our selected orbits. The quasi-Gaussian distribution is also consistent with our understanding of the elliptically shaped cusp and the expectation that the spacecraft spent less time in the cusp near dawn and dusk. Figure 4.15d shows the rate of occurrence by MLT normalized by dwell time of the spacecraft at that MLT (i.e., total time duration of filaments divided by the total dwell time for each MLT window), which indicates that there is an equal rate of occurrence (~0.08) of filaments between MLT 9.5 and 14.5 h. The lower and higher occurrence rates from 8.5 to 9.5 h MLT and 14.5 to 15.5 h MLT, respectively, are statistical effects from the normalization by dwell times less than 5 min. Hence, we do not consider these two MLT ranges further in our analysis. Figure 4.15e shows the dwell-time-normalized rate of occurrence by MLT for different $P_{\mathrm{th},\perp}$ ranges. For filaments with $P_{\mathrm{th},\perp}$ between 6 and 12 nPa, the rate of occurrence fluctuates around 0.04, and there is no clear dependence of $P_{\mathrm{th},\perp}$ on MLT. However, there is a higher rate of occurrence for stronger filaments (i.e., 12–18 nPa) near dawn than dusk. This dawn-dusk asymmetry in filament occurrence is also observed for a $P_{\mathrm{th},\perp}$ range of 18–24 nPa (grey line) but is weaker as $P_{\mathrm{th},\perp}$ increases further. Future studies of the dependence of filament occurrence on MLT and $P_{\mathrm{th},\perp}$ should extend the range of local times and increase the number of filaments observed for each local time to reduce the statistical errors from limited sampling.

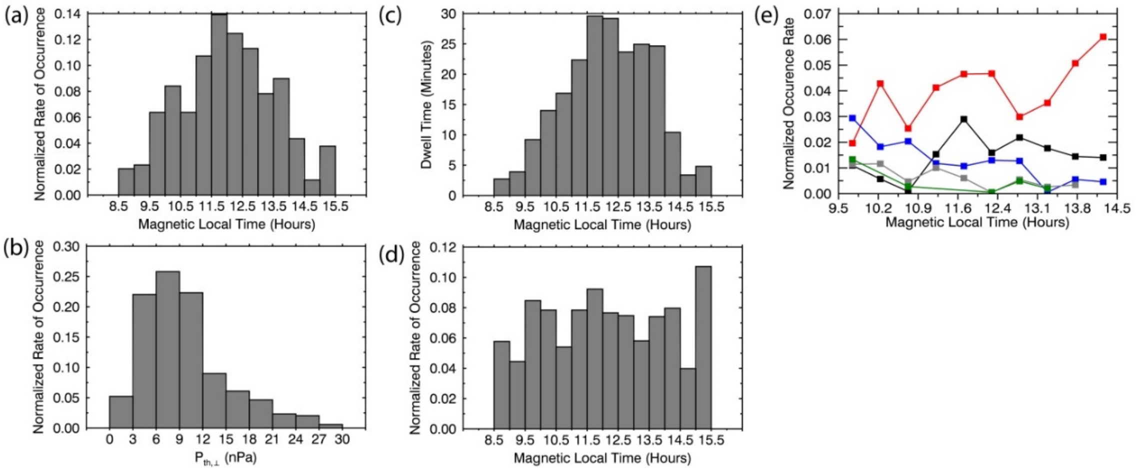

Figure 4.15 (a) Normalized rate of occurrence of filaments as a function of magnetic local time and (b) perpendicular thermal pressure $P_{\mathrm{th},\perp}$. (c) Histogram of MESSENGER dwell time as a function of magnetic local time. (d) Dwell-time-normalized rate of occurrence of filaments as a function of magnetic local time and (e) as a function of magnetic local time at different $P_{\mathrm{th},\perp}$ ranges. The $P_{\mathrm{th},\perp}$ ranges are 0–6 nPa (black), 6–12 nPa (red), 12–18 nPa (blue), 18–24 nPa (grey), and 24–30 nPa (green).

4.6 Discussion

MESSENGER observations of cusp filaments during 3 years of high-altitude and, later, 3 months of low-altitude observations were examined with minimum variance analysis and statistical methods. The analyses presented here strongly suggest that cusp filaments are diamagnetic in nature. Hot plasma ions with energies similar to those of magnetosheath ions [*Gershman et al.,* 2013] gyrate around the magnetic field lines to create a net diamagnetic current. This current then produces a magnetic field that opposes the background field, decreasing the total field magnitude, forming a diamagnetic filament. Statistical analysis at different altitudes shows that these ~2–3-s-long filamentary structures are highly localized with a mean size of 7–8 magnetosheath proton gyro-radii.

Our MVA results show that the high- and low-altitude filaments can be divided into four populations. The magnetic signatures and MVA results of Population I filaments are consistent with the basic picture of a quasi-cylindrical flux tube, i.e., a filament that is filled with hot ions having peak energy of ~1 keV. Population II filaments show the presence of “residual twist” to their magnetic structure. The implication of the “residual twist” structure for Population II filaments is discussed below. Population III filaments have MVA signatures similar to those of Population I filaments with a nearly constant magnetic field component in the intermediate direction, whereas Population IV filaments have MVA signatures that are poorly defined.

The total particle precipitation rate onto Mercury's surface from cusp plasma filament may be determined from our analysis of low-altitude filaments. The distribution of MESSENGER's dwell time with magnetic latitude and magnetic local time for the time period of this study is shown in Figure 4.16a. The figure shows that MESSENGER spent more time in the dawn-dusk sector than the noon sector during the orbits analyzed in this study. The spacecraft also spent ~10 h less time at higher latitudes than lower latitudes. The distribution of identified filaments is shown in the same projection in Figure 4.16b. The figure shows that majority of the filaments were observed near local noon and near ~70° in magnetic latitude. Another interesting feature of this figure is that filaments were seen at lower latitudes near local noon. This observation has implications for the formation and evolution of filaments, a point on which we elaborate below.

By extrapolating from the best-fit linear relation between $P_{\mathrm{th},\perp}$ and altitude determined in Figure 4.12b and under the assumption $P_{\mathrm{surface}} \sim P_{\mathrm{th},\perp}$, we can estimate a lower limit on the proton precipitation flux onto Mercury's surface with each plasma filament:

$$\Phi = \frac{P_{\mathrm{surface}}}{\sqrt{2\pi m k_{\mathrm{B}} T}} \tag{4.6}$$

where k_{B} is the Boltzmann constant, and m and T are the mass and temperature of a proton, respectively [e.g., *Winslow et al.*, 2012]. The average number of ions $\langle N \rangle$ precipitating onto Mercury's surface for each pixel in Figure 4.16 is then given by the relation $\langle N \rangle = \langle \Phi \pi \left(\frac{d}{2}\right)^2 \rangle$, where d is the diameter of a cylindrical filament estimated earlier. Figure 4.16c shows the distribution of the mean particle precipitation rate $\langle N \rangle$. The figure shows that the region with the highest filament occurrence has an approximately uniform mean precipitation rate, and filaments with the highest precipitation rate occur at lower latitudes. This result suggests that magnetic field lines that map to lower latitudes were reconnected as magnetic reconnection (i.e., magnetic erosion) at the dayside magnetopause intensified and the cusp boundary "migrated" to lower latitudes as a result of magnetic flux transfer into the tail.

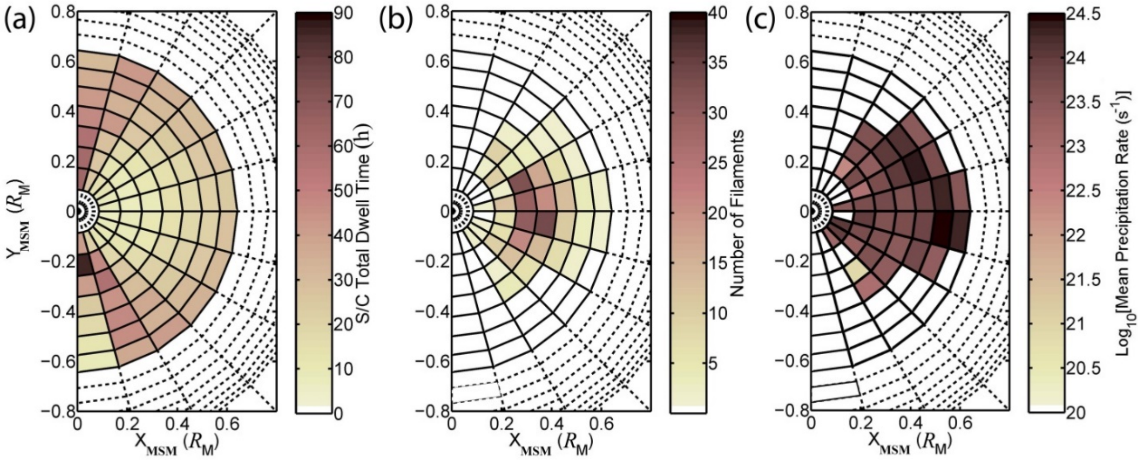

Figure 4.16 (a) Distribution of total MESSENGER dwell time for the time period of this study. Each pixel spans 5° in MLAT, from 50° to 85°N, and 1 h in MLT, from 6 h to 18 h, with values represented by the color bar displayed. (b) Distribution of number of filaments in the same format. (c) Distribution of mean particle precipitation rate in the same format ($\log_{10}$ scale).

We can sum up the mean particle precipitation rate in each pixel and estimate the integrated particle precipitation rate to be 2.7×10^{25} s^{-1} with a standard mean error of $\pm$ 0.9 $\times 10^{24}$ s^{-1}. This result is an order of magnitude larger than the rate of $(1.1\pm0.6) \times 10^{24}$ s^{-1} derived in earlier studies of the average cusp [*Winslow et al.*, 2012; 2014; *Raines et al.,* 2014]. This difference suggests that the average particle precipitation rate in the cusp is an aggregate of the flux delivered by individual filaments, and the filament events identified in this study contribute the most intense injections of magnetosheath plasma. This result is also consistent with findings at Earth, where the large-scale cusp is considered to be the aggregation of individual plasma injections from magnetic reconnection at the magnetopause [*Burch et al.,* 1982; *Smith and Lockwood,* 1990]. Interestingly, the individual cusp filaments at Mercury appear to be more easily identified than at Earth. This outcome is likely due to the high solar wind densities in the inner solar system and the weaker intrinsic magnetic field at Mercury.

Slavin et al. [2014] suggested that the formation of cusp filaments is related to the occurrence of FTEs at the dayside magnetopause. Our analysis results strongly suggest that the filaments observed in Mercury's cusp are indeed low-altitude extensions of the FTEs occurring at the dayside magnetopause. The simultaneous observation of FTEs and discrete series of cusp filaments at Mercury can also be explained with the "pulsating cusp" model first proposed by *Lockwood and Smith* [1990] for the terrestrial cusp. FTEs were first observed at Earth by *Russell and Elphic* [1978] and attributed to transient reconnection occurring on the dayside magnetopause. The prevailing theories for the formation of FTEs are based on the multiple X-line model [*Lee and Fu,* 1985] by which FTEs are formed by simultaneous reconnection at multiple locations or the sequential model [*Raeder,* 2006] with reconnection taking place at multiple X-lines but at different times on the dayside magnetopause. High rates of magnetic reconnection at Mercury's dayside magnetopause [*Slavin et al.,* 2009; *DiBraccio et al.,* 2013] result in the formation of FTEs in rapid succession, which has been observed at Mercury as "FTE showers" [*Slavin et al.,* 2012]. Each FTE is a flux-rope-type structure with one end connected to the solar wind and the other to the planetary surface at the cusp. When the flux rope is first formed, the newly opened magnetic field lines will create a bulge equatorward of the polar cap boundary, separating the open and closed field lines, as has been proposed for Earth [*Cowley,* 1984; *Southwood,* 1987]. As more FTEs form at the magnetopause, the polar cap boundary also undergoes variations on the time scale of the FTE recurrence rate. More recently, cusp filaments have been documented in the polar cap boundary layer at the boundary between open and closed field lines [*Gershman et al.,* 2016]. Such a temporal variation in the terrestrial cusp formed the basis for the pulsating cusp model [*Lockwood and Smith,* 1990] in which the cusp is an aggregation of multiple FTE ionospheric footprints during bursts of reconnection at the dayside magnetopause.

Magnetosheath plasma, originally "tied" to the interplanetary magnetic field (IMF), becomes connected to the planetary field through the FTE. Force imbalance along the axis of the FTE and thermal gradients between the magnetosheath and planetary plasma will accelerate the plasma inside the FTE along the newly opened field lines into the cusp [*Ma et al.,* 1994]. At the same time, the flux tube convects poleward in order to release magnetic tension from the kink between the end of the flux tube connected to the IMF and the FTE. The observation of Population II filaments with "residual twist," as evidenced by the MVA hodograms, and flux ropes with a core field quasi-parallel to the background field further support our idea that filaments are low-altitude extensions of FTEs. Moreover, the presence of Population III and IV filaments suggest dynamic temporal and spatial variability in the evolution of these FTEs and plasma transport within each filament. This inference begs the question of why a large fraction of the filaments exhibit the magnetic structure of a quasi-cylindrical flux tube (i.e., Population I) whereas others exhibit weak helicity (Population II) or variability (Populations III and IV) in their magnetic structure. Are the different populations reflective of the temporal and spatial evolution of FTEs?

To understand the relation between FTEs and filaments, we compared our results with those of previous FTEs studies. *Slavin et al.* [2010] identified 6 FTEs with durations of ~1 to 6 s and axial magnetic fluxes of ~1–200 kWb during MESSENGER's first two flybys of Mercury. *Imber et al.* [2014] identified 58 large-amplitude FTEs with a mean duration of ~2.48 s. Out of the 58 FTEs *Imber et al.* [2014] identified, a force-free model was fit to 17 FTEs and their mean axial magnetic flux was calculated to be ~60 kWb. For the frozen-in condition to hold, magnetic flux must be conserved. Our calculated mean magnetic flux of ~ 3 kWb is comparable to those of the smaller FTEs identified by *Slavin et al.* [2010], and the maximum magnetic flux of ~ 25 kWb is comparable to the mean flux of the FTEs identified by *Imber et al.* [2014]. Even though our statistical results are consistent with previous studies of FTEs, the histograms in Figure 4.12g and 4.12h show that ~78% of the filaments have magnetic flux less than 5 kWb, a figure that corresponds to the smaller (i.e., shorter duration) FTEs in the study by *Slavin et al.* [2010]. Hence, it is important to understand the limitations in our comparisons of magnetic flux.

To date, there has been no extensive study of the occurrence and evolution of FTEs at Mercury. Understanding the evolution of FTEs with respect to the filaments is essential to the accurate comparison of magnetic flux and, most importantly, the connectivity between FTEs and filaments. Simulations and FTE studies at Earth [*Ma et al.*, 1994; *Zhang et al.*, 2010] have shown that as the plasma inside an FTE is transported into the cusp because of force imbalance along the FTE, the reduction in thermal pressure inside the FTE can cause an enhancement in the core field and a reduction in the size of the flux rope. Subsequently, the plasma transported into the filament will reduce the local magnetic field and lead to an expansion of the flux tube. Hence, observations of diamagnetic decreases in filaments serve as a tracer for plasma flow from the FTEs into the cusp in discrete flux tubes. However, this argument also implies that without understanding the temporal and spatial variation of plasma transport in FTEs, it is difficult to distinguish between the observed and actual size of the filament that maps to the size of the corresponding FTE. Therefore, our estimate of filament size and magnetic flux serve only as lower limits to the actual quantities. It is very difficult to establish a clear relationship between FTEs and filaments, given the limited information on mid- to high-latitude FTEs and time variability of FTE-filament interaction. Further study on the FTEs and their relation to cusp filaments at Mercury is warranted.

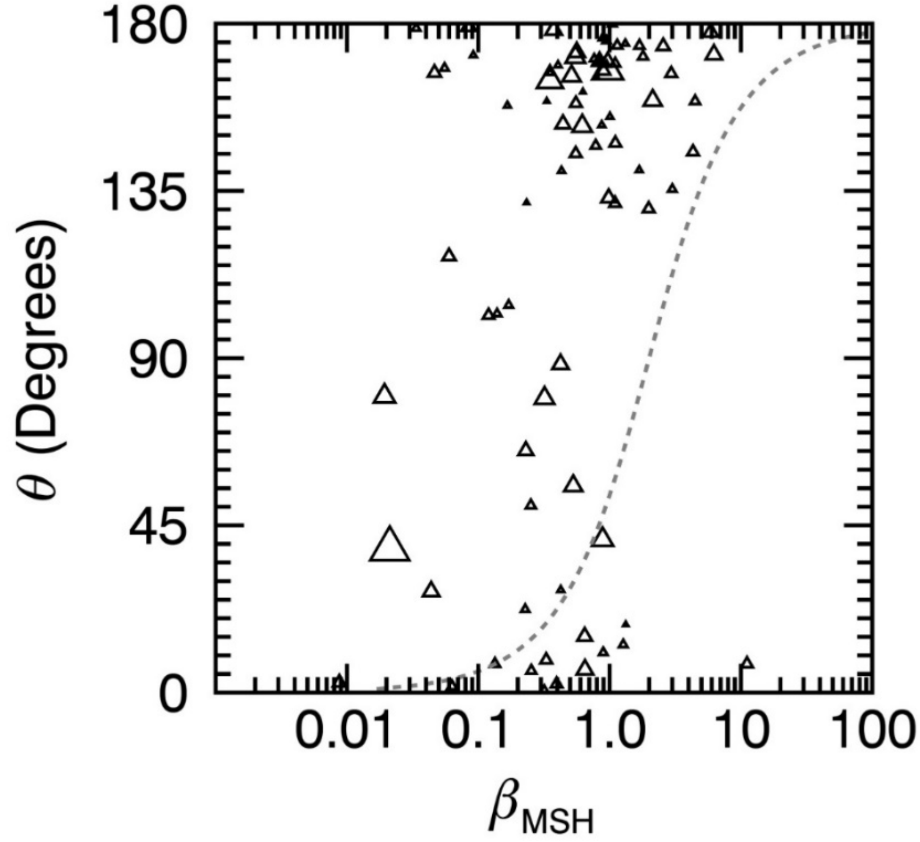

Figure 4.17 Magnetosheath plasma β_{MSH} versus IMF shear angle θ for the orbits of this study. The size of each symbol is proportional to the number of filaments identified on that orbit. β_{MSH} is computed under the assumption of pressure balance between the solar wind and the planetary magnetic field at the magnetopause, given that plasma pressure in the magnetosphere is approximately zero. θ is defined as the angle between the IMF and planetary field inside the dayside magnetosphere. The components and magnitude of the magnetic field in the solar wind and Mercury's magnetosphere are obtained by averaging 10 s of magnetic field measurements immediately inbound and outbound of the magnetopause crossing. The dashed gray line shows the *Swisdak et al.* [2010] condition for diamagnetic suppression of magnetic reconnection at the dayside magnetopause $\Delta\beta > \frac{2L}{d_{\mathrm{i}}}\tan\left(\frac{\theta}{2}\right)$ with $L = d_{\mathrm{i}}$.

At Earth, the downward flow of magnetosheath plasma in FTEs, travelling into the polar cap, has been observed in situ as discrete injection of ions and electrons [*Lockwood and Smith,* 1989] and by ground-based observations as regions of high-density plasma "patches" in the F-layer [*Lockwood and Carlson,* 1992]. Most recently, *Walsh et al.* [2014] also showed simultaneous indirect ground-based and in situ space-based observations of

FTEs at the magnetopause and ionospheric injection of ions in the polar cap. The filaments observed at Mercury appear to be the same phenomenon as observed at Earth. Despite the lack of sufficient plasma data, MESSENGER was able to observe the magnetic effects of these high-density plasma injections into Mercury's cusp due to the formation of FTEs at the magnetopause. The similarity between Mercury's filaments and Earth's ionospheric FTE footprints raise the question of whether we could also observe localized decreases of magnetic field strength in the terrestrial cusp.

Our study of cusp filaments is not complete without understanding the solar wind conditions that drive their formation. Since our results strongly suggest that filaments are the low-altitude extensions of FTEs forming at the dayside magnetopause and the rate at which FTEs were formed is primarily driven by magnetic reconnection, we have looked for any correlation between the magnetosheath plasma β (the ratio of thermal pressure to magnetic pressure), the shear angle θ between magnetosheath and planetary magnetic field, and the occurrence of filaments. Figure 4.17 shows a plot of magnetosheath plasma β, calculated using the method of *DiBraccio et al.* [2013] under the assumption of pressure balance, and shear angle θ for the orbits of this study. The magnetosheath plasma β and shear angle θ for each orbit are calculated by averaging 10s of magnetic field measurements immediately before and after the magnetopause crossing. The dashed gray line represents the condition for diamagnetic suppression of magnetic reconnection [*Swisdak et al.,* 2010] with $L = d_\mathrm{i}$ given by the relation:

$$\Delta\beta > \frac{2L}{d_\mathrm{i}} \tan\left(\frac{\theta}{2}\right) \tag{4.7}$$

where $\Delta\beta$ is the difference in plasma β across the magnetopause. Under the assumption that β inside the magnetosphere is negligible, $\Delta\beta \approx \beta_\mathrm{MSH}$, where β_MSH is the plasma β in the magnetosheath. The curve for diamagnetic suppression of reconnection separates Figure 4.17 into two regions; the regions to the right and left of the curve suppress and favor magnetic reconnection at the magnetopause, respectively. Figure 4.17 shows that ~ 85% of the orbits with cusp filaments lie to the left of the *Swisdak et al.* [2010] relation, indicating that most of the filaments occur under conditions when magnetic reconnection is favored. This high fraction supports a causal relationship between magnetic reconnection and the occurrence of filaments. Moreover, Figure 4.17 shows that cusp filaments appear to form preferentially under low β, i.e., $\beta < 1$, and high shear angle. This result agrees with experience at Earth, where magnetic reconnection is more likely to occur under high shear and low-β conditions [*Paschmann et al.*, 1986; *Trenchi et al.*, 2008; *Phan et al.*, 2010]. On the other hand, there are also a number of orbits in our study with low θ, and on some of those orbits high numbers of filaments were observed, but only for $\beta <$ 0.1–1. This finding is in agreement with the studies by *DiBraccio et al.* [2013] and *Slavin et al.* [2014], which concluded that the reconnection rate at Mercury's magnetopause is independent of the shear angle at low β. Therefore, the results in Figure 4.17 suggest that the strong dependence of filament occurrence on solar wind parameters is similar to those governing magnetic reconnection at the magnetopause and, therefore, further strengthen the concept that filaments are the high-latitude extensions of FTEs.

In this chapter, we examined the cusp plasma filaments observed in Mercury's northern cusp and investigated its relation to FTEs formed at the dayside magnetopause. The magnetic flux contained within the cusp filaments and FTEs is then convected into Mercury's magnetotail, changing its configuration and driving plasma dynamics in the current sheet. Naturally, the follow-up discussion of physical processes at Mercury in the next chapter is to examine the structure of Mercury's magnetotail and the nature of current sheet dynamics.

References

Alexeev, I. I., *et al.* *(*2010*)*, Mercury's magnetospheric magnetic field after the first two MESSENGER flybys, *Icarus, 209*, 23–39, *doi:*10.1016/j.icarus.2010.01.024.

Anderson, B. J., M. H. Acuña, D. A. Lohr, J. Scheifele, A. Raval, H. Korth, *and* J. A. Slavin *(*2007*)*, The Magnetometer instrument on MESSENGER, *Space Sci. Rev.*, *131*, 417–450, *doi:*10.1007/s11214-007-9246-7.

Anderson, B. J., J. A. Slavin, H. Korth, S. A. Boardsen, T. H. Zurbuchen, J. M. Raines, G. Gloeckler, R. L. McNutt Jr., *and* S. C. Solomon *(*2011*)*, The dayside magnetospheric boundary layer at Mercury, *Planet. Space Sci.*, *59*, 2037–2050.

Anderson, B. J., C. L. Johnson, H. Korth, J. A. Slavin, R. M. Winslow, R. J. Phillips, R. L. McNutt Jr., and S. C. Solomon (2014), Steady-state field-aligned currents at Mercury, *Geophys. Res. Lett.*, *41*, 7444–7452, doi:10.1002/2014GL061677.

Andrews, G. B., *et al.* *(*2007*)*, The Energetic Particle and Plasma Spectrometer instrument on the MESSENGER spacecraft, *Space Sci. Rev.*, *131*, 523–556, *doi:*10.1007/s11214-007-9272-5.

Balikhin, M. A., R. Z. Sagdeev, S. N. Walker, O. A. Pokhotelov, D. G. Sibeck, N. Beloff, *and* G. Dudnikova *(*2009*)*, THEMIS observations of mirror structures: Magnetic holes and instability threshold, *Geophys. Res. Lett.*, *36*, *L03105*, *doi:*10.1029/2008GL036923.

Baumgärtel, K., K. Sauer, *and* E. Dubinin *(*2003*)*, Towards understanding magnetic holes: Hybrid simulations, *Geophys. Res. Lett.*, *30(*14*)*, *1761*, *doi:*10.1029/2003GL017373.

Boardsen, S. A., B. J. Anderson, M. H. Acuña, J. A. Slavin, H. Korth, *and* S. C. Solomon *(*2009*)*, Narrow-band ultra-low-frequency wave observations by MESSENGER during its January 2008 flyby through Mercury's magnetosphere, *Geophys. Res. Lett.*, *36*, *L01104*, *doi:*10.1029/2008GL036034.

Burch, J. L., P. H. Reiff, R. A. Heelis, J. D. Winningham, W. B. Hanson, C. Gurgiolo, J. D. Menietti, R. A. Hoffman, *and* J. N. Barfield (1982), Plasma injection and transport in the midlatitude polar cusp, *Geophys. Res. Lett.*, *9*, 921–924.

Cowley, S. W. H. (1984), Solar wind control of magnetospheric convection, *in Achievements of the International Magnetospheric Study, (IMS), Spec. Pub. 217, pp.* 483–494, *European Space Agency*, *Noordwijk*, The Netherlands.

DiBraccio, G. A., J. A. Slavin, S. A. Boardsen, B. J. Anderson, H. Korth, T. H. Zurbuchen, J. M. Raines, D. N. Baker, R. L. McNutt Jr., *and* S. C. Solomon *(*2013*)*, MESSENGER observations of magnetopause structure and dynamics at Mercury, *J. Geophys. Res. Space Physics*, *118*, 997–1008, *doi:*10.1002/jgra.50123.

DiBraccio, G. A., J. A. Slavin, J. M. Raines, D. J. Gershman, P. J. Tracy, S. A. Boardsen, T. H. Zurbuchen, B. J. Anderson, H. Korth, R. L. McNutt Jr., *and S. C. Solomon (*2015*),* First observations of Mercury's plasma mantle by MESSENGER, *Geophys. Res. Lett., 42, 9666–9675, doi:*10.1002/2015GL065805.

Domingue D. L., *et al. (2014)*, Mercury's weather-beaten surface: Understanding Mercury in the context of lunar and asteroidal space weathering studies, *Space Sci. Rev., 181*, 121–214.

Elphic, R. C., *and* C. T. Russell *(*1983*),* Magnetic flux ropes in the Venus ionosphere: Observations and models, *J. Geophys. Res., 88,* 58–72, *doi:*10.1029/JA088iA01p00058.

Gershman, D. J., J. A. Slavin, J. M. Raines, T. H. Zurbuchen, B. J. Anderson, H. Korth, D. N. Baker, *and* S. C. Solomon *(*2013*),* Magnetic flux pileup and plasma depletion in Mercury's subsolar magnetosheath*. J. Geophys. Res. Space Physics, 118,* 7181–7199, *doi:*10.1002/2013JA019244.

Gershman, D. J., J. M. Raines, J. A. Slavin, T. H. Zurbuchen, T. Sundberg, S. A. Boardsen, B. J. Anderson, H. Korth, *and* S. C. Solomon *(*2015*),* MESSENGER observations of multiscale Kelvin-Helmholtz vortices at Mercury*. J. Geophys. Res. Space Physics, 120,* 4354–4368, *doi:*10.1002/2014JA020903.

Gershman, D. J., J. C. Dorelli, G. A. DiBraccio, J. M. Raines, J. A. Slavin, G. Poh, and T. H. Zurbuchen (2016), Ion-scale structure in Mercury's magnetopause reconnection diffusion region, *Geophys. Res. Lett.*, *43*, in press, doi:10.1002/2016GL069163.

Hasegawa, A. *(*1969*),* Drift mirror instability in the magnetosphere, *Phys. Fluids, 12,* 2642–2650.

Hill, T. W., *and* P. H. Reiff *(*1977*),* Evidence of magnetospheric cusp proton acceleration by magnetic merging at the dayside magnetopause, *J. Geophys. Res., 82,* 3623–3628, *doi:*10.1029/JA082i025p03623.

Imber, S. M., J. A. Slavin, S. A. Boardsen, B. J. Anderson, H. Korth, R. L. McNutt Jr., *and* S. C. Solomon *(*2014*),* MESSENGER observations of large dayside flux transfer events: Do they drive Mercury's substorm cycle?*, J. Geophys. Res. Space Physics, 119,* 5613–5623, *doi:*10.1002/2014JA019884.

Jia, X., J. A. Slavin, T. I. Gombosi, L. K. S. Daldorff, G. Toth, *and* B. van der Holst *(*2015*),* Global MHD simulations of Mercury's magnetosphere with coupled planetary interior: Induction effect of the planetary conducting core on the global interaction*. J. Geophys. Res. Space Physics, 120,* 4763–4775*. doi:*10.1002/2015JA021143.

Johnson. C. L., M. E. Purucker, H. Korth, B. J. Anderson, R. M. Winslow, M. M. H. Al Asad, J. A. Slavin, I. I. Alexeev, R. J. Phillips, M. T. Zuber and S. C. Solomon (2012), MESSENGER observations of Mercury’s magnetic field structure. *J. Geophys. Res., 117*, E00L14, doi:10.1029/2012JE004217.

Killen, R. M., and W.-H. Ip (1999), The surface-bounded atmospheres of Mercury and the Moon, *Rev. Geophys.*, *37*, 361–406, doi:10.1029/1999RG900001.

Lee, L. C., *and* Z. F. Fu *(*1985*)*, A theory of magnetic flux transfer at the Earth's magnetopause, *Geophys. Res. Lett.*, *12*, 105–108.

Liljeblad. E., T. Sundberg, T. Karlsson, *and* A. Kullen (2014), Statistical investigation of Kelvin-Helmholtz waves at the magnetopause of Mercury, *J. Geophys. Res. Space Physics*, *119*, 9670–9683.

Lockwood, M., *and* H. C. Carlson *(*1992*)*, Production of polar cap electron density patches by transient magnetopause reconnection, *Geophys. Res. Lett.*, *19*, 1731–1734, *doi:*10.1029/92GL01993.

Lockwood, M., *and* M. F. Smith (1989), Low-altitude signatures of the cusp and flux transfer events, *Geophys. Res. Lett.*, *16*, 879–882.

Massetti, S., S. Orsini, A. Milillo, *and* A. Mura *(*2007*)*, Modelling Mercury's magnetosphere and plasma entry through the dayside magnetopause, *Planet. Space Sci.*, *55*, 1557–1568.

Ness, N. F., K. W. Behannon, R. P. Lepping, Y. C. Wang, *and* K. H. Schatten *(*1974*)*, Observations of magnetic field near Mercury: Preliminary results from Mariner 10, *Science*, *185*, 151–159.

Newell, P. T., *and* C.-I. Meng *(*1987*)*, Cusp width and B_z: Observations and a conceptual model, *J. Geophys. Res.*, *92*, 13,673–13,678.

Paschmann, G., I. Papamastorakis, W. Baumjohann, N. Sckopke, C. W. Carlson, B. U. Ö. Sonnerup, *and* H. Lühr *(*1986*)*, The magnetopause for large magnetic shear: AMPTE/IRM observations, *J. Geophys. Res.*, *91*, 11,099–11,115, *doi:*10.1029/JA091iA10p11099.

Phan, T. D., J. T. Gosling, G. Paschmann, C. Pasma, J. F. Drake, M. Oieroset, D. Larson, R. P. Lin, *and* M. S. Davis *(*2010*)*, The dependence of magnetic reconnection on plasma β and magnetic shear: Evidence from solar wind observations, *Astrophys. J.*, *719*, L199–L203.

Pokhotelov, O. A., R. Z. Sagdeev, M. A. Balikhin, O. G. Onishchenko, *and* V. N. Fedun *(*2008*)*, Nonlinear mirror waves in non-Maxwellian space plasmas, *J. Geophys. Res.*, *113*, *A04225*, *doi:*10.1029/2007JA012642.

Raeder, J. (2006), Flux transfer events: 1. Generation mechanism for strong southward IMF, *Annal. Geophys.*, *24*, 381–392, *doi:*10.5194/angeo-24-381-2006.

Raines, J. M., D. J. Gershman, J. A. Slavin, T. H. Zurbuchen, H. Korth, B. J. Anderson, G. Gloeckler, *and* S. C. Solomon (2014), Structure and dynamics of Mercury's magnetospheric cusp: MESSENGER measurements of protons and planetary ions, *J. Geophys. Res. Space Physics*, *119, 6587–6602, doi:*10.1002/2014JA020120.

Russell, C. T., *and* R. C. Elphic (1978), Initial ISEE magnetometer results: Magnetopause observations, *Space Sci. Res.*, *22*, 681–715.

Scurry, L., C. T. Russell, *and* J. T. Gosling (1994), Geomagnetic activity and the beta dependence of the dayside reconnection rate, *J. Geophys. Res.*, *99*, 14,811–14,814, *doi:*10.1029/94JA00794.

Shi, Q. Q., *et al.* (2009), Spatial structures of magnetic depression in the Earth's high-altitude cusp: Cluster multipoint observations, *J. Geophys. Res.*, *114, A10202, doi:*10.1029/2009JA014283.

Shue, J.-H., *et al.* (1998), Magnetopause location under extreme solar wind conditions, *J. Geophys. Res.*, *103*, 17,691–17,700, *doi:*10.1029/98JA01103.

Slavin, J. A., *and* R. E. Holzer (1979), The effect of erosion on the solar wind stand-off distance at Mercury, *J. Geophys. Res.*, *84*, 2076–2082, *doi:*10.1029/JA084iA05p02076.

Slavin, J. A., *et al.* (2008), Mercury's magnetosphere after MESSENGER's first flyby, *Science*, *321*, 85–89.

Slavin, J. A., *et al.* (2009), MESSENGER observations of magnetic reconnection in Mercury's magnetosphere, *Science*, *324*, 606–610.

Slavin, J. A., *et al.* (2010), MESSENGER observations of large flux transfer events at Mercury, *Geophys. Res. Lett.*, *37, L02105, doi:*10.1029/2009GL041485.

Slavin, J. A., *et al.* (2014), MESSENGER observations of Mercury's dayside magnetosphere under extreme solar wind conditions, *J. Geophys. Res. Space Physics*, *119*, 8087–8116, *doi:*10.1002/2014JA020319.

Smith, M. F., *and* M. Lockwood (1990), The pulsating cusp, *Geophys. Res. Lett.*, *17*, 1069–1072.

Smith, D. E., et al. (2012), Gravity field and internal structure of Mercury from MESSENGER, *Science*, *336*, 214–217.

Sonnerup, B. U. Ö., *and* L. J. Cahill Jr. (1967), Magnetopause structure and attitude from Explorer 12 observations, *J. Geophys. Res.*, *72*, 171–183.

Sonnerup, B. U. Ö., *and* M. Scheible *(*1998*)*, Minimum and maximum variance analysis, *in Analysis Methods for Multi-Spacecraft Data*, *edited by* G. Paschmann *and* P. W. Daly, *ISSI Scientific Report SR-001*, *pp.* 185–220, *European Space Agency,* Noordwijk, The Netherlands.

Sonnerup, B. U. Ö., G. Paschmann, I. Papamastorakis, N. Sckopke, G. Haerendel, S. J. Bame, J. R. Asbridge, J. T. Gosling, *and* C. T. Russell *(*1981*)*, Evidence for magnetic field reconnection at the Earth's magnetopause, *J. Geophys. Res.*, *86*, 10,049–10,067, *doi:*10.1029/JA086iA12p10049.

Soucek, J., E. Lucek, *and* I. Dandouras *(*2008*)*, Properties of magnetosheath mirror modes observed by Cluster and their response to changes in plasma parameters, *J. Geophys. Res.*, *113*, *A04203*, *doi:*10.1029/2007JA012649.

Southwood, D. J. (1987), The ionospheric signature of flux transfer events, *J. Geophys. Res.*, *92*, 3207–3213.

Southwood, D. J., W. J. Hughes (1983), Theory of hydromagnetic waves in the magnetosphere, *Space Sci. Rev.*, *35*, 301–366.

Southwood, D. J., *and* M. G. Kivelson *(*1993*)*, Mirror instability: 1. Physical mechanism of linear instability, *J. Geophys. Res.*, *98*, 9181–9187.

Stevens, M. L., *and* J. C. Kasper *(*2007*)*, A scale-free analysis of magnetic holes at 1 AU, *J. Geophys. Res.*, *112*, *A05109*, *doi:*10.1029/2006JA012116.

Sundberg, T., S. A. Boardsen, J. A. Slavin, B. J. Anderson, H. Korth, T. H. Zurbuchen, J. M. Raines, *and* S. C. Solomon *(*2012*)*, MESSENGER orbital observations of large-amplitude Kelvin-Helmholtz waves at Mercury's magnetopause, *J. Geophys. Res.*, *117*, *A04216*, *doi:*10.1029/2011JA017268.

Swisdak, M., B. N. Rogers, J. F. Drake, *and* M. A. Shay *(*2003*)*, Diamagnetic suppression of component magnetic reconnection at the magnetopause, *J. Geophys. Res.*, *108*(A5), 1218, *doi:*10.1029/2002JA009726.

Trenchi, L., M. F. Marcucci, G. Pallocchia, G. Consolini, M. B. Bavassano Cattaneo, A. M. Di Lellis, H. Rème, L. Kistler, C. M. Carr, *and* J. B. Cao *(*2008*)*, Occurrence of reconnection jets at the dayside magnetopause: Double star observations, *J. Geophys. Res.*, *113*, *A07S10*, *doi:*10.1029/2007JA012774.

Tsurutani, B. T., E. J. Smith, R. R. Anderson, K. W. Ogilvie, J. D. Scudder, D. N. Baker, S. J. Bame *(1982)*, Lion roars and nonoscillatory drift mirror waves in the magnetosheath, *J. Geophys. Res.*, *87*, 6060–6072.

Turner, J. M., L. F. Burlaga, N. F. Ness, *and* J. F. Lemaire *(*1977*),* Magnetic holes in the solar wind, *J. Geophys. Res., 82,* 1921–1924*.*

Walsh. B. M., J. C. Foster, P. J. Erickson, and D. G. Sibeck (2014), Simultaneous ground- and space-based observations of the plasmaspheric plume and reconnection, *Science*, *343*, 1122–1125, doi:10.1126/science.1247212.

Winslow, R. M., C. L. Johnson, B. J. Anderson, H. Korth, J. A. Slavin, M. E. Purucker, *and* S. C. Solomon *(*2012*),* Observations of Mercury's northern cusp with MESSENGER's Magnetometer, *Geophys. Res. Lett.*, *39, L08112, doi:*10.1029/2012GL051472.

Winslow, R. M., B. J. Anderson, C. L. Johnson, J. A. Slavin, H. Korth, M. E. Purucker, D. N. Baker, *and* S. C. Solomon *(*2013*)*, Mercury's magnetopause and bow shock from MESSENGER Magnetometer observations, *J. Geophys. Res. Space Physics*, *118,* 2213–2227, *doi:*10.1002/jgra.50237.

Winslow, R. M., et al. (2014), Mercury’s surface magnetic field determined from proton-reflection magnetometry, *Geophys. Res. Lett.*, *41*, 4463–4470, doi:10.1002/2014GL060258.

Winterhalter, D. M., M. Neugebauer, B. E. Goldstein, E. J. Smith, S. J. Bame, *and* A. Balogh *(*1994*),* Ulysses field and plasma observations of magnetic holes in the solar wind and their relation to mirror-mode structures, *J. Geophys. Res.*, *99*, 23,371–23,281.

Xiao, C. J., Z. Y. Pu, Z. W. Ma, S. Y. Fu, Z. Y. Huang, *and* Q. G. Zong *(*2004*),* Inferring of flux rope orientation with the minimum variance analysis technique, *J. Geophys. Res.*, *109, A11218, doi:*10.1029/2004JA010594.

CHAPTER V

MERCURY'S CROSS-TAIL CURRENT SHEET: STRUCTURE, X-LINE LOCATION AND STRESS BALANCE

This chapter is taken from Gangkai Poh, James A. Slavin, Xianzhe Jia, Jim M. Raines, Suzanne M. Imber, Wei-Jie Sun, Daniel J. Gershman, Gina A. DiBraccio, Kevin J. Genestreti, Andy W. Smith (2016), Mercury's Cross-tail Current Sheet: Structure, X-line Location and Stress Balance, *Geophys. Res. Lett.*, *43*, doi:10.1002/2016GL071612.

Abstract:

The structure, X-line location and magnetohydrodynamics (MHD) stress balance of Mercury's magnetotail were examined between $-2.6 < X_{MSM} < -1.4\ R_M$ using MESSENGER measurements observed from 319 central plasma sheet (CPS) crossings. The mean plasma β in the CPS calculated from MESSENGER data is ~ 6. The CPS magnetic field was southward (i.e., tailward of X-line) ~ 2 – 18% of the time. Extrapolation of downtail variations in B_Z indicates an average X-line location at $-3\ R_M$. Modelling of magnetic field measurements produced a cross-tail current sheet (CS) thickness, current density and inner CS edge location of $0.39\ R_M$, $92\ nA/m^2$ and $-1.22\ R_M$, respectively. Application of MHD stress balance suggests that heavy planetary ions may be important in maintaining stress balance within Mercury's CPS. Qualitative similarities between Mercury's and Earth's magnetotail are remarkable given the differences in upstream conditions, internal plasma composition, finite gyro-radius scaling, and Mercury's lack of ionosphere.

5.1 Introduction

The dominant process transferring solar wind energy into Mercury's magnetosphere is magnetic reconnection at the dayside magnetopause [*Slavin et al.,* 2009; *DiBraccio et al.,* 2013]. Following dayside reconnection, opened magnetic flux is transported anti-sunward by the flow of the solar wind, forming a magnetotail with two open magnetic field regions, i.e., the two tail lobes. These open field lines have one end connected to the planetary magnetic field and the other to the interplanetary magnetic field (IMF). The northern and southern tail lobes contain fields oriented in opposite directions. Separating the two tail lobes is the higher β (i.e. ratio of plasma thermal to magnetic pressure) and closed field line region known as the plasma sheet. Between each tail lobe and the plasma sheet is a region of lower-β (~ 0.1 at Earth [*Baumjohann et al.,* 1988]) flux tubes recently "closed" by magnetic reconnection known as the plasma sheet boundary layer (PSBL). The CPS layer contains an embedded cross-tail current, which flows in the dawn-to-dusk direction [*Rich et al.,* 1972]. The crossing of a CPS is identified by the reversal of the sunward/anti-sunward component of the magnetic field and a decrease in the magnitude |**B**|. Due to the weak magnetic field and presence of hot, dense plasma, β is typically >> 1 in Mercury's CPS [*Gershman et al.,* 2014].

The MErcury Surface, Space ENvironment, GEochemistry, and Ranging (MESSENGER) spacecraft conducted three flybys of Mercury before it became the first spacecraft to orbit Mercury on 18th March 2011. During these flybys, MESSENGER sampled Mercury's magnetotail at downtail distances up to 3 R_M away from Mercury and provided an opportunity to characterize the structure and dynamics of the magnetotail. Initial analysis of MESSENGER flybys data [*Slavin et al.,* 2010; 2012a] have shown that Mercury's magnetotail is highly variable with timescales of seconds to minutes, which is consistent with the high magnetopause reconnection rates that had been predicted for Mercury [*Slavin and Holzer,* 1979]. MESSENGER observed relatively large magnetic field component normal to the magnetopause [*DiBraccio et al.,* 2013] and showers of large flux transfer events [*Slavin et al.,* 2012b; *Imber et al.,* 2014], which are indicative of high magnetopause reconnection activity, increase the tail magnetic flux content by up to a factor of 2 [*Slavin et al.,* 2010; 2012a] via the Dungey cycle [*Dungey,* 1961] at Mercury.

This intense loading of magnetic flux in the lobes increases the overall flaring of the nightside magnetopause and enhances the solar wind pressure exerted on the magnetotail. These pressure enhancements lead to thinning of the cross-tail CS and tail reconnection. Observations of plasmoids [*Slavin et al.*, 2012a; *DiBraccio et al.*, 2015; *Sun et al.*, 2016], dipolarizations [*Sundberg et al.*, 2012] and substorms [*Slavin et al.*, 2010; *Sun et al.*, 2015] strongly support the rapid dissipation of magnetotail energy through magnetic reconnection in a manner similar to that observed at Earth [*Sharma et al.*, 2008]. MESSENGER's orbit around Mercury provided continuous magnetic field [*Anderson et al.*, 2007] and plasma ion [*Andrews et al.*, 2007] measurements, which allow the large-scale structure in Mercury's magnetotail to be characterized. Here we examine the structure, X-line location and MHD stress balance in Mercury's magnetotail.

5.2 MESSENGER Instrumentation and Tail Current Sheet Crossing Identification

In this study, we utilize the full-resolution data from MESSENGER's Magnetometer (MAG) (20 vectors/s) and Fast Imaging Plasma Spectrometer (FIPS) (1 energy scan/10s). Figure 4.1a shows MESSENGER's magnetic field observations during a traversal of Mercury's cross-tail CS on 3 February 2013 in the aberrated Mercury solar magnetospheric (MSM') coordinate system. The MSM system is centered on Mercury's offset internal dipole [*Alexeev et al.*, 2010; *Anderson et al.*, 2011], the X- and Z-axes are sunward and parallel to the planetary spin axis, respectively. The Y-axis completes the right-handed system. We accounted for the aberration effect (i.e., orbital motion of Mercury with respect to the solar wind) by rotating the MSM X- and Y-axes such that X' is opposite to the solar wind velocity vector and corresponds to the central axis of the magnetotail. The rotation angle was calculated using daily averages of Mercury's orbital motion and an assumed radial solar wind velocity of 400 km/s. In Figure 5.1, the spacecraft first encountered the southern lobe, characterized by the strong, low-variance magnetic fields of ~ 60 nT, predominantly oriented in the negative $B_{X'}$ direction. The PSBL (yellow) was identified by small decreases in $|\mathbf{B}|$ (~ 10%) and moderate fluctuations of ~ 20 nT as compared to the lobe field [*Slavin et al.*, 1985]. The spacecraft then entered the CPS (red) characterized by a further decrease in the $|\mathbf{B}|$, and reversal of $B_{X'}$ across the magnetotail current layer. Lastly, MESSENGER entered the northern lobe when |**B**| increased back to 60 nT with low levels of fluctuations in |**B**|. Before exiting into the northern lobe, MESSENGER observed two large-scale CS oscillations or flapping motions (i.e., fluctuations in $B_{X'}$, which are common in planetary magnetotails [see *Volwerk et al.*, 2013]).

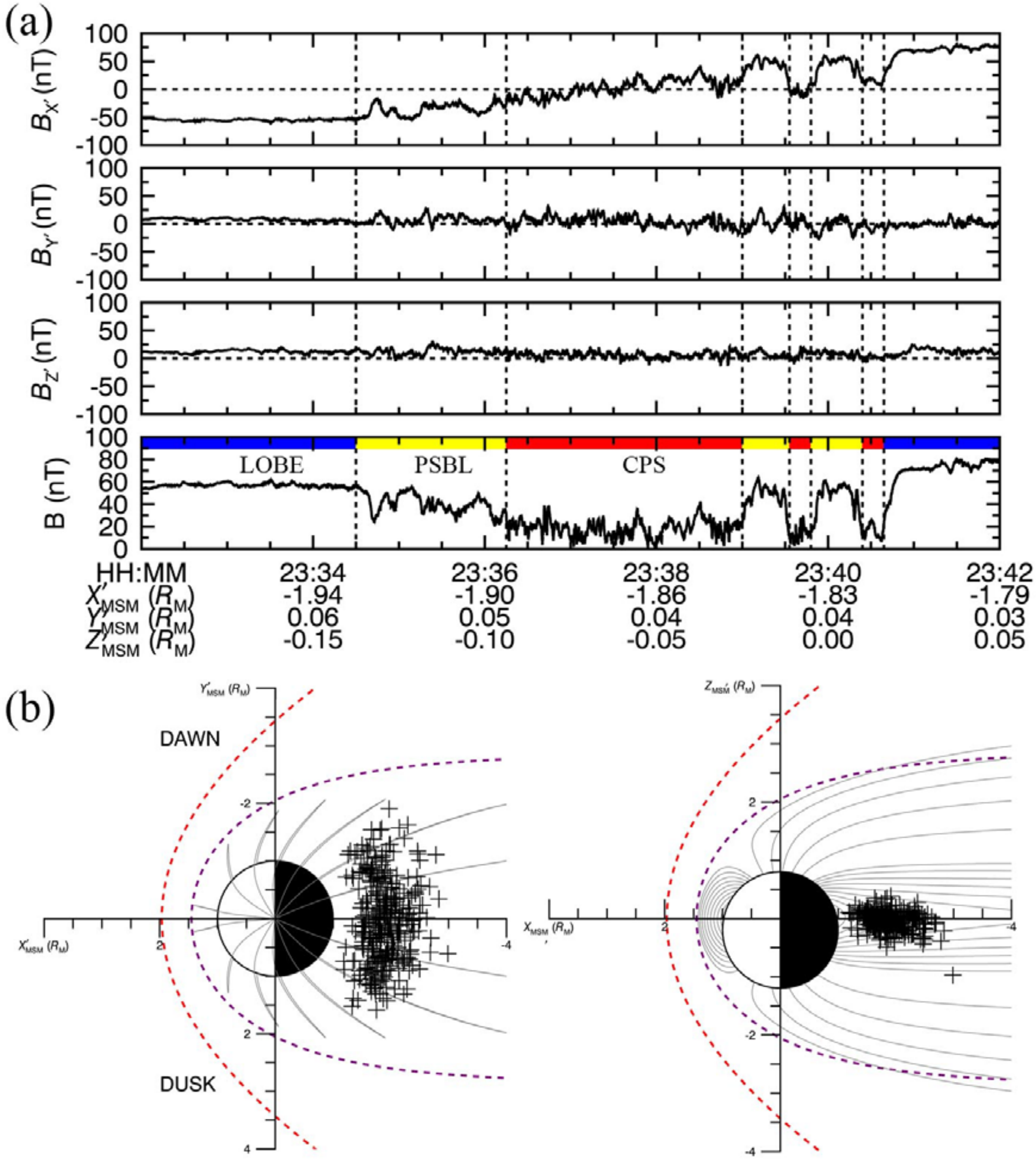

Figure 5.1 (a) Full-resolution MESSENGER magnetic field measurements on February 3rd 2013. (b) Average positions of each CS crossing in the equatorial (left) and meridional (right) plane. Model bow shock (BS) and magnetopause (MP) from *Winslow et al.* [2013] are shown.

We surveyed four years of MESSENGER's MAG data and identified a total of 319 CPS crossings based on the following selection requirements:

- Well-defined boundary between the moderately fluctuating magnetic field intensity in the PSBL and the highly fluctuating, large decrease in magnetic field intensity in the CPS.
- Clear reversal of B_x embedded in the CPS corresponding to the cross-tail CS.
- Average |**B**| in the CPS must be less than 50% of the |**B**| lobe averaged over the lobe interval during individual traversal.

The locations of each of the CPS crossings identified in this study are plotted in Figure 5.1b in the equatorial (X'_{MSM}–Y'_{MSM}) and meridional (X'_{MSM}–Z'_{MSM}) planes along with the T96-modelled magnetic field lines [*Tsyganenko,* 1996] scaled to the size of Mercury's magnetosphere by dividing with a factor of 8 [*Ogilvie et al.,* 1977]. The CPS crossings were evenly distributed around midnight (Y'_{MSM} ~ 0) and covered a range of downtail distances from -1.1 – -3.0 R_M.

5.3 Analysis

5.3.1 Downtail Variation of CPS and Lobe Magnetic Field

We examined the variation of the magnetic field intensity in the lobe (B_{lobe}) and CPS (B_{CPS}) as a function of downtail distances (i.e., X'_{MSM}). Using MESSENGER's (MSGR) and Mariner 10's (M10) flyby magnetic field data, *Slavin et al.* [2012a] showed that a power law relation can be used to describe the decrease in B_{lobe} with X'_{MSM} due to the decrease in flaring of the magnetotail as it becomes more cylindrical:

$$|B|(|X'_{MSM}|) = A|X'_{MSM}|^G + B_0 \tag{5.1}$$

where A is the scaling constant, G is the power-law exponent and B_0 is the asymptotic magnetic field. The MSGR $<B_{lobe}>$ values are averaged in 0.1 R_M bins along X'_{MSM} for the entire orbital phase and displayed in Figure 5.2a. Our result shows that B_{lobe} falls off with

G ~ 3.1 ± 0.1 and has an asymptotic value of B_0 ~ 41.4 ± 1.4 nT. The fitted curve suggests that lobe flaring ceases near X'_{MSM} ~ -3.5 R_M, where B_{lobe} becomes constant. Figure 5.2b shows the MSGR $<B_{CPS}>$ for orbital phase as a function of X'_{MSM}, where all measured B_{CPS} values are averaged in 0.1 R_M bins. Our results show that $<B_{CPS}>$ decreases with G ~ -8.9 ± 0.1 and asymptotes at X'_{MSM} ~ -1.8 R_M with B_0 ~ 16.6 ± 0.7 nT. As compared to *Slavin et al.* [2012a] earlier analysis of Mercury's CPS during the first flyby (M1) when the IMF was northward, our observation of weaker magnetic field is attributed to the presence of a denser and hotter plasma sheet. In fact, assuming pressure balance between the lobe and CPS, we can derive an equation for the CPS $\beta = \left[\left(\frac{B_{lobe}^2}{B_{CPS}^2}\right) - 1\right]$. The asymptotic lobe and CPS field intensities determined earlier imply an average value of β ~ 5.2. This agrees with our calculated β of ~ 6.5 using FIPS measurements (not shown here).

The normalized probability distribution of B_Z in Figure 5.2c is derived by binning all measurements into 5 nT bins of B_Z, four X'_{MSM} ranges between -1.4 to -2.6 R_M at intervals of 0.3 R_M and within ±0.4 R_M away from Y'_{MSM} = 0. In a 2-dimensional geometry of the X-line, the two anti-parallel lobe fields reconnect to form closed (open) magnetic field lines which move sunward (anti-sunward) at the local Alfvén speed. The closed, sunward (open, anti-sunward) moving magnetic field line has a positive (negative) B_Z polarity. Figure 4.2c shows that B_Z is predominantly positive for all X'_{MSM} ranges and the $<B_Z>$ of the distributions decreases with increasing X'_{MSM}. Therefore, we can conclude that MESSENGER crosses the CPS slightly planetward of the statistical X-line, also known as the Near Mercury Neutral Line (NMNL), most of the time. Not shown here, the mean of all measured B_Z measurements is ~ 9.5 nT.

The probability distribution in Figure 5.2c also shows that MESSENGER spent ~ 2% of the CPS crossing occurred tailward of the X-line (B_Z < 0). As X'_{MSM} decreases, the time MESSENGER spent tailward of the X-line also increases. At the furthest downtail region (-2.3 < X'_{MSM} (R_M) < -2.6), MESSENGER spend ~ 18% of its CPS crossing time tailward of the X-line. Figure 5.2d shows the relationship between the percentage time MESSENGER spent tailward of the X-line (Σt) and X'_{MSM}. We fit the data using an exponential function and estimated the statistical location of the NMNL (i.e., Σt = 50%) to be X'_{MSM} ~ -2.95 R_{M}.

5.3.2 Harris Current Sheet Modelling

Due to MESSENGER's highly-inclined (~ 80°) orbit, the spacecraft trajectories through the cross-tail CS are expected to be nearly normal to the tail current sheet on average. The Harris current sheet model [*Harris*, 1962] is the one-dimensional equilibrium solution to the Maxwell-Vlasov equation that describes the planetary magnetotail magnetic field structure in the Z'_{MSM} direction. It has been used extensively in magnetotail studies by Cluster [e.g., *Nakamura et al.*, 2002; *Narita et al.*, 2013] and reconnection simulations [e.g., *Birn et al.*, 2001]. The relationship between B_{X} and the cross-tail current density (J_{Y}) is given by:

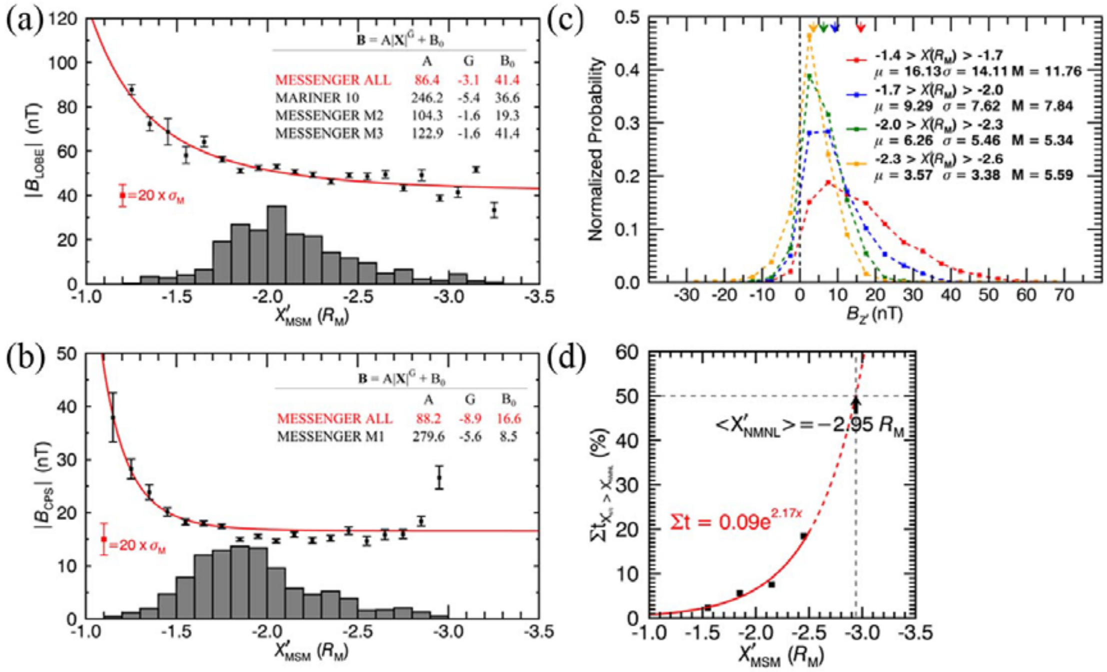

Figure 5.2 (a) B_{lobe} and (b) B_{CPS} as a function of X'_{MSM}. A power law relation was fitted to the data points (red line) with fitting coefficients shown in the table. The histogram for number of data points in each bin is also shown. (c) Normalized probability distributions of B_{Z} for four downtail regions and the colored arrows represent the mean of each respective distribution. (d) Σt as a function of X'_{MSM}. An exponential relation (red line) is fitted to the data points.

$$B_X(z) = B_0 \, tanh\left(\frac{z - z_0}{L}\right) \quad (5.2)$$

$$J_Y(z) = \frac{B_0}{\mu_0 L} sech^2\left(\frac{z-z_0}{L}\right) \tag{5.3}$$

where B_0 is the asymptotic lobe field, z_0 is the north-south position of the CS center and L is the characteristic half-thickness of the CS. These are free parameters, which we determined by a least-square fitting procedure of the Harris model to the magnetic field measurements.

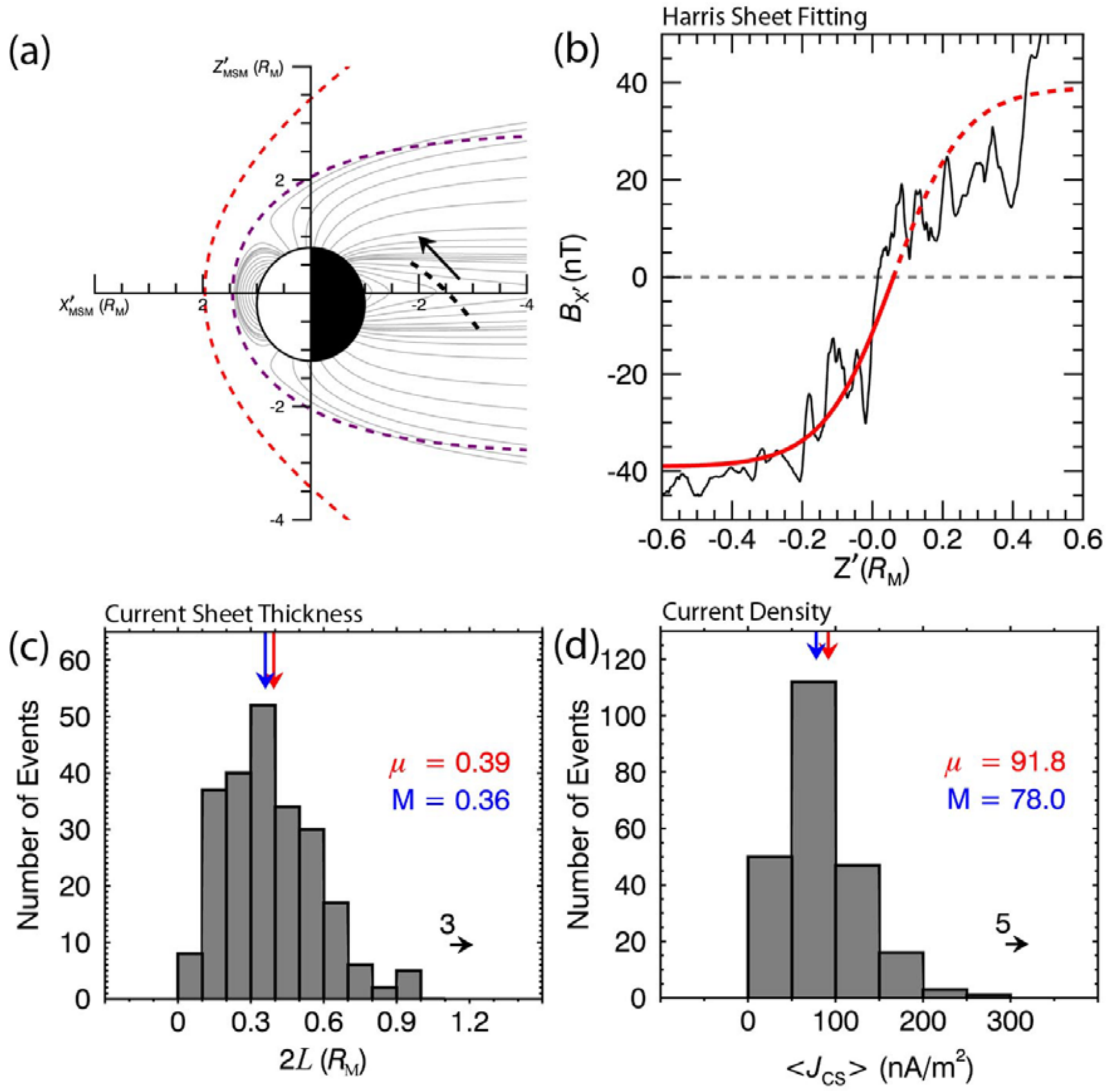

Figure 5.3 (a) Meridional view of MESSENGER crossing of the cross-tail CS on 23 August 2011. Arrow denotes the spacecraft travelling direction. (b) B_X measurements as a function of Z'_{MSM}. A Harris CS model is fitted to the smoothed data. Histograms of (c) 2L and (d) J_{CS} calculated from Harris model fits. μ and M represents mean and median of the distribution, respectively.

Figure 5.3a shows MESSENGER's trajectory across the cross-tail CS on 23 August 2011 in the meridional plane. Due to the high-latitude (~ 60°) periapsis of its orbit, MESSENGER moved rapidly towards Mercury at high northern latitudes, as it leaves the CPS, and the dipole magnetic field becomes dominant. For this reason, the fitting procedure is performed only for the southern half of the CS (i.e., $B_X < 0$). To remove the high frequency B_X fluctuations common to Mercury's CPS, 40-s sliding boxcar averages of the magnetic field are used to low-pass filter the data prior to fitting. Figure 5.3b shows the averaged B_X measurements (black) and the Harris model result (red) for the 23 August 2011 CPS crossing as a function of Z'_{MSM}. The normalized chi-square χ^2 for this fit is 0.005. This event meets the requirement of $\chi^2 \leq 0.01$ that we have set for acceptable fits. Out of the 319 cross-tail CS crossings identified in this study, 234 (~73%) were found to fit the Harris model with $\chi^2 \leq 0.01$. The high percentage of successful model fits suggests that the longer-wavelength structure of Mercury's cross-tail CS is usually well-represented by a Harris-type CS. Figures 5.3c and 5.3d show the distribution of full thickness ($2L$) and current density averaged over each CS crossing (J_{CS}) calculated from the Harris fitting procedure, respectively. Our analysis indicates that Mercury's CS has a mean $<2L>$ and $<J_{CS}>$ of ~ 0.39 R_M and ~ 92 nA/m^2, respectively.

5.3.3 Downtail Variation of B_Z and Plasma Pressure in the Central Plasma Sheet

We also examined how B_Z in the CPS varies with X'_{MSM}. The measured B_Z in the CPS can be modelled as a superposition of Mercury's intrinsic northward dipole field ($B_{Z,DIPOLE}$), magnetic field perturbations due to the cross-tail CS (δB_Z) and the contribution from Chapman-Ferraro current on the magnetopause surface ($B_{Z,CF}$). $B_{Z,CF}$ decreases approximately as 1/r away from the magnetopause surface. With a total current of ~ 10^5 A, we estimate that $B_{Z,CF}$ is only ~ 1 – 4 nT in the CPS, which is negligible as compared to $B_{Z,DIPOLE}$ or δB_Z. Hence, the $B_{Z,CF}$ term is ignored in our calculations.

The B_Z and $B_{Z,DIPOLE}$ as a function of X'_{MSM} are shown in Figure 5.4a. We calculated δB_Z by subtracting $B_{Z,DIPOLE}$ from B_Z as a function of X'_{MSM} as shown in Figure 5.4b. These data show a distinct local minimum at X'_{MSM} ~ -1.22 R_M. This minimum corresponds to the inner edge of the CS, where the southward magnetic field perturbation from the CS is the strongest and decreases exponentially sunward from this point. We also calculated the magnetic field perturbation of a two-dimensional semi-infinite CS slab model (red line) with thickness and uniform current density of ~ 0.39 R_M and 78 nA/m^2 taken from our fitting of the Harris model to the magnetic field profiles measured across the CS. The locations of the inner and outer edge of the CS slab model are free parameters in the least-square fitting between X'_{MSM} ~ -1.05 to -2.85 R_M. The outer edge of the CS slab model is ~ -4.5 R_M. We used the median, instead of the mean, of the current density distribution in this slab model since the median is a more accurrate measure of the true distribution due to the presence of outliers (events with high current density).

We also determined the downtail variation of the thermal plasma pressure in the CPS using the FIPS H$^+$ plasma data ($P_{th,FIPS}$). In this manner, the H$^+$ density (n) and temperature (T) were determined with ~ 1 minute resolution and used to compute $<P_{th,FIPS}>$ for each CPS crossing. The values were used to determine the downtail variation as shown in Figure 5.4c. The downtail profile of $P_{th,FIPS}$ is similar to that of $|B_{lobe}|^2$, which is expected when the CPS plasma thermal pressure is balanced by the lobe magnetic pressure. To determine the global stress balance of Mercury's CPS, we approximate, to zero-order, the downtail profile of $P_{th,FIPS}$ between X'_{MSM} = -1.2 and -2.2 R_M to be linear. It was found that $<P_{th,FIPS}>$ decreases linearly at a rate of ~ 0.62 ± 0.02 nPa/R_M and reaches a constant value of ~ 0.7 nPa at X'_{MSM} ~ -2.0 R_M.

5.3.4 Central Plasma Sheet Stress Balance

For an isotropic plasma sheet in static equilibrium (i.e., $\frac{dv}{dt} = 0$), ∇P must be balanced by the magnetic stress ($\mathbf{J} \times \mathbf{B}$) (i.e., $\nabla \mathrm{P} = \mathbf{J} \times \mathbf{B}$). Given $<J_{CS}>$ ~ 78 nA/m^2 and $<B_Z>$ ~ 9.5 nT as determined earlier, we estimate the $<\mathbf{J} \times \mathbf{B}>$ stress to be ~ 1.81 nPa/R_M, which is ~ 3 times greater than $\frac{dP_{\mathrm{th}}}{dX}$ (~ 0.62 nPa/R_M) determined by FIPS. The discrepancy suggests that pressure gradient in the H$^+$ ions alone is insufficient to maintain stress balance in the measured magnetic field in Mercury's CPS. This begs the question of whether the pressure gradient contribution from the heavy planetary ions plays an important part in maintaining

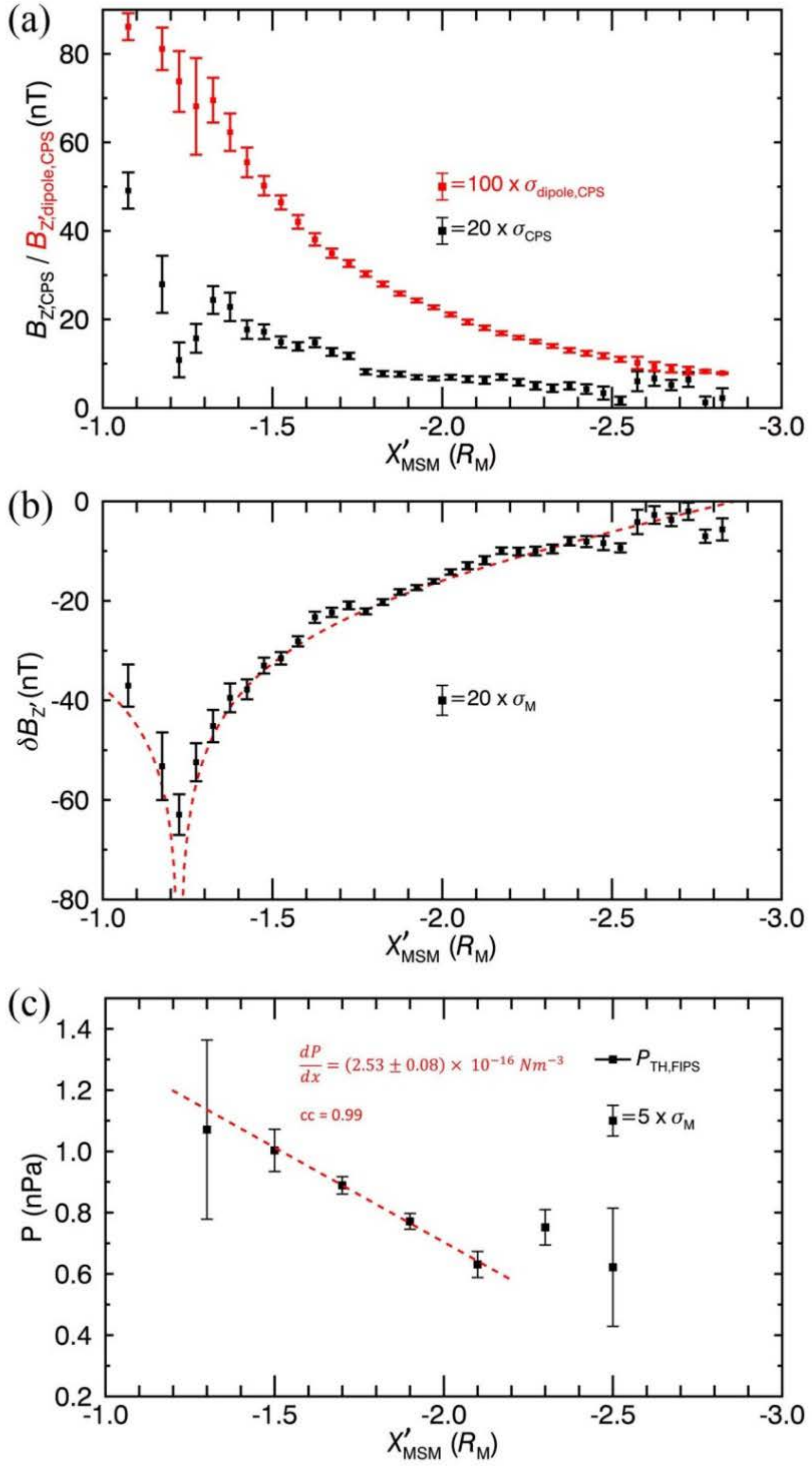

Figure 5.4 (a) Magnitude of measured B_Z and dipole magnetic field in the CPS and (b) δB_Z as a function of X'_{MSM}. (c) $P_{th,FIPS}$ as a function of X_{MSM}.

equilibrium in Mercury's CPS as is the case in Earth's magnetotail [*Kistler et al.,* 2005]. *Gershman et al.,* [2014] showed that Na^+ ions are present with a number density ~ 10% of the H^+ density. For the heavy planetary ions to play an important role in maintaining equilibrium in Mercury's CPS, the rate of decrease of plasma pressure with X'_{MSM} would have to be greater than that of the protons. *Rich et al.* [1972] showed that pressure anisotropy in the dominant H^+ ion is required in Earth's CPS to maintain stress balance. However, further analyses of the FIPS measurements, which are beyond the scope of this study, are required in order to evaluate the possible role of proton temperature anisotropies in maintaining equilibrium within Mercury's CPS.

5.4 Discussion

We have conducted the first comprehensive study of Mercury's central plasma sheet and the embedded cross-tail current sheet using MESSENGER's MAG and FIPS measurements. Results from the analysis of 319 cross-tail CS traversals indicate that the magnetic field profiles are well-described using a Harris model, with full CS thickness and mean current density of 0.39 R_M and 92 nA/m^2, respectively. This thickness is in good agreement with earlier results [*Johnson et al.* 2012; *Sun et al.* 2016]. Our current density determination is much higher than at Earth, i.e., ~ 4 to 25 nA/m^2 [*Artemyev et al.,* 2011], but it is in good agreement with global MHD simulations of Mercury's magnetosphere [*Jia et al.,* 2015].

We also report the first determination of the inner edge of Mercury's CS derived from MESSEGNER's magnetic field data. This local minimum in δB_Z indicates that the inner edge of the CS is located at ~ -1.22 R_M. At Earth, the inner edge of the CS is located at X'_{GSM} ~ 10 – 12 R_E during quiet intervals and shifts earthward to ~ 6 – 7 R_E during active times [*Wang et al.,* 2004; *Kalegaev et al.,* 2014]. Using the scaling factor of ~ 8, the quiet-time location of the inner edge of Mercury's CS based on the Earth value would be ~ 1.25 R_M, which agrees well our MESSENGER results. Determination of the inner edge location is important to better constrain the physical properties of Mercury's CS in empirical

[*Alexeev et al.,* 2010, *Korth et al.,* 2015] and global simulation models [*Trávníček et al.,* 2007; *Jia et al.*, 2015].

Our statistical analyses of the MESSENGER data show that B_{lobe} decreases with increasing X'_{MSM} with an exponent of ~ 3.1. At Earth, this exponent ranges from ~ 0.9 to 2.7 for downtail distances [*Nakai et al.,* 1999], which is lower than our Mercury results. This suggests that magnetotail flaring should cease comparatively closer to Mercury than is the case at Earth. At Earth, the flaring of the lobes is observed to cease at X_{GSM} ~ -100 – -120 R_{E} [*Slavin et al.*, 1985]. We would expect flaring of Mercury's lobe to cease at ~ -12 – -15 R_{M}, which is outside the range of MESSENGER's orbit. Hence the distance at which the flaring ceases is still an open question, calling for future measurements at X'_{MSM} < -3 R_{M}. The rate of decrease of B_{CPS} was also shown to follow a power law, with an exponent of ~ 8.9. The corresponding rate of decrease in Earth's CPS ranges from ~ 1.14 to 3.36 for different downtail distances [*Nakai et al.,* 1999], which is significantly slower than the Mercury values determined here.

Our analysis shows that the $<B_{\mathrm{Z}}>$ in the CS region sampled by MESSENGER is primarily positive, which suggests that the spacecraft spent most of its time crossing the CS planetward of the NMNL. The estimated mean location of the NMNL based upon the rate of decrease in B_{Z} is ~ -2.95 R_{M}. The location of the near Earth neutral line (NENL) had been a widely debated within the community due to importance of reconnection onset location in substorm models. Similarly, the location of the NMNL is important in understanding Mercury's plasma sheet conditions during substorm initiation. The average NENL location has been shown to occur between X_{GSM} ~ -20 and -30 R_{E} [e.g. *Nagai and Machida,* 1998]. A THEMIS survey of magnetotail flux ropes and travelling compression regions estimated the NENL to be located closer to -30 R_{E} during solar minimum [*Imber et al.,* 2011]. The location of NMNL is then expected to be ~ -2.5 – -3.8 R_{M}, which agrees with our estimated NMNL location of -2.95 R_{M}. Furthermore, *Slavin et al.* [2012a] and *DiBraccio et al.* [2015] estimated the location of the NMNL to be between ~ -2 and -3 R_{M} based on the spatial distribution of sunward and anti-sunward flux ropes. Their NMNL location is closer to Mercury, most likely because they were studying intervals of intense reconnection during which X-line is expected to form closer to the planet.

Analysis of $\langle P_{th} \rangle$ in Mercury's CPS indicated that it decreases linearly with X'_{MSM} between -1.2 and -2.2 R_M at a rate of 0.62 ± 0.02 nPa/R_M. However, this is only ~ 33% of the mean measured $\mathbf{J} \times \mathbf{B}$ in the CPS (~ 1.81 nPa/R_M). Hence, we find that the pressure gradient from H^+ is insufficient to maintain pressure balance within Mercury's CPS. Contributions from heavy planetary ions and/or H+ temperature anisotropy are necessary, but further analysis of FIPS measurements is beyond the scope of this study.

In this chapter, we examined the structure, X-line location and MHD stress balance of Mercury's magnetotail by analyzing the variation of magnetic field and plasma measurements with downtail distance. In the next chapter, we will study the dawn-dusk variations of these parameters in Mercury's current sheet.

References

Alexeev, I. I., E. S. Belenkaya, S. Yu. Bobrovnikov, J. A. Slavin, *and* M. Sarantos *(*2008*)*, Paraboloid model of Mercury's magnetosphere, *J. Geophys. Res., 113, A12210, doi:*10.1029/2008JA013368.

Alexeev, I. I., et al. (2010),Mercury's magnetospheric magnetic field after the first two MESSENGER flybys, *Icarus, 209*, 23–39, doi:10.1016/j.icarus.2010.01.024.

Anderson, B. J., M. H. Acuña, D. A. Lohr, J. Scheifele, A. Raval, H. Korth, and J. A. Slavin (2007), The Magnetometer instrument on MESSENGER, *Space Sci. Rev., 131*, 417–450, doi:10.1007/s11214-007-9246-7.

Anderson, B. J., C. L. Johnson, H. Korth, M. E. Purucker, R. M. Winslow, J. A. Slavin, S. C. Solomon, R. L. McNutt Jr., J. M. Raines, and T. H. Zurbuchen (2011), The global magnetic field of Mercury from MESSENGER orbital observations, *Science*, **333**, 1859–1862, doi:10.1126/science.1211001.

Andrews, G. B., et al. (2007), The Energetic Particle and Plasma Spectrometer instrument on the MESSENGER spacecraft, *Space Sci. Rev., 131*, 523–556, doi:10.1007/s11214-007-9272-5.

Artemyev, A. V., A. A. Petrukovich, R. Nakamura, and L. M. Zelenyi (2011), Cluster statistics of thin current sheets in the Earth magnetotail: Specifics of the dawn flank, proton temperature profiles and electrostatic effects, *J. Geophys. Res., 116*, A09233, doi:10.1029/2011JA016801.

Baumjohann, W., G. Paschmann, N. Sckopke, C. A. Cattell, and C. W. Carlson (1988), Average ion moments in the plasma sheet boundary layer, *J. Geophys. Res., 93*(A10), 11507–11520, doi:10.1029/JA093iA10p11507.

Birn, J., et al. (2001), Geospace Environmental Modeling (GEM) Magnetic Reconnection Challenge, *J. Geophys. Res., 106(A3)*, 3715–3719, doi:10.1029/1999JA900449.

DiBraccio, G. A., J. A. Slavin, S. A. Boardsen, B. J. Anderson, H. Korth, T. H. Zurbuchen, J. M. Raines, D. N. Baker, R. L. McNutt Jr., and S. C. Solomon (2013), MESSENGER observations of magnetopause structure and dynamics at Mercury, *J. Geophys. Res. Space Physics, 118*, 997–1008, doi:10.1002/jgra.50123.

DiBraccio, G. A., et al. (2015), MESSENGER observations of flux ropes in Mercury's magnetotail, *Planet. Space Sci., 115*, 77–89, doi:10.1016/j.pss.2014.12.016.

Gershman, D. J., J. A. Slavin, J. M. Raines, T. H. Zurbuchen, B. J. Anderson, H. Korth, D. N. Baker, *and* S. C. Solomon *(*2014*)*, Ion kinetic properties in Mercury's pre-midnight plasma sheet, *Geophys. Res. Lett.*, *41*, 5740–5747, *doi:*10.1002/2014GL060468.

Harris, E. G., On a plasma sheath separating regions of oppositely directed magnetic field, *Nuovo Cimento*, *23*, 115–121, 1962.

Jackman, C. M., et al. (2014), Large-scale structure and dynamics of the magnetotails of Mercury, Earth, Jupiter and Saturn, *Space Sci. Rev.*, *182*, 85–154, doi:10.1007/s11214-014-0060-8.

Kalegaev V.V., Alexeev I.I., Nazarkov I.S., Angelopoulos V., Runov A. (2014) On the large-scale structure of the tail current as measured by THEMIS, *Advances in Space Research, Volume 54, Issue 9*, Pages 1773-1785, ISSN 0273-1177, http://dx.doi.org/10.1016/j.asr.2014.07.019.

Kistler, L. M., et al. (2005), Contribution of nonadiabatic ions to the cross-tail current in an O^+ dominated thin current sheet, *J. Geophys. Res.*, *110*, A06213, doi:10.1029/2004JA010653.

Korth, H., N. A. Tsyganenko, C. L. Johnson, L. C. Philpott, B. J. Anderson, M. M. Al Asad, S. C. Solomon, and R. L. McNuttJr. (2015), Modular model for Mercury's magnetospheric magnetic field confined within the average observed magnetopause. *J. Geophys. Res. Space Physics*, *120*, 4503–4518. doi: 10.1002/2015JA021022.

Imber, S. M., J. A. Slavin, H. U. Auster, *and* V. Angelopoulos *(*2011*)*, A THEMIS survey of flux ropes and traveling compression regions: Location of the near-Earth reconnection site during solar minimum, *J. Geophys. Res.*, *116*, *A02201*, *doi:*10.1029/2010JA016026.

Imber, S. M., J. A. Slavin, S. A. Boardsen, B. J. Anderson, H. Korth, R. L. McNutt Jr., and S. C. Solomon (2014), MESSENGER observations of large dayside flux transfer events: Do they drive Mercury's substorm cycle?, *J. Geophys. Res. Space Physics*, *119*,5613–5623, doi:10.1002/2014JA019884.

Jia, X., J. A. Slavin, T. I. Gombosi, L. K. S. Daldorff, G. Toth, and B.van der Holst (2015), Global MHD simulations of Mercury's magnetosphere with coupled planetary interior: Induction effect of the planetary conducting core on the global interaction. *J. Geophys. Res. Space Physics*, *120*, 4763–4775. doi: 10.1002/2015JA021143.

Johnson, C. L., *et al.* *(*2012*)*, MESSENGER observations of Mercury's magnetic field structure, *J. Geophys. Res.*, *117*, *E00L14*, *doi:*10.1029/2012JE004217.

Nagai, T. and Machida, S. (1998) Magnetic Reconnection in the Near-Earth Magnetotail, in New Perspectives on the Earth'S Magnetotail (eds A. Nishida, D.N. Baker and S.W.H. Cowley), American Geophysical Union, Washington, D. C.. doi: 10.1029/GM105p0211.

Nakai, H., Y. Kamide, and C. T. Russell (1999), Dependence of the near-Earth magnetotail magnetic field on storm and substorm activities, *J. Geophys. Res., 104(A10)*, 22701–22711, doi:10.1029/1999JA900273.

Nakamura, R., et al., (2002), Fast flow during current sheet thinning, *Geophys. Res. Lett., 29(23)*, 2140, doi:10.1029/2002GL016200.

Narita, Y., Nakamura, R., and Baumjohann, W. (2013) Cluster as current sheet surveyor in the magnetotail, *Ann. Geophys., 31*, 1605-1610, doi:10.5194/angeo-31-1605-2013.

Ogilvie, K. W., J. D. Scudder, V. M. Vasyliunas, R. E. Hartle, and G. L. Siscoe (1977), Observations at the planet Mercury by the plasma electron experiment: Mariner 10, *J. Geophys. Res., 82*, 1807–1824, doi:10.1029/JA082i013p01807.

Raines, J. M., J. A. Slavin, T. H. Zurbuchen, G. Gloeckler, B. J. Anderson,D. N. Baker, H. Korth, S. M. Krimigis, and R. L. McNutt Jr. (2011), MESSENGER observations of the plasma environment near Mercury, *Planet. Space Sci., 59*, 2004–2015, doi:10.1016/j.pss.2011.02.004.

Rich, F. J., V. M. Vasyliunas, and R. A. Wolf (1972), On the balance of stresses in the plasma sheet, *J. Geophys. Res., 77(25)*, 4670–4676, doi:10.1029/JA077i025p04670.

Sharma, A. S., et al. (2008), Transient and localized processes in the magnetotail: A review, *Ann. Geophys., 26*,955–1006.

Slavin, J. A., *and* R. E. Holzer *(*1979*)*, The effect of erosion on the solar wind stand-off distance at Mercury, *J. Geophys. Res.,* 84, 2076–2082, *doi:*10.1029/JA084iA05p02076.

Slavin, J. A., E. J. Smith, D. G. Sibeck, D. N. Baker, R. D. Zwickl, and S.-I. Akasofu (1985), An ISEE-3 study of average and substorm conditions in the distant magnetotail, *J. Geophys. Res., 90,* 10,875–10,895, doi:10.1029/JA090iA11p10875.

Slavin, J. A., *et al. (*2009*)*, MESSENGER observations of magnetic reconnection in Mercury's magnetosphere, *Science, 324,* 606–610, *doi:*10.1126/science.1172011.

Slavin, J. A., *et al. (*2010*)*, MESSENGER observations of extreme loading and unloading of Mercury's magnetic tail, *Science, 329,* 665–668, *doi:*10.1126/science.1188067.

Slavin, J. A., *et al. (*2012a*)*, MESSENGER and Mariner 10 flyby observations of magnetotail structure and dynamics at Mercury, *J. Geophys. Res., 117, A01215, doi:*10.1029/2011JA016900.

Slavin, J. A., *et al. (*2012b*),* MESSENGER observations of a flux-transfer-event shower at Mercury*, J. Geophys. Res.,117, A00M06, doi:*10.1029/2012JA017926*.*

Sun, W.-J., J. A. Slavin, S. Fu, J. M. Raines, Q.-G. Zong, S. M. Imber, Q. Shi, Z. Yao, G. Poh, D. J. Gershman, Z. Pu, T. Sundberg, B. J. Anderson, H. Korth, and D. N. Baker (2015), MESSENGER observations of magnetospheric substorm activity in Mercury's near magnetotail. *Geophys. Res. Lett., 42*, 3692–3699. doi: 10.1002/2015GL064052.

Sun, W. J., S. Y. Fu, J. A. Slavin, J. M. Raines, Q. G. Zong, G. K. Poh, and T. H. Zurbuchen (2016), Spatial distribution of Mercury's flux ropes and reconnection fronts: MESSENGER observations*, J. Geophys. Res. Space Physics, 121*, doi:10.1002/2016JA022787.

Sundberg, T., et al. (2012), MESSENGER observations of dipolarization events in Mercury's magnetotail, *J. Geophys. Res., 117,* A00M03, doi:10.1029/2012JA017756.

Trávníček, P. M., P. Hellinger, D. Schriver, D. Herčík, J. A. Slavin, and B. J. Anderson (2009), Kinetic instabilities in Mercury's magnetosphere: Three-dimensional simulation results, *Geophys. Res. Lett.*, *36*, L07104, doi:10.1029/2008GL036630.

Tsyganenko, N. A., and D. P. Stern (1996), Modeling the global magnetic field of the large-scale Birkeland current systems, *J. Geophys. Res.*, *101*(A12), 27187–27198, doi:10.1029/96JA02735.

Volwerk, M., et al. (2013),Comparative magnetotail flapping: an overview of selected events at Earth, Jupiter and Saturn, *Ann. Geophys., 31,* 817–833, doi:10.5194/angeo-31-817-2013.

Wang, C.-P., L. R. Lyons, M. W. Chen, and F. R. Toffoletto (2004), Modeling the transition of the inner plasma sheet from weak to enhanced convection, *J. Geophys. Res., 109,* A12202, doi:10.1029/2004JA010591.

CHAPTER VI

ON THE DAWN-DUSK ASYMMETRY OF MERCURY'S CROSS-TAIL CURRENT SHEET

This chapter is taken from Gangkai Poh, James A. Slavin, Xianzhe Jia, Jim M. Raines, Suzanne M. Imber, Wei-Jie Sun, Daniel J. Gershman, Gina A. DiBraccio, Kevin J. Genestreti, Andy W. Smith (2016), On The Dawn-Dusk Asymmetry Of Mercury's Cross-Tail Current Sheet, manuscript in preparation.

Abstract:

Using 4 years of MESSENGER magnetic field and plasma data, we analyzed 319 crossings of Mercury's cross-tail current sheet. We determined that the measured B_Z in the current sheet is observed to be higher on the dawn side than the dusk side by approximately a factor of three and that the asymmetry decreases with increasing downtail distance. This result is consistent with expectations; MHD stress balance would imply that magnetic fields threading the more (less) stretched current sheet in the dusk side (dawn side) have a higher (lower) plasma beta. Least squares fitting of MESSENGER's observations to a Harris current sheet model confirm this behavior with mean current sheet thickness being greatest on the dawn side when B_Z is largest. We suggest that enhancement of heavy ions in the dusk side current sheet found by earlier studies, due to centrifugal acceleration of ions from the cusp and gradient-curvature drift in the current sheet, provides at least a partial explanation of the dawn-dusk current sheet asymmetries found in this study. We also report the first possible observation of Mercury's substorm current wedge (SCW) and estimate the total current due to the pileup of magnetic flux to be ~ 6 kA. The inertial current carried by an individual high speed flow (i.e., Bursty Bulk Flow) is estimated to be ~ 20% of the

total current of the SCW. This suggests that Mercury's SCW could possibly form as the aggregate effect of many individual high speed sunward flows, similar to the SCW formation mechanism proposed at Earth. The most likely current closure path for these SCW currents would be similar to that for Mercury's Region 1 field-aligned currents, where the current close radially through Mercury's resistive regolith, then across the surface of the planet's highly conductive iron core.

6.1 Introduction

The availability of continuous in-situ magnetic field and plasma measurements has allowed us to conduct large scale statistical studies to understand and characterize the physical properties of planetary magnetotails. From these studies, we have learned that dawn-dusk asymmetry of the magnetotail properties is a ubiquitous phenomenon in terrestrial [See *Walsh et al.,* 2014] and the Jovian magnetotails, such as Jupiter and Saturn [e.g., *Bunce et al.,* 2001; *Arridge et al.,* 2015a; *Smith et al.*, 2016] where the asymmetries are caused by internal plasma dynamics. To date, no comprehensive studies on asymmetries in Mercury's magnetotail have been conducted.

Magnetotail asymmetries at Earth are most extensively studied since multi-point measurements are readily available. *Slavin et al.,* [1985] reported ISEE 3 observation of higher B_Z by ~ 1 nT in the near Earth ($|X| < 100R_E$) dawn side plasma sheet. *Fairfield et al.,* [1981] reported similar asymmetry observation using IMP 6, 7 and 8 data. More recent studies using Geotail [*Wang et al.,* 2006; *Vasko et al.,* 2015] confirmed the asymmetries in B_Z and current sheet thickness in the terrestrial magnetotail. The magnitude of B_Z is an indicator of the magnetic field geometry of the current sheet. A stronger B_Z indicates a less stretched, thicker current sheet while a weaker B_Z indicates a more stretched, thinner current sheet. This asymmetry in current sheet thickness had been observed by AMPTE/IRM [*Baumjohann et al.*, 1990].

Thin current sheets are often associated with the onset of magnetic reconnection; hence a thinner dusk-side magnetotail current sheet means reconnection may occur preferentially on the dusk than dawn-side. Recent studies on the location of magnetotail reconnection sites [*Nagai et al.,* 2013a; *Genestreti et al.,* 2014; 2015] show that reconnection sites tends to occur on the dusk side of the current layer for the entire solar cycle. The occurrence of magnetic structures formed as a result of magnetotail reconnection, such as flux ropes, travelling compression regions (TCR) [*Imber et al.,* 2011] and dipolarization fronts [*Liu et al.,* 2013] are also found to have similar dawn-dusk asymmetries with higher occurrence rate on the dusk-side. Extensive statistical studies had been conducted at Earth's magnetotail to characterize asymmetries in the magnetotail dynamics and the list of work done on this persistent magnetotail phenomenon is not exhaustive. We will refer the reader to the review paper by *Walsh et al.,* [2014] for a complete review of asymmetries of all magnetotail processes and properties.

Since the flybys of Mariner 10 spacecraft, it was known that Mercury possess a magnetotail similar to the Earth's due to solar wind interaction with its largely dipolar magnetic field. Magnetic reconnection opens magnetic flux at the dayside magnetopause, which is then transported anti-sunward into the tail lobes. The northern and southern tail lobes contain sunward and anti-sunward magnetic field, respectively; a magnetotail current sheet divides the two lobes with the diamagnetic cross-tail current flowing from dawn to dusk of Mercury's magnetotail. However, the Mariner 10 spacecraft only performs flybys of Mercury's magnetotail, which do not provide enough data points to conduct a systematic study on magnetotail asymmetries at Mercury. The continuous plasma and magnetic field measurements from the Mercury Surface, Space Environment, Geochemistry, and Ranging (MESSENGER) provide us with the opportunity to conduct such a study when it became the first spacecraft to orbit Mercury in 2011. Recently, *Poh et al.* [2017] identified a total of 319 current sheet crossings over 4 years of MESSENGER data, and showed that the overall structure of Mercury's current sheet can be well-represented by a Harris current sheet model [*Harris,* 1962]. From the analysis on downtail variation of B_Z, *Poh et al.* [2017] also concluded that MESSENGER is planetward of the statistical Near Mercury Neutral Line (NMNL) location throughout its orbital mission.

Magnetic reconnection processes at Mercury's magnetotail is also found to be very similar to that of Earth's. High reconnection rates at Mercury's magnetopause [*Slavin and Holzer,* 1979; *Slavin et al.,* 2009; *Dibraccio et al.,* 2013] increase the overall energy in

Mercury's magnetotail by loading it with magnetic flux. Observations of dipolarization [*Sundberg et al.,* 2012], substorms activity [*Sun et al.,* 2015] and plasmoids [*Slavin et al.,* 2010; *DiBraccio et al.,* 2015; *Sun et al.,* 2016] supports the idea of rapid dissipation of magnetic energy in the tail through magnetic reconnection. Magnetotail reconnection sends newly-reconnected closed (i.e., connected to Mercury) and open (i.e., connected to solar wind) magnetic field lines planetward and tailward of the reconnection X-line, respectively. At Earth, these newly-reconnected closed field lines embedded in high speed bursty-bulk flows (BBFs) brake as they encounter the stronger magnetic fields and higher plasma pressures found in the inner magnetosphere [*Nakamura et al.,* 2002]. The aggregate effect of multiple dipolarization events is the formation of Earth's substorm current wedge (SCW) and the onset of the auroral substorm [*Hesse and Birn,* 1991; *Shiokawa et al.,* 1998; *Baumjohann et al.,* 1999]. *Slavin et al.* [2007] reported evidence of possible observations of field-aligned current FAC associated with a terrestrial-type SCW at Mercury using Mariner 10 measurements and estimated the total current to be ~ 1.6 MA. To date, there is no direct observation of a possible terrestrial-type SCW at Mercury.

With our current understanding of Mercury's magnetotail dynamics, this paper aims to answer the question of whether any dawn-dusk asymmetries, similar to that at Earth, in the magnetotail properties and processes are also present at Mercury. One might expect the same dawn-dusk asymmetries to also be present in Mercury's magnetotail since Mercury's global magnetosphere structure is similar to Earth, with the exception that Mercury has a dipole moment ~ 100 times weaker than Earth's [*Alexeev et al.,* 2010; *Anderson et al.,* 2011] and a stronger solar wind effect due to its close proximity to the sun. MESSENGER had a highly-inclined polar orbit where the spacecraft traverse the magnetotail current sheet in a plane that is almost normal to the current layer, thereby allowing us to study the vertical profile of the current sheet.

The paper is organized as follows. In the next section, we summarize the structure of Mercury's current sheet based on MESSENGER observations from the list of identified current sheet crossings from *Poh et al.* [2017] and present the case study results of Mercury's current sheet dynamics. In section 3, we present the results of statistical analyses performed to identify asymmetries in the physical properties of the current sheet and report the first possible measurement of Mercury’s substorm current wedge. In section 4, we discuss possible explanations for the observed magnetotail asymmetries, the nature of Mercury’s substorm current wedge and the implications of our results.

6.2 MESSENGER Instrumentation and Event Selection

In this study, we utilize the full-resolution magnetic field and plasma data from MESSENGER’s Magnetometer (MAG) (20 vectors/s) and Fast Imaging Plasma Spectrometer (FIPS) (1 energy scan per 10s), respectively. The coordinate system used in our analysis is the aberrated Mercury solar magnetospheric (MSM’) coordinate system. In the MSM system centered on Mercury’s offset internal dipole, the *X*-axis is sunward along the Sun-Mercury line, *Z*-axis is parallel to the planetary spin axis and *Y*-axis completes the right-handed system. We also rotate the MSM *X*- and *Y*-axes such that X'_{MSM} is opposite to the solar wind velocity vector to account for the aberration effect (i.e., orbital motion of Mercury with respect to the solar wind); the rotation angle was calculated daily by assuming a radial solar wind with constant speed of 400 km/s. We also used the total of 319 current sheet crossings identified in *Poh et al.* [2017] (hereafter referred as Poh17); these current sheet crossings were identified based on a set of criteria (see Poh17 for more details). To characterize the properties of Mercury’s current sheet, Poh17 fitted the magnetic field measurements of each current sheet crossing to the one-dimensional Harris current sheet [*Harris*, 1972] model using a reduced least-squares method. The relationship between B_X and Z'_{MSM} is given by:

$$B_X(Z'_{MSM}) = B_0\, tanh\left(\frac{Z'_{MSM}-z_0}{L}\right) \quad (6.1)$$

where B_0 is the asymptotic lobe field, z_0 is the north-south position of the current sheet (CS) center and L is the characteristic half-thickness of the CS. These are the free parameters in the reduced least-squares fitting procedure of the Harris model to the $B_{X'}$ magnetic field measurements. The corresponding equation for the cross-tail current density (J_Y) is given by:

$$J_Y(Z'_{MSM}) = \frac{B_0}{\mu_0 L} sech^2\left(\frac{Z'_{MSM}-z_0}{L}\right) \tag{6.2}$$

A χ^2 value of 0.01 was set as the criterion for goodness of fit. Their results showed that ~ 73% of the 319 cross-tail current sheet crossings have $\chi^2 \leq 0.01$, which suggests that the long-wavelength structure of Mercury's current sheet is well-represented by a Harris-type

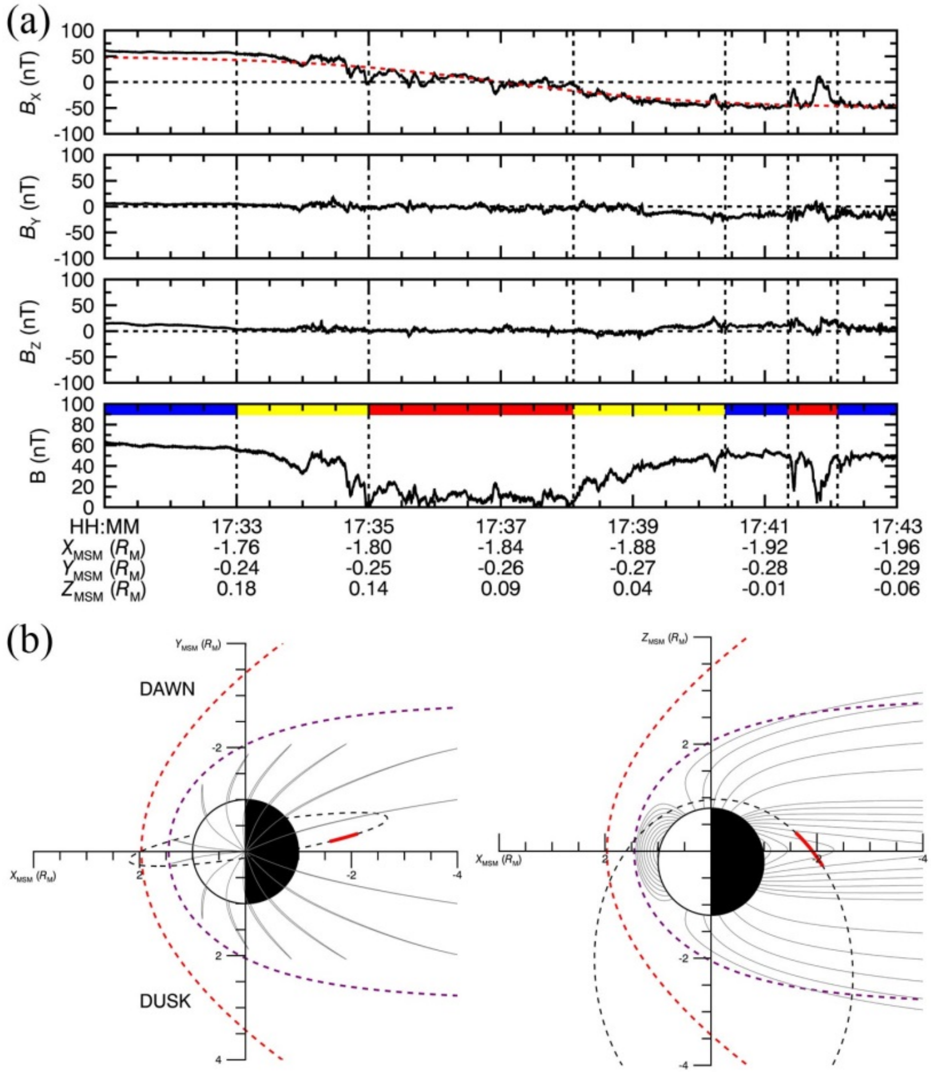

Figure 6.1 (a) Full-resolution magnetic field measurements of an example MESSENGER orbit on 28th August 2013 in aberrated Mercury solar magnetic (MSM') coordinates. The dotted lines and color bars separate each regions of Mercury's magnetotail, with blue, yellow and red color bars representing the northern/southern tail lobe, plasma sheet boundary layer and current sheet respectively. (b) The orbit of MESSENGER on 28th August 2013 in the equatorial (left) and meridional (right) plane. The model bow shock (BS) and magnetopause (MP) from *Winslow et al.*, [2013], scaled to fit observed average boundary crossings are shown in dotted lines; the Sun is to the left and the scaled T96 model magnetic field lines [*Tsyganenko*, 1995] using a linear scaling factor of 8 is shown in grey solid lines. Red line indicates the interval when MESSENGER traversed Mercury's current sheet.

current sheet. The reader is referred to Poh17 for more details on the Harris current sheet fitting procedure.

Figure 6.1a shows MESSENGER's magnetic field observation of Mercury's cross-tail CS traversal on 28 August 2013. The normalized χ^2 value of this reduced least-square fitting is ~ 0.003 and the Harris current sheet fitting result (red) is shown in top panel of Figure 6.1a. The interval starts off with MESSENGER in the northern tail lobe as shown by the blue bar, where $B_{X'} > 0$ and $|\mathbf{B}|$ is constant at ~ 60 nT. The spacecraft then encounters the plasma sheet boundary layer (PSBL) at ~ UT 17:33, where $|\mathbf{B}|$ decreases and fluctuates with amplitudes of ~ ±10 nT. MESSENGER enters the central plasma sheet at UT 17:35 before crossing the embedded current sheet (i.e., $B_{X'}$ reverses polarity) at ~ UT 17:37 and exits into the southern tail lobe ($B_{X'} < 0$). MESSENGER also observed short-wavelength decreases in $|\mathbf{B}|$ with corresponding increases in $B_{X'}$ (i.e., "re-encountering" of the current sheet in short timescale) when the spacecraft is deep in the southern tail lobe. These magnetic field signatures are typical of a transient magnetotail process known as tail flapping, where the magnetotail moves in the north-south direction relative to the spacecraft. It is a common phenomenon observed in Earth's [*Volwerk et al.*, 2013] and other planetary magnetotail (e.g. Venus [*Rong et al.*, 2015b] and Mars [*DiBraccio et al.*, 2015]).

6.3 Analysis

6.3.1 Cross-tail Variation of $B_{Z'}$

From the current sheet crossings identified by Poh17, we examined the variation of the *z*-component of the central plasma sheet magnetic field (i.e., $B_{Z'}$) as a function of cross-tail distance (i.e., Y'_{MSM}). Figure 6.2 is derived by binning all measurements into four X'_{MSM} ranges between -1.4 to -2.6 R_M at intervals of 0.3 R_M and eight Y'_{MSM} ranges between -1.6 to 1.6 R_M at intervals of 0.4 R_M. Note that the error bar for each point represents the standard error of data points in each bin and is magnified by 100 times in Figure 6.2 for clarity. Figure 6.2 shows two important magnetic field features of Mercury's current sheet.

First, Figure 6.2 shows significant dawn-dusk asymmetry of varying degrees in B_Z, where B_Z is higher at the dawn side than dusk side of the current sheet and the strength of the asymmetry decreases with increasing downtail distances. Panel 1 of Figure 5.2 shows

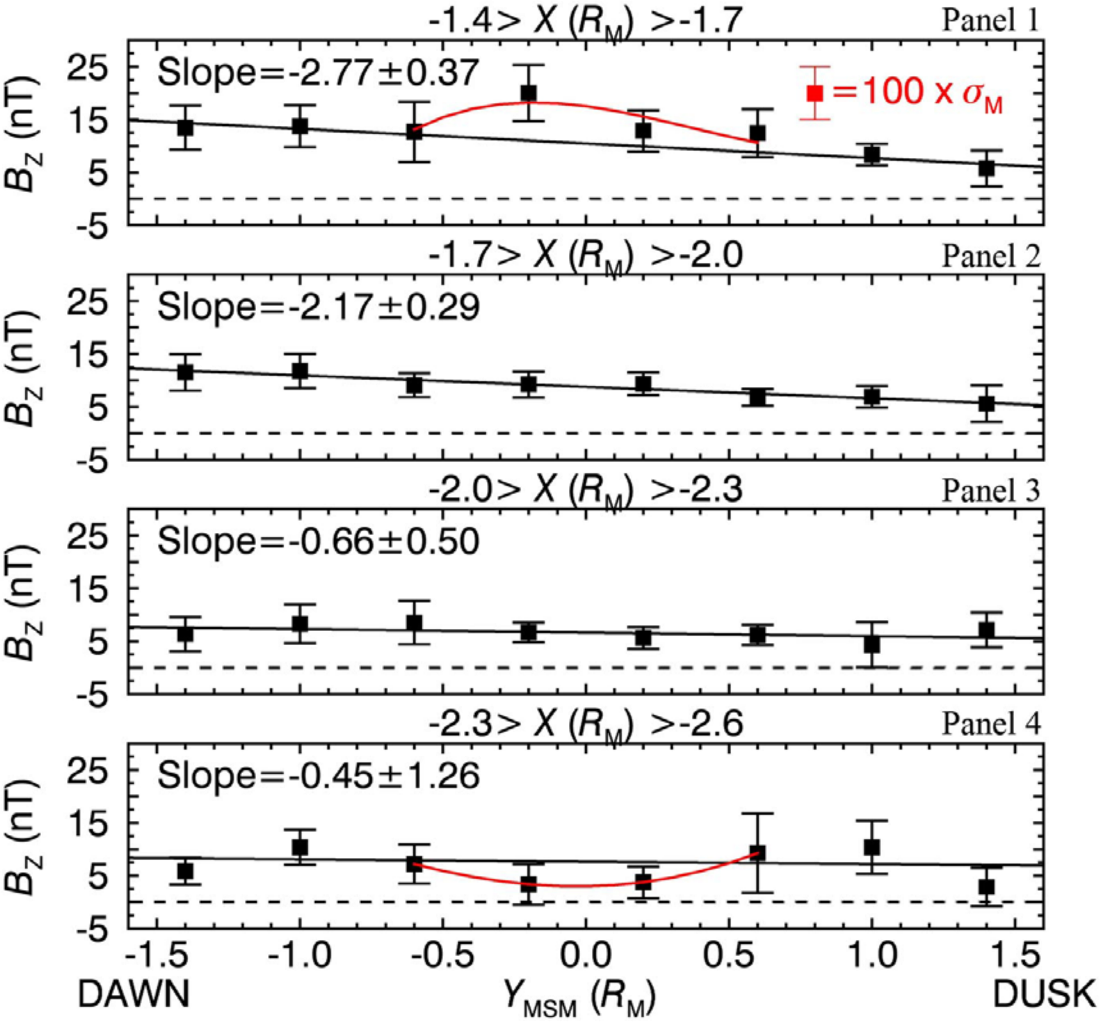

Figure 6.2 Plot of B_Z as a function of X'_{MSM} and Y'_{MSM}. B_Z is binned into four downtail distance from X'_{MSM} = -1.4 R_M to -2.6 R_M at bins of 0.3 R_M and dawn-dusk direction from Y'_{MSM} = -1.6 R_M to 1.6 R_M at bins of 0.4 R_M. The error bars are standard error of the mean B_Z in each bin and the error bars are magnified by 100 times for visual purposes. The strength of the dawn-dusk asymmetry in each downtail distance is determined by the slope of least-square fitted lines (black). Least-squares fitted red lines for closest (i.e. -1.4 $R_M > X'_{MSM} >$ -1.7 R_M) and furthest (i.e. -2.3 $R_M > X'_{MSM} >$ -2.6 R_M) represents magnetic flux pileup and enhanced reconnection region, respectively.

that the dawn side B_Z (~ 15 nT) is 3 times larger than dusk side B_Z (~ 5 nT) in the region closest to Mercury (i.e. $-1.4 < X'_{MSM}$ (R_M) < -1.7). As the downtail distance increases (Panel 2 and 3), the dawn-dusk difference in B_Z decreases (i.e. ~ 7.5 nT and 2.5 nT, respectively) with the dawn side B_Z greater than the dusk side. Panel 4 of Figure 6.2 shows no distinct dawn-dusk B_Z asymmetry feature in the region furthest from Mercury (i.e. $-2.3 < X'_{MSM}$ (R_M) < -2.6). The decrease in the degree of asymmetry is also evident from the decreasing negative slope of the least-square linear fit (black line) from 2.77 to 0.45. Such dawn-dusk asymmetry had also been observed and studied at Earth [*Slavin et al.,* 1985; *Wang et al.,* 2006; *Vasko et al.*, 2015]. However, the asymmetry is stronger at Mercury as compared to Earth and possible explanation for this phenomenon will be discussed in Section 6.4.2.

Second, our analysis suggests the possible observation of a substorm current wedge (SCW) in Mercury's magnetotail. Apart from the dawn-dusk asymmetry, Panel 1 shows a further increase in B_Z (red line) around the midnight meridian. We believe that this increase in B_Z is due to the pileup of magnetic flux as the planetward convecting magnetic field lines, from a reconnection X-line further downtail, brake into the stronger near-Mercury magnetic field. Such process is analogous to the formation of a substorm current wedge (SCW) at Earth [*McPherron et al.,* 1973; *Kepko et al.*, 2015]. Consequently, a weak decrease in B_Z (red line), due to enhanced reconnection occurring, was also observed near the midnight meridian in the downtail region of $-2.3 < X'_{MSM}$ (R_M) < -2.6 as shown in Panel 4. Our result also shows that the pileup region of magnetic flux is not centered on the midnight meridian. The peak increase in B_Z occurs at Y'_{MSM} ~ -0.2 R_M (i.e., shifted towards postmidnight current sheet). This indicates that more magnetic flux is being pileup dawn side than dusk side, suggesting dawn-dusk asymmetry in tail reconnection. To determine whether this asymmetric preference of flux pile-up is a real feature, we remove the magnetic field contributions from both Mercury's planetary dipole field and the cross-tail current sheet by subtracting the B_Z values in Panel 1 with the baseline values determined from the least-squares fitted line. As shown in Figure 6.3a, the remaining magnetic field perturbation due to Mercury's substorm current wedge is plotted as a function of Y'_{MSM}. Our analysis shows a persistent dawn-dusk asymmetry in the amount of flux pile-up in the near-Mercury current sheet. Implications of this result will be discussed in Section 6.4.1.

6.3.2 Plasma Beta *β*

We also examined the dawn-dusk dependency of plasma beta β_{CS} in the current sheet. The current sheet β_{CS} can be calculated using the plasma measurements from the FIPS instrument. However, the viewing geometry of the FIPS instrument during the current sheet crossing doesn't allow the instrument to observe a full phase space distribution function. By assuming subsonic flow in the current sheet and integrating several plasma measurements into one measurement of plasma parameters, we can calculate the average β_{CS} for each current sheet crossing. We can also estimate β_{CS} in the current sheet using the magnetic field measurements. Assuming pressure balance between the tail lobe and current sheet and that the plasma pressure in the tail lobe P_{Lobe} ~ 0, we can derive the following equation:

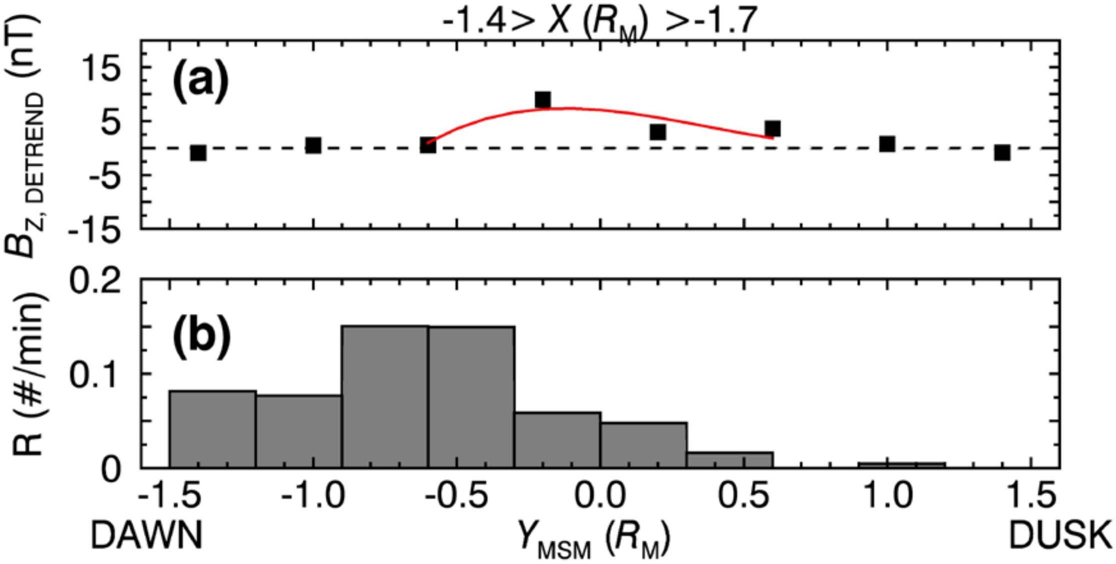

Figure 6.3 (a) Detrended B_Z as a function of Y'_{MSM} for downtail distance X'_{MSM} between -1.4 R_M to -1.7 R_M. The plot format is similar to Figure 6.2. The detrended B_Z values are calculated by subtracting B_Z values with the "baseline values", which is determined from the least-squares fitted line in panel 1 of Figure 6.2. The red line shows the persistent asymmetry of flux pile-up in the substorm current wedge after subtraction of baseline values. (b) Distribution of occurrence rate (in number per minute) of reconnection fronts observed by MESSENGER [*Sun et al.*, 2016].

$$\beta_{CS} = \left(\frac{B_{Lobe}}{B_{CS}}\right)^2 - 1 \tag{6.3}$$

Where B_{Lobe} and B_{CS} are the mean magnetic field magnitude of the tail lobe and current sheet, respectively. The β_{CS} calculated using both methods outlined above are plotted as a function of the mean Y'_{MSM} position in Figure 6.4a. Both methods of calculating β_{CS} using FIPS (red) and magnetic field (blue) measurements independently show good general agreement, hence lending confidence to the use of magnetic field-derived β_{CS} as proxy while plasma measurements are not available. Figure 6.4a also shows a significant dawn-dusk asymmetry in β_{CS} with the asymmetry being in an opposite sense as B_Z (i.e. β_{CS} is higher on the dusk side current sheet than the dawn side). This is again consistent with our earlier results of B_Z being higher on the dawn side than dusk side current sheet. From the magnetohydrodynamics (MHD) stress balance equation ($\mathbf{J} \times \mathbf{B} = \boldsymbol{\nabla}\text{P}$), as the plasma pressure increases, the tailward pressure gradient force also increases, hence stretching the magnetic field lines. B_Z decreases as the magnetic field lines are stretched and the current sheet is thinned. Therefore, our results are consistent with that expected from the MHD stress balance and show the inverse relationship between B_Z and β_{CS}. Consequently, our statistical results on B_Z and β_{CS} further suggest that the current sheet is thinner on the dusk side than dawn side (i.e. dawn-dusk asymmetry similar to B_Z).

6.3.3 Current Sheet Thickness and Current Density

The hypothesis of a dawn-dusk asymmetry in the current sheet thickness *d* and current density J_Y, is also investigated in this study using the Harris current sheet model fitting results determined by Poh17. Figure 6.4b shows the dawn-dusk distribution of the full current sheet thickness calculated from the Harris CS model fitting of the 234 selected events that satisfy the criteria of $\chi^2 \leq 0.01$. Our results show a very clear dawn-dusk asymmetry in the current sheet thickness with the dusk side current sheet ~ 1.5 times thinner than the dawn side, thus supporting our earlier B_Z and β_{CS} asymmetry results. This is also consistent with earlier Earth's magnetotail studies, which found evidence of a thinner current sheet on the dusk side of the terrestrial magnetotail [*Artemyev et al.,* 2011; *Rong et al.,* 2011]. Furthermore, our result shows that the current sheet is thicker on the flanks than the noon-midnight center of the magnetotail. The average current sheet thickness is ~ 0.3 R_M around the midnight region and grows to ~ 0.7 R_M and 0.5 R_M towards the dawn side and dusk side current sheet, respectively. This result is also consistent with Earth's magnetotail observations [*Fairfield,* 1979; *Slavin et al.,* 1985; *Vasko et al.,* 2015]. Another interesting result in Figure 6.4b is that the current sheet thicknesses for majority of the 234 events are larger than a proton inertial length (grey line), which suggest that the observed asymmetry is very likely to be in the MHD, rather than kinetic, scale.

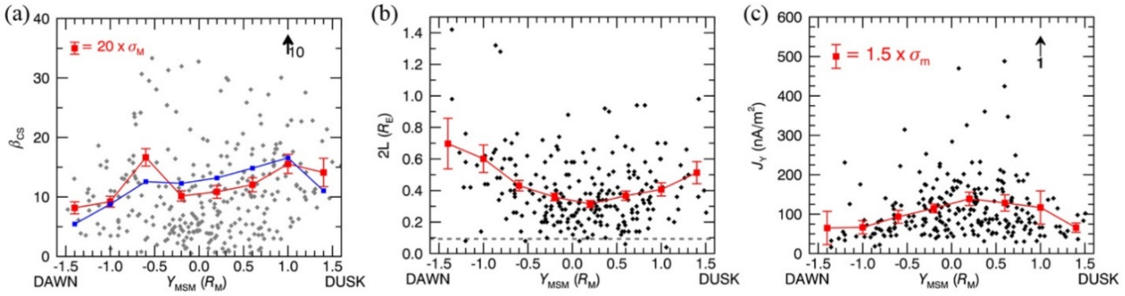

Figure 6.4 (a) Dawn-dusk distribution of current sheet plasma beta β_{CS} as shown by grey data points determined from the FIPS instrument. Red line represents the binned data points at bin size of $0.4R_M$ and the error bars represents the standard error of the mean for each bin. Note: the error bars are magnified 20 times for visual purposes. The blue line represents the binned current sheet plasma beta determined from the MAG instrument. (b) Current sheet full thickness $2L$ and (c) cross-tail current density J_Y of 234 current sheet crossings determined from the Harris current sheet model fitting. For both derived parameters, the data points (black) were binned into bins of 0.4 R_M between Y'_{MSM} = -1.6 R_M and 1.6 R_M as shown by the red data points. The error bars represent the standard error of the mean in each bin. Note: the error bars in (c) are multiplied by 1.5 for clarity.

Since MESSENGER is not a multi-spacecraft mission, and it does not have high-resolution plasma measurements, we could not independently calculate the cross-tail current density in Mercury's magnetotail. However, the Harris CS modelling allows us to estimate an upper limit on the current density J_Y as shown in Figure 6.4c. There is also an opposite dawn-dusk asymmetry in J_Y as the thickness, as expected from our earlier results. We also determine the highest mean J_Y in the midnight sector to be ~ 120 nA/m^2, which is an order of magnitude higher than Earth (~ 4 - 25 nA/m^2) [*Artemyev et al.,* 2011].

6.4 Discussion

MESSENGER observations of 319 current sheet crossings were examined with statistical analysis and model fitting. Our results can be summarized as follows:

I. A dawn-dusk asymmetry in B_Z, β_{CS} and current sheet thickness, *d*, is observed; B_Z, β_{CS} and *d* are lower, higher and thinner, respectively, on the dusk side than dawn side current sheet.
II. An enhancement in B_Z in the nearest downtail region provides tentative evidence of Mercury's substorm current wedge.

6.4.1 Mercury's Asymmetric Cross-tail Current Sheet

Our statistical analysis shows that B_Z in the cross-tail current sheet sunward of the NMNL is higher on the dusk side than dawn side. Furthermore, the strength of the asymmetry decreases with increasing downtail distance. Plasma beta, β_{CS}, and the thickness of Mercury's current sheet are also observed to have an opposite and similar dawn-dusk asymmetries as B_Z, respectively. Consistent with MHD stress balance, higher plasma pressure (i.e. lower β_{CS}) stretches the current sheet magnetic field lines more, resulting in weaker B_Z and a thinner current sheet. A summary illustration of the asymmetries observed in this study is shown in Figure 5. Magnetotail asymmetries have also been observed and studied extensively at Earth [e.g. *Walsh et al.,* 2014]. With ISEE-3 and Geotail data, B_Z in Earth's magnetotail is observed to be higher at dawn than dusk [*Slavin et al.,* 1985; *Wang et al.,* 2006] and the plasma sheet is observed to be thicker on the dawn side than dusk side [*Artemyev et al.,* 2011; *Rong et al.,* 2011]. The stark similarities in magnetotail asymmetries between Earth and Mercury beg the question of whether the cause of Mercury's magnetotail asymmetry is similar to that of Earth's.

At Earth, the ionosphere is a significant source of O^+ and the contribution of O^+ to the total plasma sheet was observed to maximize on the dusk side of the tail [*Peterson et al.,* 1981; *Ohtani et al.,* 2011]. Mercury's plasma sheet was observed to consist of primarily H^+ and Na^+, with a similar premidnight-oriented asymmetry in the observed Na^+ density [*Raines et al.,* 2013; *Gershman et al.,* 2014]. Note: O^+ is observed only as a minor species in Mercury's plasma sheet. Even though the observed density of Na^+ in Mercury's plasma sheet is smaller than H^+ by a factor of 10 [*Gershman et al.,* 2014], the mass density of Na^+ is comparable to the H^+ because Na^+ is 23 times heavier than H^+. Combining our results with earlier observations [*Raines et al.,* 2013; *Gershman et al.,* 2014], we propose a possible explanation for the observed asymmetries. Since the MESSENGER spacecraft spent most of its orbital time sunward of the statistical NMNL [*Poh et al.,* 2017], the plasma convecting sunward from a NMNL further downtail would undergo gradient-curvature drift in addition to the $\mathbf{E} \times \mathbf{B}$ drift imposed by the cross-tail electric field. The ions (i.e. H^+, Na^+ and O^+) drift duskward (premidnight) into the inner current sheet to energies of 1–5 keV [*Zurbuchen et al.,* 2011] while the electrons drift dawnward. Furthermore, *Delcourt et al.,* [2013] shows that cold Na^+ and O^+ originating from Mercury's cusp can be accelerated due to centrifugal drift and undergo non-adiabatic Speiser-type orbits moving preferentially into the dusk side inner current sheet. This process is similar to the ionospheric cusp outflow of oxygen ions moving into the plasma sheet at Earth. The mass loading of energetic heavy ions from the NMNL and cusp increases the thermal plasma pressure dusk side of the current sheet, resulting in stretching (weaker B_Z) and thinning of the dusk side current sheet (bottom right panel of Figure 5).

Consequently, this leads to the question on the effects of mass loading on current sheet dynamics at Mercury's dusk side inner-tail current sheet. Specifically, does the thinning of Mercury's dusk side inner-tail current sheet due to higher amount of heavy ions make it unstable to magnetic reconnection planetward of the NMNL? At Earth, studies on reconnection-related processes (e.g. near-Earth reconnection signatures [*Eastwood et al.,* 2010; *Nagai et al.,* 2013]) and structures (e.g. plasmoids/travelling compression regions [*Slavin et al.,* 1985; *Imber et al.,* 2011] and dipolarization fronts [*Liu et al.,* 2013]) observed higher occurrence rates towards dusk, which strongly indicates that reconnection is more likely to occur duskward of the current sheet. The asymmetry of O^+ presence in the terrestrial magnetotail leads us to question if there is any relationship between heavy ions and reconnection. The effect of O^+ on reconnection in the magnetotail remains controversial within the scientific community. *Baker et al.,* [1982] first argued that the asymmetric distribution of O^+ in Earth's plasma sheet may increase the growth of tearing mode instability, resulting in higher reconnection rate toward dusk. On the other hand, *Swisdak and Shay* [2004] concluded from their three-fluid simulation that the presence of O^+ can slow the reconnection rate since O^+, being a heavier ion, reduces the inflow Alfvén speed. Kinetic simulations have also shown slower dipolarization fronts speed [*Liang et al.,* 2016] and reduced frequency of secondary islands in reconnection region [*Karimabadi* *et al.*, 2010] due to nonlinear effects. Recently, multi-fluid simulations by *Zhang et al.*, [2016] suggested that earthward travelling flux ropes are more likely to form in the presence of ionospheric O^+ as it can reduce the reconnection rate of X-lines closer to Earth, leading to the formation of the dominant X-line (i.e., NENL) further downtail.

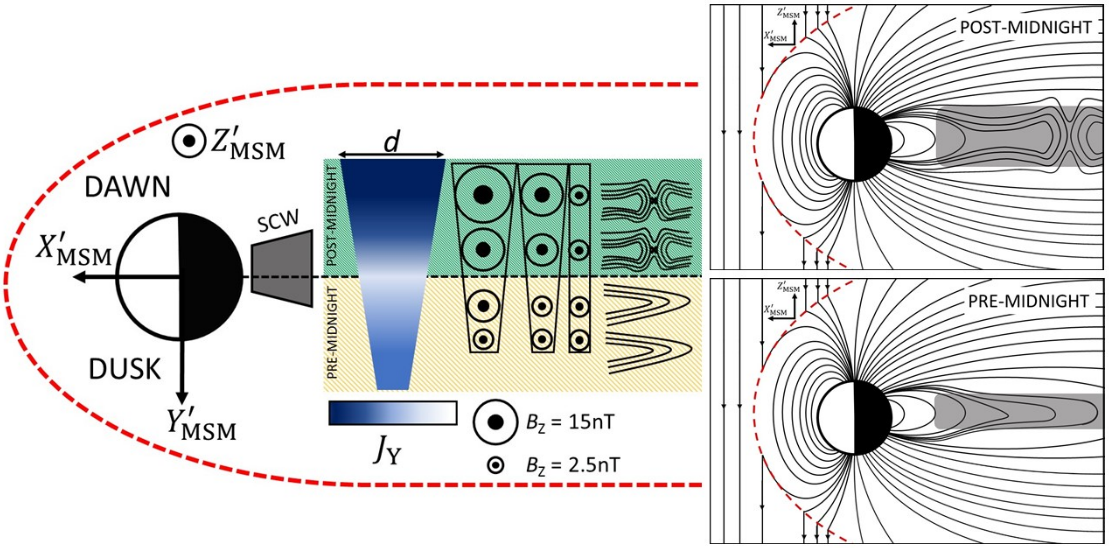

Figure 6.5 Schematic illustration of summary and explanation for all asymmetries in Mercury's current sheet observed in this study. Red dashed line represents the magnetopause. Top and bottom panels represent the post-midnight (dawn) and pre-midnight (dusk) view, respectively. The illustration shows that Mercury's current sheet is thicker and B_Z is higher on the post-midnight than the pre-midnight region. The asymmetry in B_Z also decreases in strength with increasing downtail distances. Mass loading of ions from the cusp and NMNL further downtail drift stretches the dusk side current sheet while a dawn-ward preference in reconnection occurrence sends more dipolarized flux tube towards the dawn-side current sheet, and thereby thickening the current sheet. This difference in stretching and thickening of the current sheet may explain the dawn-dusk asymmetries observed in this study.

Since Earth's and Mercury's magnetospheres have similar magnetic structure, higher occurrence rate of reconnection is expected at the stretched, duskward current sheet from the observed asymmetry of hot Na^+ [*Raines et al.*, 2013; *Gershman et al.*, 2014] and the effect might be stronger at Mercury since Na^+ is the dominant ion species for most of the time. Higher occurrence rate of magnetic reconnection products (e.g. flux ropes and dipolarization fronts) is also expected at the dusk side current sheet. However, earlier studies by *Dibraccio et al.*, [2014] observed no systematic asymmetry in the occurrence rate of plasmoids. More recently, *Sun et al.*, [2016] analyzed magnetic field data during MESSENGER orbital time period similar to earlier studies and observed a dawnward increase in the occurrence rate of plasmoids and reconnection fronts. *Lindsay et al.,* [2016] also reported more X-ray fluorescence events induced by precipitating energetic electrons from reconnection on the dawn side of Mercury's surface. These observations suggest that reconnection preferentially occur dawn side of Mercury's current sheet [*Sun et al.,* 2016]. Furthermore, the idea of dawnward preference in magnetotail reconnection supports our observation of a dawnward asymmetric magnetic flux pileup region, which is caused by the braking of dipolarized, planetward travelling flux tubes that had reconnected at an X-line further downtail. Unlike Earth, the effects of heavy ions (primarily Na^+) on magnetic reconnection at Mercury's magnetotail appear to be less controversial. Higher amount of heavy ions in the dusk side current sheet does not make it unstable to reconnection. In fact, observations presented here and earlier Mercury studies showed the opposite as heavy ions lower the reconnection rate at the dusk side current sheet. This means that the dawn side inner-tail current sheet has a relatively higher occurrence of reconnection, and therefore higher occurrence of reconnection-related dynamics, than dusk side. Despite having an opposite asymmetry pattern, the asymmetry in B_Z, current sheet thickness and β_{CS} is also consistent with the dawnward preference in reconnection. Higher occurrence of reconnection in the dawn side current sheet sends dipolarized flux tubes towards dawn side of the inner magnetotail. This thickens the post-midnight current sheet in Mercury's inner-tail region while mass loading of H^+ and heavy ions (e.g. Na^+ and O^+) continues to thin the pre-midnight current sheet, as shown in Figure 5. This process would not only create the asymmetry that was observed in this study, it also aggravates the asymmetry, which agrees with our observation of asymmetries in Mercury being stronger than that in Earth. The mechanism responsible for the asymmetries observed at Mercury appears to be very different from that of Earth. At Earth, the effects of earthward propagating dipolarized flux tubes or dipolarization events are removed when averaged over long time period. However, due to the small size of Mercury's magnetosphere, the effects of the positive B_Z (i.e., thickening of the current sheet) from the dipolarization events may be significant as suggested in this study.

6.4.2 Possible observation of Mercury's Substorm Current Wedge

An enhancement of B_Z around midnight in the innermost region ($X_{MSM} \approx$ -1.4 – -1.7 R_M) is observed in our results, which strongly suggest the possible first observation of a substorm current wedge at Mercury. Substorms at Earth had been extensively studied since its discovery by ground-based [*Akasofu,* 1964] and space-based [*McPherron et al.,* 1973; *Hesse and Birn* 1991; *Shiokawa et al.,* 1997] measurements. Many theories had been proposed to explain the substorm process at Earth but it is now widely accepted that the substorm growth phase begins when the dayside reconnection rate exceeds the nightside reconnection rate, resulting in the building up of magnetic flux in the tail lobes and stretching of magnetotail field lines. Substorm expansion phase is initiated when a sudden burst of reconnection (i.e. unloading of lobe magnetic flux) occurs in the plasma sheet and launches an Alfvénic flow burst, carrying dipolarized flux tubes towards and away from Earth. It is the braking of the earthward Bursty Bulk Flows (BBFs) due to the tailward pressure gradient force and diversion of plasma flow as it approaches the strongly dipolar, high-β inner magnetotail that creates the substorm current wedge (See *Kepko et al.,* [2015] for complete review).

The formation of Mercury's substorm current wedge would be very similar to that of Earth's. Planetary substorm current wedge is not well-understood due to the lack of in-situ observations. The presence of a Mercury substorm current wedge has been observed in global hybrid simulations [e.g., *Janhunen and Kallio,* 2004]. Although FIPS cannot measure these earthward fast plasma flows due to limitations imposed by the spacecraft, MESSENGER constantly observed dipolarization fronts [*Sundberg et al.,* 2012; *Sun et al.,* 2015; 2016] associated with these BBFs, which brakes as they encounter the stronger inner-tail magnetic field. At Earth, BBFs are rarely observed inside of 9 R_E [*McPherron et al.,* 2011] and the probability of observing these high-speed flows exceeding 400km/s decreases sharply at X_{GSM} ~ -13 R_E [e.g. *Shiokawa et al.,* 1997]. Hence, the location of the substorm current wedge (i.e., braking region) would be at X_{GSM} > -13 R_E. Scaling of the terrestrial SCW location with a factor of 8 [*Ogilvie* et al., 1977], the location of Mercury's SCW is expected to be X'_{MSM} > -1.7 R_M, which agrees with the downtail region of our observed magnetic flux pileup. Hence, our observation of a possible SCW in Mercury's inner-tail region corroborates with terrestrial expectations.

The braking of the BBFs and flow diversion around the strong dipole field generates currents perpendicular to the magnetic field ($\mathbf{j}_\perp$), which then divert into field-aligned currents at the edge of the substorm current wedge. $\mathbf{j}_\perp$ is given by the equation:

$$\mathbf{j}_\perp = \frac{\mathbf{B}}{B^2} \times \rho \frac{d\mathbf{u}}{dt} + \frac{\mathbf{B}}{B^2} \times \nabla \mathrm{P} \qquad (6.4)$$

where ρ is the number density, P is thermal pressure and **u** is plasma velocity. The first term on the left hand side of equation (6.4) is the transient inertial current generated from the deceleration of BBF. The inertial current vanishes when the fast plasma comes to a stop (i.e., $\frac{d\mathbf{u}}{dt} = 0$). The second term is the pressure gradient current generated by the azimuthal magnetic stresses and thermal pressure gradient resulting from flow diversion after braking of the flow burst [*Birn et al.,* 1999]. This current continues to flow even after the fast plasma flow comes to a stop, hence, it is the important driver for the formation of substorm current wedge.

At Earth, the currents in the substorm current wedge, especially the pressure gradient current, is difficult to calculate due to the lack of *in situ* magnetic field and plasma measurements in the near-Earth tail region where the substorm current wedge exist. With the help of simulations, we are able to get a rough sense of the order of magnitude for each of the terms in equation 6.4. This is the same for Mercury, where earlier studies [e.g., *Slavin et al.,* 1997] attempt to estimate the strength of the substorm current wedge current. However, the results presented in this study is the direct measurement of the magnetic field perturbation caused by the presence of a substorm current wedge. From Ampere's Law, we can estimate the total current I_{total} in each hemisphere of the current wedge required to the observed perturbation δB_{Z} given by the equation:

$$I_{\mathrm{total}} = \frac{1}{\mu_0 \mathrm{d}} \delta B_{\mathrm{Z}} \qquad (6.5)$$

where d is the thickness of the current sheet. Using values of d ~ 0.3 RM and δB_{Z} ~ 10 nT, we estimated the current to be ~ 6 kA, which is approximately two order of magnitude smaller than the total current carried by Earth's SCW (~ 200 kA [*Kepko et al.,* 2015]). Our estimation of the total SCW current at Mercury is also ~ 10 times smaller than the total FACs during substorm at Mercury calculated by *Sun et al.,* [2015].

The electric potential Φ across the SCW is given by the following equation:

$$\Phi = V_{\mathrm{X}} B_{\mathrm{Z}} \Delta \mathrm{y} \tag{6.6}$$

where Δy is the length of the pileup region in the Y'_{MSM} direction and is ~ 0.8 R_{M} as shown in Figure 6.2. V_{X} is the antisunward component (i.e., X_{MSM}) of BBF flow velocity before braking. The view direction of FIPS when MESSENGER traverse the current sheet is in the north-south direction. Hence, FIPS cannot measure plasma velocity in the *X*-direction. Since the BBF are accelerated to local Alfven speed at the outflow region of the reconnection X-line, we can use the average Alfvén velocity in the plasma sheet calculated by *DiBraccio et al.,* [2015] and V_{X} ~ 465 km/s. From equation 6.6, we estimate the potential across the substorm current wedge to be ~ 9 kV and hence, an electrical conductance of ~ 0.7 S.

Our estimated value of Mercury's surface conductance from the substorm current wedge agrees reasonably with the net electrical conductance of ~ 1 S calculated from Mercury's Birkeland current [*Anderson et al.,* 2014]. This suggest the possibility of a similar current closure mechanism between Mercury's substorm current wedge and the field-aligned Region 1 currents. *Anderson et al.*, [2014] was the first to identify and model Region 1 FACs at Mercury. Their analysis and modelling of the MESSENGER magnetometer data revealed field aligned currents with intensities of tens of kilo-amperes flowing downward on the dawn-side and upward on the dusk-side of the auroral oval (i.e., Region 1 currents). They found that their measurements were consistent with the current closing radially through resistive regolith, then on the surface of Mercury's highly conductive iron core (See Figure 4a in *Anderson et al.*, [2014]). Therefore, it is very likely that the current in Mercury's substorm current wedge closed in similar manner, despite the absence of an ionosphere.

Since the formation of the SCW is related to BBFs and dipolarization fronts, the inertial current associated with each high speed flow is determined to be ~ 1 kA with duration of dipolarizations Δt ~ 1s [*Sundberg et al.*, 2012], which is ~ 20% of the total current of Mercury's SCW. At Earth, the total current carried by an individual high speed flow is also ~ 20% of the total current of the terrestrial SCW [*Kepko et al.,* 2015]. This further raises the possibility of Mercury's SCW formation being similar to the scenario proposed for Earth, where the terrestrial SCW is an aggregate effect of smaller current wedges formed from individual BBFs (i.e. a "wedgelets") [e.g. *Liu et al.,* 2013].

Another interesting aspect of our analysis is the higher magnetic flux in the post-midnight magnetic flux pileup region (see Figure 3a). As mentioned earlier, the pileup region (or SCW) is caused by the braking of dipolarized earthward travelling flux tubes that had reconnected further downtail [*Shiokawa et al.*, 1997]. Therefore, the higher magnetic flux in the post-midnight flux pileup region also suggests a dawnward preference in the occurrence of magnetic reconnection. This result has very important implications on the nature of magnetic reconnection in the inner-tail region of Mercury's magnetotail. For example, *Sun et al.,* [2016] analyzed 86 dipolarization fronts identified in Mercury's plasma sheet. They concluded that there is a dawnward preference in occurrence of reconnection fronts observed at Mercury (Figure 3b), which has similar asymmetry pattern as our B_Z results. This further provides support for our explanation of the observed asymmetries mentioned in earlier sections, where the difference in stretching (mass loading of ions) and thickening (dipolarized flux tube) of Mercury's current sheet may explain the asymmetries in B_Z and current sheet thickness.

References

Akasofu S.-I., (1964) The development of the auroral substorm, *Planetary and Space Science, Volume 12, Issue 4*, Pages 273-282, ISSN 0032-0633, http://dx.doi.org/10.1016/0032-0633(64)90151-5.

Alexeev, I. I., et al. (2010), Mercury's magnetospheric magnetic field after the first two MESSENGER flybys, *Icarus*, *209*, 23–39, doi:10.1016/j.icarus.2010.01.024.

Anderson, B. J., M. H. Acuña, D. A. Lohr, J. Scheifele, A. Raval, H. Korth, and J. A. Slavin (2007), The Magnetometer instrument on MESSENGER, *Space Sci. Rev.*, *131*, 417–450, doi:10.1007/s11214-007-9246-7.

Anderson, B. J., C. L. Johnson, H. Korth, M. E. Purucker, R. M. Winslow, J. A. Slavin, S. C. Solomon, R. L. McNutt Jr., J. M. Raines, and T. H. Zurbuchen (2011), The global magnetic field of Mercury from MESSENGER orbital observations, *Science*, *333*, 1859–1862, doi:10.1126/science.1211001.

Anderson, B. J., C. L. Johnson, H. Korth, J. A. Slavin, R. M. Winslow, R. J. Phillips, S. C. Solomon, and R. L. McNutt Jr. (2014), Steady-state field-aligned currents at Mercury, Geophy. Res. Lett., 41, 7444–7452, doi:10.1002/2014GL061677.

Andrews, G. B., et al. (2007), The Energetic Particle and Plasma Spectrometer instrument on the MESSENGER spacecraft, *Space Sci. Rev.*, *131*, 523–556, doi:10.1007/s11214-007-9272-5.

Arridge, C. S., M. Kane, N. Sergis, K. K. Khurana, and C. M. Jackman (2015a), Sources of local time asymmetries in magnetodiscs, *Space Sci. Rev.*, *187(1)*, 301–333, doi:10.1007/s11214-015-0145-z

Artemyev, A. V., A. A. Petrukovich, R. Nakamura, and L. M. Zelenyi (2011), Cluster statistics of thin current sheets in the Earth magnetotail: Specifics of the dawn flank, proton temperature profiles and electrostatic effects, *J. Geophys. Res.*, *116*, A09233, doi:10.1029/2011JA016801.

Baker, D. N., Hones, E. W., Young, D. T. and Birn, J. (1982), The possible role of ionospheric oxygen in the initiation and development of plasma sheet instabilities. *Geophys. Res. Lett.*, *9*, 1337–1340,doi:10.1029/GL009i012p01337.

Baumjohann, W., G. Paschmann, *and* H. Lühr *(*1990*)*, Characteristics of high-speed ion flows in the plasma sheet, *J. Geophys. Res., 95(A4),* 3801–3809, *doi:*10.1029/JA095iA04p03801.

Baumjohann, W., M. Hesse, S. Kokubun, T. Mukai, T. Nagai, and A. A. Petrukovich (1999), Substorm dipolarization and recovery, *J. Geophys. Res., 104(A11)*, 24995–25000, doi:10.1029/1999JA900282.

Birn, J., et al. (2001), Geospace Environmental Modeling (GEM) Magnetic Reconnection Challenge, *J. Geophys. Res., 106(A3)*, 3715–3719, doi:10.1029/1999JA900449.

Bunce E.J., S.W.H. Cowley, (2001), Local time asymmetry of the equatorial current sheet in Jupiter's magnetosphere, *Planetary and Space Science*, *Volume 49*, *Issues 3–4*, Pages 261-274, ISSN 0032-0633, doi:10.1016/S0032-0633(00)00147-1.

Delcourt, D. C. (2013), On the supply of heavy planetary material to the magnetotail of Mercury, *Ann. Geophys.*, *31*, 1673-1679, doi:10.5194/angeo-31-1673-2013.

DiBraccio, G. A., J. A. Slavin, S. A. Boardsen, B. J. Anderson, H. Korth, T. H. Zurbuchen, J. M. Raines, D. N. Baker, R. L. McNutt Jr., and S. C. Solomon (2013), MESSENGER observations of magnetopause structure and dynamics at Mercury, *J. Geophys. Res. Space Physics*, *118*, 997–1008, doi:10.1002/jgra.50123.

DiBraccio, G. A., et al. (2015), MESSENGER observations of flux ropes in Mercury's magnetotail, *Planet. Space Sci.*, *115*, 77–89, doi:10.1016/j.pss.2014.12.016.

Dungey, J. W. (1961), Interplanetary magnetic field and the auroral zones, *Phys. Rev. Lett.*, *6*, 47.

Eastwood, J. P., T. D. Phan, M. Øieroset, and M. A. Shay (2010), Average properties of the magnetic reconnection ion diffusion region in the Earth's magnetotail: The 2001–2005 Cluster observations and comparison with simulations, *J. Geophys. Res.*, *115*, A08215, doi:10.1029/2009JA014962.

Fairfield, D. H. (1979), On the average configuraton of the geomagnetic tail, *J. Geophys. Res.*, *84(A5)*, 1950–1958, doi:10.1029/JA084iA05p01950.

Fairfield, D. H., R. P. Lepping, E. W. Hones Jr., S. J. Bame, J. R. Asbridge *(1981)* Simultaneous measurements of magnetotail dynamics by IMP spacecraft, *J. Geophys. Res.*, *86*, 1396–1414.

Garcia-Sage, K., T. E. Moore, A. Pembroke, V. G. Merkin, and W. J. Hughes (2015), Modeling the effects of ionospheric oxygen outflow on bursty magnetotail flows, *J. Geophys. Res. Space Physics*, *120*, 8723–8737, doi:10.1002/2015JA021228.

Genestreti K.J., Fuselier S.A., Goldstein J., Nagai T., Eastwood J.P., (2014) The location and rate of occurrence of near-Earth magnetotail reconnection as observed by Cluster and Geotail, *Journal of Atmospheric and Solar-Terrestrial Physics, Volume 121*, Part A, Pages 98-109, ISSN 1364-6826.

Gershman, D. J., J. A. Slavin, J. M. Raines, T. H. Zurbuchen, B. J. Anderson, H. Korth, D. N. Baker, and S. C. Solomon (2014), Ion kinetic properties in Mercury's pre-midnight plasma sheet, *Geophys. Res. Lett., 41*, 5740–5747, doi:10.1002/2014GL060468.

Harris, E. G. (1962), On a plasma sheath separating regions of oppositely directed magnetic field, *Nuovo Cimento, 23*, 115–121.

Hesse, M., and J. Birn (1991), On dipolarization and its relation to the substorm current wedge, *J. Geophys. Res., 96(A11)*, 19417–19426, doi:10.1029/91JA01953.

Kalegaev V.V., Alexeev I.I., Nazarkov I.S., Angelopoulos V., Runov A. (2014) On the large-scale structure of the tail current as measured by THEMIS, *Advances in Space Research, Volume 54, Issue 9*, Pages 1773-1785, ISSN 0273-1177, http://dx.doi.org/10.1016/j.asr.2014.07.019.

Karimabadi, H., V. Roytershteyn, C. G. Mouikis, L. M. Kistler, and W. Daughton (2011), Flushing effect in reconnection: Effects of minority species of oxygen ions, *Planet. Space Sci., 59(7)*, 526–536.

Kepko, L., McPherron, R.L., Amm, O. et al. (2015) Substorm Current Wedge Revisited, *Space Sci Rev, 190*: 1. doi:10.1007/s11214-014-0124-9

Korth, H., N. A. Tsyganenko, C. L. Johnson, L. C. Philpott, B. J. Anderson, M. M. Al Asad, S. C. Solomon, and R. L. McNuttJr. (2015), Modular model for Mercury's magnetospheric magnetic field confined within the average observed magnetopause. *J. Geophys. Res. Space Physics, 120*, 4503–4518. doi: 10.1002/2015JA021022.

Lepping, R. P., J. A. Jones, and L. F. Burlaga (1990), Magnetic field structure of interplanetary magnetic clouds at 1 AU, *J. Geophys. Res., 95(A8)*, 11957–11965, doi:10.1029/JA095iA08p11957.

Liang, H., M. Ashour-Abdalla, G. Lapenta, and R. J. Walker (2016), Oxygen impacts on dipolarization fronts and reconnection rate, *J. Geophys. Res. Space Physics, 121*, 1148–1166, doi:10.1002/2015JA021747.

Liu, J., V. Angelopoulos, A. Runov, *and* X.-Z. Zhou *(*2013*)*, On the current sheets surrounding dipolarizing flux bundles in the magnetotail: The case for wedgelets, *J. Geophys. Res. Space Physics, 118,* 2000–2020, *doi:* 10.1002/jgra.50092.

S.T. Lindsay, M.K. James, E.J. Bunce, S.M. Imber, H. Korth, A. Martindale, T.K. Yeoman, MESSENGER X-ray observations of magnetosphere–surface interaction on the nightside of Mercury (2016), *Planetary and Space Science, Volume 125*, Pages 72-79, ISSN 0032-0633, http://dx.doi.org/10.1016/j.pss.2016.03.005.

Imber, S. M., J. A. Slavin, H. U. Auster, *and* V. Angelopoulos *(*2011*),* A THEMIS survey of flux ropes and traveling compression regions: Location of the near-Earth reconnection site during solar minimum, *J. Geophys. Res.*, *116, A02201, doi:*10.1029/2010JA016026.

Janhunen, P. and Kallio, E. (2004), Surface conductivity of Mercury provides current closure and may affect magnetospheric symmetry, *Ann. Geophys., 22*, 1829-1837, doi:10.5194/angeo-22-1829-2004.

Jia, X., J. A. Slavin, T. I. Gombosi, L. K. S. Daldorff, G. Toth, and B.van der Holst (2015), Global MHD simulations of Mercury's magnetosphere with coupled planetary interior: Induction effect of the planetary conducting core on the global interaction. *J. Geophys. Res. Space Physics*, *120*, 4763–4775. doi: 10.1002/2015JA021143.

McPherron, R. L., C. T. Russell, and M. P. Aubry (1973), Satellite studies of magnetospheric substorms on August 15, 1968: 9. Phenomenological model for substorms, *J. Geophys. Res.*, *78(16)*, 3131–3149, doi:10.1029/JA078i016p03131.

McPherron, R. L., T.-S. Hsu, J. Kissinger, X. Chu, and V. Angelopoulos (2011), Characteristics of plasma flows at the inner edge of the plasma sheet, *J. Geophys. Res.*, *116*, A00I33, doi:10.1029/2010JA015923.

Nagai, T. and Machida, S. (1998) Magnetic Reconnection in the Near-Earth Magnetotail, in New Perspectives on the Earth'S Magnetotail (eds A. Nishida, D.N. Baker and S.W.H. Cowley), American Geophysical Union, Washington, D. C.. doi: 10.1029/GM105p0211.

Nagai, T.*,* I. Shinohara, S. Zenitani, R. Nakamura, T. K. M. Nakamura, M. Fujimoto, Y. Saito*, and* T. Mukai *(*2013*),* Three-dimensional structure of magnetic reconnection in the magnetotail from Geotail observations*, J. Geophys. Res. Space Physics, 118,* 1667–1678*, doi:*10.1002/jgra.50247.

Nakai, H., Y. Kamide, and C. T. Russell (1999), Dependence of the near-Earth magnetotail magnetic field on storm and substorm activities, *J. Geophys. Res.*, *104(A10)*, 22701–22711, doi:10.1029/1999JA900273.

Nakamura, R., et al., (2002) Fast flow during current sheet thinning, *Geophys. Res. Lett., 29(23)*, 2140, doi:10.1029/2002GL016200.

Narita, Y., Nakamura, R., and Baumjohann, W. (2013) Cluster as current sheet surveyor in the magnetotail, *Ann. Geophys., 31*, 1605-1610, doi:10.5194/angeo-31-1605-2013.

Ogilvie, K. W., J. D. Scudder, V. M. Vasyliunas, R. E. Hartle, and G. L. Siscoe (1977), Observations at the planet Mercury by the plasma electron experiment: Mariner 10, *J. Geophys. Res., 82*, 1807–1824, doi:10.1029/JA082i013p01807.

Ohtani, S., M. Nosé, S. P. Christon, and A. T. Y. Lui (2011), Energetic O^+ and H^+ ions in the plasma sheet: Implications for the transport of ionospheric ions, *J. Geophys. Res., 116*, A10211, doi:10.1029/2011JA016532.

Peterson, W. K., R. D. Sharp, E. G. Shelley, R. G. Johnson, and H. Balsiger (1981), Energetic ion composition of the plasma sheet, *J. Geophys. Res., 86(A2)*, 761–767, doi:10.1029/JA086iA02p00761.

Poh, G., J. A. Slavin, X. Jia, J. M. Raines, S. M. Imber, W.-J. Sun, D. J. Gershman, G. A. DiBraccio, K. J. Genestreti, and A. W. Smith (2017), Mercury's cross-tail current sheet: Structure, X-line location and stress balance, *Geophys. Res. Lett., 44*, 678–686, doi:10.1002/2016GL071612.

Raines, J. M., J. A. Slavin, T. H. Zurbuchen, G. Gloeckler, B. J. Anderson, D. N. Baker, H. Korth, S. M. Krimigis, and R. L. McNutt Jr. (2011), MESSENGER observations of the plasma environment near Mercury, *Planet. Space Sci., 59*, 2004–2015, doi:10.1016/j.pss.2011.02.004.

Raines, J. M., et al. (2012), Distribution and compositional variations of plasma ions in Mercury's space environment: The first three Mercury years of MESSENGER observations, *J. Geophys. Res. Space Physics, 118*, 1604–1619, doi:10.1029/2012JA018073.

Rong, Z. J., W. X. Wan, C. Shen, X. Li, M. W. Dunlop, A. A. Petrukovich, T. L. Zhang, and E. Lucek (2011), Statistical survey on the magnetic structure in magnetotail current sheets, *J. Geophys. Res., 116*, A09218, doi:10.1029/2011JA016489.

Russell, C. T., D. N. Baker, and J. A. Slavin (1988), The magnetosphere of Mercury, in Mercury, edited by F. Vilas, C. R. Chapman, and M. S. Matthews, pp. 514–561, *Univ. of Ariz. Press*, Tucson.

Shiokawa, K., W. Baumjohann, and G. Haerendel (1997), Braking of high-speed flows in the near-Earth tail, *Geophys. Res. Lett.*, *24*, 1179–1182, doi:10.1029/97GL01062.

Slavin, J. A., *and* R. E. Holzer *(*1979*)*, The effect of erosion on the solar wind stand-off distance at Mercury, *J. Geophys. Res.*, 84, 2076–2082, *doi:*10.1029/JA084iA05p02076.

Slavin, J. A., E. J. Smith, D. G. Sibeck, D. N. Baker, R. D. Zwickl, *and* S.-I. Akasofu *(*1985*)*, An ISEE 3 study of average and substorm conditions in the distant magnetotail, *J. Geophys. Res.*, *90*, 10,875–10,895.

Slavin J. A., J.C.J. Owen, J.E.P. Connerney, S.P. Christon (1997), Mercury: The Planet and its Magnetosphere Mariner 10 observations of field-aligned currents at Mercury, *Planetary and Space Science*, *Volume 45, Issue 1*, Pages 133-141, ISSN 0032-0633, http://dx.doi.org/10.1016/S0032-0633(96)00104-3.

Slavin, J. A., *et al. (*2009*)*, MESSENGER observations of magnetic reconnection in Mercury's magnetosphere, *Science*, *324*, 606–610, *doi:*10.1126/science.1172011.

Slavin, J. A., *et al. (*2010*)*, MESSENGER observations of extreme loading and unloading of Mercury's magnetic tail, *Science*, *329*, 665–668, *doi:*10.1126/science.1188067.

Slavin, J. A., *et al. (*2012*)*, MESSENGER and Mariner 10 flyby observations of magnetotail structure and dynamics at Mercury, *J. Geophys. Res.*, *117, A01215, doi:*10.1029/2011JA016900.

Smith, A. W., C. M. Jackman, and M. F. Thomsen (2016), Magnetic reconnection in Saturn's magnetotail: A comprehensive magnetic field survey, *J. Geophys. Res. Space Physics*, *121*, 2984–3005, doi:10.1002/2015JA022005.

Sun, W.-J., J. A. Slavin, S. Fu, J. M. Raines, Q.-G. Zong, S. M. Imber, Q. Shi, Z. Yao, G. Poh, D. J. Gershman, Z. Pu, T. Sundberg, B. J. Anderson, H. Korth, and D. N. Baker (2015), MESSENGER observations of magnetospheric substorm activity in Mercury's near magnetotail. *Geophys. Res. Lett.*, *42*, 3692–3699. doi: 10.1002/2015GL064052.

Sundberg, T., et al. (2012), MESSENGER observations of dipolarization events in Mercury's magnetotail, *J. Geophys. Res.*, *117*, A00M03, doi:10.1029/2012JA017756.

Shay, M. A., and M. Swisdak (2004), Three-species collisionless reconnection: Effect of O+ on magnetotail reconnection, *Phys. Rev. Lett.*, *93*, 175001, doi:10.1103/PhysRevLett.93.175001.

Thompson, S. M., M. G. Kivelson, K. K. Khurana, R. L. McPherron, J. M. Weygand, A. Balogh, H. Réme, and L. M. Kistler (2005), Dynamic Harris current sheet thickness from Cluster current density and plasma measurements, *J. Geophys. Res., 110*, A02212, doi:10.1029/2004JA010714.

Vasko, I. Y., A. A. Petrukovich, A. V. Artemyev, R. Nakamura, *and* L. M. Zelenyi *(*2015*)*, Earth's distant magnetotail current sheet near and beyond lunar orbit*, J. Geophys. Res. Space Physics*, *120*, 8663–8680*, doi:*10.1002/2015JA021633.

Volwerk, M., et al. (2013),Comparative magnetotail flapping: an overview of selected events at Earth, Jupiter and Saturn, *Ann. Geophys.*, 31, 817–833, doi:10.5194/angeo-31-817-2013.

Walsh, A. P., Haaland, S., Forsyth, C., Keesee, A. M., Kissinger, J., Li, K., Runov, A., Soucek, J., Walsh, B. M., Wing, S., and Taylor, M. G. G. T.: Dawn–dusk asymmetries in the coupled solar wind–magnetosphere–ionosphere system: a review, *Ann. Geophys.*, *32*, 705-737, doi:10.5194/angeo-32-705-2014, 2014.

Wang, C.-P., L. R. Lyons, M. W. Chen, and F. R. Toffoletto (2004), Modeling the transition of the inner plasma sheet from weak to enhanced convection, *J. Geophys. Res.*, *109*, A12202, doi:10.1029/2004JA010591.

Wang, Y. L., R. C. Elphic, B. Lavraud, M. G. G. T. Taylor, J. Birn, C. T. Russell, J. Raeder, H. Kawano, *and* X. X. Zhang *(*2006*)*, Dependence of flux transfer events on solar wind conditions from 3 years of Cluster observations, *J. Geophys. Res., 111, A04224, doi:*10.1029/2005JA011342.

Zhang, B., O. J. Brambles, W. Lotko, J. E. Ouellette, and J. G. Lyon (2016), The role of ionospheric O+ outflow in the generation of earthward propagating plasmoids, *J. Geophys. Res. Space Physics*, *121*, 1425–1435, doi:10.1002/2015JA021667.

Zurbuchen, T. H., et al. (2011), MESSENGER observations of the spatial distribution of planetary ions near Mercury, *Science*, *333*, 1862–1865, doi:10.1126/science.1211302.

CHAPTER VII

CONCLUSIONS

In this work, we have studied various cusp and magnetotail phenomena at Mercury by analyzing MESSENGER's magnetic field and plasma measurements. Through these studies, we seek to understand and explain (1) the structure, formation and evolution of cusp plasma filaments, (2) the structure and stress balance of Mercury's tail current sheet, and (3) observed asymmetries in Mercury's magnetotail. Here, we summarize the main conclusions reached to answer our guiding science questions.

Q1. What are cusp plasma filaments? What impact do they have on Mercury's cusp region?

The study on cusp plasma filaments has shown that the brief, ~ 2–3-s-long, deep ($< \frac{\delta B}{B} > \sim 22\%$) decreases in magnetic field intensity observed in and around Mercury's magnetospheric cusp by MESSENGER are diamagnetic in nature and most likely due to plasma being injected along the flux tubes at the magnetopause by localized reconnection. MVA results have shown that the majority of the filaments are quasi-cylindrical or slightly flattened cylindrical magnetic flux tubes aligned with the ambient dayside magnetic field. The FIPS plasma measurements indicate that the plasma in the filaments has energy levels similar to those of the magnetosheath plasma. Analysis of measurements from MESSENGER's low-altitude campaign indicates that these filaments extend down to very low altitudes, < 50 km, and probably are observable on the surface.

This result strongly suggests that most of the plasma in each filament eventually precipitates onto Mercury's surface in the vicinity of the cusp by the time the flux tubes are swept into the magnetotail. The same impulsive reconnection at the magnetopause that produces FTEs increases the velocity parallel to the magnetic field and injects plasma down the flux tubes and into the cusp. As the magnetic field magnitude increases with decreasing altitude, the particles gain more perpendicular energy and produce the diamagnetism observed in these filaments. Observations of filaments with "residual twist" similar to the helical structure of magnetic flux ropes, but without the core field, support our hypothesis that cusp filaments map to FTEs at the magnetopause. We estimated the integrated particle precipitation rate from the filaments to be ~ $(2.70\pm0.09) \times 10^{25}$ s^{-1}. This rate is larger than estimates determined in previous studies of the average cusp magnetic field depression by more than an order of magnitude. This result has important implications for surface sputtering and space weathering in the cusp region at Mercury. Our estimation provides an upper limit on flux precipitation by cusp filaments at Mercury. During extreme solar wind conditions, the total flux of precipitating particles contributed by the filaments could be the dominant source of particles for sputtering neutral atoms off the surface and related space weathering effects.

Q2. What is the structure of Mercury's cross-tail current sheet? Do the stresses measured by MESSENGER balance? What is the location of the statistical X-line in Mercury's current sheet?

We have examined the structure of Mercury's magnetotail and concluded that Mercury's current sheet can be described with a Harris current sheet model reasonably well. From the Harris current sheet modeling results, we determined the average Mercury's current sheet thickness to be ~ 0.39 R_M and current density ~ 92 nA/m^2. From the analysis of B_Z polarity, we concluded that MESSENGER spent most of its mission time planetward of the statistical X-line and calculated the average NMNL to be X'_{MSM} ~ -3 R_M. By modelling Mercury's current sheet using a slab current sheet model, we calculated the inner edge of current sheet location to be X'_{MSM} ~ -1.22 R_M.

FIPS measurements are also used in this study. We examined the downtail variation of the proton thermal pressure, fitted a straight line to the data points and calculated the gradient of thermal pressure to be ~ 0.62 nPa/R_M. Using previous results of current density and magnetic field, we also calculate the $\mathbf{J} \times \mathbf{B}$ term to be ~ 1.81 nPa/R_M, which is ~ 33% of the gradient of thermal pressure. Therefore, stress balance is not maintained and we determined that heavy ions and H^+ temperature anisotropy are important in maintaining stress balance within Mercury's CPS. Previous investigations have revealed many qualitative similarities between Mercury's and Earth's magnetotails, despite the differences in upstream conditions, internal plasma composition, finite gyro-radius scalings, and Mercury's lack of ionosphere.

Q3. Are asymmetries present in Mercury's cross-tail current sheet?

MESSENGER's magnetic field and plasma observations in Mercury's magnetotail allowed us to model and understand the structure of Mercury's current sheet. We present the first MESSENGER observations of a dawn-dusk asymmetry in B_Z, β_{CS} and the thickness of Mercury's current sheet. They are consistent with MHD stress balance and similar to the magnetotail asymmetries observed at Earth. B_Z, β_{CS} and thickness are lower, higher and thinner, respectively, on the dusk side than dawn side current sheet.

We propose that the asymmetry observed in our study is the result of mass loading of Na^+ into the dusk side current sheet from the NMNL and cusp. This mass loading leads to closed flux tubes stretching and a thinner dusk side (than dawn side) current sheet. Furthermore, our analysis shows that B_Z is higher in the dawn side magnetic pileup region, which suggest higher reconnection occurrence in the dawn side current sheet. The thicker dawn side current sheet found in our study requires a source of sunward closed magnetic flux, which is stronger on the dawn side. Accidentally, our observed asymmetry in B_Z sunward of the NMNL is consistent with the higher occurrence of magnetic reconnection reported by earlier studies on the basis of the occurrence of dipolarization fronts and plasmoids. This aggravates the dawn-dusk asymmetry already present due to mass loading of Na^+ in the dusk side inner-tail region.

Another result of our dawn-dusk asymmetry study is the possible observation of a substorm current wedge in Mercury's inner magnetotail. We estimated the total FAC associated with Mercury's SCW is ~ 6 kA, which is ~ two order of magnitude lower than that of Earth's. We also estimated the potential across the substorm current wedge to be ~ 9 kV and a conductance of ~ 0.7 S to close the current in the current wedge. Our calculated conductance value of Mercury's surface is similar to an earlier study on the field-aligned Region 1 currents. Therefore, we propose that the substorm current wedge current closes radially through the resistive regolith and across the surface of the highly conductive core.

CHAPTER VIII

FUTURE WORK

8.1 Case Study of Mercury's Flux Transfer Event and Filament Showers

The statistical results presented in Chapter IV clearly show that Mercury's cusp plasma filaments are high altitude extensions of the flux transfer events (FTEs) formed at Mercury's dayside magnetopause. The main question from the cusp filament study in Chapter IV is: *How are the cusp plasma filaments related to FTEs and/or FTE showers at Mercury?* Hence, a natural extension of the cusp plasma filament work is to analyze magnetic field measurements during orbits when MESSENGER simultaneously observed cusp filaments and FTE/FTE showers.

In summary, FTEs are helical magnetic flux ropes formed by simultaneous or sequential multiple X-lines reconnection on the dayside magnetopause. FTEs can also compress the surrounding magnetic field lines to create travelling compression regions (TCRs) as they slide along the surface of the magnetopause while being transported nightside. At Mercury, due to frequent and intense magnetic reconnection, FTEs with durations of ~ 1 - 3 s are observed to form in "showers" that last for tens of minutes [*Slavin et al.,* 2012]. FTEs have one end connected to the solar wind and the other connected to the planetary surface at the cusp. At Mercury, the low-altitude extensions of FTEs were observed as cusp plasma filaments, which are magnetic structures, characterized by highly-localized ~ 3-s-long decrease in |**B**|, formed from diamagnetic effects of precipitating plasma at Mercury's cusp. Here, we present a case study of magnetopause crossings on 28th April 2013 with observations of FTE & cusp filament showers. Figure 8.1 show

MESSENGER's orbit (left) during magnetopause crossing on 28th April 2013 and the magnetic field measurements (right) in the same time interval, respectively.

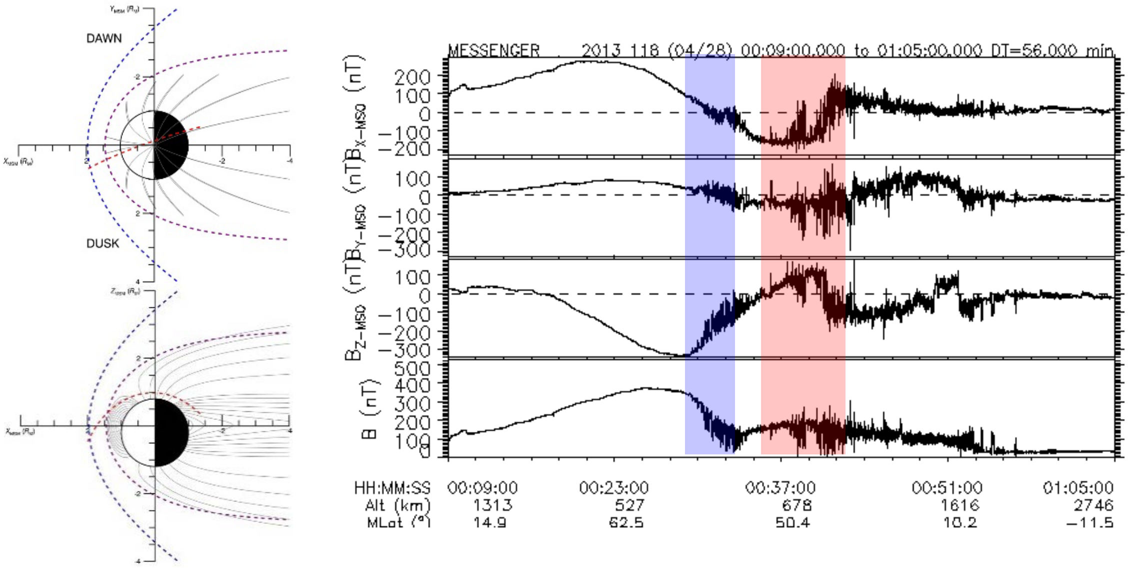

Figure 8.1 (left) MESSENGER's orbit during magnetopause crossing on 28th April 2013. A scaled-T89 magnetic field model [*Tsyganenko*, 1996], with a model bow shock and magnetopause [*Winslow et al.*, 2012], are also plotted. (right) Magnetic field measurements in the MSO coordinate system on 28th April 2013. Red shaded region represents the magnetopause crossing and blue shaded region represents cusp traversal.

The time intervals of magnetopause and cusp crossings were identified as shown in Figure 8.1. The magnetic field measurements during the magnetopause crossing is then converted into the LMN-coordinate system with **N** = [0.81, 0.06, -0.56], **M** = [-0.31, 0.89, 0.34], **L** = [-0.50, -0.45, 0.74] as shown in the top panel of Figure 8.1. In this coordinate, the characteristic bipolar signature of a FTE or TCR is displayed in the **N**-direction of the magnetic field measurements (See Chapter 1.4 for more information). A total of 30 FTEs and TCRs were observed in rapid successions, with an average separation time of ~ 8 s. Subsequently, 20 cusp plasma filaments, with average separation time of ~ 13 s, were also identified as MESSENGER enters Mercury's cusp at higher latitude and lower altitude as shown in bottom panel of Figure 8.2.

Sequential observation of FTEs/TCRs and cusp plasma filaments indicates that occurrence of cusp plasma filament is correlated with high FTE showers activity and is consistent with the idea of Mercury's cusp being an aggregate of individual cusp filaments, which are low altitude footprints of FTEs in the cusp. Time duration of FTEs and filaments are ~ 1–2s and ~ 4–5s, respectively. If the FTEs and filaments were magnetically connected, then one would intuitively think that the ratio of time separation and duration between FTE and filament should be 1:1; but they are not. Could the coalescence of small FTEs into larger ones as demonstrated in PIC simulations and observations at Earth explain this inconsistency? Are the larger, irregular filaments remote observations of FTE dynamics occurring simultaneously at Mercury's magnetopause? What is the temporal dependency of FTE showers and cusp filaments occurrence and properties on the upstream solar wind conditions? Continuation of this work would be to determine the physical properties of the identified FTEs and filaments using some of the analysis methods mentioned in Chapter I and III (i.e., MVA and force-free flux rope modelling). This will further our understanding of the microphysics of FTEs and cusp filaments dynamics.

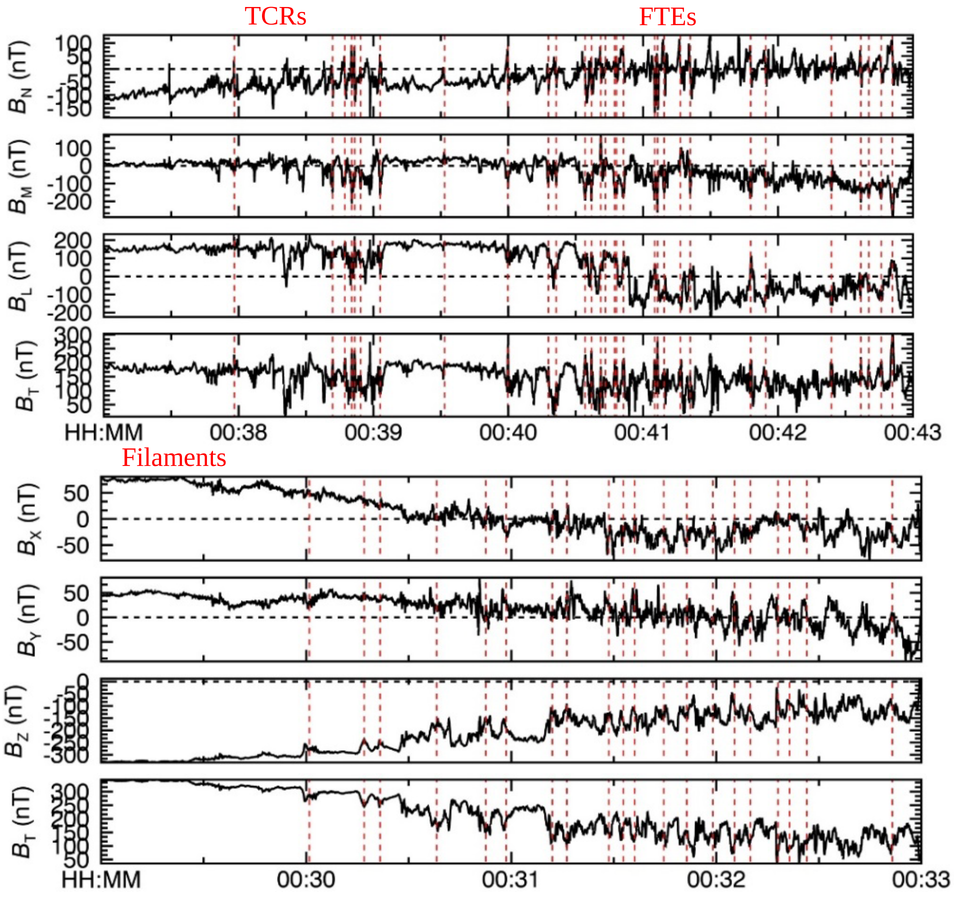

Figure 8.2 (top) Closed-up magnetic field measurements of magnetopause crossing on 28th April 2013. Red dashed lines represent identified FTEs/TCRs. Plot is shown in boundary normal coordinate. (bottom) Closed-up magnetic field measurements of cusp encounter on 28th April 2013. Red dashed lines represent identified cusp plasma filaments.

Statistical studies of more magnetopause crossings with simultaneous observations of FTEs and cusp filaments should also be performed to determine any solar wind dependencies in the occurrence and properties of FTEs and cusp filaments. Studies to advance the understanding of cusp plasma filaments are of high importance to the dayside magnetosphere community. FTEs carry open magnetic flux that drives global magnetospheric convection and hence, it is important to know the total contribution of open flux from these FTEs. At Earth, it is believed that the total flux contribution from terrestrial FTEs are underestimated due to the lack in understanding of total number of FTEs at the magnetopause [*Robert Fear*, private communication]. This is even more so at Mercury, where FTEs are formed in "showers". Since FTEs and cusp filaments are magnetically connected, cusp filaments are the "remote" observations of the FTEs that are forming at the dayside magnetopause at that specific time. Therefore, the current and future work on cusp filaments will lead to enormous advances in our understanding of magnetospheric processes.

8.2 Mercury's Substorm Current Wedge

In Chapter VI, we reported the first possible observation of the Mercury's substorm current wedge and concluded that the total current is ~ 6 kA with a possible current mechanism similar to the observed field-aligned currents. Mercury remains an importance to the magnetospheric substorm community because it has a magnetosphere structurally similar to Earth's, yet the substorm process is so different in many aspects (e.g., timescale). Therefore, it is a perfect natural laboratory to test the validity and robustness of any terrestrial substorm theories, and continuation of future research to study Mercury's SCW is of utmost importance.

However, the research methodology for Mercury's SCW is different than that of Earth's. At Earth, large scale ionospheric response to the braking of the fast flow and formation of the substorm current wedge can be easily observed, thereby allowing simultaneous two-point measurements (ground and space-based) in the study of the substorm processes. At Mercury, we can only rely on in situ magnetic field and plasma measurements from orbit since there aren't any ground-based mesurements of Mercury's substorm current wedge at higher latitude of its nightside magnetosphere due to the lack of an ionosphere. Therefore, continuation of the work presented in Chapter VI would include performing large-scale statistical studies by utilizing the fast timescale of Mercury's substorm process to establish a more complete picture of substorm activities at Mercury. Comparison of data with simulations is also necessary to confirm the existence and advance our understanding of the Mercury's substorm current wedge.

Looking further into the future, analysis of magnetic field and plasma measurements from the upcoming European Space Agency's (ESA) Bepi-Colombo mission will bring our understanding of Mercury's magnetospheric dynamics to the next level. The limitations of MESSENGER orbit and plasma measurements have left many questions unanswered. The Bepi-Colombo mission, which consists of two orbiters (Mercury Planetary Orbiter and Mercury Magnetospheric Orbiter) orbiting Mercury at an apogee of X'_{MSM} ~ -1.6 R_M and -5 R_M, respectively, would allow simultaneous two-point observations at a wide range of downtail distances and in both northern and southern hemispheres. These unprecedented observational capabilities will greatly improve our understanding of Mercury's magnetospheric dynamics and response to coronal mass ejections events.

References

Slavin, J. A., et al. (2012), MESSENGER observations of a flux-transfer-event shower at Mercury, *J. Geophys. Res.*, *117,* A00M06, doi:10.1029/2012JA017926.

Tsyganenko, N. A., and D. P. Stern (1996), Modeling the global magnetic field of the large-scale Birkeland current systems, *J. Geophys. Res.*, *101*(A12), 27187–27198, doi:10.1029/96JA02735.

Winslow, R. M., C. L. Johnson, B. J. Anderson, H. Korth, J. A. Slavin, M. E. Purucker, and S. C. Solomon (2012), Observations of Mercury's northern cusp with MESSENGER's Magnetometer, *Geophys. Res. Lett., 39, L08112,* doi:10.1029/2012GL051472.